Development of Accelerator Based Spatially Resolved Ion Beam Analysis Techniques for the Study of Plasma Materials Interactions in Magnetic Fusion Devices

by

Harold Salvadore Barnard
B.S. Applied and Engineering Physics, Cornell University (2006)
S.M. Nuclear Science and Engineering, Massachusetts Institute of Technology (2009)

Submitted to the Department of Nuclear Science and Engineering
in partial fulfillment of the requirements for the degree of
Doctor of Science in Nuclear Science and Engineering
at the
MASSACHUSETTS INSTITUTE OF TECHNOLOGY
February 2014

ARCHIVES
MASSACHUSETTS INSTITUTE OF TECHNOLOGY
APR 08 2014
LIBRARIES

© Massachusetts Institute of Technology 2014. All rights reserved.

Author ....
Department of Nuclear Science and Engineering
January 27, 2014

Certified by..... .....
Dennis G. Whyte
Professor of Nuclear Science and Engineering
Thesis Supervisor

Certified by .....
Richard C. Lanza
Senior Research Scientist
Thesis Reader

Accepted by ....
Mujid Kazimi
TEPCO Professor of Nuclear Engineering
Chair, Department Committee on Graduate Students

Development of Accelerator Based Spatially Resolved Ion Beam Analysis Techniques for the Study of Plasma Materials Interactions in Magnetic Fusion Devices

by

Harold Salvadore Barnard

Submitted to the Department of Nuclear Science and Engineering
on January 20, 2014, in partial fulfillment of the
requirements for the degree of
Doctor of Science

Abstract

Plasma-material interactions (PMI) in magnetic fusion devices pose significant scientific and engineering challenges for the development of steady-state fusion power reactors. Understanding PMI is crucial for the develpment of magnetic fusion devices because fusion plasmas can significantly modify plasma facing components (PFC) which can be severely detrimental to material longevity and plasma impurity control. In addition, the retention of tritium (T) fuel in PFCs or plasma co-deposited material can disrupt the fuel cycle of the reactor while contributing to radiological and regulatory issues.

The current state of the art for PMI research involves using accelerator based ion beam analysis (IBA) techniques in order to provide quantitative measurement of the modification to plasma-facing surfaces. Accelerated ~MeV ion beams are used to induce nuclear reactions or scattering, and by spectroscopic analysis of the resulting high energy particles (γ, p, n, α, etc.), the material composition can be determined. PFCs can be analyzed to observe erosion and deposition patterns along their surfaces which can be measured with spatial resolution down to the ~1 mm scale on depth scales of $10 - 100$ μm. These techniques however are inherently ex-situ and can only be performed on PFCs that have been removed from tokamaks, thus limiting analysis to the cumulative PMI effects of months or years of plasma experiments. While ex-situ analysis is a powerful tool for studying the net effects of PMI, ex-situ analysis cannot address the fundamental challenge of correlating the plasma conditions of each experiment to the material surface evolution. This therefore motivates the development of the in-situ diagnostics to study surfaces with comparable diagnostic quality to IBA in order resolve the time evolution of these surface conditions.

To address this fundamental diagnostic need, the Accelerator-Based In-Situ Materials Surveillance (AIMS) diagnostic [22] was developed to, for the first time, provide in-situ, spatially resolved IBA measurements inside of the Alcator C-Mod tokamak. The work presented in this thesis provided major technical and scientific contributions to the development and first demonstration AIMS. This included accelerator development, advanced simulation methods, and in-situ measurement of PFC surface properties and their evolution.

The AIMS diagnostic was successfully implemented on Alcator C-Mod yielding the first spatially resolved and quantitative in-situ measurements of surface properties in a tokamak, with thin boron films on molybdenum PFCs being the analyzed surface in C-Mod. By combining AIMS neutron and gamma measurements, time resolved and spatially resolved measurements of boron were made, spanning the entire AIMS run campaign which included lower single null plasma discharges, inboard limited plasma discharges, a disruption, and C-Mod wall conditioning procedures. These measurements demonstrated the capability to perform inter shot measurements at a single location, and spatially resolved measurements over longer timescales. This demonstration showed the first in-situ measurements of surfaces in a magnetic fusion device with spatial and temporal resolution which constitutes a major step forward in fusion PMI science.

In addition, an external ion beam system was implemented to perform ex-situ ion beam analysis (IBA) for components from Alcator C-Mod Tokamak. This project involved the refurbishment of a 1.7 MV tandem linear accelerator and the creation of a linear accelerator facility to provide IBA capabilities for MIT Plasma Science and Fusion Center. The external beam system was used to perform particle induced gamma emission (PIGE) analysis on tile modules removed after the AIMS measurement campaign in order to validate the AIMS using the well established PIGE technique. From these external PIGE measurements, a spatially resolved map of boron areal density was constructed for a section of C-Mod inner wall tiles that overlapped with the AIMS measurement locations. These measurements showed the complexity of the poloidal and toroidal variation of boron areal density between PFC tiles on the inner wall ranging from 0 to 3μm of boron. Using these well characterized ex-situ measurements to corroborate the in-situ measurements, AIMS showed reasonable agreement with PIGE, thus validating the quantitative surface analysis capability of the AIMS technique.

Thesis Supervisor: Dennis G. Whyte
Title: Professor of Nuclear Science and Engineering

Thesis Reader: Richard C. Lanza
Title: Senior Research Scientist

Acknowledgements

There are so many people who have made my journey as a graduate student and as a scientist an important and fulfilling part of my life. The scientists, engineers, and staff at the Plasma Science and Fusion Center were incredibly helpful with my research and are generally great people to have as friends and colleagues. So many of my fellow students have become my closest friends and it was a real pleasure to have spent my time at MIT in such great company.

I would like to thank my advisor Dennis Whyte for supporting and encouraging me in my research while giving me the personal and intellectual freedom to be creative. This flexibility allowed me to explore new places, projects, ideas, and other personally fulfilling endeavors no matter how tangential they may have been to my thesis research. I would also like to thank Pete Stahle for all of the excellent engineering advice and for the good times we had over the many years we spent working together on accelerators. I would also like to thank the accelerator group, particularly Zach Hartwig and Brandon Sorbom for their camaraderie and all of their hard work in helping to make the AIMS diagnostic a success.

In my time at MIT I also had the opportunity to be a graduate resident tutor in East Campus. Being involved with the undergraduate community was a very satisfying part my graduate experience but was also consistently filled with great friends, constant shenanigans, and unbelievably interesting experiences.

Finally, I would especially like to thank my family who have been with me every step of the way. I am truly grateful because, without growing up in a family of wonderful, caring physicists, I would have never made it to where I am today.

Contents

1 Introduction **21**

1.1 The Alcator C-Mod Tokamak 22

1.1.1 Operating principles 23

1.2 Plasma-Material Interactions in Tokamaks 25

1.2.1 A Motivating Example for PMI 26

1.3 PMI Diagnostics for Fusion 27

1.4 Accelerator-Based In-Situ Materials Surveillance (AIMS) 28

1.5 High-Z PFCs and Wall Conditioning in Alcator C-Mod 29

1.6 Contributions 30

1.7 Chapters 31

2 Ion Beam Analysis for Fusion Materials **34**

2.1 Particle Induced Gamma Emission 35

2.2 Gamma Detection 35

2.2.1 PIGE Analysis with an External Beam 37

2.3 Beam Induced Reactions for PIGE 37

2.3.1 Reactions for Boron Detection 39

2.4 Modeling Ion Beam Interactions With Matter 40

2.4.1 External Beam Energy Loss 40

2.5 PIGE Data Analysis 41

2.5.1 Calculating Gamma Yield 41

2.5.2 Calibration and Normalization 42

2.5.3 Gamma Yield Calculation 43

2.5.4 Error Analysis for External PIGE 43

2.5.5 Boron Areal Density Correlation for External PIGE 44

2.5.6 Areal Density and Boron Thickness 47

2.6 Gamma spectroscopy for AIMS 47

2.6.1 Deuterium Induced Gamma Emission for AIMS 48

2.6.2 Gamma Yield Calculation for AIMS 49

2.6.3 Boron Areal Density Correlation for AIMS 50

2.6.4 AIMS Detection Timescales 51

2.6.5 Gamma Detection in C-Mod 52

2.6.6 Background Rejection 53

2.6.7 Detection Geometry 54
2.6.8 Detection Angle for Gamma Spectroscopy 55

3 Tandem Accelerator and External Beam Apparatus 59
3.1 Accelerator and Components 59
3.1.1 Ion Sources 60
3.1.2 Electrostatic Optics for the Injector 61
3.1.3 Acceleration of Ions 62
3.1.4 Magnetic Ion and Energy Selection 63
3.1.5 Magnetic Focusing 65
3.2 Accelerator Upgrades 66
3.2.1 Centralized Controls 67
3.2.2 Sputter Source Alignment 67
3.2.3 Improved N_2 Gas Stripper control 68
3.2.4 Improved Interlocks 69
3.2.5 Recirculating Cooling System 70
3.3 External Beam 70
3.3.1 Beamline instrumentation 70
3.3.2 External Beam Current Measurement 72
3.3.3 Window Design 73
3.3.4 Mechanical Properties 73
3.3.5 Beam Energy Loss in Window 74
3.3.6 Thermal Model for Kapton 75
3.3.7 Nuclear Properties of Kapton 76
3.3.8 Radiation and Radionuclide Production in Air 77
3.4 Photon Detection and Spectroscopy 78
3.4.1 Gamma Detectors 78
3.4.2 High-Energy Photon Conversion 79
3.4.3 Analog Pulse Processing 79
3.4.4 Common Gamma Detectors 80
3.5 Applications of external beam IBA 81
3.5.1 2-D Boron Mapping of Boron on the Inner Wall for AIMS Validation 81
3.5.2 Tungsten Erosion and Migration Study with PIXE 81
3.5.3 Measurement of Boron in the Divertor with PIGE 82
3.6 Discussion of Exteral PIGE Analysis and PMI 84

4 Integration of a Compact Ion Accelerator with a Tokamak 88
4.1 Overview of Accelerator Integration 88
4.2 Accelerator: Principles of Operation 89
4.2.1 Duoplasmatron source 90
4.2.2 Radio Frequency Quadrupole 91
4.3 RFQ Accelerator Refurbishment and Upgrades 93
4.3.1 RFQ Timing 94
4.4 RFQ Systems and Installation Overview 96

4.5 Accelerator Integration 106
4.5.1 RFQ Alignment Geometry 106
4.6 Beam Optics 108
4.6.1 Optical Sensitivity and Beam Characterization 109
4.7 Beam Diagnostics 112
4.7.1 Current Measurement 112
4.7.2 Current Transformer 113
4.7.3 Uncertainty in Current Integration 117
4.7.4 Energy Measurement of the RFQ Beam 119
4.7.5 Beam Imaging 125
4.8 Beam Energy Correlation to RF Power 126

5 Beam Dynamics and Control **131**
5.1 Beam parameters 131
5.1.1 Beam Current and Time Structure 132
5.1.2 Energy and Momentum 134
5.1.3 Beam Distribution in Phase Space 136
5.1.4 Phase Space Coordinate System 136
5.1.5 Ellipse Parameters 139
5.1.6 Beam Generated Force and Emittance Force 141
5.2 Single particles and transfer matrices 144
5.3 Linear Transformations of Beam Parameters 145
5.3.1 Sigma matrix formulation 146
5.4 Beam Dynamics in a Magnetic Field 147
5.4.1 Equations of Motion 148
5.5 Measurement of Beam Parameters 149
5.6 Beam dynamics code 151
5.6.1 Trajectory Calculation 151
5.6.2 Leapfrog Method 152
5.6.3 Adaptive Circular Arc Method 152
5.6.4 Basis Transformations to Maintain F-S Coordinates 153
5.6.5 Representation of Beam Envelope for Modeling 155
5.6.6 Calculation of Fields 155
5.6.7 Transfer Matrices for B-Fields and Gradients 158
5.6.8 E Field Impulses for Space Charge Effects 160
5.6.9 Beam Projection 161
5.7 Beam Dynamics Code: Results for AIMS 162
5.7.1 Trajectory and Beam Dynamics Calculation 162
5.7.2 Validation of Trajectory Calculation 163
5.7.3 Validation of 6-D Dynamics Calculation 164
5.7.4 Reverse Dynamics for Active Focusing Applications 170

6 Results and Discussion **173**
6.1 AIMS and PIGE Geometry . . . 174
6.2 AIMS and PIGE Timeline . . . 174
6.3 AIMS Photopeak Analysis: Boronization and Wall Conditioning . . . 177
6.3.1 Discussion of Photopeak Results . . . 179
6.3.2 AIMS Neutron Detection of Boron . . . 180
6.4 AIMS Poloidal Sweep with Single Tile Resolution . . . 187
6.5 External PIGE Results . . . 188
6.5.1 PIGE Poloidal Scan . . . 189
6.5.2 2-D Tile Map of Post Campaign Boron Areal Density . . . 189
6.6 Quantitative Boron Measurements with Combined AIMS and PIGE Results . . . 191
6.6.1 Uncertainty in Beam Target Location . . . 191
6.6.2 Validation of Neutron and Gamma Results . . . 192
6.7 AIMS Intershot Measurements . . . 193
6.7.1 Complete Time Boron History . . . 198
6.8 Conclusions . . . 199
6.9 Future Directions for AIMS . . . 200

A Road Map for the Future of AIMS **203**
A.1 Next Generation AIMS . . . 203
A.1.1 Accelerator . . . 203
A.1.2 Beam Accessibility . . . 204
A.1.3 Detection and Spectroscopy . . . 204
A.1.4 Other IBA techniques using AIMS . . . 204
A.1.5 AIMS on Other Tokamaks . . . 204
A.2 Improvements on the Current AIMS Diagnostic . . . 205
A.2.1 High Priority . . . 205
A.2.2 Short Term Improvements . . . 206
A.2.3 Long Term Improvements . . . 207

B Future Beamline Developments **208**
B.1 Beam Steering and Active Focusing . . . 208
B.2 Retractable Beam Diagnostics . . . 209
B.3 Energy Control for Fixed Energy Beams . . . 209

List of Figures

1-1 Complete cross section of the Alcator C-Mod Tokamak. Refer to section 1.1.1 for overview of each component and its function in Alcator C-Mod operations. 24

1-2 Illustrative description of the complexities of plasma-material interactions in fusion devices. Figure reproduced from Wirth et. al [63]. 25

1-3 Left:CAD model of the AIMS diagnostic installed on Alcator C-Mod. Right: Schematic of AIMS components. AIMS utilizes a radio frequency quadrupole (RFQ) accelerator produce a 900 keV D^+ beam to induce nuclear reactions on the surface of plasma facing components (PFC). Spectroscopy of the resulting neutrons and gamma rays allow for the identification and quantification of isotopes on PFC surfaces. AIMS uses beam optics and toroidal field B_ϕ to steer the beam and achive spatially resolved measurements. 29

2-1 Illustration of spectrum for generated from a PIGE measurement showing the notable features in the gamma measurement. (Horizontal axis not to scale). 36

2-2 Cross section data for the $^{10}_{5}\mathrm{B}(p,\alpha\gamma)^{7}_{4}\mathrm{Be}$ reaction ($E_\gamma = 429keV$) measured by R.Day and T.Huus [10]. 39

2-3 Correlation relating boron thickness to the gamma yield, normalized to the thick target yield Y_{tt} from a boron nitride (BN) target. 46

2-4 Deuteron induced gamma emission cross section for used for AIMS [49]. The 953 keV is the predominant gamma that is observed in AIMS because of its relatively large cross section and the energy range that is accessible with the RFQ. 49

2-5 Correlation relating 953 keV gamma yield to Boron thickness for AIMS measurements. 51

2-6 Illustration of AIMS detection timescales show the low duty factor, high intensity nature of the AIMS technique. The 900 keV ion beam current I_{beam} induces gamma and neutron reactions while detectors convert the particle detection events into voltages V_{detector}. These beam and detector signals span timescales from the sub-microsecond to timescales of >10 minutes. 52

2-7 Digitized waveform from AIMS gamma detector. 54

2-8 Calculated beam trajectories and AIMS gamma detection geometry in Alcator C-Mod. 54
2-9 Graphical definitions for detector geometry. Refer to table 5.3 for mathematical definitions. 55
2-10 Angular dependence of gamma path length(red) passing through the detector and effective detector area change as a function of incident angle θ. The gray shaded regions are the parallelogram or "bulk" portions of the detector while the blue shaded regions are the "corners". Diagrams for three ranges of θ are shown because the ray geometry is different for each of these ranges. 57
2-11 Detector efficiency as a function of incident gamma angle, normalized to efficiency at $\theta = 0$. 58

3-1 Photo of the 1.7 MV tandem accelerator in the CLASS facility 60
3-2 An annotated diagram of the cesium sputtering source. 61
3-3 Diagram of the E-field geometry in the electrostatic Einzel lens. When positive voltage +V is the applied, an E-field with a radial component is created which has net focusing effect on negative ions. 62
3-4 Schematic describing the tandem accelerator concept. Annotations 1-7 are described in table 3.1 63
3-5 Quadrupole field viewed along the beam axis, $\hat{z}$. 65
3-6 Particle Trajectories in the quadrupole lens from the top view 66
3-7 Particle Trajectories in the quadrupole lens from the top view. 66
3-8 Photo of the new arrangement of the tandem accelerator controls . . 68
3-9 A CAD model of the beam line used for external ion beam analysis. The numbers correspond to the following components: (1,6) vacuum gate valves, (2,3) y and x electrostatic steerers, (4) insertable Faraday cup, (5) beam profile monitor, (7) beam aperture/window assembly. (8) turbo pump. 71
3-10 A plot of stopping data for protons in Kapton. The theoretical data was calculated using SRIM2008 [68], and the experimental data was provided by E. Rauhala, et al [43]. 74
3-11 A plot of stopping data for protons in dry air. The data were generated using SRIM2008 [68] 75
3-12 A plot of the calculated energy-trajectories of protons as they pass through 7.5μm (0.3 mil) of Kapton (at 0 cm) followed by 10 cm of Air for 10 different initial beam energies. The vertical section of the curves at position 0 represents the energy loss of the beam in the exit foil and the sloped section represents the energy loss in air. 76
3-13 Plot of the calculated temperature profiles ($T-T_\infty$)in a Kapton exit foil from a 100 nA, 2 MeV ion beam. This calculation uses a conservative heat transfer coefficient $h = 10$ W/(m^{2}K) and assumes gaussian beam profiles with full width half maxima of $0.3, 0.7, 1.0, 1.3, 1.7[R/R_o]$ where all R_o is the exit foil radius. The beam currents were normalized such that 100 nA was incident on the window. 77

3-14 Illustration of the process by which high energy gamma photons are absorbed and converted with a scintillation detector and photo multiplier tube (PMT), then converted to a pulse height spectrum using a charge integrating pre-amplifier, a shaping amplifier, and a multi channel analyzer (MCA). 80
3-15 Photograph of the external beam PIGE analysis setup. 82
3-16 Gamma Yield measured with external proton beam PIGE analysis. Error bars quantify Poisson error. 83
3-17 Spatially resolved map of net poloidal migration of tungsten in the lower Alcator C-Mod divertor measured with external ion beam analysis. W is the tungsten tile row located near the outer divertor strike point used as the tungsten source in this study. 84
3-18 Top: map of the lower divertor showing regions that were PIGE analyzed for boron after the 2009 campaign. Bottom: spatially resolved boron measurements on a set of tiles spanning the inner divertor. . . 86
3-19 Top: spatially resolved boron measurements on a poloidal set of tiles spanning the outer divertor. Bottom: spatially resolved boron measurements on a set of tiles spanning the divertor dome which covers the EF1 poloidal field coil in the lower divertor. 87

4-1 Schematic of Duoplalsmatron Ion Source used in the DL-1. Refer to section 4.2.1 for principles of operation and component descriptions. The blue arrows represent electric field lines set by the geometry and the extraction potential. The green arrows represent the magnetic field lines and their paths through the magnetic iron body of the source and in the ionization gap. 91
4-2 Schematic of RFQ field geometry. The transverse cross section (left) shows E and B fields of the TE_{210}-mode creating quadrupole electric fields near the z axis of the cavity for transverse focusing. The longitudinal cross section (right) shows how the transverse modulations of the vane spacing create a net longitudinal E field for acceleration during 1/2 of each RF period. The spatial wavelenth λ of the modulations increase with z to keep each particle bunch with velocity $\beta_s\, c$ in synchronous phase with the time varying RF fields [55]. 92
4-3 Schematic of RFQ vane profile. The modulations increase in spatial period to allow the particle bunches to remain in synchronous phase with the RF as the velocity increases. 93
4-4 Photo of RFQ cavity with the case and end-plate removed, showing the quadrupole symmetry of the cavity and the modulations of the vane tips. 93
4-5 RFQ accelerator timing diagram. This diagram schematically shows the voltage waveforms of the accelerators control signals, feedback from instrumentation, and signals from detectors. 95
4-6 RFQ accelerator (black) with 60 kW amplifier (upper left) and ion source power supply and control rack (upper right). 98

4-7 Top view showing the layout of the RFQ accelerator's power systems in the C-Mod Cell. 98
4-8 Complete schematic of the RFQ accelerator's upgraded controls and power systems. This system wide block diagram shows the interconnections and propagation of signals throughout the RFQ accelerator system. In order to see the details of this diagram use the pdf version of the thesis. 99
4-9 Simplified block diagram of the RFQ accelerator's upgraded controls and power systems. This diagram provides a system wide overview of the RFQ accelerator. 100
4-10 Injector control module: (a) Programmable pulse signal generator for synchronizing timing of the accelerators RF, beam, and data operations. (b,c) Group III controllers with digital and analog I/O. (d) modular array for relays used for control and routing of multiple signals and power controls. (e) Control and monitor signals for the high vacuum system. (f) 8 multiplexed signal inputs for the integrated 100 MHz oscilloscope used for measuring high frequency signals from accelerator instrumentation. 101
4-11 High voltage controls: Since the ion source operates at 25 kV, the source controls and power supplies are electrically isolated in a high voltage rack that operates at 25 kV. (a) The arc pulser is used to make -300 V, 20 A pulses to initiate and sustain the plasma in the ion source. This device was redesigned and built with modern components. A schematic is shown in figure 4-13. (b) An electrolytic capacitor is used to store energy between beam puses to provide the wired charge to deliver the arc pulse. The Pierce electrode supply provides the is used store energy between beam pulses to proved the required to deliver the arc pulse to the ion source. (c) The Piece electrode supply provides allows plasma shaping in the extraction region to improve efficiency. (d) Group 3 module provides digital and analog I/O. (e) All of the components are wired into terminal modules that communicate with the group 3 modules. 102
4-12 A custom computer interface was designed for the accelerator in LabView^{TM} [35]. This interface allows the accelerator operator control every aspect of the accelerator's operation and monitor the accelerator's instrumentation. 103
4-13 Schematic of upgraded arc pulser design. This device is used to produce -300 V, 20 A pulses to initiate and sustain the plasma in the ion source. The arc pulser was redesigned using modern IGBT components and drivers for better reliability and power handling. 103
4-14 View of the RFQ accelerator installed on C-Mod (top). The RFQ accelerator being lifted into place using the gantry crane in the C-Mod cell (lower left). View of the RFQ beamline with permanent magnet quadrupole optics with the beamline connected to the beam injection flange on B-port (lower right). 104

4-15 Photos of B-Port during Alcator C-Mod vacuum break: View through beam injection port (left). View of open port flange on B-port (right). 106
4-16 Precision alignment flange to adjust beamline angle with respect to the accelerator case. 107
4-17 TRACE3D [29] simulation of the permanent magnet quadrupole optics demonstrates that the RFQ beam can be focused to a 1 cm diameter beam spot. Upper left: initial beam envelope, upper right: final beam envelope, bottom: plot of transverse vertical (red) and horizontal (blue) beam radius along the trajectory. 109
4-18 AIMS Beamline with three permanent magnet quadrupoles (gray components) for focusing and the toroidal current transformer (green). . . 109
4-19 Photograph of the AIMS Beamline with permanent magnet quadrupoles for focusing. The white ceramic section to the right is the insulating break required for proper beam current measurement with a toroidal current transformer. 110
4-20 Right: RMS Beam width in x (horizontal) direction versus changes in quad position Δz. Left: RMS Beam width in y (vertical) direction versus changes in PMQ position Δz. $\Delta z = z - z_{\text{optimal}}$ is the relative position of the quad positions relative to optimal spacing given in table 4.2. 110
4-21 In the $x - x'$ phase plane: Relative changes in β and β-sensitivity due to changes in quad position z, where Δz is the perturbation from the optimal spacing given in table4.2. 111
4-22 In the $y - y'$ phase plane: Relative changes in β and β-sensitivity due to changes in quad position z, where Δz is the perturbation from the optimal spacing given in table4.2. 111
4-23 Circuit diagram for beam current measurement resistor (R1) and secondary election suppression resistor (R2). 113
4-24 Schematic of beamline with current transformer for measuring beam current. 115
4-25 Clamp on transformer for beam current measurement. (Pearson Electronics, INC, Wide Band Pulse Current Monitor, Model 4688, Ouput: 1.0 Volts per Amp) 116
4-26 In-vacuum integrated current transformer for beam current measurement. 116
4-27 Calibration test of the in-vacuum CT for beam current measurement. The top red trace is 250 mV, 5 mA test pulse and lower blue trace is the 600 mV output from the in-vacuum CT and amplifier. The calibration factor is therefore 120 mV/mA 117
4-28 Fixed gain 100× amplifier with 4 MHz low pass filtering for current transformer signal. 118
4-29 Typical digitized output from current transformer plotted with the mean DC offset $\bar{V}_{\text{DC}}$, and uncertainties in digitized voltages σ_{Vq}. . . . 119
4-30 Vacuum insulated copper calorimeter design for measuring average beam energy. CAD model (left). Photograph of calorimeter before installation (right) 121

4-31 Heat loss mechanisms for the beam calorimeter are compared. Since most measurements are taken within 0-20 K above, ambient temperature the heat loss is small, and can be easily accounted for. 121
4-32 Calorimeter time traces are shown for three beam measurements with differing forward RF power measured at the amplifier output. The temperature $\Delta T = T(t) - T_{\text{ambient}}$ is normalized to beam current to show an equivalent comparison. The average beam energy inferred from average $\Delta T/\Delta t$ is displayed adjacent to each data set. 122
4-33 thin-film Backscattering Geometry 123
4-34 Schematic picture of the RBS from a thin-film of gold on a target substrate. 124
4-35 If range foils are used to remove backscattered particles from the substrate, straggling of D^+ Ions in the foil degrades the energy resolution. Straggling is shown for a 5 μm aluminum foil, calculated with SRIM [68] 124
4-36 RBS Simulations using SIMNRA [38] show that that 50nm gold films on SiO_2 provide good energy resolution with relatively low counts from backscattering from the substrate. 125
4-37 Implementation of a fixed target design for a thin-film backscattering spectrometer. 126
4-38 Compact beam imaging tool to align the beam with the beamline. A CAD model and photo of the beam imaging diagnostic are shown left and center. A photo (right) of the RFQ beam scintillating on quartz is shown on the right. 126
4-39 Data points and fit for direct measurement of RF amplitude versus gamma counts (left). Derivative of gamma counts N_γ with respect to RF amplitude measured within individual AIMS runs. 128
4-40 Illustration of the derivative measurements used for RF calibration. Each AIMS run is divided into regions where the average RF cavity amplitude A, average gamma count rate N, the integrated beam charge Q. The derivative can then be calculated from neighboring N_γ/Q points with respect to A 129
4-41 Calibration curve to correct for beam energy fluctuations due to changes in RF power. This curve gives the downgraded (expected) number of counts normalized to the ideal number of counts from a 900keV beam. 130

5-1 Simple illustration of a beam bunch traveling at velocity v_z 132
5-2 A schematic picture of the time structure of a pulsed beam from an RF accelerator. Timescales for the DL-1 RFQ are given in table 5.1. . 133
5-3 Simple illustration of a particle bunch's Gaussian distribution in all spatial and velocity dimensions. The distribution in each dimension has a characteristic width that evolves in time as the beam propagates in the z direction. 135

5-4 Illustration of the beam envelope in the transverse position-momentum x-x' phase plane. An initially converging beam is shown drifting in z. The minimum transverse dimension at x_2 is due to space charge forces and non-laminar effects of the beam. The x coordinate represents the spatial width of the beam and x' coordinate is the canonical momentum x' in the x direction, equivalent to the beam's angular width and analagous to the beam's transverse velocity. 137
5-5 Frenet-Serret coordinates: curvilinear coordinate system maintaining two transverse coordinates x and y and the longitudinal coordinate z with respect to the ideal trajectory s. 138
5-6 Ellipse geometry relationships for Twiss parameters of envelope functions. 139
5-7 Top: particle trajectories within a high-current, laminar beam where space charge dominates. Bottom: particle trajectories within an non-laminar beam with finite emittance. Where R and R' are the transverse position and momentum coordinates of a beam with circular cross section. Initial and final transverse phase-space beam envelopes are shown on the left and right, respectively. 142
5-8 Comparison of space charge force to emittance force for 900 keV D^+ ion beams over a range of beam currents and radii. A constant emittance $\epsilon = 9.950$ πmm·mRad is assumed which corresponds to transverse emittance of the beam from the DL-1 accelerator. The outlined shaded region highlights the operating space of the DL-1 beam used for AIMS. Since $F_{\text{emittance}}/F_{\text{Charge}}$ ratio is of order 1, both space charge and emittance are important for AIMS beam dynamics calculations. . 143
5-9 Left: Multiple trajectories can be observed for particles in a B-field for the same differential angle $d\theta_o$ depending on x and x'. Right: definitions for the Frenet-Serret coordinates in the bending plane are illustrated. 147
5-10 Left: A uniform B-field produces a weak focusing effect. Middle: A B-field with gradient ∇B that is parallel to the radius of curvature increases focusing. Right: A B-field with ∇B that is anti-parallel to the radius of curvature decreases focusing and if ∇B is large enough, can cause defocusing. 148
5-11 Block diagram of iterative procedure used to calculate trajectories using the leapfrog method. This code also defines a local F-S coordinate system during every time step and calculates the local B-fields that are later used for the beam dynamics calculations. 153
5-12 Toroidal field magnitude at $\phi = 0$ compared to the ideal $1/R$ fields in a tokamak (left). Two dimensional contour map of the tokamak toroidal field magnitude viewed from the top (right). Tokamak coils are approximated as filament currents for these calculations. 156
5-13 Vertical field magnitude at the midplane $z = 0$ (left). Two dimensional contour map of the vertical field magnitude in the R-Z plane (right). 157

5-14 A toroidal field map (left) and vertical (right) field map are shown with a nominal beam trajectory for AIMS on C-Mod shown in red. This illustrates the complexity of the fields that occur in the transition regions between coils. 158
5-15 3-D projection of calculated 900 keV D^+ trajectories and γ-detection geometry, for 4 toroidal field settings (B_ϕ = 0,0.0582, 0.1135, 0.1618 T). The blue grid denotes the plasma facing surfaces inside Alcator C-Mod. 163
5-16 Calculated beam spot geometry on target PFCS. The ellipses represent the 1-σ envelope of the beam distribution projected on the target geometry at to location where the beam centroid intercepts the PFCs. The filled in ellipses correspond to the most studied PFC locations and the dotted-grey ellipses correspond to the additional locations studied while performing a higher resolution poloidal sweep. 164
5-17 Error analysis of the beam trajectory calculation using the leapfrog method with 1 mm steps. Δr is the deviation in transverse position from an ideal helical trajectory with a pitch angle of 10°. 165
5-18 Comparison of AIMS beam dynamics code with TRACE3D for the B_ϕ = 0 T trajectory in C-Mod. Transverse and longitudinal phase planes projections are shown in addition to an transverse spatial projection with respect to the beam coordinate system. 167
5-19 AIMS beam dynamics code results comparing a 1 mA beam where space charge effects are significant to a 1 μA beam. Both trajectories are 1.5 m in length with no externally applied fields 168
5-20 Comparison of AIMS beam dynamics code with TRACE3D for a 90° sector magnet with uniform field and a bending radius of curvature R_c = 1 m. Transverse and longitudinal phase planes projections are shown in addition to an transverse spatial projection. 169
5-21 Discretized B-field Curvature for TRACE3D input. 170
5-22 Example of TRACE3D output from discretized fields. Sector magnets are used to apply magnetic fields and magnetic gradients to the beam. This plot corresponds to the fields for in C-Mod a toroidal field on axis of B_ϕ = 0.0582 T (I_{TF} = 1600 A) shown in figure 5-21. The 'modified beam matrix' parameters are used to construct a sigma matrix for comparison to the AIMS beam dynamics code. 171
5-23 Discretized B-field Curvature for TRACE3D input. 172

6-1 Calculated Beam trajectories for the four most common trajectories used for AIMS measurements on Alcator C-Mod. 174

6-2 Top: Tile map of the C-Mod inner wall, upper divertor, and lower divertor EF-1 shelf, toroidally spanning the A,B, and C port regions. Bottom: Zoomed-in tile map showing the locations of the PIGE and AIMS measurements. Top Right: Deuteron beam trajectories are shown for four trajectories spanning the range of the AIMS measurements. The tiles highlighted in yellow/red were removed and PIGE analyzed following AIMS measurements. The green ellipses indicate the calculated location and beamspots for AIMS measurements based on modeling (chapter 5). The filled ellipses represent the four locations used for the majority of the AIMS measurements corresponding to toroidal beam steering fields B_ϕ = {0.000, 0.0582, 0.1135, 0.1618} Tesla (in order from top to bottom). 175
6-3 Photograph of PIGE analyzed tiles: Circles represent beam spot sizes and locations for each measurement. Refer to figure 6-2 for tile locations in C-Mod. 176
6-4 Plot of gamma spectra from two different AIMS measurements. In the typical spectrum a 953 keV photopeak from the $^{11}B(d,p\gamma)^{12}B$ reaction is observed. From the spectrum that is blurred by thermal drift in the gain, the 953 keV peak and other features cannot be easily distinguished from background. 178
6-5 Close up view of a 953 keV photopeak in an AIMS gamma spectrum from the $^{11}B(d,p\gamma)^{12}B$. Poisson error bars are shown for each bin and demonstrate that the peak is statistically significant and distinguishable from background. The 847 keV gammas from inelastic neutron-scattering off iron is also visible and clearly distinguishable from the 953 keV photopeak. 178
6-6 Boron thickness determined with AIMS at four poloidal locations from measurements of the 953 keV $^{11}B(d,p\gamma)^{12}B$ photopeak. 180
6-7 Relative measurements of boron are made from the AIMS neutron spectra by integrating the high high energy portion of the spectrum shown in blue, corresponding to neutron from the $^{10}B(d,n)^{11}C$ and $^{11}B(d,n)^{12}C$ reactions. The 'channels' on the spectrum correspond to the binning of charge output from the detector which is related to scintillator light output and is a non-linear function of energy. The region of integration shown from 1.8 - 2.5 corresponds a region of in which only neutrons from boron are energetically allowed [21]. 181
6-8 Measured correlation between neutron N_n and gamma N_γ counts from AIMS measurement at four locations. Each point represents an AIMS measurement where N_n and N_γ were measured simultaneously with the same target, beam current, and acquisition time. A linear fit is drawn for data sets that show a statically significant correlation. . . . 182
6-9 Time history of high energy neutron counts corresponding to scattered neutrons from boron reactions. The height of each marker indicates the Poisson uncertainty in uncertainty of neutron counts. The error bars represent experimental uncertainties in charge integration and beam energy calibration. 184

6-10 Time history of boron inferred from high energy neutron counts and calibrated to best fit the AIMS gamma results. The height of the data markers indicate Poisson error and the error bars indicate the absolute error from measurement and calibration. 185
6-11 Left: Deposition profile of boronizaion measured with a quarts microbalance (QMB). Peak deposition is observed at or outboard of the upper hybrid resonance (UH) while deposition decreases sharply approaching the electron cyclotron (EC) resonance layer. The left plot was reproduced from [41] and adapted for this figure. Right: The relative position of the EC, UH, and peak boron deposition regions are shown illustrate their proximity to the AIMS measurement locations. 186
6-12 Gamma spectra from AIMS poloidal sweep with single tile resolution. It appears that, only two of these spectra have photopeaks that are suitable for quantifying boron. 187
6-13 Several overlaid gamma spectra used from external PIGE measurements of boron using the $^{10}_{5}\mathrm{B}(p,\alpha\gamma)^{7}_{4}\mathrm{Be}$ reaction. The three higher energy peaks are reactions induced in the aluminum structure supporting the beam window. 188
6-14 Top trace: poloidal profile of normalized gamma yield from the sixth column of tiles. Bottom: poloidal profile of boron areal density represented in boron thickness (assuming a solid boron surface layer). . . . 190
6-15 Boron thickness measured with external proton beam PIGE analysis . 191
6-16 Photograph taken concentric to the beam port indicates that the no-field beam trajectory intercepts the wall one tile above the original engineering design. This offset is within the expected tolerances. . . . 193
6-17 Left: Boron time history comparing AIMS(γ) photopeak results to PIGE measurements by scaling AIMS(n) neutron data for extrapolation. AIMS neutron data were scaled to match the final PIGE measurements. The shaded green area represents the inherent uncertainty in the comparison due to the differing beam spot sizes between PIGE and AIMS. Right: Map of boron measured with PIGE analysis with overlaid AIMS beamspots. The AIMS beamspots were assumed to be at the location that is indicated by a photograph taken concentric to the beam injection port (one tile above the design location). 194
6-18 Left: Boron time history comparing AIMS(γ) photopeak results to PIGE measurements by scaling AIMS(n) neutron data for extrapolation. AIMS neutron data were scaled to match the final PIGE measurements. The shaded green area represents the inherent uncertainty in the comparison due to the differing beam spot sizes between PIGE and AIMS.The AIMS beamspots were assumed to be at the location that is expected from the design of the diagnostic 195
6-19 Boron measurements through out a C-Mod run day using combined neutron and gamma data to demonstrate inter-shot AIMS measurements. 196

6-20 Views from the WIDE1 visble camera. Left: Stable ohmic inner wall limited plasma. Middle: View of plasma during disruption. Right: Black body radiation is observed as a red-orange glow tiles heated by the disruption. Solid ellipse denotes predicted beam spot, dotted ellipse denotes predicted uncertainty in position. 197
6-21 Boron time history spanning the entire AIMS run campaign 1 day of C-Mod operations followed by wall conditioning operations at the B_ϕ = 0 T location. The PIGE measurement at the end of the campaign is also shown for comparison. 199

B-1 Electrostatic quadrupole doublet from National Electrostatics Corporations [8]. 208
B-2 Left: Design for a compact retractable beam imaging target. Right: Design for a compact retractable thin film backscattering beam energy spectrometer. 210
B-3 Energy degrader disks using indexed foils to reduce beam energy in discrete increments. The design shown with 4 disks allows for 16 distinct energy settings. 211
B-4 The gas density required for degrading the beam energy per unit trajectory length was calculated using stopping data from SRIM [68]. . . 212
B-5 The Chu model [67] was used to calculate the energy straggling of the beam passing through a gas filled chamber 212

List of Tables

2.1 Common ion beam analysis techniques used for fusion materials: particle induced gamma emission (PIGE), particle induced X-ray emission (PIXE), Rutherford backscattering spectroscopy (RBS), elastic recoil detection (ERD), and nuclear reaction analysis (NRA). 35
2.2 Definitions of AIMS detection parameters. 55

3.1 Basic process of ion acceleration in a tandem accelerator 63
3.2 A list of new hardware for remotely contolling beam-lines and experiments. 67
3.3 These reactions can occur in Kapton and potentially interfere with external proton beam IBA measurements [34]. The emitted gammas overlap in energy with the reaction of interest. 78
3.4 Nuclide production rates for a 2 MeV, 100 nA proton beam passing through Kapton then stopping in air. This represents an activity of $\alpha = 1.43 \times 10^5$ Bq from prompt gamma emission and an activity of $\alpha < 1.5 \times 10^5$ Bq from accumulated radioactive nuclides for a typical external proton beam used in PIGE boron measurements (from 8 hours of operation). 78

4.1 Design parameters for a the DL-1 Radio Frequency Quadrupole Accelerator Manufactured by ACCYS [1]. Design parameters are accompanied by achieved parameters after DL-1 refurbishment. $*$ There is some uncertainty in these parameters based on conflicting information from the manual and the manufacturer. 94
4.2 Permanent magnet quadrupole parameters (PMQ) [28] with drift spacing optimized with TRACE3D [29] for a 1 cm diameter beamspot at 1 m from the last PMQ. Blue and red are fonts are used for PMQs that focus in vertical and horizontal transverse directions, respectively. . . 108

5.1 Characteristic timescales for the DL-1 accelerator used for AIMS. Graphical definitions are given for the quantities in figure 5-2. 132
5.2 Definitions of curvilinear coordinates and field parameters for beams in a magnetic fields. Coordinates with subscript o are associated with the ideal centroid trajectory, coordinates without a subscript are associated with a particle 148

5.3 Calculated target and detection geometry parameters for the 4 most common trajectories used for AIMS measurements of the Alcator C-Mod inner wall, organized by toroidal field strength. Refer to section 2.6.7 in chapter 2 for definitions of geometric quantities. 162

6.1 Timeline of AIMS measurement during the 2012 C-Mod campaign. Red represents processes that are expected to cause net erosion. The effect of the lower single null discharges on the inner wall is unknown and is shown in green. 176

6.2 Timeline of post-campaign AIMS measurement and wall conditioning. Red and blue represent processes that are expected to cause net erosion and deposition of boron, respectively. 177

6.3 Deuteron induced neutron-producing reactions and their Q-values for low-Z isotopes on C-Mod PFCs. 181

Chapter 1

Introduction

Nuclear fusion of hydrogen isotopes is perhaps the most abundant energy source in the universe. However, producing these reactions on earth presents many scientific and engineering challenges because temperatures of ~10 keV (~10^8 Celsius) – substantially hotter the core of the sun – are required for fusion to occur at an appreciable rate. Nonetheless, when the energy produced per fusion reactions (Q value) listed below is compared to energy from typical chemical reactions, it is easy to see the enormous potential fusion has to offer as an energy source if these challenges are overcome.

$$
\begin{aligned}
{}^{2}_{1}\mathrm{H} + {}^{3}_{1}\mathrm{H} &\longrightarrow {}^{4}_{2}\mathrm{He} + {}^{1}_{0}n \quad (Q = 17.6\ \mathrm{MeV}) \\
{}^{2}_{1}\mathrm{H} + {}^{2}_{1}\mathrm{H} &\longrightarrow {}^{3}_{1}\mathrm{H} + {}^{1}_{1}\mathrm{H} \quad (Q = 4.03\ \mathrm{MeV}) \\
{}^{2}_{1}\mathrm{H} + {}^{2}_{1}\mathrm{H} &\longrightarrow {}^{3}_{2}\mathrm{He} + {}^{1}_{0}n \quad (Q = 3.27\ \mathrm{MeV}) \\
\text{Chemical Reaction} &\longrightarrow (Q \approx 0.00001\ \mathrm{MeV})
\end{aligned}
$$

As a result, substantial efforts have been put forth to improve our ability to efficiently create the necessary high temperature conditions where fusion reactions can occur in order to exploit fusion energy as a source of large scale, clean, low emissions electrical power generation.

Due to the extremely high temperatures involved, the medium for fusion is the plasma state, often called the fourth state of matter, in which collective charged particle collisions dominate the behavior. The physical requirement for fusion energy is the well known Lawson criterion which states that for the D-T fusion reaction the product of the plasma thermal pressure and confinement time must reach 1 MPa-second, at a temperature of ~10 keV. At this temperature the majority of particles in the plasma tend to be ionized. This makes the plasmas particles electrically charged, allowing them to be manipulated by magnetic fields.

As result, magnetic confinement fusion devices are at the forefront of this research effort. These devices, including tokamaks, confine plasmas using strong magnetic fields, regularly reaching sufficient temperatures and pressures required to fusion. Substantial progress has been made with confinement confinement of fusion plasmas in tokamaks. For example the Joint European Torus (JET) achieved 16 MW of fusion power using deuterium-tritium fuel, reaching a fusion gain (Q = fusion power/

input power) of 0.64 in 1997 [30]. In addition, the International Thermonuclear Experimental Reactor (ITER) is expected to achieve fusion gains as high as Q=10 [27].

Containing such high temperatures in laboratory devices inevitably leads to complicated physics and engineering challenges, especially at the boundary between the plasma and the material surfaces within the device. The physics of this "boundary" plasma are complex and non-linear because of the continual and rapid interplay of plasma particles and energy between the plasma and the plasma-facing surfaces. The boundary physics is further complicated and by the confining magnetic fields that are integrally related to the dynamics of the plasma particles, and the rapid exchange of particles between the the plasma and wall materials. These plasma-material interactions (PMI) can result in material erosion and migration as well as fuel retention, plasma impurity production, and other phenomenon that can dramatically affect the longevity of materials, the fusion fuel cycle, and the performance of the plasma confinement. Developing a detailed understanding the mechanisms and consequences of PMI is therefore widely acknowledged to be critical to the successful development of fusion power reactors.

1.1 The Alcator C-Mod Tokamak

Tokamaks are plasma confinement devices that are toroidal in shape and use magnetic fields to stabilize and control their high temperature plasma. A combination of strong toroidal fields (applied with external coils) and poloidal fields (created by toroidal flow of plasma current and external coils) are used to create the proper magnetic topology to stably confine the plasma particles as they orbit along magnetic field lines. A comprehensive description of how tokamaks operate and confine plasmas can be found in reference [17] and [57].

Magnetic fusion research at MIT is performed on the Alcator C-Mod tokamak [26] which began operations in 1993. C-Mod is a compact, high field tokamak with a major radius of $R = 0.67$ m, a minor radius $a = 0.21$ m, a maximum toroidal field on axis $B_\phi = 8$ T, and a maximum plasma current $I_p = 3$ MA. C-Mod is also equipped with 4 MW of 80 MHz ion cyclotron radio frequency (ICRF) heating that couples power to the cyclotron motion of the confined ions. C-Mod also has a lower hybrid current drive (LHCD) system to drive current in the plasma non-inductively with a phased array of wave guides that launch plasma waves that couple momentum to the plasma elections in the toroidal direction [6]. These power systems along with wide variety of plasma diagnostics enable the study of high performance tokamak plasmas on with Alcator C-Mod. Because Alcator C-Mod achieves plasma pressure and power density commensurate with those expected in fusion reactors, it is a critical tool in exploring the PMI of "reactor-grade" plasma, even though C-Mod itself does not meet the Lawson criterion due to its small size.

1.1.1 Operating principles

To create and confine plasmas with thermonuclear fusion relevant temperatures and pressures, tokamaks use a combination of externally applied fields and induced plasma currents to stabilize and confine the plasma. The components of the Alcator C-Mod tokamak are shown in figure 1-1. The general operating principles of tokamaks are described below through the descriptions of the components of C-Mod:

The Toroidal Field Coils produce static toroidal magnetic fields during plasma discharges of up to 8 T along the magnetic axis ($\hat{\phi}$). At the same time, the Vertical Field Coils produce a vertical field to stabilize the plasma in the radial direction. During the plasma discharge, the Central Solenoid is pulsed with current to inductively drive plasma current in the toroidal ($\hat{\phi}$) direction in order to produce the necessary poloidal field for confinement.

The Core Plasma is confined by these magnetic fields as it is heated resistively by the current as well as RF heating systems. Due to diffusion of particles and energy within the plasma, particles leave the confined core into the Scrape Off Layer (SOL) where particles migrate along the field until they interact with wall of the tokamak.

The plasma is produced inside of the Vacuum Vessel which maintains the necessary high vacuum conditions. When the plasma forms during the discharge, the Limiter serves as a solid plasma boundary on the outboard side of the plasma while the Inner Wall serves as the boundary on the inboard side.

The Poloidal Shaping Coils are actively controlled to shape and stabilize the plasma. For high performance plasmas, shaping using an external poloidal field coils is used to 'divert' the plasma into the Divertor region. When the plasma is in the divertor configuration the divertor intentionally becomes the primary regions where the plasma interacts with the material surfaces because the exhaust power is "diverted" to these magnetic flux surfaces. The lengthening of the SOL into the divertor also allows for enhanced dissipation of the plasma momentum through ion-neutral collision and dissipation of power through radiation. These can substantially decrease peak power loading on material surfaces required to avoid thermal limits of the materials.

The Vertical and Horizontal Ports provide access for diagnostics, instrumentation for experiments and tokamak operations. The large stainless steel Coil Support Structure provides mechanical support for to coils to prevent deformation due to the magnetic forces produced by the coils. The entire C-Mod structure is then contained with in the Cryostat that provides thermal isolation so that the copper magnetic field coils can be cooled with liquid nitrogen to reduce their resistivity.

For PMI science the critical features of C-Mod are its field and power density. The plasma pressure which can be obtained is limited due to local stability limits through the β-parameter where β = plasma pressure / magnetic pressure = p/p_B. With fields up to 8 T, C-Mod obtains boundary plasma pressures similar to those expected in reactors since $p_B = (B^2/2\mu_o)$. The plasma boundary temperature tends to be highly constrained by heat conduction and atomic physics [47], therefore achieving the same pressure as a reactor produces near-equivalent plasma conditions. The power density of the compact C-Mod device, up to 1 MW/m^2 of heating over the entire plasma surface area, is also the same as expected in reactors and provides

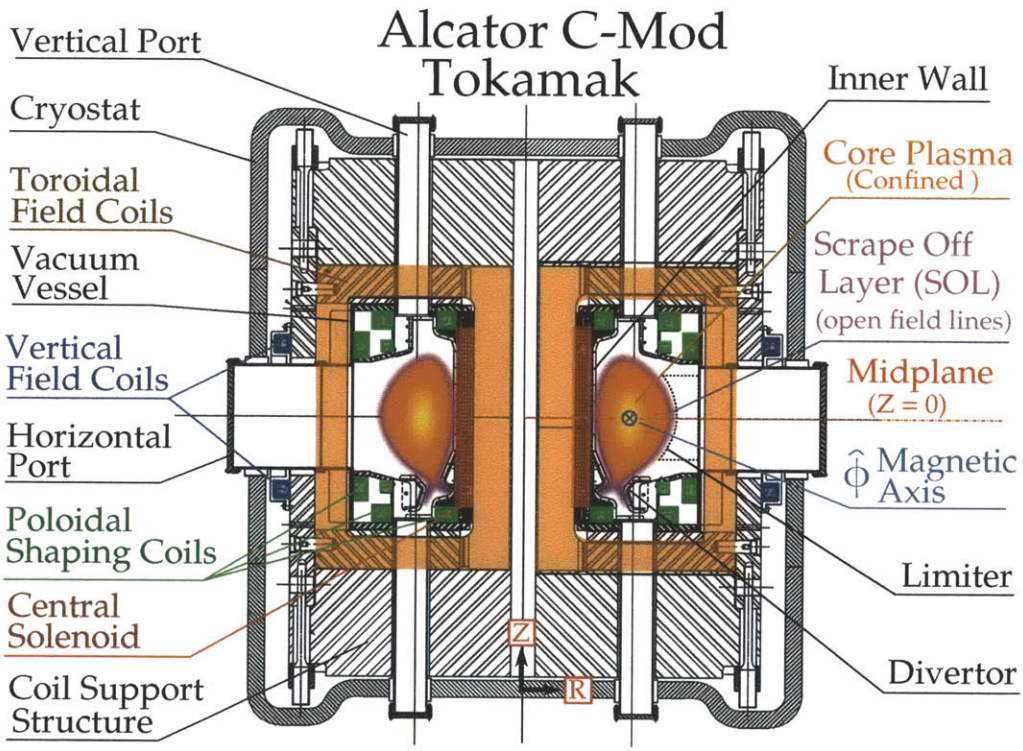

Figure 1-1: Complete cross section of the Alcator C-Mod Tokamak. Refer to section 1.1.1 for overview of each component and its function in Alcator C-Mod operations.

both high confinement core regimes and high local power density at plasma-facing surfaces which are appropriate for PMI studies. Therefore while C-Mod plasmas only operate for a few seconds due to cooling limits of the resistive coils, this timescale is substantially longer than those of plasma phenomena making C-Mod a uniquely important device for matching plasma regimes that are relevant to PMI in a reactor.

1.2 Plasma-Material Interactions in Tokamaks

The challenges of PMI have are a critically important area of study for development of fusion devices. These challenges have been reviewed for the ITER burning plasma regime and can be found in Federici et al [15] and more recently in [64].

Understanding PMI is crucial for reactors because fusion plasmas can significantly modify plasma facing components (PFC) through plasma material interactions (PMI) with disastrous implications for reactor performance if not properly understood and mitigated. As plasma particles interact with PFC surfaces they can cause erosion and migration of materials though a variety of processes including physical and chemical sputtering. These effects can have a significant impact on material longevity – a major issue for steady state reactors – and can introduce plasma impurities that degrade plasma performance in fusion experiments of any size.

In addition tritium (T) retention is an issue of great significance to reactors because long-term fuel retention of T in PFCs or co-deposited material containing T can disrupt the fuel cycle of the reactor while contributing to severe radiological and regulatory issues.

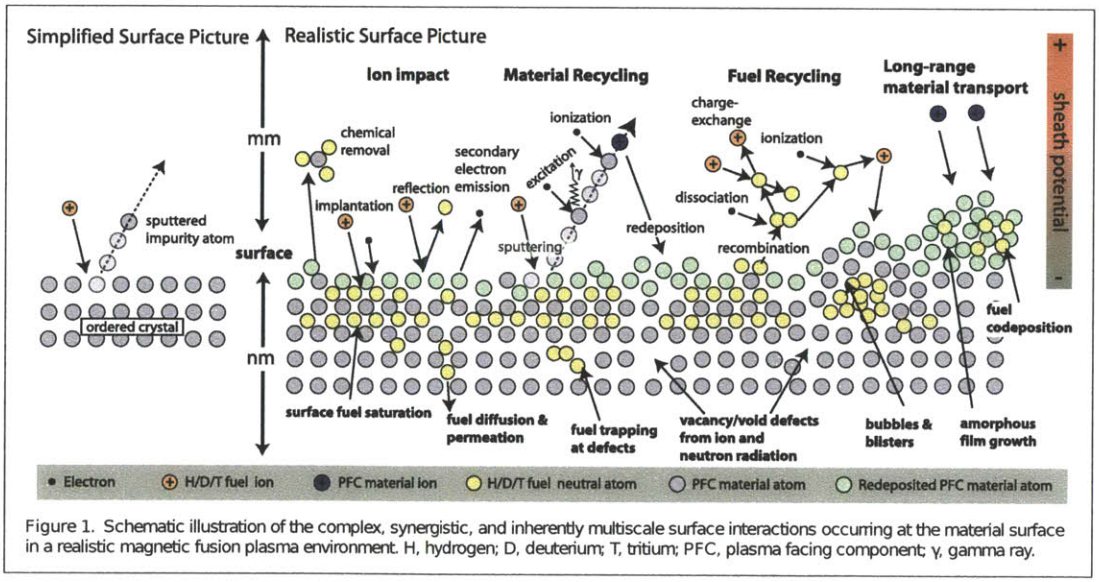

Figure 1-2: Illustrative description of the complexities of plasma-material interactions in fusion devices. Figure reproduced from Wirth et. al [63].

An illustration of the complex processes that cause PMI issues such as erosion

and T retention are shown in figure 1-2. This serves to motivate how intractable PMI issues are purely from a theoretical and modeling standpoint. It is therefore fundamentally important to develop comprehensive diagnostic tools to properly understand PMI to mitigate their consequences.

1.2.1 A Motivating Example for PMI

A recent fusion energy sciences advisory committee (FESAC) review determined that materials PMI were among the greatest science and technology challenges for fusion's development [39]. An example of the material challenges of the divertor of a tokamak is presented to motivate this point and show challenges of the PMI.

The divertor must continually exhaust a large fraction of the plasma exhaust heat, approximately 1/5 of the fusion power, in a deuterium-tritium (D-T) reactor. Simple geometric considerations indicate this will approach average surface power density $\sim$10 MW/m^2 in the divertor, which is dedicated to this power exhaust. However actively cooled components in vacuum, are fundamentally limited in the their heat exhaust capabilities due to material and coolant thermal properties. These engineering limitations prevent plasma facing components (PFC) from significantly exceeding heat flux levels of 10 MW/m^2. In addition, due to the finite thermal conductivities of materials PFCs must be relatively thin (not more than several mm) to allow for sufficient heat conduction without unacceptably high surface temperature and melting.

To access higher performance plasma regimes divertors are used to extend the scape off layer at the edge of the plasma allowing cooling of the edge plasma before it intercepts the wall. The divertor region promotes strong particle recycling such that the local plasma temperature is approximately set by atomic physics effects for ionization and radiation, leading to typical temperatures of 10 eV to be observed in experiments. Because the heat is exhausted through a plasma sheath to the material surface, this makes it possible to estimate the required incident particle flux density Φ at 10 MW/m^2.

$$\Phi = \frac{q''}{\gamma k T} \sim \frac{10^7\ [\mathrm{W/m^2}]}{7\ (1.6022 \times 10^{-19}[C/\mathrm{particle}])\ 10[\mathrm{eV}]} \sim 10^{24} \left[\frac{\mathrm{particles}}{\mathrm{m^2\ s}}\right]$$

Where $\gamma \sim 7$ is the semi-empirically derived sheath heat transmission coefficient. Since fusion design studies typically require a minimum lifetime of the divertor component of $\sim$2 years for economics, and for limiting reactor downtime, this corresponds an incredibly high fluence of particles compared to the number of particles that compose PFCs. Exposure of 10^{24} particles/m^{2}s integrated over two year corresponds to $\sim 6 \times 10^{31}$ particles/m^2, roughly 6 orders of magnitude higher than the areal density of 1 mm of solid tungsten, a common PFC material.

In effect, this means that these plasma particles that interact with the divertor must have an erosion yield of less than one part per million for the erosion levels in a reactor to be acceptable. These rates are essentially impossible with carbon

walls due to chemical erosion and push the limits of refractory materials like tungsten under ideal circumstances. Furthermore, due to the multi-scale nature of PMI, first principles prediction of erosion to such a level of control is unlikely. It is therefore imperative that high quality measurements of net PMI effects to material surfaces, such as net erosion, be made in order to explore and identify appropriate solutions to these issues.

1.3 PMI Diagnostics for Fusion

Plasma materials interactions have been recognized as major engineering challenge for fusion devices from the very beginning of fusion research, particularly for long pulse devices. Laboratory tokamaks, however, are typically short pulsed devices, with little or no access PFCs under normal operating conditions. This experimental constraint along with the priorities of the fusion community has historically resulted in a stronger emphasis plasma confinement and control, with inadequate diagnosis of PFCs. This has left PMI science understudied despite how critical it is for the success of fusion.

PMI is essentially a near surface phenomenon that typically affects surfaces on the depth scales of 10s of μm or less. This is the case because plasma erosion and deposition typically occur with rates on the order of 1-10 of nm/s as illustrated by the previous example. Since most tokamaks operate in short < 10 second pulses the net growth or erosion of surfaces occurs on the μm scale over the course of a several month to year long experimental campaign. In addition, diffusion of absorbed hydrogen, for example, typically occurs over μm length scales [66].

As a result, ion beam analysis (IBA) has become an important tool to study PMI. IBA involves using ion beams to induce nuclear reactions, elastic collisions, or atomic excitations in materials that are then used to identify and quantify isotopes in the materials surface. MeV ion beams have penetration depths of 10s to 100s of μm into solid materials and can induce many different reactions. At low beam current IBA is also non-disruptive to materials. Since IBA has the appropriate depth scale and versatility, it is therefore well suited for studying PFCs.

A review of IBA methods for fusion can be found in [53]. There are numerous examples of successful IBA studies of fusion materials. For example, erosion rates were measured in Alcator C-Mod with depth marker and Rutherford backscattering spectroscopy [54]. Another example is the use of IBA to quantify deuterium co-deposited with plasma impurity species such as beryllium, boron, carbon on PFCs in the Joint European Torus (JET) [44].

These techniques are successful at studying PFCs and serve an important function for PMI research, however standard IBA methods have several inherent limitations. The first is a practical, experimental limitation of the restrictive beam target chambers that are used in the analysis. After PFCs are removed they often need to be disassembled further to fit into an evacuated chamber for analysis. This can be a laborious process that limits the sample throughput and the size of the samples. This issue was addressed as part of this thesis with the design and implementation of an ex-

ternal ion beam system whereby, the ion beam exits the evacuated beamline through a thin, vacuum tight foil, allowing analysis to be performed in atmospheric pressure air. This enables the study of large PFC samples with relative ease and improves throughput and is introduced and described in chapters 2 and 3.

The second and most fundamental limitation is that standard IBA techniques necessarily make ex-situ measurements, meaning that a component must be removed from the fusion device, usually requiring a vacuum break. Since occasions when PFCs can be removed are relatively rare, IBA studies are typically limited to the quantification of long term net effects of PMI, often over the course of hundreds to thousands of plasma discharges. Since so many plasma discharges occur over the months of an experimental campaign, there is essentially no way to diagnose how one plasma configuration affects PFCs as compared to another.

Methods have been developed to increase the frequency of PFC access such as the Divertor materials evaluation system (DiMES) on the DIII-D tokamak [65]. This system allows samples to be inserted and removed from one location in the DIII-D divertor without a vacuum break. DiMES can significantly shorten the timescale of surface analysis, however, it comes at the expense of spatial resolution.

To date, there are no other viable methods to make measurements comparable to IBA on the timescale of a plasma discharge. To address this fundamental limitation of PMI diagnostics, a novel, spatially resolved, in-situ, and perhaps revolutionary diagnostic has been developed. This new technique, referred to as accelerator-based in situ materials surveillance (AIMS), is introduced in section 1.4.

1.4 Accelerator-Based In-Situ Materials Surveillance (AIMS)

The simple fact that PMI can only be studied as aggregate effects of hundreds or thousands of plasma discharges is a severe hindrance to PMI research, especially when a time resolution of a single discharge with spatial resolution is desired. The accelerator-based in situ materials surveillance (AIMS) technique was developed specifically to address the diagnostic need for spatial and time resolved measurements simultaneously.

AIMS utilizes a compact linear accelerator, gamma detectors, and neutron detectors to measure the evolution of PFC surface composition inside a magnetic confinement device. The technique is nondestructive to the PFCs, can access large fractions of the total PFC surface area, and is not disruptive to facility operations because it is designed to operate between plasma discharges. AIMS is essentially an ion beam analysis based in-situ diagnostic that is directly integrated with a tokamak. In and of itself, this is a novel concept for a PMI diagnostic. In addition, AIMS also provides spatially resolved measurements with approximately 2 cm spatial resolution on the shot-to-shot time scale by using the tokamak's magnetic field coils and DC supplies to steer and target the beam over a relatively large region of the plasma facing first wall [22]. The ability of AIMS to simultaneous study PMI on timescale of a single

plasma discharge with cm scale spatial resolution therefore makes AIMS an enormous leap forward in the state of the art of PMI diagnostics.

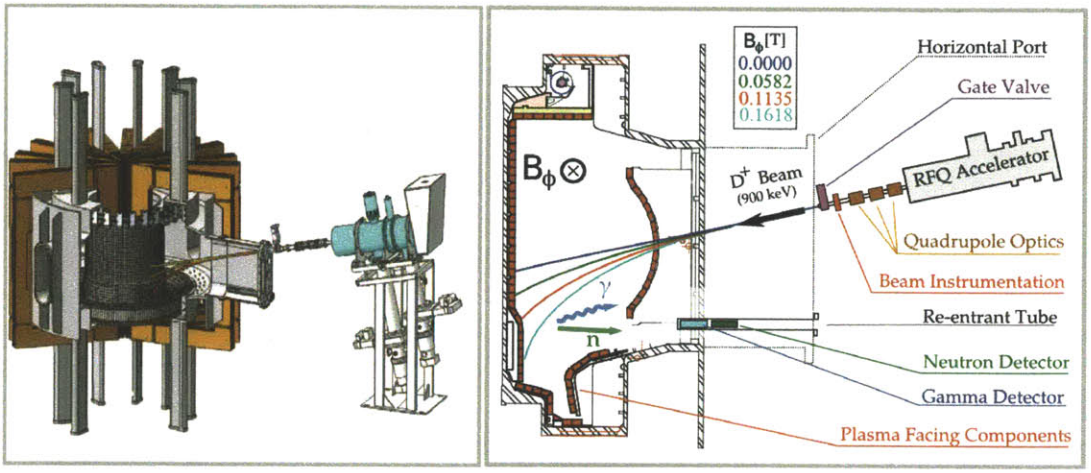

Figure 1-3: Left:CAD model of the AIMS diagnostic installed on Alcator C-Mod. Right: Schematic of AIMS components. AIMS utilizes a radio frequency quadrupole (RFQ) accelerator produce a 900 keV D^+ beam to induce nuclear reactions on the surface of plasma facing components (PFC). Spectroscopy of the resulting neutrons and gamma rays allow for the identification and quantification of isotopes on PFC surfaces. AIMS uses beam optics and toroidal field B_ϕ to steer the beam and achive spatially resolved measurements.

The development and implementation of the AIMS diagnostic, illustrated in figure 1-3, was a collaborative effort among researchers and graduate students at the MIT Plasma Science and Fusion Center with the work in the this thesis and the thesis of Z.S.Hartwig [21] contributing the bulk of the scientific, technical, and computational effort for AIMS. This diagnostic was a major undertaking involving engineering and integration of complicated accelerator systems, particle detection method in unfavorable environments, and advanced computation. The AIMS diagnostic was successfully implemented on Alcator C-Mod, making its first measurements during the 2012 experimental campaign. A review of AIMS diagnostic and its implementation is presented in [22] and the contributions of this thesis to design and implementation are outlined in section 1.6 and are presented in the following chapters.

1.5 High-Z PFCs and Wall Conditioning in Alcator C-Mod

One of the contributions of this thesis is the study boron using external IBA as well as the newly developed AIMS technique. Boron is not a PFC material per se, however it is used for 'conditioning' PFCs and plays a major role in the operation of Alcator C-Mod and other tokamaks that utilize high-Z PFCs.

From studies of PFCs for magnetic fusion reactors, there is a general consensus that the use of high-Z refractory materials, particularly tungsten, is the best choice for a reactor. This is due to tungsten's low erosion and low tritium retention and its ability to withstand high thermal loads and resist neutron damage and activation [14].

As a result, Alcator C-Mod uses almost entirely molybdenum PFCs – a high-Z refractory metal with similar properties to W. Despite the advantages of W and Mo, when high-Z elements enter the plasma energy confinement and plasma performance is degraded severely due to increased radiation from the high-Z impurities. This tends to have strong negative impact on C-Mod plasma performance when operating with bare Mo PFC, typically only achieving H-Mode plasmas with confinement quality $H_{\mathrm{ITER},89} \sim 1$.

This was solved early on with the C-Mod boronization process which plasma deposits boron on PFCs using an electron cyclotron discharge cleaning ECDC plasma with a helium-diborane gas mixture (10% B_2D_6, 90% He). The plasma is created near the ECDC resonance which is swept in the the radial direction by varying the toroidal field to distribute the boron across PFCs in the divertor (with typical parameters: field f = 2.45 GHz, B = 0.088 T at $R_o = 0.67$ m).

When PFCs are plasma coated with boron using this procedure, the impurity radiation of the confined plasma drops substantially and the performance improves, essentially doubling energy confinement time, with $H_{\mathrm{ITER},89}$ approaching 2. The improvement in performance degrades with plasma exposure yet boron remains on most surfaces according ex-situ measurements. This indicates that the decrease in performance is due to localized erosion of boron that occurs over a relatively small area of the PFCs [14].

Even though boronization is such a successful technique for improving plasma performance through impurity control, there is still relatively little quantitative understanding of its distribution after boronization and or the erosion patterns that are produced with plasma exposure. It therefore warrants further study with the newly developed AIMS technique.

Though boronization and other low-Z coating are not feasible for long pulsed devices or reactors, the erosion and deposition of boron is important to study because the regions of boron erosion that lead to impurity injection in high performance tokamaks like C-Mod can identify the regions or plasma conditions that are responsible for the degraded performance. Thus, measurements of boron can, in a sense, serve as a proxy for high-Z erosion and may play a vital role in understanding erosion in reactors as well as the complex net transport or migration of materials around the tokamak due to PMI.

1.6 Contributions

For this thesis, significant contributions were made to the field PMI research through the development of novel ion beam analysis techniques for fusion fusion devices.

A 1.7 MeV tandem accelerator was refurbished and upgraded for this thesis work,

providing the primary instrument used for ion beam analysis in the Cambridge Laboratory for Accelerator Study of Surfaces (CLASS). An external ion beam system was implemented on this accelerator to perform ex-situ ion beam analysis (IBA) on large components removed from Alcator. This effort enabled the IBA study of materials at MIT, a capability that was previously unavailable. In addition, this system was used to perform particle induced gamma emission (PIGE) on PFC tile modules to spatially map the boron content on post C-Mod and AIMS campaign boron. This provided the necessary measurements for comparison and validation of the AIMS technique.

Major contributions were also made to the development of the AIMS diagnostic, leading to its successful implementation and demonstration. The radio frequency quadrupole accelerator used for AIMS was completely refurbished as part of this thesis in addition to upgrades that allowed it operate remotely in the C-Mod cell. This was followed by the successful installation and integration of the RFQ with the Alcator C-Mod tokamak, a feat never before achieved. A suite of compact diagnostics was also developed for operation in confined spaces in vicinity of the tokamak port to aid with beam and optics characterization and alignment.

In addition, a comprehensive simulation code was developed to calculate the trajectory and 6-D phase space dynamics of the beam in order to model the beam's evolution in the complicated 3-D tokamak fields. This allowed the detection geometry of the AIMS technique to be modeled in order to make quantitative IBA measurements of boron surface density for the first time in-situ in a tokamak. In addition, modeling allowed spatial resolution to AIMS technique to be calculated.

With implementation of the AIMS diagnostic on Alcator C-Mod, measurements and analysis performed for this thesis yield the first ever large area, spatially resolved and quantitative spatially resolved and quantitative in-situ measurements of boron in a tokamak. These measurements demonstrated the capability to perform inter-shot measurements. Spatially resolved measurements over longer timescales ($\sim$ 1 hour per 4 measurements) were also achieved, showing evolution of boron resulting from C-Mod over a series of wall conditioning processes. Thus demonstrating, for the first time, both spatially and time resolved in-situ measurement of boron solid surface properties in a tokamak.

1.7 Chapters

This thesis is organized into six chapter, the first being this chapter the introduction. The following chapters describe the theory, technical developments, measurement techniques, and results that constitute the advances in PMI research demonstrated in this thesis.

Chapter 2: Ion Beam Analysis for Fusion Materials

Ion beam analysis (IBA) techniques are used to determine the quantity and distribution of elements in a materials surface. The theory and practices used for IBA are described. Particle induced gamma emission (PIGE) was the primary IBA technique

used for this thesis is described in the context of (1) external beam (in-air) ion beam analysis and (2) In the context of accelerator in-situ materials surveillance (AIMS). The applications specific theory and data analysis methodology are described presented for both PIGE and AIMS technique.

Chapter 3: Tandem Accelerator and External Beam Apparatus

External particle induced gamma emission (X-PIGE) analysis was used to generate a spatially resolved map of boron deposition on the inner wall of the Alcator C-Mod tokamak. The accelerator technology and hardware development is reviewed in this chapter, followed by the development and applications of the X-PIGE technique. This work and analysis was done to understand the spatial distribution of boron on PFCs and validate the results from the newly developed AIMS diagnostic.

Chapter 4: Integration of a Compact Ion Accelerator with a Tokamak

The AIMS diagnostic technique requires the integration of a compact accelerator with a tokamak to study plasma material interactions. The engineering requirements, solutions, and innovations for this installation are described. The refurbishment, upgrades, and principles of operation of the accelerator used for this diagnostic are also reviewed. Since this is the first integration of an RFQ accelerator with a tokamak and the first use of an RFQ for IBA of materials, significant hardware developments and necessary innovations including compact beam diagnostics and instrumentation are presented with their applications leading up to the successful implementation of accelerator for the AIMS diagnostic.

Chapter 5: Beam Dynamics and Control

The fundamental purpose of the AIMS diagnostic technique is to enable spatially resolved measurements of surface properties inside of fusion devices by localizing an injected ion beam onto the desired locations. This requires advanced beam dynamics modeling. Important aspects of particle interactions with electromagnetic fields and beam dynamics theory are presented followed by a description of the computational modeling techniques that were implemented. The computational tools that were developed demonstrate the capabilities and validation of the necessary beam simulations that used to determine the beam trajectories, detection geometry, and spatial resolution of the AIMS technique.

Chapter 6: Results and Discussion

AIMS was successfully implemented and applied to study boron erosion and deposition on the surface of plasma facing components (PFC) in Alcator C-Mod. Measurements were made on the inner wall of Alcator C-Mod using the AIMS technique before, during, and after the last run day of the 2012 C-Mod campaign to observe the effects of plasma discharges. Subsequent measurements were taken during the

months following the campaign to observe changes due to plasma conditioning operations that include boronization, electron cyclotron discharge cleaning (ECDC), and glow discharge cleaning (GDC). These results are presented with discussion of the their implications. The results of the AIMS validation with external beam PIGE analysis are also presented demonstrating the success of AIMS as a first of a kind, in-situ materials diagnostic, followed by a description of future developments to improve upon the capabilities of AIMS.

Chapter 2

Ion Beam Analysis for Fusion Materials

Ion beam analysis (IBA) techniques are used determine the quantity and distribution of elements in a material's surface. IBA involves using ion beams to induce nuclear reactions, elastic collisions, or atomic excitations in materials. Spectroscopic measurements of the reaction products are then used to identify and quantify isotopes in the material's surface. MeV ion beams can induce many different reactions and, at low beam current, are non-disruptive to materials. As a result, there are a wide range of IBA techniques that are used across many fields from semiconductor processing to non-destructive analysis of historic art pieces. A comprehensive description of these well established methods and particle detection techniques can be found in the Handbook of Modern Ion Beam Materials Analysis [51] and other references on particle detection such as [33].

As the science of plasma surface interactions has progressed, the use of IBA has become an integral part of how fusion materials are studied. There have been numerous IBA studies on components from Alcator C-Mod and other tokamaks [44]. Most of these studies use standard IBA techniques and performed on components removed from partly disassembled tokamaks and are studied under vacuum in separate accelerator facilities. These IBA ex-situ techniques, including those listed in shown in table 2.1, span a wide range of fusion applications and are vital to PMI research. However, the development of new and innovative techniques such as the AIMS diagnostic for in-situ measurements of PMI in Alcator C-Mod, and the implementation of an external ion beam analysis as part of this thesis, constitute a significant contribution to the field of PMI science.

The following sections focus on the theory and application of the gamma emission and spectroscopy that enable boron detection for external beam PIGE analysis and for AIMS. This serves to provide necessary IBA background to understand to data analysis techniques used for the implementation of X-PIGE, described in chapter 3 and the implementation of modeling of the AIMS technique in chapter 4 and 5.

Technique	Application	Mechanism
PIGE	Quantify Low-Z isotopes, depth resolution possible if resonance reactions exist	γ-Rays
PIXE	Quantify areal density of high-Z isotopes near surface	X-Rays
RBS	Depth resolved measurements of surfaces: Most effective for high-Z features in low-Z substrate	backscattered ion
ERD	Depth resolved measurements of surfaces: Most effective for low Z features in high-Z substrate	ejected atom
NRA	Depth resolved measurements of surfaces impurities: Most effective for low Z if reaction is available	reaction product (α, p, n)

Table 2.1: Common ion beam analysis techniques used for fusion materials: particle induced gamma emission (PIGE), particle induced X-ray emission (PIXE), Rutherford backscattering spectroscopy (RBS), elastic recoil detection (ERD), and nuclear reaction analysis (NRA).

2.1 Particle Induced Gamma Emission

Particle induced gamma emission (PIGE) analysis utilizes an ion beam to induce prompt gamma emission from nuclear reactions in a target material. Gamma rays from the induced reactions are detected, identified, and counted. Using known cross section data, the beam parameters from the experiment, and the detection geometry, isotopes that are present on the target surface can be quantified if they are within the penetration depth of the beam. Since PIGE analysis with ~MeV beams is best suited for measuring low-Z isotopes and can have a dynamic range of spanning a few nm up to 10s of μm, PIGE was the natural choice for analyzing PFCs in Alcator C-Mod. For this thesis, PIGE analysis is used extensively for quantifying boron and is described as it applies to external beams in section 2.2.1 and as it applies to AIMS in section 2.6.

2.2 Gamma Detection

PIGE is essentially a particle counting technique that relies on the energy resolved detection of individual photons. Each individual incoming photon that is absorbed by a detector results in a signal that is proportional to (or is some function of) the energy that was deposited by the photon. The details of the detection equipment for PIGE is described in chapter 3, section 3 and is described for AIMS in [21].

As the particles are counted, they are used to construct a histogram of gamma counts versus energy as illustrated in figure 2-1. Such a histogram is commonly referred to as a gamma spectrum. For gammas of a single energy, there are multiple

features that are observed in the spectrum that are related to the detection process.

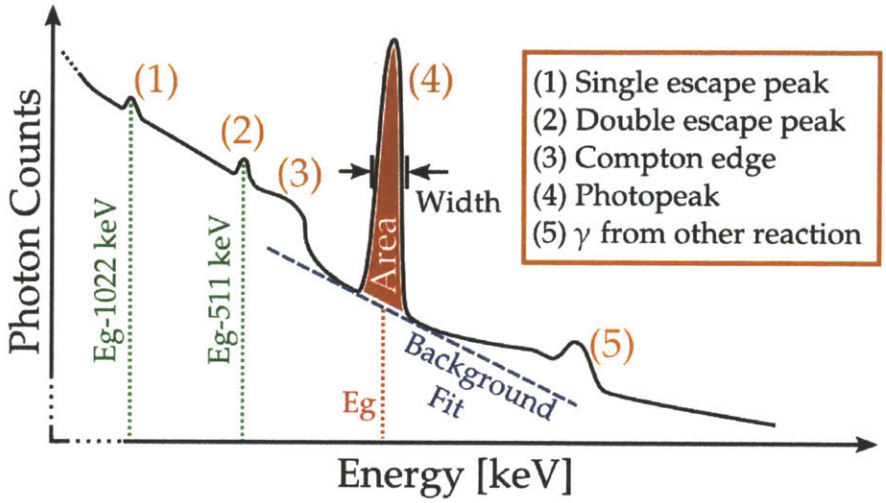

Figure 2-1: Illustration of spectrum for generated from a PIGE measurement showing the notable features in the gamma measurement. (Horizontal axis not to scale).

The most important feature is the photopeak which results form the photon being completely absorbed by a single electron in the detector. Since the gamma is produced by a specific nuclear energy level, the energy of the photopeak E_g can be used to uniquely identify the reaction. Therefore, the counts that are within the photopeak are counted and used to quantify the isotope involved in the gamma emission. The width of the peak can be caused by a variety of factors such as the temperature of the detector, the natural width relating the excitation-decay timescale, and the energy resolution of the detector. Typically for PIGE, the width is primarily due to the energy resolution of the detector and, for the purposes quantifying a reactions photopeak, the peak width is is only important if there are neighboring peaks that could overlap and interfere with the measurement [31].

The spectrum also contains a continuum of lower energy elastically scattered gammas ending with a maximum energy $E_g - m_e c^2/2$ below the photopeak due to Compton scattering. For higher energy gammas ($E_g > 1.022$ MeV $= 2m_e c^2$), there are two additional peaks resulting from pair production (the conversion of a photo to a electron β^- and positron β^+ pair). When the β^+ annihilates with an electron, there is some probability that one or two of these gammas will escape the detector without being reabsorbed. These events therefore appear to the detector like gammas with energy $E_{g,\text{det}} = E_g - m_e c^2$ or $E_{g,\text{det}} = E_g - 2m_e c^2$, which are called single and double escape peaks, respectively [31].

Most often for PIGE measurements, only the photopeak is of interest for quantifying the reacting isotope. To properly determine the number of counts in the peak due to reaction, the background in the spectrum is subtracted. The background beneath the photopeak is caused by a combination sources including Compton scattered gammas from higher Q-reactions, natural radioactive decay, and cosmic rays. Usually the background can be subtracted using a peak finding algorithm that linearly inter-

polates the background across the region of the peak. These background subtraction algorithms are well established and often built into analysis software [42, 21]. After the background subtraction is complete, the peak can be integrated to give the total number of gammas from that reaction of interest that were counted by the detector. Since these photopeak counts are directly related to the quantity of the isotope that is present, analyzing these results with the accompanying beam physics, detection geometry and nuclear data are the subject of the following sections.

2.2.1 PIGE Analysis with an External Beam

PIGE analysis is usually conducted in an evacuated chamber because beams lose energy and gamma rays are attenuated as they pass through a gas such as air. However, if the interaction of the air with the beam and detection geometry are well understood, PIGE analysis can be performed in atmospheric pressure air. With proper analysis this can be accomplished implementing a thin vacuum tight exit foil to allow the beam to pass from the evacuated beamline to the sample in air at atmospheric pressure.

Analyzing the sample in air is highly advantageous because the size of sample is not limited to the size by the vacuum chamber – a common limitation with standard in-vacuum IBA. Also, large samples can be repositioned and studied at multiple locations with relative ease. Samples can be replaced or repositioned without venting vacuum chamber for repositioning with complicated vacuum-mechanical feedthroughs. For fusion PMI research, where large areas of plasma-facing surfaces are of interest, external beams are thus highly valuable.

With the advantages of external beam IBA, there are also some experimental considerations that must be accounted for in the analysis. In particular, the beam's energy distribution is changed significantly as the beam passes through the exit foil and air. Due the energy dependence of nuclear reaction cross sections, this is an important consideration for making external PIGE measurements and discussed in section 2.4.1. In addition, more of the practical and experimental implications of using external beams are described in detail in chapter 3.

2.3 Beam Induced Reactions for PIGE

Ion beams of several MeV can readily penetrate the Coulomb barrier of light nuclei making PIGE most effective for detecting light elements with $Z < 30$. Most of these elements have measurable (p, γ) and (d, γ) cross sections at energies less than 10 MeV [50]. PIGE is therefore useful for measuring low-Z elements on PFCs such as boron. The probabilities of reactions resulting from energetic particle interactions are tabulated in the form of a cross section $\sigma(E)$. Cross sections have units of area, commonly given in of units of barns (1 b = 10^{-28} m^2), and are dependent on the energies of the interacting particles. Cross sections are convenient because the probability P of a reaction per incident particle per unit distance is given by the relation $\frac{dP}{dx} = n_t \, \sigma$ for energetic particles passing through stationary target particles with volumetric density

$n_t(x)$. The reaction probability P can also be represented in terms of uniform layers with areal density Φ by relation $P = \Phi\,\sigma$. These probabilities are then related to the reaction yield Y by the number of incident ions Ni from the relationships given in equation 2.1. The function dependences of these functions on beam energy, beam range, and position are discussed further in section 2.5.1.

$$Y = N_i \int_{range} n_t\,\sigma\,dx\,, \quad Y = N_i\,\Phi\,\sigma \tag{2.1}$$

Reaction data are also tabulated as a quantity referred to as the astrophysical S-factor, commonly with units $[eV \cdot b]$. The S-factor $S(E)$ is related to the cross section $\sigma(E)$ by an exponential fitting function given by equation 2.2 and the Sommerfeld parameter given in equation 2.3.

$$\sigma(E) = S(E)\exp(-2\pi\eta)\frac{1}{E} \tag{2.2}$$

$$\eta \equiv \frac{Z_1 Z_2 e^2}{\hbar\nu} = 0.1575 Z_1 Z_2 \left(\frac{A}{E}\right)^{1/2} \tag{2.3}$$

Where E and Z_i are the energy [MeV] and nuclear charge of the ions, respectively and A is the reduced mass of in [AMU]. The S-factor is usually a weakly varying function of energy and has a functional form that is derived from the Coulomb barrier tunneling probability for colliding charged particles. Since the functional form of the S-factor captures the physics of low energy nuclear reactions, it can be used to make reasonable extrapolations for charged particle induced nuclear reaction cross sections to energies where no data is available [2]. This can be useful in the context of PIGE analysis when integrating the low energy portion of the cross section. However, this is often not necessary since the low energy portion of the cross section produces negligible contribution to the yield in many cases.

Due to the quantized energy states within nuclei, an ion with an energy that closely matches a particular nuclear excitation is more probable. This can cause a reaction cross sections to be sharply peaked at a specific resonance energy E_r. These resonant reactions, can be useful in some cases because they allow elemental depth profiling using measurements at multiple energies, especially if the resonance peak is large compared to the non-resonant part of the cross section. However, in the context of using PIGE to obtain the total boron areal surface density on the PFC surfaces, resonant reactions tend to complicate the relationship between boron thickness and a gamma yield causing a hypersensitivity to boron density at a certain depth but not at others. Therefore, for determining areal surface density, the beam energy is chosen to avoid such resonances.

2.3.1 Reactions for Boron Detection

$^{10}_{5}\mathrm{B}(p,\alpha\gamma)^{7}_{4}\mathrm{Be}$

The most useful reaction for external beam boron detection on C-Mod tiles is the $^{10}_{5}\mathrm{B}(p,\alpha\gamma)^{7}_{4}\mathrm{Be}$ reaction. Cross section data for this reaction is shown in figure 2-2 [10]. This reaction has a very large cross section relative to other boron reactions and is dominant in the gamma spectrum even though natural boron is only 20% ^{10}B and 80% ^{11}B. In addition it produces gamma photons with energy $E_\gamma = 429$ keV which are low enough in energy to be in the range where the NaI detection efficiency is the highest.

This reaction was therefore the natural choice for external PIGE analysis of boron. Since this cross section $\sigma(E)$ has a resonance around 1.5 MeV, a beam energy close to 2.5 MeV was chosen to avoid the resonance while utilizing the part of the $\sigma(E)$ curve that still has a large cross section but varies weakly with energy. This ensured that the measurement would have sufficient counts and would not be overly sensitive to beam energy due uncertainty in sample positioning.

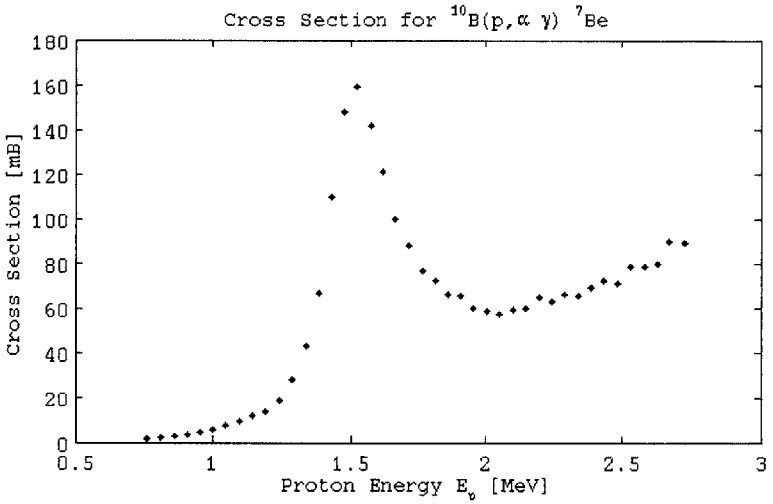

Figure 2-2: Cross section data for the $^{10}_{5}\mathrm{B}(p,\alpha\gamma)^{7}_{4}\mathrm{Be}$ reaction ($E_\gamma = 429keV$) measured by R.Day and T.Huus [10].

$^{11}_{5}\mathrm{B}(p,\gamma)^{12}_{6}\mathrm{C}$

This reaction was also considered for PIGE detection of Boron. The cross section for this reaction has several resonance energies ($E_r = 163, 675, 1390keV$). The resonant peak at $E_r = 1390keV$, is very broad (1270 keV width). Though the 1390 keV peak is classified as a resonance, the cross section is relatively flat and therefore favorable because this weak variation in energy causes the gamma yield to be roughly linear with boron thickness. However, this reaction has a relatively small cross section even at resonance ($\sigma_r = 0.053$ mb) and yields several relatively high energy gammas, $E_\gamma = 4.43, 12.80$, and $17.23MeV$ which are absorbed less efficiently by the detector

[50]. Its resonance is broad enough that the cross section will be approximately constant over the expected thickness of the boron. Since this reaction was much more difficult to detect, the ${}^{10}_{5}\mathrm{B}(p,\alpha\gamma){}^{7}_{4}\mathrm{Be}$ was used for the analysis instead.

2.4 Modeling Ion Beam Interactions With Matter

To extract meaningful information from IBA data, information about the ion beam's trajectory as it passes through the sample material must be calculated. In particular, for depth profiling, the energy as a function of penetration depth x must be known. The beam's trajectory is dependent on several parameters which are interrelated: the atomic densities of the matter's constituent elements $n_j(x)$, the incident ion beam energy E_b and the ion stopping power of the material, $S(E) = -dE/dx$.

The physical situation causes several of these functions to be implicit functions of each other. As the ion beam passes through the material it loses energy at a smooth continuous rate due to small angle scattering off electrons. This slowing down rate is characterized by the stopping $S(E, \rho_j(x))$ at a rate that is dependent on the energy of the beam and the density of each atomic species j. Since the densities $\rho_j \equiv m_j \cdot n_j(x)$ of the elements that make up the target material are generally a function of depth x in the direction normal to the surface, the ion stopping $S(x, E)$ of the target material can be calculated using Bragg's Rule shown in equation 2.4.

$$S(E)_{total} = \sum_i \left(\frac{1}{\rho}\frac{\partial E}{\partial x}\right)_i \cdot \rho_i \tag{2.4}$$

The energy of the beam at a depth x depends on the initial energy of the beam E_b on the sample and implicitly depends $S(x, E)$ and is given by the following integral (2.5):

$$E(E_b, n(x), x) = E_b - \int_0^x S(x, E(x))dx \tag{2.5}$$

2.4.1 External Beam Energy Loss

To study proton induced reactions, it is necessary to determine or predict the energy of the beam as it interacts with the sample. Accelerators used for IBA typically produce nearly mono-energetic beam with a well calibrated energy, however the beam loses energy as it passes through the vacuum-air exit foil (described in section 3.3.5), the air, and the sample. The energy loss in these regions must be quantified so that the proper beam energy and cross sections can be used to interpret gamma yields.

To calculate the energy loss of the ion beam as it passes through the window and air gap on its way to the target requires solving equation 2.5 numerically. This is accomplished by iterating equation 2.6 over a 1-D spatial grid x_n.

$$E(x_{n+1}) = E(x_n) - S\left(E(x_n)\right) \cdot (x_{n+1} - x_n) \tag{2.6}$$

2.5 PIGE Data Analysis

In order determine the areal density of an isotope with PIGE analysis, the photopeaks in the gamma spectra corresponding to the reaction of interest must be identified and integrated. The gamma counts from the photopeak must be properly normalized to beam and detection parameters and then related to the areal density of the isotope that produced the gamma emission. This is done by numerically calculating the reaction yield for an assumed density profile $n(x)$ for an array of different profiles to generate a relationship between gamma yield and density profile.

Since $n(x)$ is not known, a profile for $n(x)$ must be assumed for the yield calculation. If the density profile is expected to be complex and if depth profiling is required, the profile must be reconstructed from a series of measurements at different energies and iterated upon until a solution (not necessarily unique) is reached. However, since boron is plasma deposited on the surface of C-Mod PFCs with typical thicknesses $x \sim 1$ μm which is much less than than be beam's range ($x \ll R(E_b)$), the profile does not have a significant effect on the yield. Therefore, it is possible to calculate the yield in a straightforward way by assuming the boron is a uniform solid surface layer.

2.5.1 Calculating Gamma Yield

As the ion beam passes through the material the number of gamma photons produced is dependent on the reaction cross section $\sigma(E)$, target density $n(x)$ and the properties of the beam. The total gamma yield Y, defined as the number of gammas produced, is determined by an integral over the the ion beam's range, given equation 2.7.

$$Y(E_b, n(x)) = N_i \cdot \int_0^{R(E_b)} n(x)\sigma(E(x))dx \tag{2.7}$$

Where $R(E_b)$ is the ion beam range, $\sigma(E(x))$ is the cross section of the reaction, and $N_i = \frac{Q}{e\,Z_i}$ is the number of ions incident on the surface of the target. These quantities can be defined in terms of experimentally measured parameters: The incident beam current I_b, the charge $Q = \int_t I_b\,dt$ equivalent to the integral of I_b over duration of the measurement and ion charge $e\,Z_i$.

Since the probability that the reaction will occur is energy dependent, given by the cross section $\sigma(E)$, the yield can be equivalently represented as an integral over the beam particles' energy as they slow down, weighted by the reaction cross section as shown in equation 2.8.

$$Y(E_b, n(x)) = N_i \cdot \int_{E_b}^{0} \left[\frac{n(x)\sigma(E)}{-S(x,E)}\right] dE \tag{2.8}$$

Though equations 2.7 and 2.8 can be used to mathematically describe the gamma yield for PIGE experiments, they generally cannot be integrated analytically. This is because the ion stopping $S(x, E)$ is simultaneously dependent on position x and energy E which are implicit functions of each other. Numerical integration is therefore

necessary and is described in section 2.5.3.

2.5.2 Calibration and Normalization

Proper calibration is necessary because the count rates in these experiments are dependent on a number of factors and experimental parameters some of which can vary in time. Absolute calibration is often challenging because many aspects of IBA experiments such as detection efficiency, losses due to attenuation, and other geometric effects, cannot be easily determined. This issue is further complicated because many of these effects, including detection efficiency and attenuation, are dependent on energy E_γ. It is therefore advantageous, and often times necessary, to use known standards to normalize out the detection parameters to avoid systematic experimental error.

When taking PIGE measurements, all of the beam parameters can be kept constant except for the beam current due to fluctuations in the ion source. These fluctuations are usually fairly small ($< 5\%$) during a 100 second experiment, but over the course 10s or 100s of measurements, the beam current can often drift by a factor of two or three. Since the current dQ/dt varies throughout the measurement and the yield of the reactions is directly related to the total number of incident ions Q/e by the reaction cross sections, the total charge must be integrated and used to normalize the data.

Often with PIGE analysis the current can be measured directly from the sample with the appropriate secondary electron suppression techniques to recollect the electrons that are ejected from the material surface by the beam. This method however is not reliable for external beams as discussed in section 3.3.2. Instead the beam current is measured from aperture that supports the beam window using charge digitizer. Measuring the beam current that is clipped by the aperture is only a relative current measurement but it is highly repeatable from one measurement to the next and is representative of the total beam current on the sample. Since the beam current is necessarily a relative measurement in this case, external ion beam relies on normalization to standards for quantitative measurements.

Since the gamma detection systems generally have a small but finite amount of 'dead time' as they are processing each absorbed photon, the charge collected must be scaled so that it reflects the total charge collected by the sample when the detector was active. This is done by multiplying collected charge Q by the ratio of the detector live time τ to the real time t.

To remove the detection geometry and detector efficiency from measurement, the most convenient normalization for PIGE are thick target yield measurements of known targets. Since the experimental parameters are the same between the samples and the standard and the composition of each standard is known, dividing the yields from each sample by the yield from the standard will cause the experimental constants to cancel. The normalized yield $\bar{Y}$ used for comparing and analyzing data is given by equation 2.9. Where the subscript 1 denotes the quantities associated with the unknown sample and subscript 0 denotes those associated with the calibration target.

$$\bar{Y} = \left(\frac{N_1}{Q_1 \cdot \frac{\tau_1}{t_1}}\right) / \left(\frac{N_0}{Q_0 \cdot \frac{\tau_0}{t_0}}\right) \tag{2.9}$$

Since the details of the geometry and detector have been factored out of the equation, the absolute gamma yield from the sample can be inferred simply from the gamma yield of the known target, removing the uncertainties that may exist in the detection setup. The normalized yield can then be used in the analysis with cross section data to make quantitative measurements.

2.5.3 Gamma Yield Calculation

To calculate the gamma yield for a specified material density profile, equation 2.7 must be integrated. This expression can be numerically integrated over the position x_i coordinate using the following method, described by equations 2.10, 2.11, 2.12, and 2.13.

$$x_{n+1} = x_n + \Delta x \tag{2.10}$$

$$S(x_n) = \sum_j \left(\frac{1}{\rho}\frac{\partial E}{\partial x}\right)_j \cdot m_j \cdot n_j(x_n) \tag{2.11}$$

$$E(x_{n+1}) = E(x_n) - S(x_n) \cdot \Delta x \tag{2.12}$$

$$Y_k(x_{n+1}) = Y_k(x_n) + n_k(x_n) \cdot \sigma_k\left(E(x_n)\right) \cdot \Delta x \tag{2.13}$$

First, the initial beam energy E_b, the cross section $\sigma(E)$ and the mass density $\rho_j(x) = m_j \cdot n_j(x)$ of the elements is specified. The stopping power $S(x, E)$ is dependent on the particles' energy and the target material so the total stopping $S(x_n)$ must be recalculated at every value of x_n, using the tabulated stopping data $S(E) = \frac{1}{\rho}\frac{dE}{dx}$ [68] for each element in the material (equation 2.11). Next, the energy is calculated using the $S(x_n)$ (Equation 2.12). The yield per incident particle $Y_k(x_n)$ is calculated for the cross section $\sigma_k(E(x_n))$ of reaction k (Equation 2.13).

This method can be used to calculate the gamma yield for any assumed density profile $n(x)$. Since this density profile is not necessarily known for the sample, $n(x)$ must be assumed. Some iterative profiling techniques to determine $n(x)$ were explored in a previous work [3], however, as mentioned earlier, a uniform surface density of boron is assumed for this study for since the boron films are relatively thin compared to the proton range and are insensitive to the profile shape.

2.5.4 Error Analysis for External PIGE

The data collected in IBA experiments are essentially counting measurements where each count is an independent, uncorrelated, random event. The uncertainty in the measurement is therefore calculated using Poisson statistics. The same is true with

the integrated current measurement made with the charge digitizer. As such, the uncertainty in the number of counts N from these measurements is simply $N \pm \sqrt{N}$ with fractional uncertainty $1/\sqrt{N}$. Since there are also other experimental uncertainties that scale the yield measurement, the fractional uncertainties of all of these variables must be added in quadrature [31].

The primary experimental uncertainty is due uncertainty in the charge integration process. The Poisson statistics of the charge digitization produce negligible uncertainty, however, as the beam shape drifts over time, the ratio of beam current passing through the exit-window to the current that is intercepted by the aperture can vary slightly. Measurements with a calibration standard are taken as often as possible to minimize this uncertainty however it typically leads to uncertainties of 3-4%. This can be measured by the fluctuations in normalized yield of calibration standard and is the dominant contribution to the $\Delta Q/Q$ terms in equation 2.15.

Another experimental uncertainty is due to the precision of the sample positioning which can be expected to be a fraction of a millimeter. Variations in position slightly change the beam energy which changes the range of the beam and the average cross section over the range. The fractional change in counts N in each measurement due to changes in position x is given by equation 2.14. Where the stopping power of air S_{air} and the cross section σ form a function $f_x(E_{\text{beam}})$ which varies smoothly with beam energy E_{beam} except in the vicinity of resonances. If the positioning uncertainty is assumed to be $\Delta x = 0.2$ mm, the contribution of Δx is small, but non-trivial.

$$\frac{1}{N}\frac{dN}{dx} = \left(\frac{1}{\sigma}\frac{d\sigma}{dE}\right)\left(\frac{dE}{dx}\right)_{\text{air}} = \frac{S_{\text{air}}}{\sigma}\frac{d\sigma}{dE}\bigg|_{E_{\text{beam}}} = f_x(E_{\text{beam}}) \tag{2.14}$$

$$\frac{\Delta\bar{Y}}{\bar{Y}} = \left[\frac{1}{N_1} + \frac{1}{N_0} + \left(\frac{\Delta Q_1}{Q_1}\right)^2 + \left(\frac{\Delta Q_0}{Q_0}\right)^2 + f_x^2\Delta x_0^2 + f_x^2\Delta x_1^2\right]^{1/2} \tag{2.15}$$

The uncertainties in t and τ could also be considered, but they are known to very high precision and are negligible. The total uncertainty, based the experimental and counting uncertainties are therefore combined in quadrature and given in equation 2.15 to give the fractional uncertainty in $\bar{Y}$.

2.5.5 Boron Areal Density Correlation for External PIGE

For the external PIGE measurements of C-Mod inner wall tiles used for AIMS validation, the apparatus described in chapter 3 was used to produce a proton beam for boron analysis. A 2.5 MeV proton beam was used to induce the $^{10}_{5}\mathbf{B}(p,\alpha\gamma)^{7}_{4}\mathbf{Be}$ reaction in the plasma deposited boron on the C-Mod and in the boron nitride (BN) standard target. An energy of 2.5 MeV was chosen because the cross section for $^{10}_{5}\mathbf{B}(p,\alpha\gamma)^{7}_{4}\mathbf{Be}$ is greater than 60 mb and has a relatively shallow slope above 1.75 MeV (see figure 2-2 for cross section).

Since the boron layers are expected to be on the order of several μm or less and the stopping of boron is $\sim$27 keV/μmm at this energy, the energy of the beam is not expected to vary by more than $\sim$100 keV within the boron layer. This means that

the shallow slope and approximately constant stopping power in this energy range should cause the gamma yield to vary nearly linearly with boron thickness.

The relationship between gamma yield and boron was calculated more rigorously using the methods for gamma yield calculation described in section 2.5.3. A correlation was generated to relate the measured gamma yield to the areal density of boron present on the surface. This is done by numerically calculating the reaction yield for a solid boron layer of thickness x for an array of different profiles to generate a relationship between gamma yield and density profile. Due to the energy dependence of the cross section and stopping power, this relationship is unique to this specific beam energy and reaction.

To create this correlation, first the beam energy on the target surface was calculated form the initial beam energy degraded by the kapton vacuum-exit foil and the 5 mm air gap between the window and the sample using the methods in section 2.4. The calculated beam energy is listed bellow at the following locations along its trajectory:

- Energy from Accelerator = 2.50 MeV
- Energy after Kapton = 2.36 MeV
- Energy on target after 5 mm of air = 2.29 MeV

For the 2.29 MeV proton beam on target, the gamma yield $Y(x_B)$ was calculated for a range of boron thickness x_B values by numerical integration of the cross section data as described in section 2.5.3. Similarly the 'thick target' yield $Y_t t$ was calculated for boron nitride with a thickness greater than the beam's range. The calculated $Y(x_B)/Y_{tt}$ curve therefore provides a direct correlation between the thickness of boron on the surface a sample the gamma yield normalized to the thick target yield from a boron nitride target with the same detection geometry. This calculated correlation is shown in figure 2-3.

As expected, this curve is approximately linear in the range from 0 up to >10 μm of boron thickness. The slope of the linear region is $\frac{\Delta x_B}{\Delta Y_N} = 17.04\mu$m essentially gives the proportionality between normalized gamma counts and boron thickness. Furthermore, since the cross section in this region has slope of $\frac{1}{\sigma}\frac{d\sigma}{dE} = 0.587$ [MeV^{-1}], the uncertainty introduced by positioning of the sample can be estimated. The contribution of the sample positioning uncertainty can be calculated from 3^{rd} and 4^{th} terms of equation 2.15, giving the relationship in equation 2.17. As expected, this calculation shows that uncertainty due to sample positioning is quite small.

$$\frac{\Delta x_B}{x_B} = \left[\left(\frac{S_{\text{air}}}{\sigma}\frac{d\sigma}{dE}\right)^2 \Delta x_0^2 + \left(\frac{S_{\text{air}}}{\sigma}\frac{d\sigma}{dE}\right)^2 \Delta x_1^2\right]^{1/2} \simeq \sqrt{2}\, S_{\text{air}} \left(\frac{1}{\sigma}\frac{d\sigma}{dE}\right) \Delta x \qquad (2.16)$$

$$\left.\begin{array}{rcll} \frac{1}{\sigma}\frac{d\sigma}{dE} & = & 0.587 & [\text{MeV}^{-1}] \\ S_{\text{air}} & = & 14.85 & [\text{keV/mm}] \\ \Delta x_{1,2} & = & 0.2 & [\text{mm}] \end{array}\right\} \quad \Rightarrow \quad \left(\frac{\Delta x_B}{x_B}\right)_{\text{air}} = 0.00247 \qquad (2.17)$$

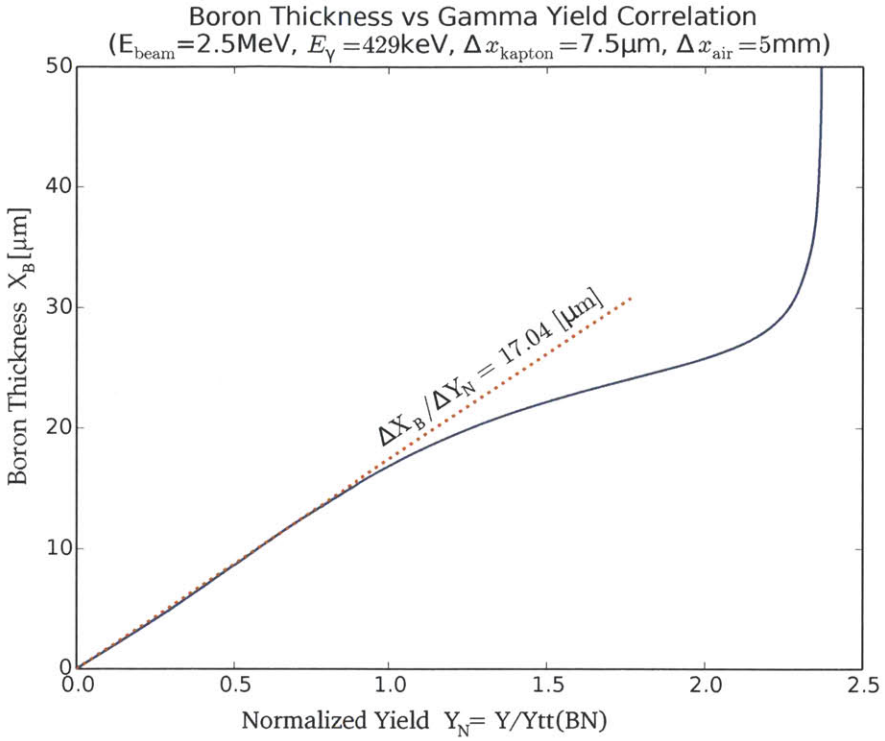

Figure 2-3: Correlation relating boron thickness to the gamma yield, normalized to the thick target yield Y_{tt} from a boron nitride (BN) target.

Another potential source uncertainty in the measurement of boron the assumption that that all of the boron is present on the surface. Due to the complexities of PMI, it possible that there is some mixing between boron and molybdenum in C-Mod. This could potentially be an issue because Mo has a substantially higher stopping power than boron and does not contribute to the gamma emission.

Since the boron layers are ~ 1 μm thick, the cross section is approximately linear over this range and while the stopping power is approximately constant. To observe the effects of B/Mo mixing, the average beam energy over beams transit through the surface layer should be considered. Since the stopping approximately S is constant, the average energy of the beam $\bar{E}$ within the layer of thickness Δx_{layer} is given by equation 2.18.

$$\bar{E} = E_{\text{beam}} \left(1 - \frac{S}{2} \Delta x_{\text{layer}} \right) \tag{2.18}$$

For uniform layers, only areal density is relevant for stopping and for gamma yield. If a 1 μm thick solid B layer is superimposed with a solid Mo layer of the same number density, this is equivalent to creating a mixed layer of B and Mo equal proportions while keeping the B areal density constant. Considering equation 2.18, this means that change in average energy loss of the beam within the layer will be 1/2 the the energy loss caused by the Mo. Therefore, for thin layers where S is constant and σ is

linear, the change in reaction yield Y is given by equation 2.19.

$$\frac{\Delta Y}{Y} = \frac{1}{\sigma}\frac{d\sigma}{dE}\Delta\bar{E} = \frac{1}{\sigma}\frac{d\sigma}{dE}\frac{S_{\mathrm{Mo}}\Delta x_{\mathrm{layer}}}{2} \tag{2.19}$$

From this, the fractional change in the boron measurement $(\Delta x_B/x_B)_{\mathrm{B/Mo}}$ can be calculated as shown in equation 2.20. This shows that even if a 1 μm B layer is mixed with Mo to form a layer that is half B and half Mo ($n_B/n_{\mathrm{Mo}} = 1$), the resulting measurement will only differ by 1.8%. Since Mo mixing is expected to be substantially less than than this, it is likely that mixing will contribute $< 1\%$ to the uncertainty of the measurement.

$$\left.\begin{array}{rcll} \frac{1}{\sigma}\frac{d\sigma}{dE} & = & 0.587 & [\mathrm{MeV}^{-1}] \\ S_{\mathrm{Mo}} & = & 60.68 & [\mathrm{keV}/\mu\mathrm{m}] \\ n_B/n_{\mathrm{Mo}} & = & 1 & [-] \\ x & = & 1 & [\mu\mathrm{m}] \end{array}\right\} \quad \Rightarrow \quad \left(\frac{\Delta x_B}{x_B}\right)_{\mathrm{B/Mo}} = \frac{S_{\mathrm{Mo}}\Delta x_{\mathrm{layer}}}{2} = 0.018 \tag{2.20}$$

2.5.6 Areal Density and Boron Thickness

The measurement of boron thickness described in the precious section are actually a measure of an areal density of boron [atoms/m^2]. The thickness is a convenience for physical interpretation but uses an assumption of density which actually does not affect the quantification of surface boron. To convert between areal density Φ and thickness x assuming a density $\rho_B = 2.34$ [g/cm^3], the conversion is given for reference in equation 2.21. Where $M_B = 10.81$ [g/mole] is the atomic mass of boron is $A_o = 6.022 \times 10^{23}$ [atoms/mole] is Avogadro's number.

$$\Phi = \frac{\rho A_o}{M}x \Rightarrow \begin{cases} 1.0000\ \mathrm{nm} & = & 1.3036 \times 10^{20}[\mathrm{atoms/m^2}] \\ 1.0000\ \mu\mathrm{m} & = & 1.3036 \times 10^{23}[\mathrm{atoms/m^2}] \\ 7.6713\ \mathrm{nm} & = & 1.0000 \times 10^{21}[\mathrm{atoms/m^2}] \end{cases} \tag{2.21}$$

2.6 Gamma spectroscopy for AIMS

The analysis of AIMS gamma spectroscopy data is similar to PIGE but with more complicated geometry and without standard targets to normalize out the experimental conditions such as detector efficiency, solid angle, etc. AIMS is essentially an ion beam analysis technique however, it achieves spatially resolved in-situ measurements with the use of magnetic steering field inside of tokamak in very much non-standard IBA conditions. There are a number of complicating factors that make it more challenging than standard PIGE analysis:

1. **High instantaneous current** ($\sim$ 1mA) is a consequence of the accelerator's compact RFQ design. High current leads to count rates of $10^5 - 10^6$ counts/second which exceed the limitations of standard spectroscopy electronics. To accommodate these high count rates and simultaneous gamma and

neutron detection, digitizers were used were used to record the waveforms from the detectors and post processing algorithms were developed for of gamma and neutron analysis [21].

2. **Low beam duty factor** $D < 2\%$ is also result of the RFQ design. It can make detection challenging because even with high instantaneous count rates, the time averaged detection rate can be low. The advantage however is that, by synchronizing and triggering the data acquisition system to acquire only during the beam pulses, the total background counts are reduce by a factor of D. This is beneficial because tokamak components can become activated from runaway electron beams or possibly fusion neutrons in longer pulsed devices. For the AIMS measurements on C-Mod, the background was essentially negligible compared to beam induced reactions because of the low duty factor and high beam current.

3. **In-Situ Beam Steering** is major feature of the AIMS technique. Successful beam steering requires detailed trajectory and dynamics modeling in the tokamak fields to accurately determine the target location and the spatial resolution of the measurement.

4. **In-Situ Spectroscopy** of gammas and neutrons is also a primary feature of AIMS and requires precise modeling to determine the pathlength, scattering properties, and attenuation of beam induced gammas and neutrons. All of these parameter change, often dramatically, with beam steering. The solid angle of the detector and detection angle with respect to the target must also be calculated to properly account for the angularly dependent efficiency of the detector. The nuclear data and kinematics also plays an important role in AIMS measurements. In particular many of the cross sections, particularly for neutron reactions, vary with angle. These cross sections and their angularly dependent properties must be incorporated into the analysis so measurements can be properly compared between target locations.

2.6.1 Deuterium Induced Gamma Emission for AIMS

The RFQ accelerator used for AIMS produces a 900 keV D^+ ion beam. This is lower in energy than most beams used for PIGE analysis and as a result, there are not very many reactions that are accessible. However, boron (gamma emission) and deuterium (fusion) are among the accessible reactions. This limits the isotopes that can be quantified with AIMS, but is also advantageous because there are few known reactions that compete with the reactions used for AIMS.

The primary reaction used for detecting boron is the $^{11}B(d,p\gamma)^{12}B$ reaction shown in figure 2-4 [49]. This reaction has two reaction channels that produce gammas of different energies $E_\gamma = 953$ keV and $E_\gamma = 1674$ keV. These two channels have different cross sections and only the cross section for the 953 keV gamma is large enough at energies below 900 keV to be readily observed.

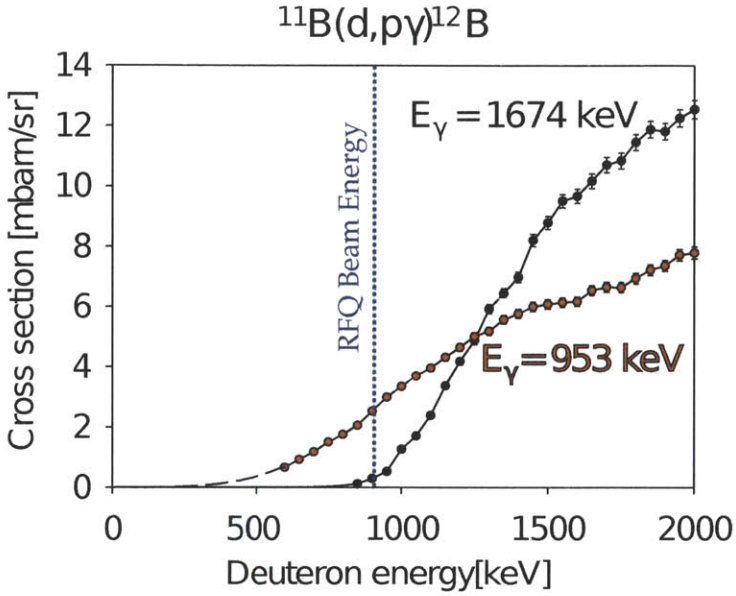

Figure 2-4: Deuteron induced gamma emission cross section for used for AIMS [49]. The 953 keV is the predominant gamma that is observed in AIMS because of its relatively large cross section and the energy range that is accessible with the RFQ.

2.6.2 Gamma Yield Calculation for AIMS

Due to geometric complexity of AIMS, there are a number of quantities that vary with time or position. So, to develop the analysis technique, it is most useful to begin with a general expression for the gamma yield produced by the beam, then apply the proper assumptions based on the experimental conditions. The simplified expression can then be solved numerically to provide a relationship that connects the experimental parameters and gamma yield to the thickness or areal density of an isotope such as boron. The generalized integral equation for the number of gamma photons that reach the detector Y_{exp} are given by equation 2.22.

$$Y_{exp} = \int_0^t \frac{I(t)}{e\, Z_i} dt \int_{\Omega_{det}} \eta(\theta_{inc}) d\Omega \int_0^{x_B} n_B(x)\, \sigma(E(x), \Omega)\, dx \tag{2.22}$$

The first integral of the beam current $I(t)$ gives the total number of incident particles of charge $e\, Z_i$ on the target with total incident charge Q. This is a quantity that is measured in the experiment through current integration so it can be simplified as Q_{exp}. For this analysis, a solid, uniform layer of boron of thickness $x_{B\perp}$ is assumed with a density of n_B. It is also important to note that, due to the off-normal incident angle the beam angle, the beam will travel a distance x_B though the boron layer that is longer than $x_{B\perp}$. This relationship is given by equation 2.23 where $\hat{n}$, $\hat{p}_{beam}$ and θ_{inc} are the unit normal vector to the surface, direction of the beam momentum, and incident angle of the beam.

$$x_{B\perp} = x_B(\hat{n} \cdot \hat{p}_{beam}) = x_B \cos(\theta_{inc}) \tag{2.23}$$

The detection geometry changes as the beam position moves so the solid angle Ω_{det} subtended by the detector must be properly accounted for in the analysis. Since the detector area $\Delta A_{det} \ll r^2$, where r the distance from the target to the detector, the detection efficiency η_{det} and solid angle Ω_{det} are given by equation 2.24.

$$\eta_{det}\,\Omega_{det} = \int \eta(\theta_{det}) \frac{dA_{det}}{r^2} \simeq \eta(\theta_{det})\,\frac{\Delta A_{det}}{r^2} \tag{2.24}$$

Since the detector is not spherical, the detector efficiency is dependent on the incident angle θ_{det} of the incoming gammas. Since the linear dimensions d of the detector are small compared to the distance from the target ($d \ll r$), the angle of the detector is also removed from the integral as shown in equation 2.24 and becomes an angularly dependent quantity that is constant within a measurement. This angular dependence is calculated in detail in section 2.6.8. In addition, the gamma cross sections of interest can vary with polar angle (w.r.t. the beam direction). However, the effect is small enough to ignore in this context and is assumed isotropic.

$$Y_{exp} = \frac{Q_{exp}\,\eta(\theta_{det})\,\Omega_{det}\,n_B}{e\,Z_i\,\cos(\theta_{inc})} \int_0^{x_B} \sigma(E(x))\,dx \tag{2.25}$$

Combining all of these assumptions, equation 2.22 is simplified to become equation 2.25 which provides the relationship between the experimentally measured gamma yield Y_{exp} and the boron layer thickness (areal density) on the surface.

2.6.3 Boron Areal Density Correlation for AIMS

The gamma yield calculation described in the previous section directly relates the the gamma counts to boron content on the PFC as given in equation 2.25. As with external IBA, there is no implicit need for normalization, however since there no calibration standard is used, all of the experimental parameters must be known to quantify boron.

The integral given in 2.25 is not analytically solvable due to the x dependence of the energy E. However, the integral can be calculated numerically for values of x_B with the methods described in earlier in section 2.5.3. Since all of the parameters outside of the integral in equation 2.25 are constant for a given location or are measured during each AIMS measurement, it is advantageous to solve the integral so that it is normalized to the simplest geometric situation relevant to AIMS so that only one correlation is required. The total gamma yield Y_γ for a beam with normal incidence is therefore calculated because it can be related back to the experimental measurements by Q_{exp}, $\eta(\theta_{det})$, Ω_{det}, n_B, $e\,Z_i$, and θ_{inc} as shown in equation 2.26 and 2.27.

$$\bar{Y}(x_B) = \frac{Y_\gamma}{Q_o\,\Omega_o} = \frac{n_B}{4\pi e} \int_0^{x_{B_\perp}} \sigma(E(x))\,dx \tag{2.26}$$

$$\bar{Y}(x_B) = \frac{Z_i\,\cos(\theta_{inc})}{Q_{exp}\,\eta(\theta_{det})\,\Omega_{det}}\,Y_{exp} \tag{2.27}$$

The integral for the gamma yield $\bar{Y}(x_B)$ per unit solid-angle Ω_o per unit integrated beam charge Q_o is given in equation 2.26. $\bar{Y}(x_B)$ is calculated for an array of values of x_B to generate a correlation relating $\bar{Y}$ to x_B, shown in 2-9. Using this correlation $\bar{Y}(x_B)$, the experimentally measured yield can be directly related to the boron thickness x_B with equation 2.27 if all of the geometric and detection parameters are known.

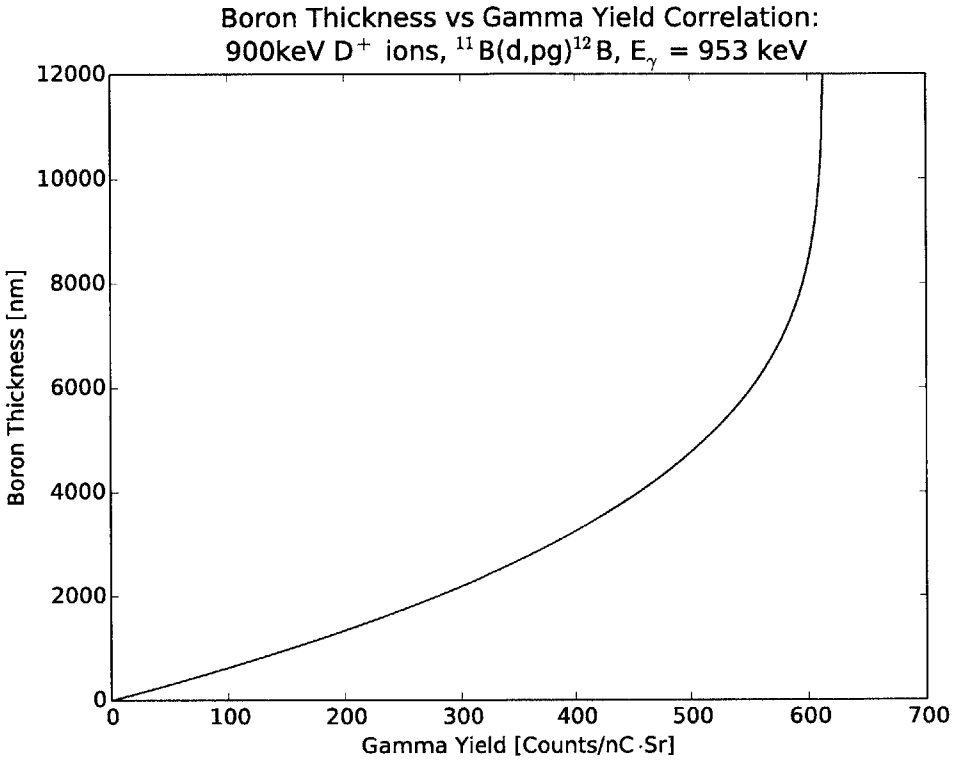

Figure 2-5: Correlation relating 953 keV gamma yield to Boron thickness for AIMS measurements.

As with the external PIGE analysis, for thin films, the yield is nearly linear with boron thickness. As the boron thickness increases, the yield departs from its linearity and becomes increasingly insensitive to boron at larger thicknesses as the beam slows down in the material and the cross section becomes negligible. Another important feature is that because the correlation is monotonic due to the cross section which is also monotonic, the interpretation of boron from these measurements is unambiguous.

2.6.4 AIMS Detection Timescales

The timescales of the AIMS measurements are unconventional for IBA of materials and are largely the result of the accelerator technology that is used. AIMS requires high beam current in order to induce sufficient gammas due to the small solid angle of the detectors. The accelerator is also constrained by the tokamak environment

so it necessarily had to be compact and non-magnetic. Since RFQ accelerators are best suited to satisfy these criteria, and are also inherently short beam pulse devices, AIMS naturally becomes a low duty factor, high count rate technique that spans several timescales from the nanosecond timescale to the 1000s of seconds timescale. An illustration of the timescales of AIMS detection is shown in figure 2-6.

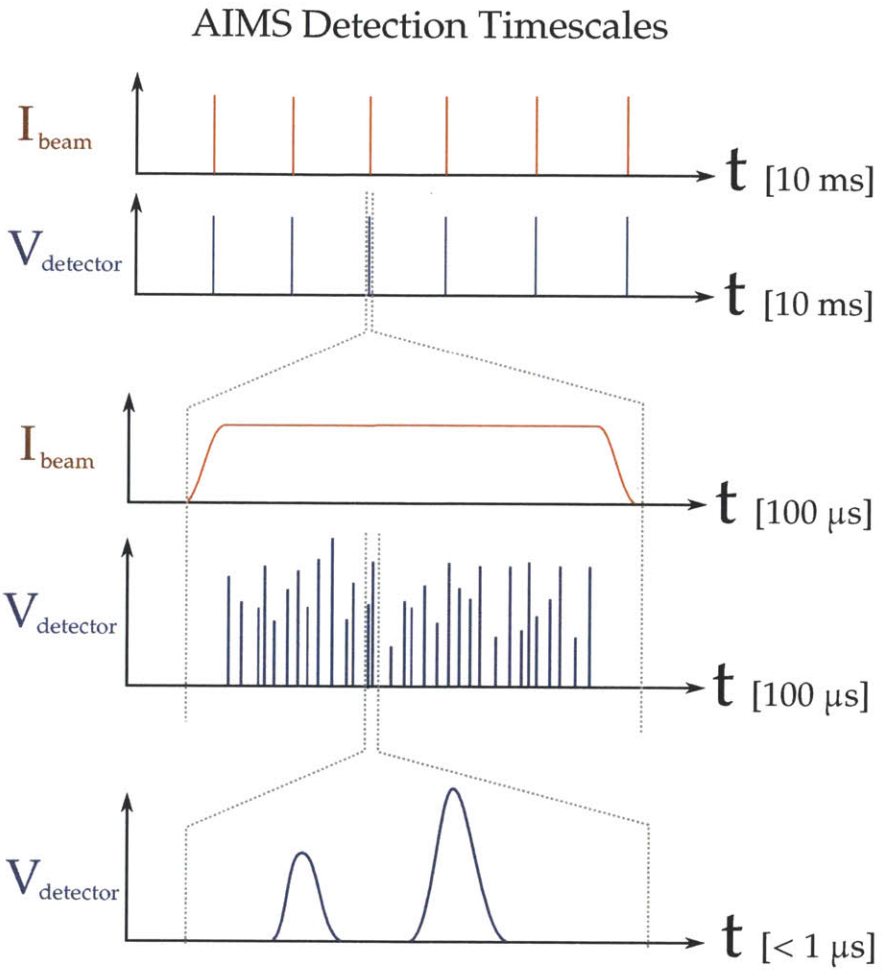

Figure 2-6: Illustration of AIMS detection timescales show the low duty factor, high intensity nature of the AIMS technique. The 900 keV ion beam current I_{beam} induces gamma and neutron reactions while detectors convert the particle detection events into voltages V_{detector}. These beam and detector signals span timescales from the sub-microsecond to timescales of >10 minutes.

2.6.5 Gamma Detection in C-Mod

Gamma spectroscopy in C-Mod presents significant challenges in the tokamak environment. The high gamma and neutron production rates and the small detector solid angle present a challenge because there is a much higher probability that particles will

scatter and produce a large gamma continuum as opposed to being absorbed directly in the detector. This essentially eliminates the possibility of using detectors outside of the tokamak.

Significant efforts were therefore made to mount the detector as close as possible to the PFC target locations inside of the tokamak. To accomplish this, the detectors where housed in a re-entrant tube inserted the horizontal port below the beam injection point. Being inside of the tokamak fields the detectors had to be designed to operate in high magnetic fields. Due to the restrictive size of the re-entrant tube the detector had to be compact so high detection efficiency was required. The need to operate in magnetic fields also prevented the use of a photomultiplier tube (PMT), a standard component in most scintillation detectors. To address these issues a cerium doped lanthanum bromide ($LaBr_3$) scintillator was used because of its high detection efficiency for its compact size. The $LaBr_3$ crystal was coupled to a silicon avalanche photo-diode in place of a PMT. Also, due to the extremely low duty factor of gamma measurement and high gamma count rates the voltage waveforms from the output detector and amplifier had to be directly digitized which is fundamentally different than standard particle detection with analog electronics and was the subject the Ph.D. thesis of Hartwig [21].

The details of hardware are not inherently important to the spectrum analysis methods however, it is important to consider how there experimental condition affect the spectrum. The major issues that result are as follows: The low duty factor and high count rate means that all detection events must be measured over a short period of time. From a typical digitized waveforms such as the waveform shown in figure 2-7 from an AIMS measurements, the count rate cannot be increased by more than a factor of several without detection events beginning to overlap and interfere. While the count rate cannot be substantially increased, the continuum in the spectrum from Compton scattered gammas tends to be much larger than the photopeaks from reactions of interest. Compared to PIGE, more optimization of the beam and detection parameters are necessary to collect enough gamma counts to have statistically significant peaks acceptable levels of uncertainty.

2.6.6 Background Rejection

The low duty factor of the beam and the correspondingly short data acquisition window is advantageous for background radiation rejection. Since background gamma count rates are typically $10^2 - 10^3$ cps while the deuteron induced gamma rates are typically $\sim 10^6$ cps, the measured count rate from the induced gammas are at least 3 orders of magnitude higher than the background. Also, since the typical duty factor for the AIMS measurements was 0.15-0.3%, the probability of even detecting a background gamma <1% within an acquisition window. Because of this, even if the vessel becomes activated from plasma operations, the high instantaneous count rate and low duty factor essentially eliminates the background in the measurement.

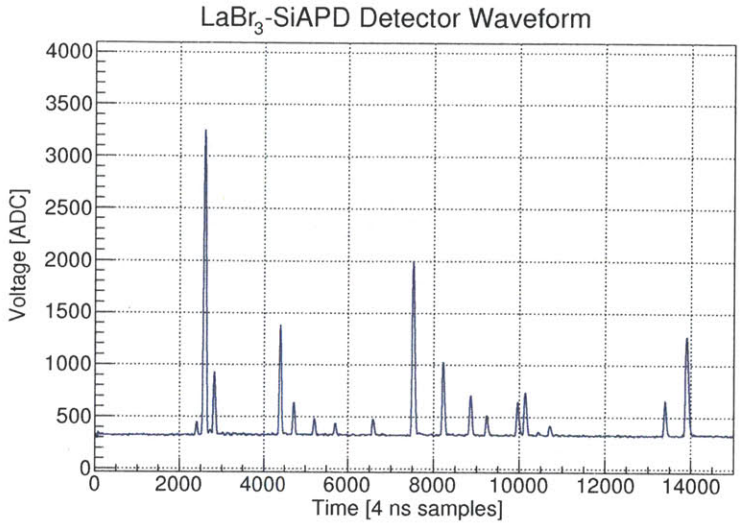

Figure 2-7: Digitized waveform from AIMS gamma detector.

2.6.7 Detection Geometry

The modeling of the AIMS beam trajectory and detection geometry is one of the major developments that enables the AIMS technique. Beam modeling is presented and discussed in detail in chapter 5. A 3-D plot of beam trajectories is shown in figure 2-8 illustrating the complexity of the geometry and the need for modeling.

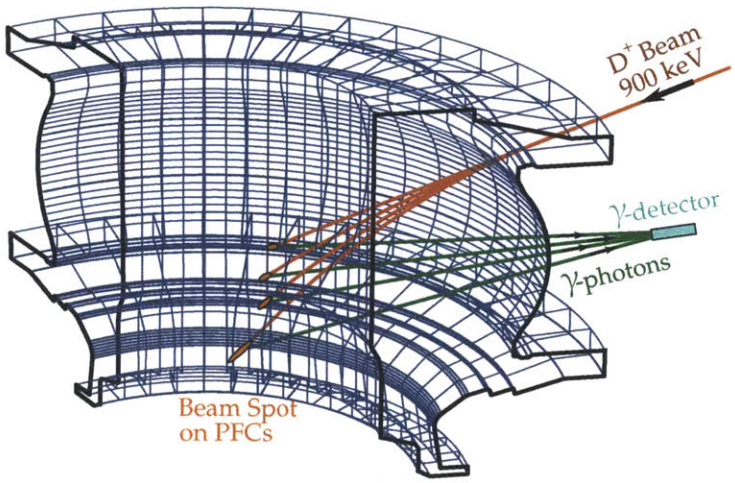

Figure 2-8: Calculated beam trajectories and AIMS gamma detection geometry in Alcator C-Mod.

Using this trajectory and target data produced by the beam simulations, the detection parameters, listed in table 5.3, are calculated and used to fully specify the detection geometry .

Detection Parameter	Symbol	Definition
Radial Unit Vector	$\hat{\mathbf{R}}$	*see figure* 2-9
Vertical Unit Vector	$\hat{\mathbf{Z}}$	*see figure* 2-9
Toroidal Unit Vector	$\hat{\boldsymbol{\phi}}$	$\hat{\boldsymbol{\phi}} = \hat{\mathbf{Z}} \times \hat{\mathbf{R}}$
Beam Unit Vector	$\hat{\mathbf{b}}$	*see figure* 2-9
Target Normal Unit Vector	$\hat{\mathbf{n}}$	*see figure* 2-9
Detector Axis Unit Vector	$\hat{\mathbf{d}}$	*see figure* 2-9
Target Position	$\vec{\mathbf{r}}_{\mathrm{t}}$	$\vec{\mathbf{r}}_{\mathrm{t}} = R_{\mathrm{t}}\,\hat{\mathbf{R}} + Z_{\mathrm{t}}\,\hat{\mathbf{Z}}$
Detector Position	$\vec{\mathbf{r}}_{\mathrm{det}}$	$\vec{\mathbf{r}}_{\mathrm{det}} = R_{\mathrm{det}}\,\hat{\mathbf{R}} + Z_{\mathrm{det}}\,\hat{\mathbf{Z}}$
Gamma Path Length	L_{det}	$L_{\mathrm{det}} = \lvert\vec{\mathbf{r}}_{\mathrm{det}} - \vec{\mathbf{r}}_{\mathrm{t}}\rvert$
Gamma Unit Vector	$\hat{\mathbf{g}}$	$\hat{\mathbf{g}} = (\vec{\mathbf{r}}_{\mathrm{det}} - \vec{\mathbf{r}}_{\mathrm{t}})/L_{\mathrm{det}}$
Target Toroidal Angle	ϕ	*see figure* 2-9
Beam Incident Angle	θ_{bn}	$\cos\theta_{bn} = \hat{\mathbf{b}} \cdot \hat{\mathbf{n}}$
Gamma-Target Angle	$\theta_{\gamma n}$	$\cos\theta_{\gamma n} = \hat{\mathbf{g}} \cdot \hat{\mathbf{n}}$
Gamma-Beam Angle	$\psi_{\gamma b}$	$\cos\psi_{\gamma n} = \hat{\mathbf{g}} \cdot \hat{\mathbf{b}}$
Detector-Gamma Angle	$\chi_{\gamma d}$	$\cos\chi_{\gamma d} = \hat{\mathbf{g}} \cdot \hat{\mathbf{d}}$

Table 2.2: Definitions of AIMS detection parameters.

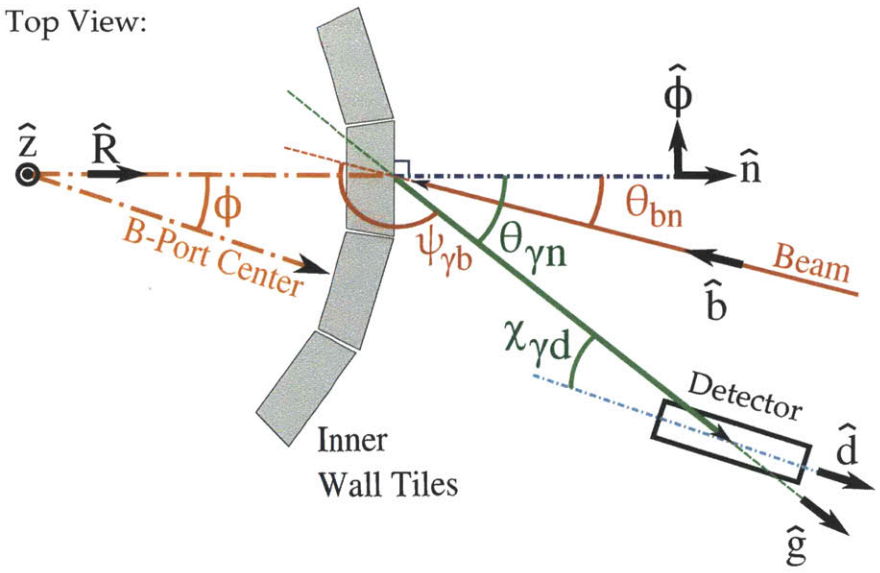

Figure 2-9: Graphical definitions for detector geometry. Refer to table 5.3 for mathematical definitions.

2.6.8 Detection Angle for Gamma Spectroscopy

Since the detector width is considerably shorter than the length ($w/L = 0.36$), the orientation of the detector with respect to the beam target affects the detector solid angle and the path length of the absorbed gamma rays. These effects can have a significant impact on the detection efficiency. To approximate the angular depen-

dence, an analytic expression was derived for the detector efficiency as a function of angle θ, length L, and width w. This derivation assumes that distance between the detector and gamma source d_{source} is large compared to the dimensions of the detector $L_{\text{det}}/d_{\text{source}} \ll 1$ so that the gamma rays are approximately parallel as they pass through the detector. It is also assumed that the detector efficiency is directly proportional to the number of gamma photons absorbed, neglecting other effects within the detector such as Compton scattering and pair production. This is a reasonable assumption because, for 953 keV gammas from boron, photoelectric absorption efficiency is relatively high, pair production is impossible and only a moderate number of gammas are Compton scattering in the detector.

The $LaBr_3$ detector used for AIMS has dimensions $0.9 \times 0.9 \times 3.5$ cm ($w = 0.9$ cm, $L = 3.5$ cm). Since the $w \times w$ end faces the inner wall, the detector area A_0 and absorption probability P_0 are calculated with equations 2.28 and used to normalize the equations for $\theta > 0$.

$$\theta = 0 \begin{cases} P_0 &= 1 - \exp(-\mu L) \\ A_0 &= w^2 \end{cases} \tag{2.28}$$

Where μ is the gamma attenuation coefficient of $LaBr_3$ calculated with mass-attenuation coefficient data provided by NIST [11]. The value for $\mu = \mu_{\text{LaBr}_3}$ is given with relevant data in equation 2.29.

$$\left.\begin{array}{rcll} (\mu/\rho)_{\text{La}} &=& 0.06103 & [\text{cm}^2/\text{g}] \\ (\mu/\rho)_{\text{Br}} &=& 0.05896 & [\text{cm}^2/\text{g}] \\ \rho_{\text{LaBr}_3} &=& 5.06 & [\text{g/cm}^3] \end{array}\right\} \longrightarrow \mu_{\text{LaBr}_3} = 0.30219\ [\text{cm}^{-1}] \tag{2.29}$$

When the incident angle is increased above 0, the path length of the gammas becomes a function the location where gamma intercepts the detector. In addition, the effective area of the detector changes with angle. The rectangular geometry can be broken up into to sections, the bulk: a parallelogram shaped section with uniform path length, and the corners: shown in figure 2-10.

The gamma rays in the bulk section all have the same geometric attenuation length for a given angle whereas the gamma rays that pass through the corners have an attenuation length varies linearly with position. Solving for the gamma absorption probability is solved for in the bulk P_4 and the corners P_3 along with their effective areas A_4, A_3 by applying the geometry shown in figure 2-10 to equation 2.30.

$$\begin{aligned} A_\perp \bar{P}_{\text{abs}} &= \int dy \int dz \int_0^{X(\theta,z)} dx[\exp(-\mu\, x)] \\ &= A_\perp \int dz\ [1 - \exp(-\mu\, X(\theta, z))\ ] \\ &= A_3 P_3 + A_4 P_4 \end{aligned} \tag{2.30}$$

Where $\bar{P}_{\text{abs}}$ is the gamma absorption probability, $X(\theta, z)$ is the maximum gamma path length in the detector and μ is the gamma attenuation coefficient. The normalized detector efficiency η/η_o is then given by equation 2.31.

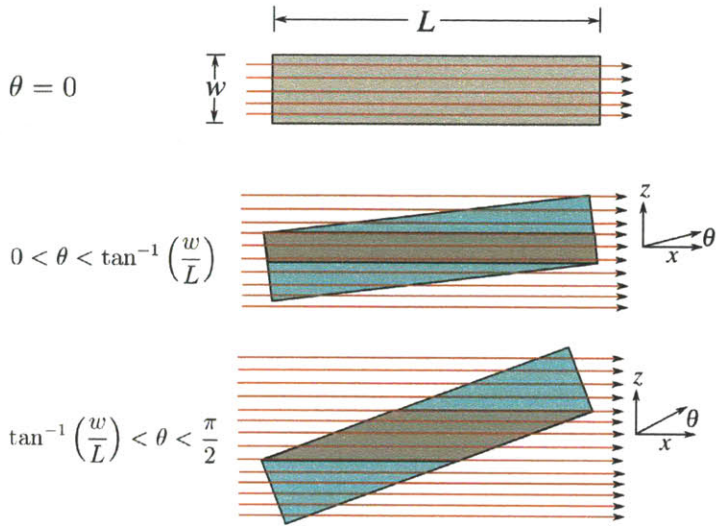

Figure 2-10: Angular dependence of gamma path length(red) passing through the detector and effective detector area change as a function of incident angle θ. The gray shaded regions are the parallelogram or "bulk" portions of the detector while the blue shaded regions are the "corners". Diagrams for three ranges of θ are shown because the ray geometry is different for each of these ranges.

$$\frac{\eta}{\eta_o} = \frac{A_3 P_3 + A_4 P_4}{A_0 P_0} \tag{2.31}$$

The integrated equations for each of these terms and the domains for θ where they are valid are given by equations 2.28, 2.32, and 2.33.

$$0 < \theta < \tan^{-1}(w/L) \begin{cases} P_4 &= 1 - \exp(-\mu \frac{L}{\cos\theta}) \\ A_4 &= w\,(w - L\sin\theta) \\ P_3 &= \frac{1-\exp\left(-\mu\left(\tan\theta+\frac{1}{\tan\theta}\right)L\sin\theta\right)}{\mu\left(\tan\theta+\frac{1}{\tan\theta}\right)} \\ A_3 &= 2\,w\,L\sin\theta \end{cases} \tag{2.32}$$

$$\tan^{-1}(w/L) < \theta < \pi/2] \begin{cases} P_4 &= 1 - \exp(-\mu \frac{w}{\sin\theta}) \\ A_4 &= w\left(L - \frac{w}{tan\theta}\right) \\ P_3 &= \frac{1-\exp\left(-\mu\left(\tan\theta+\frac{1}{\tan\theta}\right)w\cos\theta\right)}{\mu\left(\tan\theta+\frac{1}{\tan\theta}\right)} \\ A_3 &= 2\,w^2\cos\theta \end{cases} \tag{2.33}$$

Using this model, a calibration curve was generated (figure 2-11) to provide the total detector efficiency $\eta \cdot \Omega$ normalized to the detector efficiency $\eta_o \cdot \Omega_o$ when the angle is 0. It is clear that the efficiency is very sensitive to incident angle. The detector normalized efficiency changes by a factor of 2.5 within the first 30 degrees, reaches a peak, then decreases back to nearly the same value as the end-on case at 90 degrees. Since the detection angle tends to vary by 10s of degrees while sweeping

the beam, it is important to factor in this correction into spectroscopic results when comparing absolute boron measurements at different positions.

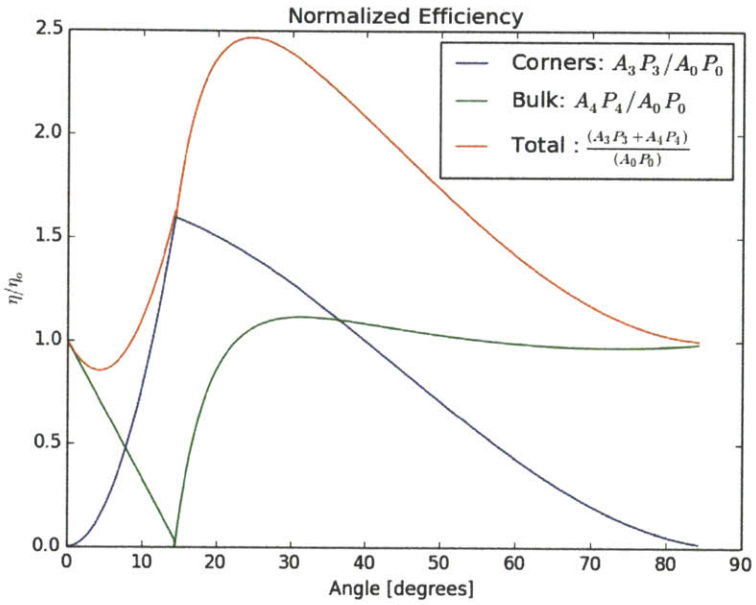

Figure 2-11: Detector efficiency as a function of incident gamma angle, normalized to efficiency at $\theta = 0$.

This modeling suggests that other geometric configurations for the gamma detector should be explored for removing this sensitivity from AIMS.

Chapter 3

Tandem Accelerator and External Beam Apparatus

For this thesis work, the use of external proton beam techniques have been developed and used to perform ion beam analysis on fusion materials. In this study, external particle induced gamma emission (X-PIGE) analysis was used to generate a spatially resolved map of boron deposition on the inner wall of the Alcator C-Mod tokamak. This was done to understand the spatial distribution of boron on PFCs and validate the results from the newly developed AIMS diagnostic. The accelerator technology and hardware development is reviewed in this chapter, followed by the development and applications of the X-PIGE technique.

3.1 Accelerator and Components

The accelerator used in this study is a 1.7 MV Tandetron^{TM} tandem accelerator designed by General Ionex Inc. The accelerator was reconstructed and refurbished for the Cambridge Laboratory for Accelerator Study of Surfaces (CLASS) and is shown in figure 3-1.

Tandem accelerators have a long history of providing measurement capabilities for nuclear physics research and are very useful for studying materials. They produce stable, continuous, well characterized beams which work well for measuring nuclear cross sections and for performing ion beam analysis.

As the term implies, a 'tandem' accelerator consists of two successive linear accelerators that use the same power supply. Negative ions are injected into the first stage and are accelerated toward the positive high voltage (HV) terminal. The ions are then stripped of some of their electrons by nitrogen gas that is injected inside the HV terminal (carbon foils can also be used in other designs). The now positive ions are then accelerated away from the HV terminal through the second stage, then exit the accelerator. Though the terminal is at high potential, ions are injected into the first stage at ground potential, then exit the second stage at high energy, into a beamline that is also at ground potential. The tandem arrangement therefore allows for the entire accelerator structure to reside inside of an electrically insulated structure

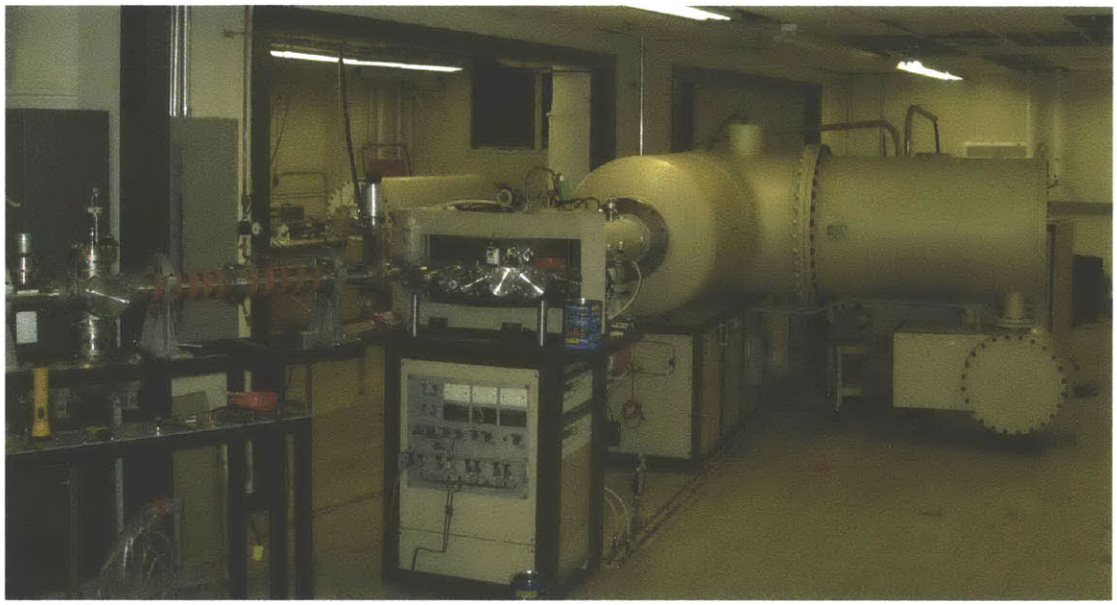

Figure 3-1: Photo of the 1.7 MV tandem accelerator in the CLASS facility

that is at ground potential. This greatly improves laboratory access to the attached beamline and injector components.

Tandetrons are designed to accommodate most low energy ion beam analysis (IBA) techniques that are typically used for studying materials. The accessible energies and beam currents are well suited for Rutherford backscattering spectroscopy (RBS), elastic recoil detection (ERD), particle tnduced x-ray Emission (PIXE) and various types of nuclear reaction analysis (NRA) including particle induced gamma emission (PIGE) [18].

3.1.1 Ion Sources

The injectors for tandem accelerators are designed to produce a variety of ion beam species with negative charge. This can be challenging because many elements and compounds do not readily form negative ions. As a result, many negative ion sources rely on charge exchange processes that involve elements with very low electro negativity (which are typically very reactive and difficult to handle). These ion sources are also electrically isolated with from the injector and biased with the extraction potential (typically 10-20 kV) so that all of the injector beamline components can be at ground potential. The Tandetron has two negative ion sources: a cesium sputtering source and a recently installed RF-charge exchange source for produce He^- ions.

Cesium Ion Sputtering Source

The cesium sputtering source can produce negative ions from most elements that can exist in solid state in vacuum, with low vapor pressure. The negative ions are produced by a several step process involving sputtering and charge-exchange. An

annotated diagram of the sputter source is shown in figure 3-2. The ions are produced

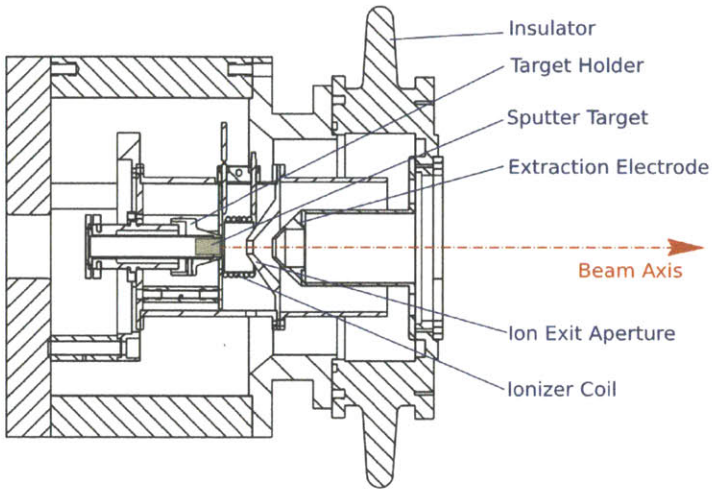

Figure 3-2: An annotated diagram of the cesium sputtering source.

from a cylindrical target made from (or containing) the species of interest. The target is biased with $-3\ kV$, relative to the source potential and is bombarded with Cesium (Cs^{1+} ions). The Cs is first evaporated from liquid Cs in a chamber heated to $\sim 150^{o}$ C. The vapor is then thermally ionized by a resistive heater that is $\sim 700^{o}$ C. The $\sim$3 keV Cs ions sputter particles from the target while Cs vapor accumulates on the surface of the target as a thin layer. The sputtered particles are usually positive ions or neutral atoms and undergo one or more charge-exchange interactions with the solid Cs at the surface to gain an extra electron to become negative ions. These negative ions are then extracted from the source by a -15 kV potential relative to the extraction electrode at ground potential, after which, they leave the source towards the accelerator [19]. The cesium sputtering source was used to produce H^- beams from titanium hydride (TiH_2) targets PIGE analysis. For more details on H^- and other ion beams, a comprehensive guide to making negative ion beams with cesium sputtering sources can be found in reference [40].

RF Charge Exchange Ion Source

The RF charge exchange ion source produces an inductively coupled plasma with helium gas. Positive helium ions are extracted and pass though a heated section of beamline containing rubidium vapor to charge exchange with the He^+ ions to produce He^- ions. This source was not used in this study. For more information on its design and capabilities, see reference [8].

3.1.2 Electrostatic Optics for the Injector

As the beam emerges from the ion source, it is divergent and requires alignment for injection into the accelerator. Due to imperfections in the mechanical alignment of the

source, electrostatic steering is necessary to deflect the beam in the vertical direction, in conjunction with magnetic steering in the horizontal plane (section 3.1.4). This is accomplished straightforwardly with parallel electrostatic deflection plates with opposing potentials that can be adjusted to ±500 V.

The beam also has a divergence angle of $> 1^o$. Since the inner diameter of the acceleration column is < 1 cm and beam path between the source and the accelerator is several meters, focusing is required to prevent substantial beam loss. In the Tandetron, this is accomplished with an electrostatic Einzel lens. To produce the focusing effect, the Einzel lens creates an axisymmetric E-field between a wire mesh grid at a high voltage (3-5 kV) and two co-linear cylinders at ground potential. This design creates an E-field geometry, shown in figure 3-3, that causes no net acceleration but has a radial component that causes the negative ions to be focused.

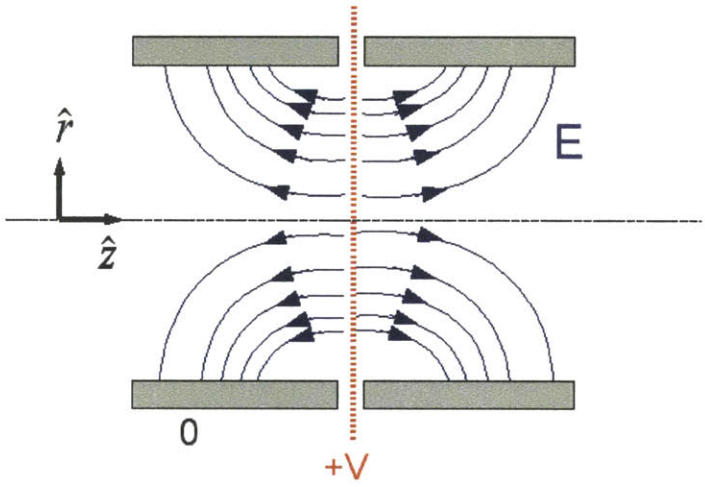

Figure 3-3: Diagram of the E-field geometry in the electrostatic Einzel lens. When positive voltage +V is the applied, an E-field with a radial component is created which has net focusing effect on negative ions.

3.1.3 Acceleration of Ions

The accelerator uses a high DC voltage to accelerate the ions. The high voltage is created by a feedback stabilized 30 kHz oscillating 10 kV supply powering a sulfur-hexafluoride (SF_6) insulated Cockroft-Walton charging network. The power supply is adjustable, and generates a very stable, steady-state terminal voltage of up to 1.7 MV ± 200 V which is connected directly to the acceleration sections of the accelerator (referred to as acceleration columns).

The tandem design uses two acceleration columns joined by an ionization section (or electron stripper) which is connected directly to the high-voltage terminal. The design allows the accelerator to exploit the ionization of accelerated negative ions by an electron stripping medium (nitrogen gas in this case) to convert negative ions, accelerated in the first section, into positive ions which are then accelerated in the

next section. This increases the effective acceleration potential of the power supply by a factor of two for singly charged ion species, or by a factor of $(1 + Z_i)$ for final charge states of Z_i. The tandem accelerator concept is shown schematically in figure 3-4 and described in table 3.1.

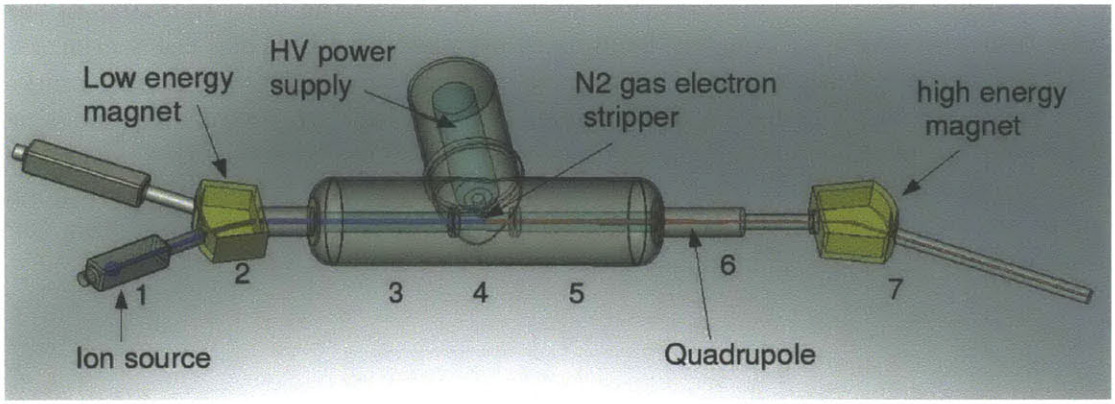

Figure 3-4: Schematic describing the tandem accelerator concept. Annotations 1-7 are described in table 3.1

1	Negative ions are produced by an ion source.
2	The desired ion species are selected and injected toward terminal by low energy magnet.
3	Negative ions are accelerated toward the (positive) high voltage terminal.
4	Electrons are stripped from ions by N_2 gas that is injected at terminal.
5	Ions are now positive and accelerate away from the HV terminal to reach a final energy $E_i = (Z_i + 1) \cdot V_{terminal}$ where Z_i is the final charge state of the ion species.
6	The ion beam is focused by the magnetic quadrupole lens.
7	Desired ion species/charge-state are steered into beam line towards the experiment.

Table 3.1: Basic process of ion acceleration in a tandem accelerator

3.1.4 Magnetic Ion and Energy Selection

A large electromagnet is used to select the desired ion species to be injected into the accelerator. This magnet is referred to as the low energy (LE) magnet. After acceleration, and the quadrupole focusing section, a second magnet called the high energy (HE) magnet, is used to steer the high energy ion beam to select the desired ion beam charge state and direct it into the proper beam-line.

Ion Species Selection

The LE magnet is used much like a mass/charge spectrometer. From the Lorentz force on the charged particle $\mathbf{F} = q\mathbf{v} \times \mathbf{B}$, the bending radius R_B in a uniform magnetic field is given by equation 3.1.

$$R_B = \frac{\sqrt{2mE}}{qB_o} = \frac{10^{-4}}{B_o[\mathrm{T}]}\sqrt{\frac{2\ m[\mathrm{amu}]\ E[\mathrm{eV}]}{Z_{ion}}} \tag{3.1}$$

Where B_o is the magnitude of the magnetic field, and q,m,E are the particle's charge, mass, and kinetic energy, respectively, first in SI units, then in more practical units. For accuracy better than 2%, the numerical constant 10^{-4} should be replaced by the square root of the mass/charge ratio of a proton $1.021747740 \times 10^{-4}$.

The ion source has a constant extraction potential V_{ext} such that each ion has an energy of V_{ext} [eV]. Since the magnet current I_m is proportional to the magnetic field, assuming a fixed V_{ext}, the expression for R_B results in relation 3.2.

$$I_m \propto \sqrt{\frac{m_i}{q_i}} \quad \longrightarrow \quad \frac{I_{mi}}{I_{m0}} = \sqrt{\frac{m}{m_0}} \tag{3.2}$$

Where m_i, q_i are the ions' mass and charge respectively. This relationship is useful because it allows the accelerator operator to identify and select the desired ion species simply by varying the magnet current. Using the second relationship, if one ion species can be identified (such as H^-, the lightest ion usually present), the rest of the ion species from the source can be identified.

Energy Selection

The HE magnet is used for bending the beam of high energy ions so that they are directed into the correct beam line to the desired experiment. This is necessary since ionization in the N_2 stripper creates a spectrum of charge states, leading to populations of ions of different energies. From the geometry of the magnet and the angle of beam deflection θ_B from the axis of the accelerator, is given by equation 3.3.

$$\sin(\theta_B) = \frac{d_o}{R_B} \quad \longrightarrow \quad \sin(\theta_B) = \frac{qB_o d_o}{\sqrt{2m_i E}} \tag{3.3}$$

Where d_o is the length of the magnet in the direction of the incident beam, R_B is the bending radius, B_o is the field q, m_i, E are the ion's charge, mass, and kinetic energy, respectively (SI units). For tandem accelerators the final energy E of the accelerated ion depends on the initial charge state $Z_{(-)}$ (which is essentially always $-1e$), the final charge state $Z_{(+)}$ of the ion, and the high voltage terminal potential V_o. Equation 3.3 can be rewritten for the tandem accelerator account for the charge state dependence of E, shown in equation 3.4. From this equation the convenient scaling rule (3.5) is given to determine the charge state/energy of the ion selected by the HE magnet, assuming the LE magnet selects a single ion species (with Z=-1e) by mass. Ions of a single mass and charge state can therefore be selected after acceleration to

produce the desired mono-energetic beam.

$$\sin(\theta_B) = B_o\, d_o \sqrt{\frac{e}{2m_i V_o}} \left(\frac{Z_{(+)}}{\sqrt{Z_{(+)} + Z_{(-)}}} \right) \tag{3.4}$$

$$I_m \propto \frac{\sqrt{m_i\, V_o\, (Z_{(+)} + 1)}}{Z_{(+)}} \tag{3.5}$$

3.1.5 Magnetic Focusing

A magnetic quadrupole lens is used to focus the beam immediately following the electrostatic acceleration section. Though quadrupoles cause more aberrations than an axisymmetric electrostatic lens, they are necessary because the required voltages would be much too high to electro-statically focus the high energy beam in an axis-symmetric manner. Quadrupole lenses use two focusing sections, each with two magnets with four pole pieces that produce a magnetic quadrupole field, shown in figure 3-5. The second section is the same as the first except rotated by 90^0.

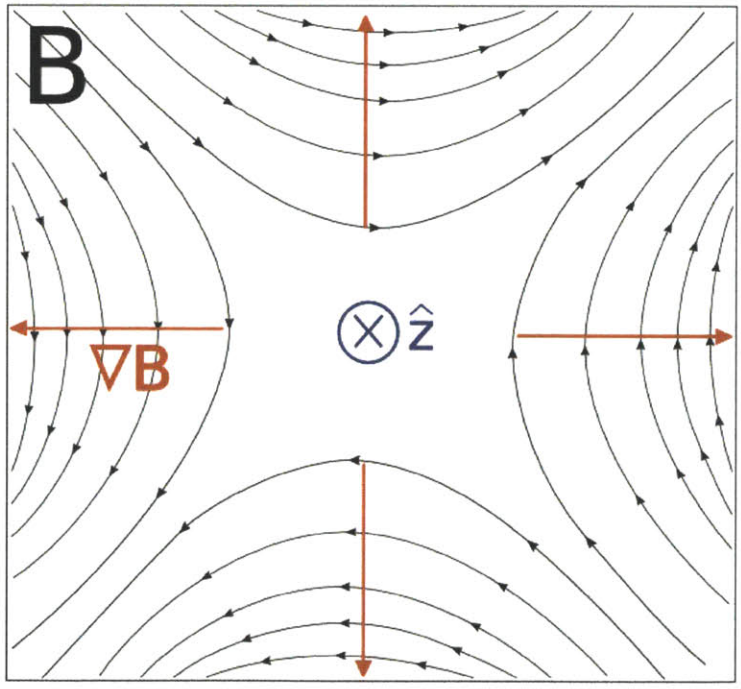

Figure 3-5: Quadrupole field viewed along the beam axis, $\hat{z}$.

In the two side quadrants of the quadrupole lens, the particle trajectories bend radially inward in the first section causing a focusing effect, and then are slightly defocused because of the second section as shown in figure 3-6. The defocusing effect is less pronounced in the second section due to the B-field gradient. The ions are

focused by the beam in a stronger part of the field and travel radially inward where the defocusing field of the next section is weaker.

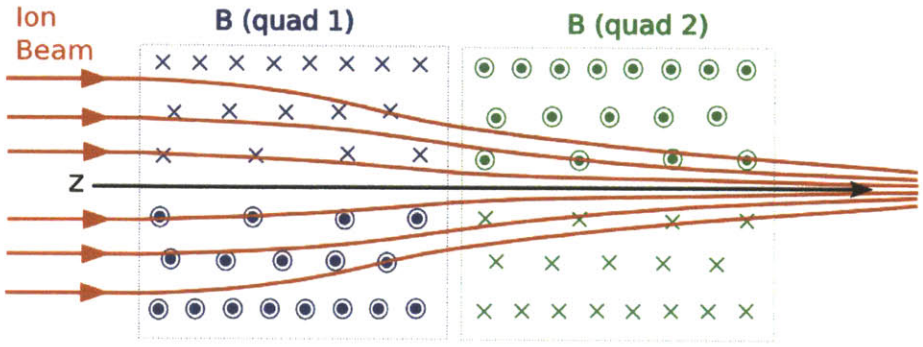

Figure 3-6: Particle Trajectories in the quadrupole lens from the top view

The opposite process occurs in the top and bottom quadrants but still produces the same effect. The particles are defocused by the first section (quad 1) and move radially outward. They then enter the second section (quad 2) in a region of higher field which focuses the beam to a larger extent than quad 1. This process has a net focusing effect as illustrated in figure 3-7. The quadruoples are critical in the beams transverse dimensions and angular profile in order to properly transport the beam through the energy selection magnet and beamline, and focus it on the target or exit-foil for external IBA.

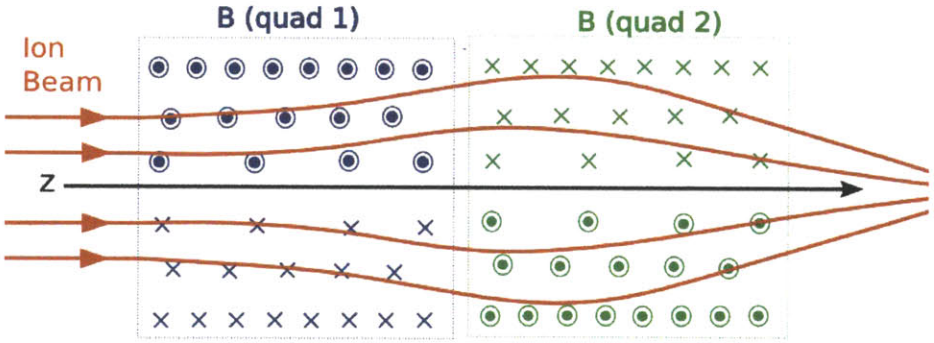

Figure 3-7: Particle Trajectories in the quadrupole lens from the top view.

3.2 Accelerator Upgrades

While refurbishing the accelerator for this thesis work, many of the power supplies and hardware were repaired or replaced. In addition, several systems were upgraded either to improve the accelerators operational capabilites:

3.2.1 Centralized Controls

The accelerators controls have been centralized so that most major accelerator components including the sources, HV supply, steering magnets, and beam lines can be operated from the accelerator control station. The accelerators original design had one control rack for the HV supply and beam alignment, and a two source control racks with power-supplies and controls for each of the ion sources, but did not have the hardware to operate the experiments remotely. To centralize all of the controls the three original racks were set up in the same location and an additional rack was added for controlling the beam line hardware remotely. A list of the list of new hardware added in the beam-line control rack is given by table 3.2.

	Beam-line Control Rack
1	6 channel controller for pneumatic beam-line hardware such as gate valves and Faraday cups
2	$\pm 1000V$ power supplies for x and y electrostatic steerers
3	18 channel BNC patch panel for routing signals from the experiments to the control center
4	Digital data logging oscilloscope for recording data and using beam profile monitor
5	Nuclear instrumentation module (NIM) bin and space for additional equipment

Table 3.2: A list of new hardware for remotely contolling beam-lines and experiments.

All of the hardware in the new rack is routed internally to a patch panel on the HE magnet table. A photo of the control center is shown in figure 3-8.

3.2.2 Sputter Source Alignment

Prior to its repair, the sputter source (figure 3-2) had several severe alignment problems. The misalignments caused the beam trajectory to deviate from the axis of the injector beamline enough that it inhibited proper electrostatic steering focusing, producing beams with negligible currents. The most significant misalignment was between the source and the extraction electrode. This problem arose because the two flanges on either side of the insulator were not concentric; their centers off by 1.8 mm. Since the components in the source require alignment tolerances of ± 25 μm, correcting the misalignment was absolutely necessary.

This was accomplished by redesigning the the extraction electrode such that its position could be adjusted relative to the source. The source was then mounted on a rotary table on a milling machine and was reassembled with each part aligned using a dial indicator to within the required tolerances. The second misalignment was between the source and electrostatic Einzel lens. For the lens to focus properly it is critical that the beam pass through the center. The beam however did not pass through the center and could not be adjusted because source was rigidly mounted to

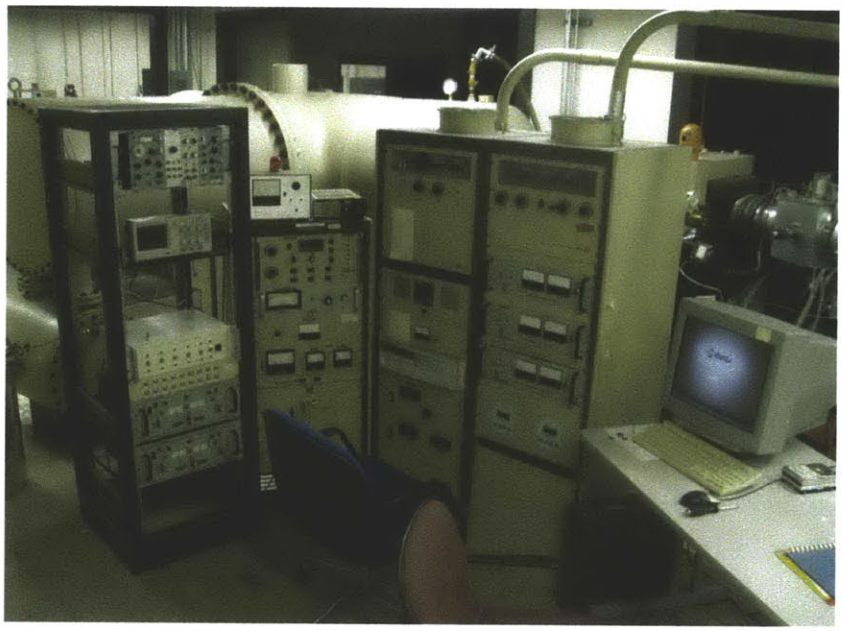

Figure 3-8: Photo of the new arrangement of the tandem accelerator controls

the lens. This problem was solved by replacing a rigid section of beamline between the source and lens with with vacuum bellows with compression bolts to correct the angular misalignment. After the source's alignment was complete, the beam could be focused through the injector aperture ($\sim$ 0.5 cm diameter) with greater than 90% transmission efficiency.

3.2.3 Improved N_2 Gas Stripper control

At the high voltage terminal when the two accelerator tubes join, it is necessary to inject a small amount of gas (dry nitrogen) to strip the electrons from the negative ions to produce positive ions for the second acceleration stage. The stripper gas inflow and outflow due to pumping, will reach an equilibrium with a constant average density. This density is proportional to the probability that an electron will be stripped from the negative ion. Since too much gas leads to vacuum degradation and electric breakdown, and too little causes insufficient stripping, fine control of the stripper gas flow is advantageous for maximizing the stripping efficiency.

The original design used a flow valve mounted on to the stripper section of the accelerator. This valve was controlled by a knob that turned a metal rod which passed through a swagelock fitting, then to a $\sim$ 2 m nylon rod that turned the valve. The swagelock fitting made a very poor feed-through, so it was necessary to replace it with a high pressure feed-through that can be rotated with little friction. Currently, the flow can be adjusted manually by rotating the feed-through, however, in the future, this feed-through can be adapted to a stepper motor and controlled remotely if necessary.

3.2.4 Improved Interlocks

The accelerator was designed with a built-in interlock system that disables the appropriate systems when the necessary conditions for vacuum, cooling, air pressure, arcing, or stripper-gas are not satisfied. This system was expanded to include an interlock system for the beamlines and radiation interlock for machine protection and personnel safety.

Beamline Interlock

The new interlock system connected for the beam-lines allows for six reconfigurable interlock chains to be connected to a relay that closes the first gate-valve at the high energy end of the accelerator. If any of the interlock chains on the beam-lines or experiments are broken, or if the radiation alarm is activated, the gate valve will close preventing any beam from reaching the experiments. Since this interlock allows the ion beam to be contained without shutting down any major components or power supplies, the operator does not need to restart or re-adjust the accelerator.

Radiation Interlocks

Linear accelerators like the Tandetron that operate with a static acceleration potential in the MeV range, can produce ionizing radiation, particularly X-rays. These X-rays can be generated as stray high energy electrons or free electron collision in the gas stripper region. In the Tandetron, these sources of radiation are mitigated with lead shielding and by electron suppression using permanent magnets in the ion sources and a slightly helical E-field in the acceleration columns. Radiation can also be produced within the experimental setups at the end of the beamlines either intentionally for IBA measurements or unintentionally, so there are three permanently installed radiation alarms

Two alarmed radiation monitors with Geiger-Mueller detectors were installed; one at the high energy end of the accelerator, and the other behind the control racks at the low energy end. In addition a neutron detector was installed near the experiment section. These radiation monitors were set up to interface with the accelerators interlock system to shuts down the high voltage supply and close the gate-valves between the accelerator and the beam lines. Because of this modification, if a radiation hazard arises, the lights and alarms will warn the operator, and the high voltage supply will shut down, preventing further radiation exposure and potential damage to accelerator components.

Due to the wide range of beam energies, ion species, and targets that can be used for IBA, proper calculations must be made to determine which precautions should be taken for each experiment, however, in the event of unexpected radiation producing reactions or accelerator failure modes, the operator is now protected from unforeseen radiation hazards.

3.2.5 Recirculating Cooling System

Many of the accelerators components require water cooling including the turbo pumps, steering magnets, and beam-line components. Refrigerated water is piped into the lab from the building's recirculating chilled water system. The system however, is very old and the water is often discolored and filled with particulate matter (such as flakes of rust). The debris could potentially cause clogs to form if it were piped directly into the accelerators hardware. To avoid this problem, a new cooling system was built which has a self contained recirculating cooling loop for the accelerator which transfers its heat to the chilled water system through a heat exchanger. Though cooling systems are relatively is a straightforward, this system was a significant improvement because it was connected to series of manifolds that are reconfigurable and available to experiments on the beam lines as necessary.

3.3 External Beam

The optimized design and implementation of an external beam for PFC analysis was a significant contribution from this thesis work. IBA is typically conducted in an evacuated chamber. However it is possible to configure a beamline such that the beam passes through a thin vacuum tight exit foil (or window) so it can be used for IBA of samples that are in air, at atmospheric pressure. This is referred to as an external beam. The external beam set up was implemented in 2008 and has since been used for this thesis as well as notable PMI studies described in section 3.5.2 and 3.5.3.

External IBA is advantageous for the study of PFCs because samples can be arbitrarily large and can be positioned with relative ease to achieve high spatial resolution. The most notable disadvantages however, are the increased uncertainty in the incident energy due to straggling from the window and the air and inaccuracies in the sample position. In addition there can be increased background radiation causing a decrease in signal to noise ratio [5].

The capability for handling large samples is particularly useful for studying PFCs such as divertor tiles from C-Mod because each section is large in size and contains tens or hundreds of $\sim$ 2cm $\times$ 2cm tiles. Since no vacuum chamber or pump-down time is required, many individual tiles or even sections of the divertor or limiters can be repeatedly repositioned and analyzed quickly. This allows hundreds of measurements to be made in a matter of hours. Such fast throughput makes analysis with high spacial resolution possible as well as analysis aimed at measuring macroscopic trends from tile to tile. A CAD model of the beam line for external IBA is shown in figure 3-9.

3.3.1 Beamline instrumentation

Many applications including the external beam require the beam to be focused or aimed properly at a sample target (in this case an exit foil/aperture). This requires several instruments; an X-Y steerer, a Faraday cup, located in the beam line for rough

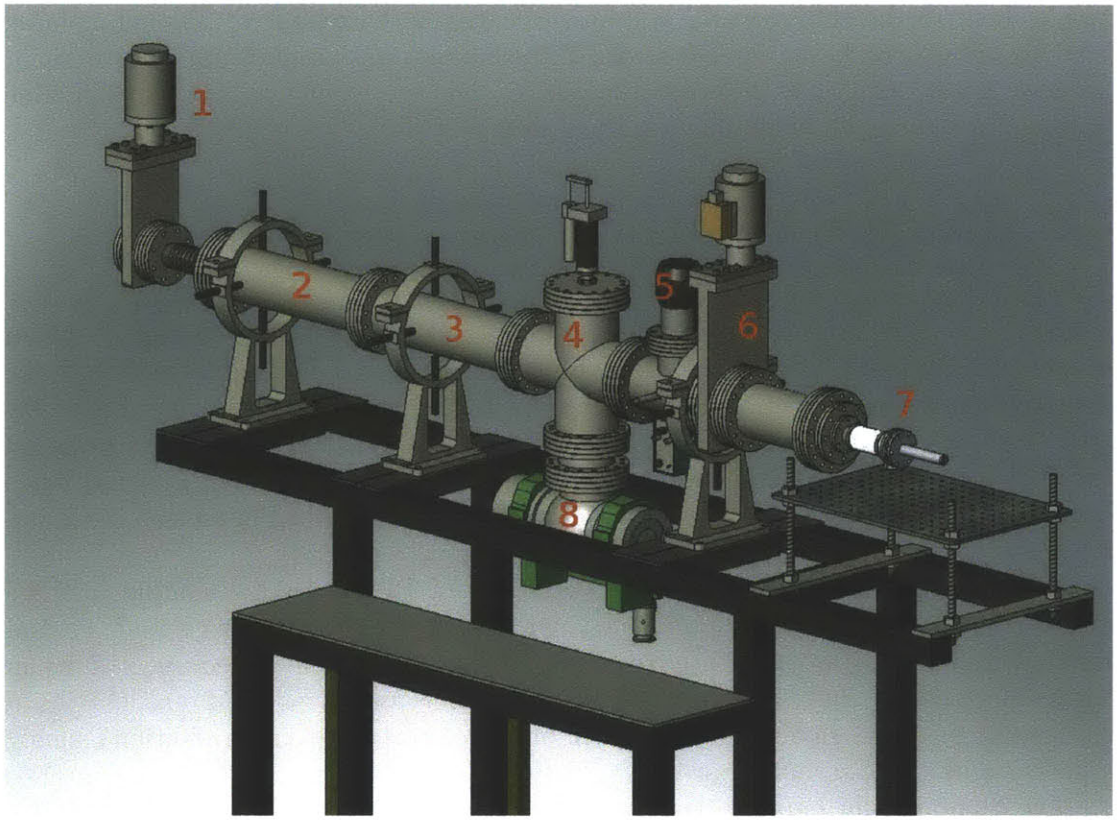

Figure 3-9: A CAD model of the beam line used for external ion beam analysis. The numbers correspond to the following components: (1,6) vacuum gate valves, (2,3) y and x electrostatic steerers, (4) insertable Faraday cup, (5) beam profile monitor, (7) beam aperture/window assembly. (8) turbo pump.

beam alignment, and a quadrupole lens and, possibly, a beam profile monitor for focusing and the final alignment. Instruments for precisely measuring beam current are also necessary for proper normalization of measurements.

Faraday Cup

A Faraday cup is a fairly simple device that is used for directly measuring beam current. It is essentially a micro-ammeter that is connected to a metal cup, that can be inserted into the path of the ion beam. The cup is positively biased (or surrounded by a negatively biased enclosure) to capture the secondary electrons that are emitted as the cup absorbs the ions from the beam. There is one Faraday cup built into the beam line that can inserted with a pneumatic actuator. It is used for rough alignment of the beam and can be used to measure the beam current incident on the window.

3.3.2 External Beam Current Measurement

With external analysis, the beam's transit through air leaves a trail of ionized gas creating current pathways to beamline and ground. If current is measured directly from the sample in air, this makes secondary electron suppression less reliable, often leading to leakage currents from the e^- suppression supply to be larger than the beam current. Instead, for external PIGE measurements, the samples are electrically isolated from their support structure and beam current is measured with a charge digitizer connected to the aperture supporting the beam exit-foil. Since some of the beam is clipped by the outer edge of the aperture before passing through the window, this current is be used for making a relative measurement of the beam current that passes through the window so the reaction yield measurements can be normalized to beam current. This provides adequate, repeatable current measurements provided that that beamspot stays constant in shape and position. Since this is only a relative measurement, the relationship between beam current measured and beam current on target must be measured with a know target with known cross section.

Beam Profile Monitor

The beam profile monitor (BPM) that was installed in the beamline is an instrument made by National Electrostatics Corporation. It consists of a helical wire mounted on a $\sim$ 20 Hz rotary drive (such that the axis of rotation is perpendicular to the beam). As the wire rotates, it passes through the beam. Since the wire is helical, part of each cycle provides a horizontal sweep and part produces a vertical sweep. When energetic particles in the beam collide with the surface of the wire, secondary electrons are emitted and absorbed by a cylindrical collector. Since the secondary electron emission measured by the collector is proportional to the local beam current, as the wire sweeps through the beam in both directions due to its helical shape, the collector signal can be used to measure X and Y profiles in real time [9]. The beam profile monitor can thus be used to determine the local shape of the beam and to optimize focusing with the quadrupoles. This instrument is useful to have on the

beamline, however it was not necessary for the external beam measurements because the beam alignment could be determined and maximized by directly measuring of beam current with an external Faraday cup.

3.3.3 Window Design

When designing a beam window there are several issues that must be considered:

1. The window must be thick enough and mechanically strong enough to maintain vacuum on one side with atmospheric pressure on the other.

2. The window must be thin enough that ion beam loses as little energy as possible as it passes through.

3. The energy lost by the beam must also be dissipated by the window to prevent it from melting. All of these conditions must be simultaneously satisfied by choosing a suitable window material and properly choosing maximum beam current and window dimensions.

There are a variety of materials that can be used to make windows that are typically less than 10μm thick and several millimeters in diameter [5]. It also possible make larger diameter windows by supporting the foil with a solid metal or carbon mesh with a high transparency fraction.

Metallic foils are often ductile and can be made very thin and typically have high thermal conductivities for good heat dissipation. However, energy loss approximately increases with thickness and Z^2, so only low-Z metals or extremely thin metallic windows are suitable. Some polymer foils, particularly Kapton, are also suitable for beam windows.

Kapton® is a polymer made by DuPont. It is designed for many applications and is commonly used in electronics. It is particularly useful because of its ability to maintain its mechanical and electrical properties over a wide range of temperatures (-269°C to 400°C). It can also can also withstand higher radiation doses than most other polymers [13]. Due to its availability and favorable properties, Kapton was chosen as the preferred exit-foil beam window material.

3.3.4 Mechanical Properties

In order to make a vacuum tight window of minimal thickness, it is often necessary to choose a film that is thin enough that atmospheric pressure causes it to exceed its yield strength and plastically deform. It is difficult to accurately model thin films that are plastically deformed so it would require considerable effort to optimize the window geometry from first principles. It is not necessarily advantageous to push mechanical limits of the window, because beam heating will undoubtedly change the properties of the exit foil and radiation damage will eventually degrade its strength.

For this study a $1/8^{\text{th}}$ inch (3 mm) diameter aperture was used with an unsupported, 7.5μm Kapton exit foil. This geometry was chosen based on the minimum

available Kapton thickness and conservative, estimates of the maximum window diameter. The foil supporting aperture was made with a rounded edge to minimize the curvature of the foil to reduce the shear stress at the edges. The structural integrity of this window was then verified experimentally with a vacuum pump.

3.3.5 Beam Energy Loss in Window

It is important to minimize the amount of ion energy that is lost in the window to ensure that ions are able to exit the window with sufficient energy to be useful for IBA. The rate that the ions lose energy as they pass through a material depends on the material's stopping power $S = -dE/dx$. S is dependent on many factors, most importantly: the energy of the ions, the ion species, and the composition of the target material. To determine loss of ion energy, the stopping power vs. energy data $S(E)$ was generated with the 'Stopping and Range of Ions in Matter' code (SRIM2008) [68].

The energy loss of the beam was calculated numerically using theoretical and experimental proton stopping data using the method described in section 2.4.1. The stopping data for Kapton ($H_{25.64}\ C_{56.41}\ N_{5.13}\ O_{12.8}$) is given in figure 3-10 and the stopping data for dry air ($C_{0.02}\ O_{21.08}\ N_{78.43}\ Ar_{0.47}$) is given by figure 3-11. Using

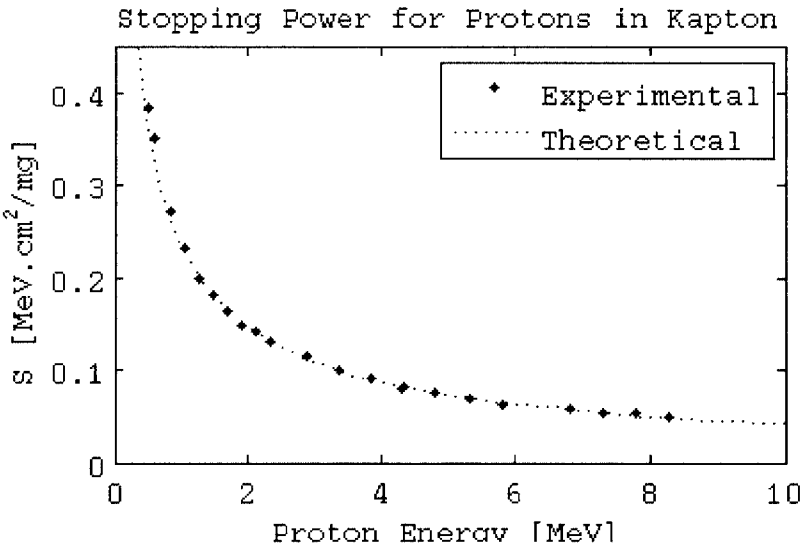

Figure 3-10: A plot of stopping data for protons in Kapton. The theoretical data was calculated using SRIM2008 [68], and the experimental data was provided by E. Rauhala, et al [43].

the stopping data for Kapton and dry air, the energy of a proton as a function of its distance traveled can be calculated numerically. The proton energy-trajectories were calculated for several different initial energies for the thinnest available Kapton film. These calculations are shown in figure 3-12 for 7.5μm (0.3 mil) Kapton.

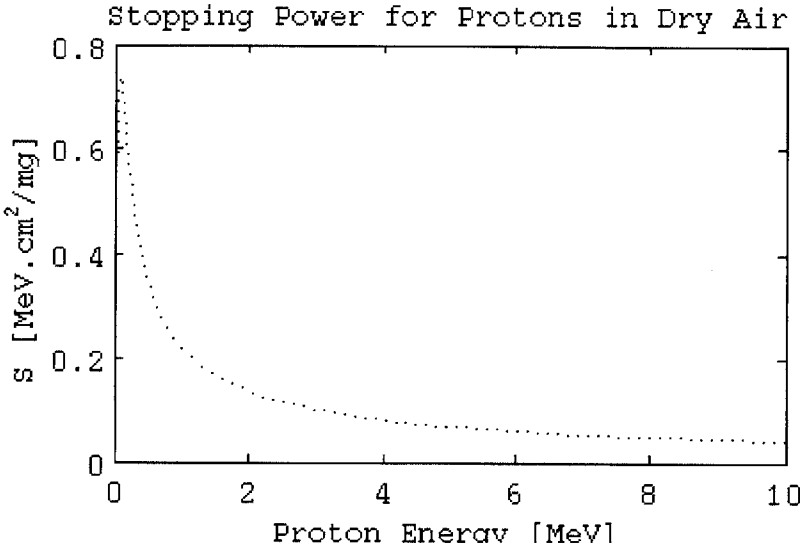

Figure 3-11: A plot of stopping data for protons in dry air. The data were generated using SRIM2008 [68]

3.3.6 Thermal Model for Kapton

Energy loss of the beam also has practical implications for the window because it directly leads to volumetric heating of the window. Kapton has a relatively low thermal conductivity (0.37 $Wm^{-1}K^{-1}$) [13] so it is likely to reach equilibrium over its 7.5 μm thickness, but is not likely to conductively dissipate much of its heat to the edges. The dissipation of the heat deposited by the beam is, therefore, dominated by convection by the air on the surface of the window.

To model the thermal properties of the Kapton window, a 1-D (cylindrical) thermal relaxation code was written to calculate the radial temperature profile of the window for a given beam energy and current. The code first calculates the beam power absorbed by the window. Then, from an initial temperature profile, it iteratively redistributes and dissipates the heat among the radial locations r_i by conduction, radiation, and convection. As the system approaches equilibrium, the time steps increase so that the simulation converges to steady state. The code essentially iterates equation 3.6 in time until it relaxes an equilibrium solution. Where A is area of each concentric volume element with radius r, density ρ, thermal conductivity κ, and heat capacity c_p.

$$q_{beam} \pm q_{conduction} - q_{convection} = \frac{\partial}{\partial t} U_{internal}$$

$$\dot{q}_i V_i + k\left(A_{i(-\hat{r})}\frac{T_i - T_{i-1}}{r_i - r_{i-1}} + A_{i(+\hat{r})}\frac{T_i - T_{i+1}}{r_i - r_{i+1}}\right) - hA_{i\hat{z}}(T_i - T_\infty) = \rho c_p V_i \frac{\partial T}{\partial t} \quad (3.6)$$

Like many thermal modeling problems, however, it is difficult to accurately determine the heat transfer coefficient h. These h coefficients are usually determined from

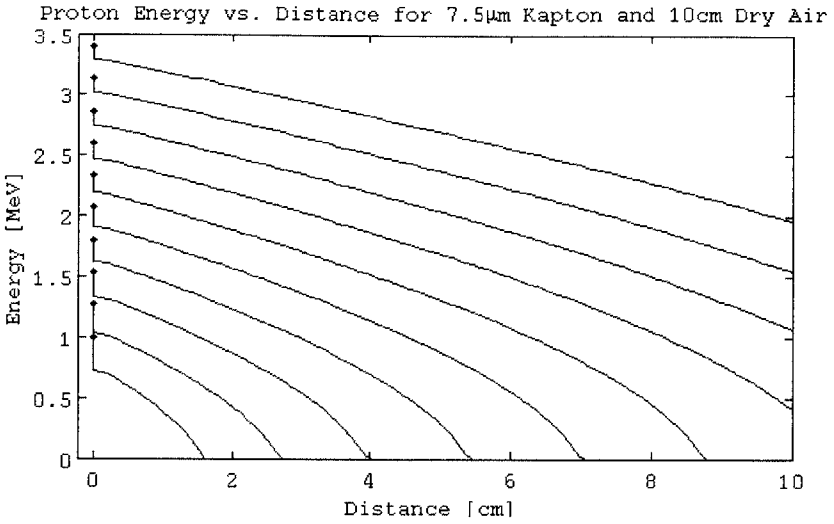

Figure 3-12: A plot of the calculated energy-trajectories of protons as they pass through 7.5μm (0.3 mil) of Kapton (at 0 cm) followed by 10 cm of Air for 10 different initial beam energies. The vertical section of the curves at position 0 represents the energy loss of the beam in the exit foil and the sloped section represents the energy loss in air.

experimentally derived correlations because they can vary over a wide range based flow conditions and geometry. Depending on the conditions, h for air can vary as much as an order of magnitude within the range $10 - 100$ W/(m^{2}K). To accommodate this large range, 10 W/(m^{2}K) was used in the calculations to make a conservative estimate. The results of this calculation are shown in figure 3-13. These results suggest that a Kapton window can survive steady state exposure to 100 nA of beam current at 2 MeV if the beam is not highly focused. A 7.5μm Kapton exit foil was implemented and used with $1-2$ MeV beams up to >100nA for >50 hours without thermal failure. This experimental result validated predictions from the model and the window design. In addition, to accommodate higher currents, a 1/8 inch compressed-air line was added to actively cool the exit foil.

3.3.7 Nuclear Properties of Kapton

Kapton is a polymer with a the chemical formula $C_{22}H_{10}N_2O_5$. Therefore Kapton can produce background radiation from particle induced reactions of carbon, hydrogen, nitrogen and oxygen. Some possible interfering reactions are shown in table 3.3. None of these elements however, produce neutrons at energies below the maximum energy for protons in the Tandetron, 3.4 MeV [34]. Fortunately these background reactions tend to be negligible compared to the boron reaction used in this study because of their low cross section.

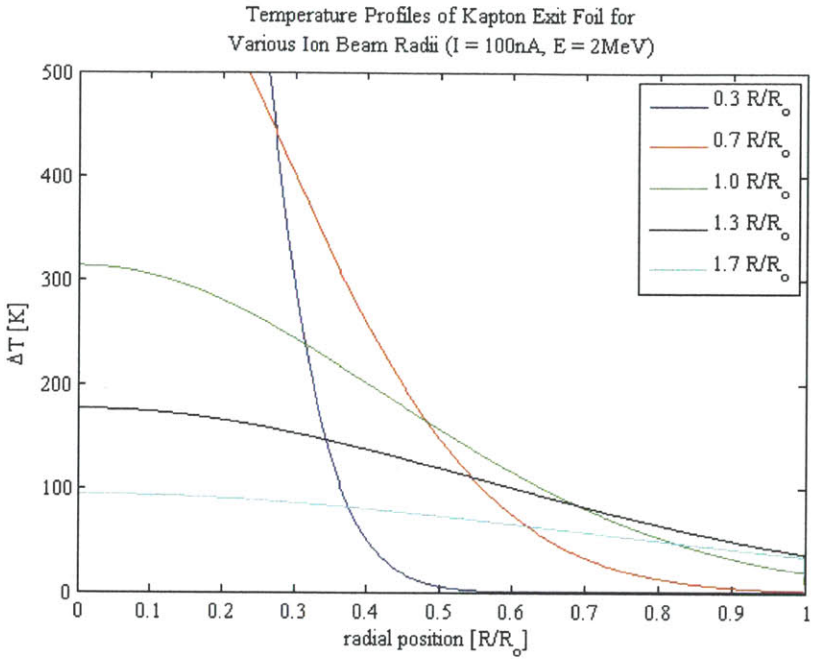

Figure 3-13: Plot of the calculated temperature profiles $(T - T_\infty)$in a Kapton exit foil from a 100 nA, 2 MeV ion beam. This calculation uses a conservative heat transfer coefficient $h = 10$ W/(m^{2}K) and assumes gaussian beam profiles with full width half maxima of $0.3, 0.7, 1.0, 1.3, 1.7[R/R_o]$ where all R_o is the exit foil radius. The beam currents were normalized such that 100 nA was incident on the window.

3.3.8 Radiation and Radionuclide Production in Air

A potential issue for external beam is the radiation produced by reactions in the air. To make an estimate for the radiation production or activity α [Bq], all of the the relevant cross sections σ_t are averaged over the beam's energy range then multiplied by the maximum beam ion current $I_{max}/Z_i e$ $[s^{-1}]$, the range R_{max} $[m]$ at the maximum energy, and the target particle densities n_t $[m^{-3}]$, as shown in equation 3.7.

$$\alpha = n_t \cdot \left(\frac{I_{max}}{Z_i e} \right) \cdot \bar{\sigma}_t \cdot R_{max} \tag{3.7}$$

Using this method, the radionuclide production rates were calculated for the most significant nuclear reactions induced by a proton beam in air. The results are shown in table 3.4. For a typical external proton beam used in PIGE boron measurements, these reactions produce an activity of $\alpha = 1.43 \cdot 10^5$ Bq from prompt gamma emission and an activity of $\alpha \sim 1.5 \cdot 10^5 Bq$ from accumulated radioactive nuclides (from 1 hour of operation). This activity is small and is well below acceptable limits.

Proton-Gamma Reactions	Q [MeV]
C_6^{12} (p,g) N_7^{13}	1.943
C_7^{13} (p,g) N_7^{14}	7.551
N_7^{14} (p,g) O_8^{15}	7.297
N_7^{15} (p,g) O_8^{16}	12.127
O_8^{16} (p,g) F_9^{17}	0.600

Table 3.3: These reactions can occur in Kapton and potentially interfere with external proton beam IBA measurements [34]. The emitted gammas overlap in energy with the reaction of interest.

Reaction	Rate [nuclides/s]	$Q_{reaction}[MeV]$	$\tau_{1/2}$	$Q_{decay}[MeV]$
$^{16}_{8}$O (p,γ) $^{17}_{9}$F	$1.43{\cdot}10^5$	0.600	64.49 sec	2.761
$^{14}_{7}$N (p,γ) $^{15}_{8}$O	$1.51{\cdot}10^3$	7.297	122.24 sec	2.754
$^{12}_{6}$C (p,γ) $^{13}_{7}$N	$8.47{\cdot}10^2$	1.943	9.965 min	2.220

Table 3.4: Nuclide production rates for a 2 MeV, $100nA$ proton beam passing through Kapton then stopping in air. This represents an activity of $\alpha = 1.43 \times 10^5$ Bq from prompt gamma emission and an activity of $\alpha < 1.5 \times 10^5$ Bq from accumulated radioactive nuclides for a typical external proton beam used in PIGE boron measurements (from 8 hours of operation).

3.4 Photon Detection and Spectroscopy

IBA measurements are generally made by exposing a sample to an ion beam then counting the scattered or emitted particles with an energy analyzing detector. The features in the energy spectrum can then be correlated to specific properties of the sample. Photon counting measurements are made with a detector that "absorbs" the photon energy and converts it into an electronic signal (usually a current pulse). The signal is typically amplified then converted to voltage pulses that are counted by a multi-channel analyzer (MCA) [32]. Different detectors must be used depending on the energy range of the photons. Detectors that are relevant to this study are described in the following sections.

3.4.1 Gamma Detectors

For PIGE analysis, using (p,γ) reactions, it is necessary to detect the gamma-ray photons that are produced within the irradiated samples. Since each (p,γ) reaction produces photons with an energy that is characteristic of the reacting isotope, it is also necessary to discriminate between photon energies. This is done by converting the energy from the gamma photon into a form that can be measured electronically.

3.4.2 High-Energy Photon Conversion

All gamma detectors stop photons by the same basic processes. At low energies below several MeV photoelectric absorption dominates whereby each absorbed photon is absorbed by single electron, creating a high energy (or fast) electron; this is the preferred interaction for photon detection because it produces a distinct peak in the energy spectrum. For medium energy photons $\sim 3 - 7MeV$, Compton scattering dominates whereby photons elastically scatter off of electrons, producing background continuum in the spectrum. And with high energy photons the dominant process is pair-production, the spontaneous creation of an electron-positron pair. In addition to the full absorption photo peak, pair-production also produces two peaks with energies that are 0.511 MeV and 1.022 MeV lower in energy than the photopeak due to the escape of positron-electron annihilation photons. As the energy of the gammas increases they are less likely to be absorbed. This means that the efficiency of the detector usually decreases as the gamma energy increases [32].

After a photon is absorbed by a photo-electron, the energy must be converted to a measurable signal. For scintillation detectors, this is done through the 'scintillation process' where the fast photo-electron deposits its energy by in a medium that converts the energy loss of the election into low energy photons which are subsequently measured. In inorganic scintillators, this occurs because the fast particle causes a number of bound electrons in the valence band of the scintillation crystal to be excited to the conduction band. Each electron-hole pair then migrates until it de-excites and emits a low energy photon that is detected by a photomultiplier tube, resulting in a current pulse that contains an amount of charge Q that proportional to the energy of the photon.

Semiconductor detectors operate somewhat differently. They are essentially large volume diodes made from ultra-pure semiconducting materials such as germanium. The detector is cooled, typically to liquid nitrogen temperatures, to avoid thermal noise and prevent thermally induced breakdown before since it is reverse biased with >100 V to create a large depletion region. When a high energy photon is absorbed to create a photo-electron, charge carriers are liberated as the electron deposits its energy in the bulk of the detector. The migration of those charge carriers can then be measured directly as a current pulse. There the total charge measured is again proportional to the energy of the photon.

3.4.3 Analog Pulse Processing

Each gamma that is detected produces a very short current pulse, often 10s of nanoseconds in length. With modern digital electronics, it is possible to digitize these pulses, however, for most standard photon counting experiments, only the charge Q contained in each pulse is important because Q is proportional to the gamma energy. Since Q is the relevant quantity the shape of the pulse is not important in this case, the gammas can be detected with analog electronics through a several step process, shown in figure 3-14.

This process essentially takes a very short current pulse, amplifies it, and converts

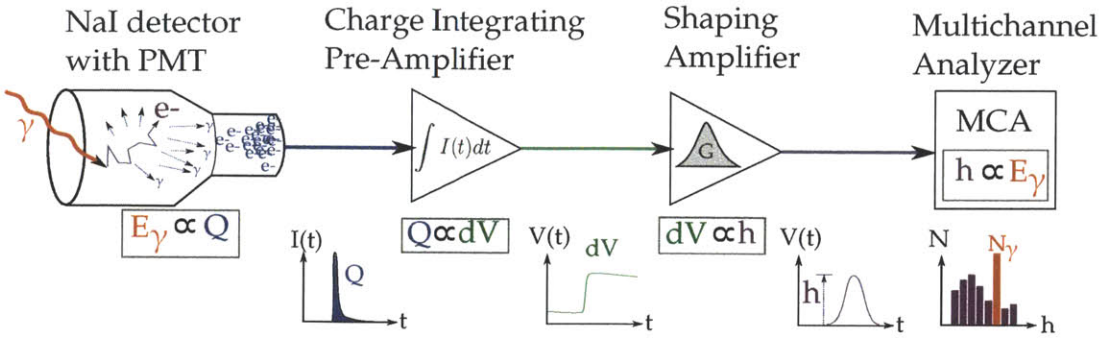

Figure 3-14: Illustration of the process by which high energy gamma photons are absorbed and converted with a scintillation detector and photo multiplier tube (PMT), then converted to a pulse height spectrum using a charge integrating pre-amplifier, a shaping amplifier, and a multi channel analyzer (MCA).

it into a longer, smoother, easily measurable voltage pulse. First the gamma is absorbed in the detector producing the current pulse Q. The ~ns pulse is then integrated with an analog current integrating amplifier with an RC timeconstant that is much longer than the pulse. Then on the μs timescale, the output voltage that is produced is essentially a voltage step dV that is proportional to Q. This signal is then processed with a 'shaping amplifier' which outputs an approximately Gaussian voltage pulse with a long risetime and fall time with a height h that is proportional to dV. Now that the pulses are smoothed and lengthened and have a height (voltage) that is proportional to the photon energy, the final step is count the pulses and histogram them based on height. This is done with a multi channel analyzer (MCA) which is essentially a digital counter with many channels, each of which can only count pulses between voltage V and $V + \Delta V$. This creates histogram that is binned in terms of pulse height h. Since $h \propto dV \propto Q \propto E_\gamma$, this histogram gives gamma energy spectrum when calibrated to gammas from known radioactive sources.

3.4.4 Common Gamma Detectors

There are many types of gamma detectors available. Common scintillation crystals for gamma spectroscopy include sodium iodide (NaI) and bismuth germanate (BGO) crystals [32]. The most common semiconductor detectors are high purity germanium detectors which are large, semiconductor devices that convert the absorbed photon energy directly into a current pulse.

Sodium Iodide NaI(Tl)

Sodium iodide (NaI) detectors are the most common scintillation detectors available. NaI detectors use a NaI crystal doped with Thallium which is optically coupled to a photo multiplier tube. Over all, NaI scintillators have the highest light output of all commonly available gamma detectors, and have moderately good energy resolution.

Bismuth Germanate

Bismuth Germanate (BGO) detectors are another type of scintillation detector. BGO has a lower light output than NaI. However, because of of Bismuth's high nuclear charge (and thus higher electron density), BGO a has greater ability to stop and detect high energy photons than NaI. This significantly improves BGO detection efficiency for photons with energies greater than 3-5 MeV.

High Purity Germanium

High purity Germanium (HPGe) detectors are semiconductor devices that have extremely precise energy resolution which makes them excellent for discriminating photopeaks from reactions that nearly overlap in energy. They are less convenient to use because they must be operated at cryogenic temperatures. They are also more difficult to manufacture with large detector volumes so they generally have a smaller active volume than scintillators and therefore have lower detection efficiencies.

3.5 Applications of external beam IBA

3.5.1 2-D Boron Mapping of Boron on the Inner Wall for AIMS Validation

After the AIMS measurements were made on the inner-wall of C-Mod, four inner-wall tile modules, with 16 tiles each, were removed following the 2012 C-Mod campaign and subsequent wall conditioning operations. The external beam PIGE analysis set-up shown in figure 3-15 was used to generate a map of the of the boron content on the surface of these tiles. Since some of these tiles overlapped with the locations of the AIMS measurements these tiles provided a method to validate boron measurements with the AIMS technique. All of the 64 available tiles were analyzed to generate the map shown in figure 3-16. This plot shows the gamma yield, normalized to the integrated beam current during the measurement which is directly related to boron content. This provided an effective method to quantify the boron over the analyzed section of the inner wall. Analysis and discussion of these results are provided in chapter 6 section 6.5.

3.5.2 Tungsten Erosion and Migration Study with PIXE

In 2009, an IBA study of tungsten was performed set of C-Mod Divertor tiles, giving the first spatially resolved measurements of tungsten migration in C-Mod as well as the first erosion rates, presented in [4]. For this study, a toroidally-continuous row of bulk tungsten (W) tiles was installed near the typical location of the outer strike-point in the Alcator C-Mod divertor and was removed for analysis after two campaigns (3151 plasma discharges). External beam particle induced X-ray emission (PIXE) analysis – a technique similar to PIGE – was used to observe campaign-integrated W

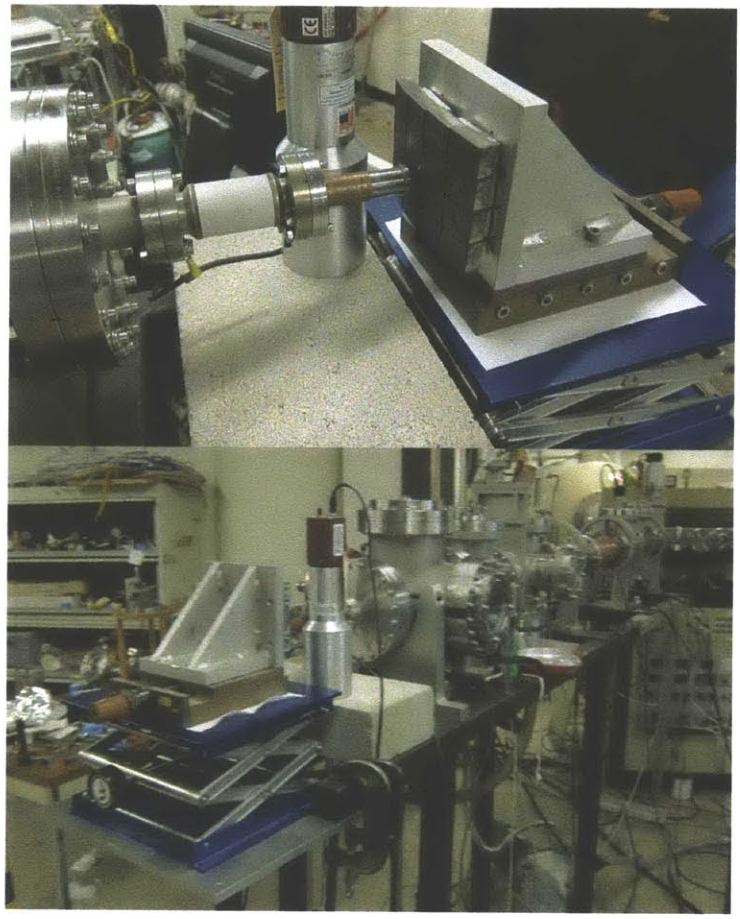

Figure 3-15: Photograph of the external beam PIGE analysis setup.

migration patterns in the otherwise Mo divertor using the W as a tracer for divertor erosion and transport.

Using a set of high spatial resolution PIXE measurements (3 mm resolution), a poloidal profile of W migration was constructed, shown in figure 3-17. This result shows W redeposition of up to 1.5×10^{21} atoms/m^2 ($\sim$20 nm equivalent thickness) on the outer and inner divertor, and in the private-flux region. The campaign-integrated deposition on the analyzed tiles corresponds to net W erosion of $\sim$60 nm ($>$0.014 nm/s) demonstrating reactor like high-Z errosion on C-Mod PFCs. The migration profiles indicate sputtering and prompt redeposition in the outer divertor, neutral and ion transport through the private - flux region, and transport in the scrape off layer. This study demonstrates the capabilities of external IBA and constituted the first ever poloidal measurement of tungsten migration in the C-Mod divertor.

3.5.3 Measurement of Boron in the Divertor with PIGE

In parallel with the 2009 Tungsten erosion study, boron profiles were measured with external beam PIGE analysis on the same set of tiles. These results are presented

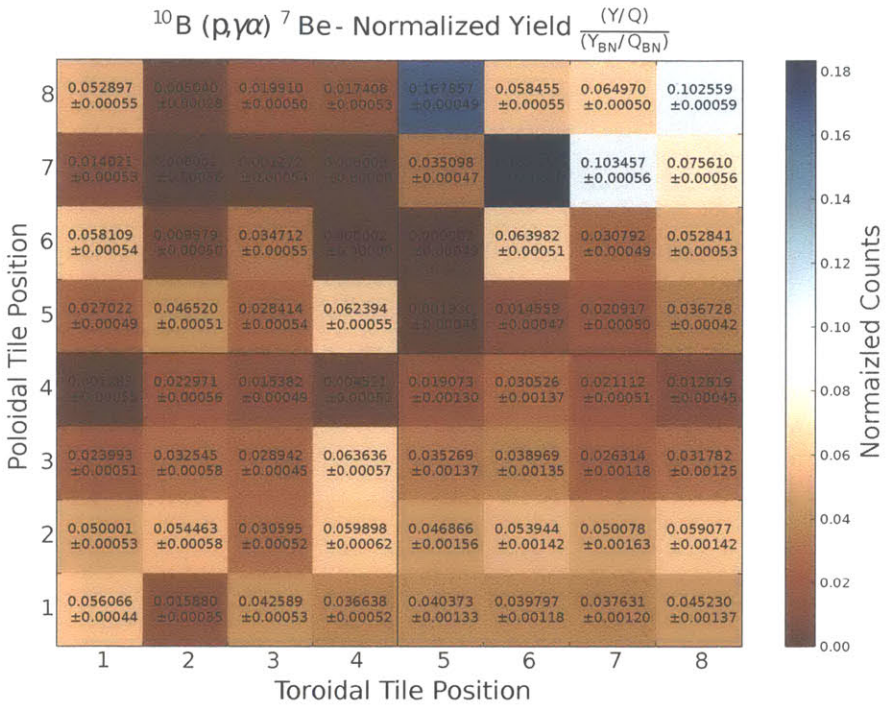

Figure 3-16: Gamma Yield measured with external proton beam PIGE analysis. Error bars quantify Poisson error.

in [3]. A map of the analyzed tiles and the boron profile from the inner divertor are shown in figure 3-18. The boron profile for the outer divertor and divertor dome (covering the EF1 coil) are shown in figure 3-19. All of the measurements were made with spatial resolution of 3-4 mm, using 3 mm diameter proton beam.

For the 2009 campaign, the inner divertor was made up of ramped tiles that were designed to shade the bolt hole in the middle of the tile from the direct impact of plasma particles. The spatial resolution of the external PIGE measurement allowed for each of the three sloped regions of each ramped tile to be studied. These boron patterns on the inner divertor did not seem to follow a trend and seemed to be most affected by the slope of the tiles. The deposition in the inner divertor is also higher than any other region of the divertor even though boronization is not expected to cause significant deposition in this region. This indicates that the inner diveror was a region of net boron deposition during the 2009 campaign. This pattern was very different from the tungsten measurements on the inner divertor which were highly localized towards the bottom of the inner divertor near the strikepoint.

Boron on the outer diveror seems to show a pattern that is essentially identical to the profile of tungsten from the tungsten migration study of the same tiles. This indicates that the both low-Z and high-Z materials migrate through the similar transport mechanisms in the outer divertor. The divertor dome spans the region of the vessel where the EC resonance is expected to deposit boron during boronization. Most of this region also resides in the private flux region which is topologically excluded from

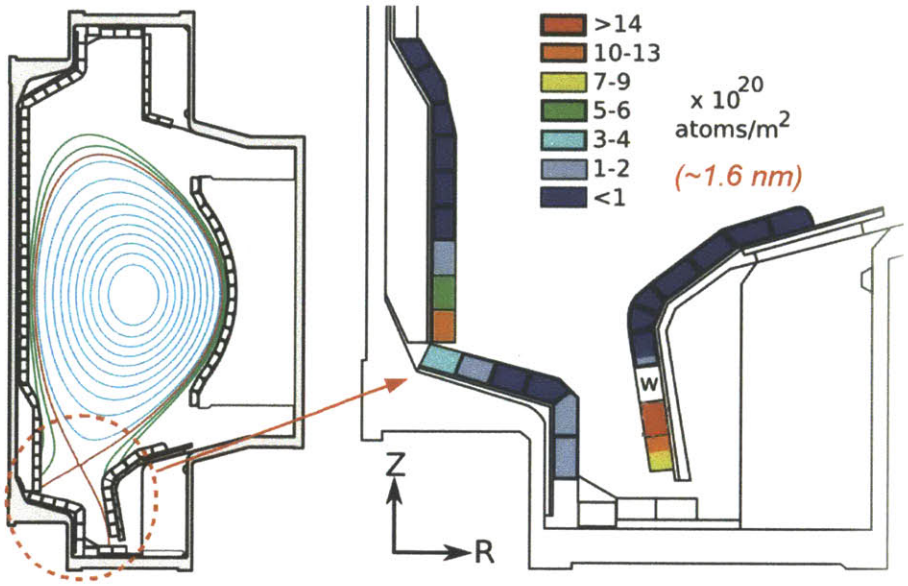

Figure 3-17: Spatially resolved map of net poloidal migration of tungsten in the lower Alcator C-Mod divertor measured with external ion beam analysis. W is the tungsten tile row located near the outer divertor strike point used as the tungsten source in this study.

the edge-plasma so erosion is expected to be minimal. As a result most of the EF1 dome region appears to have a relatively smoothly varying profile whereas there is substantially more scatter in the data and an increase in boron close to the inner divertor near the inner divertor strike-point.

3.6 Discussion of Exteral PIGE Analysis and PMI

These measurements demonstrate that external IBA is effective for measuring long term integrated effects of PMI. Extrapolating from the measurements, boron deposition rates appear to exceed 10 cm/year (of plasma exposure) in some cases. Tungsten erosion rates also extrapolate to > 0.4 mm/year in the outer divertor. For tungsten in particular, these rate are approaching the maximum acceptable erosion rates for high-Z PFCs which are likely to be implemented in future reactor scale fusion devices, yet it is difficult to understand the mechanisms these erosion and deposition patters when the available measurements techniques can only capture net effects that are integrated over thousands of plasma experiments.

The PMI effects produce a complex spatial pattern that can be measured with IBA in great detail, but with no method to determine when and how these changes occurred it is not possible correlate the observation of materials changes to specific to plasma conditions. While ex-situ analysis clearly exposes the problems of PMI and is a powerful tool for studying long term effects of PMI, ex-situ analysis is fundamentally limited by the measurement timescale. Adequate time resolution requires in-situ

measurement techniques to study surfaces of with comparable diagnostic quality in order resolve the time evolution of surface conditions. Thus, this fundamental diagnostic need motivates the development of accelerator in-situ materials surveillance (AIMS).

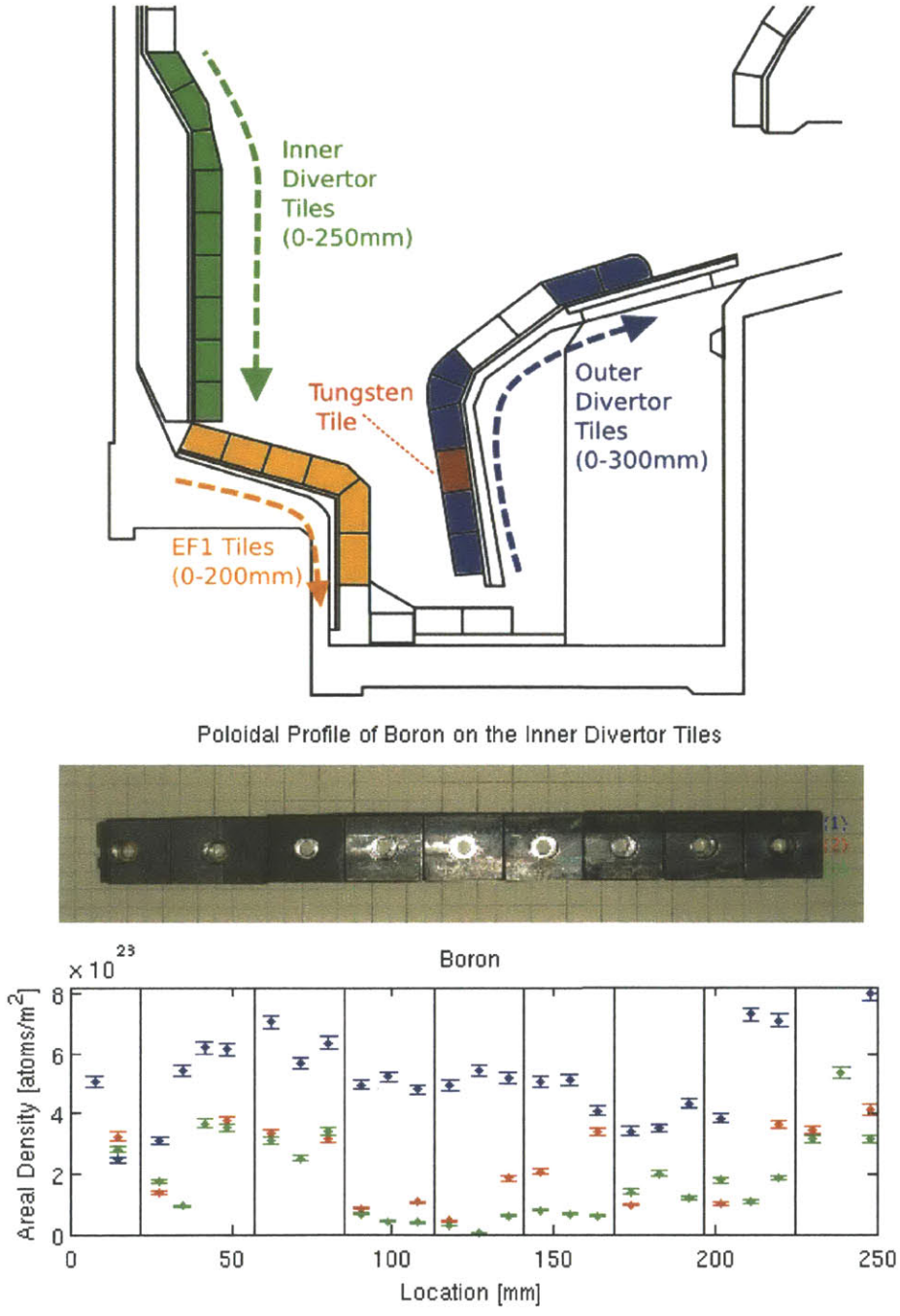

Figure 3-18: Top: map of the lower divertor showing regions that were PIGE analyzed for boron after the 2009 campaign. Bottom: spatially resolved boron measurements on a set of tiles spanning the inner divertor.

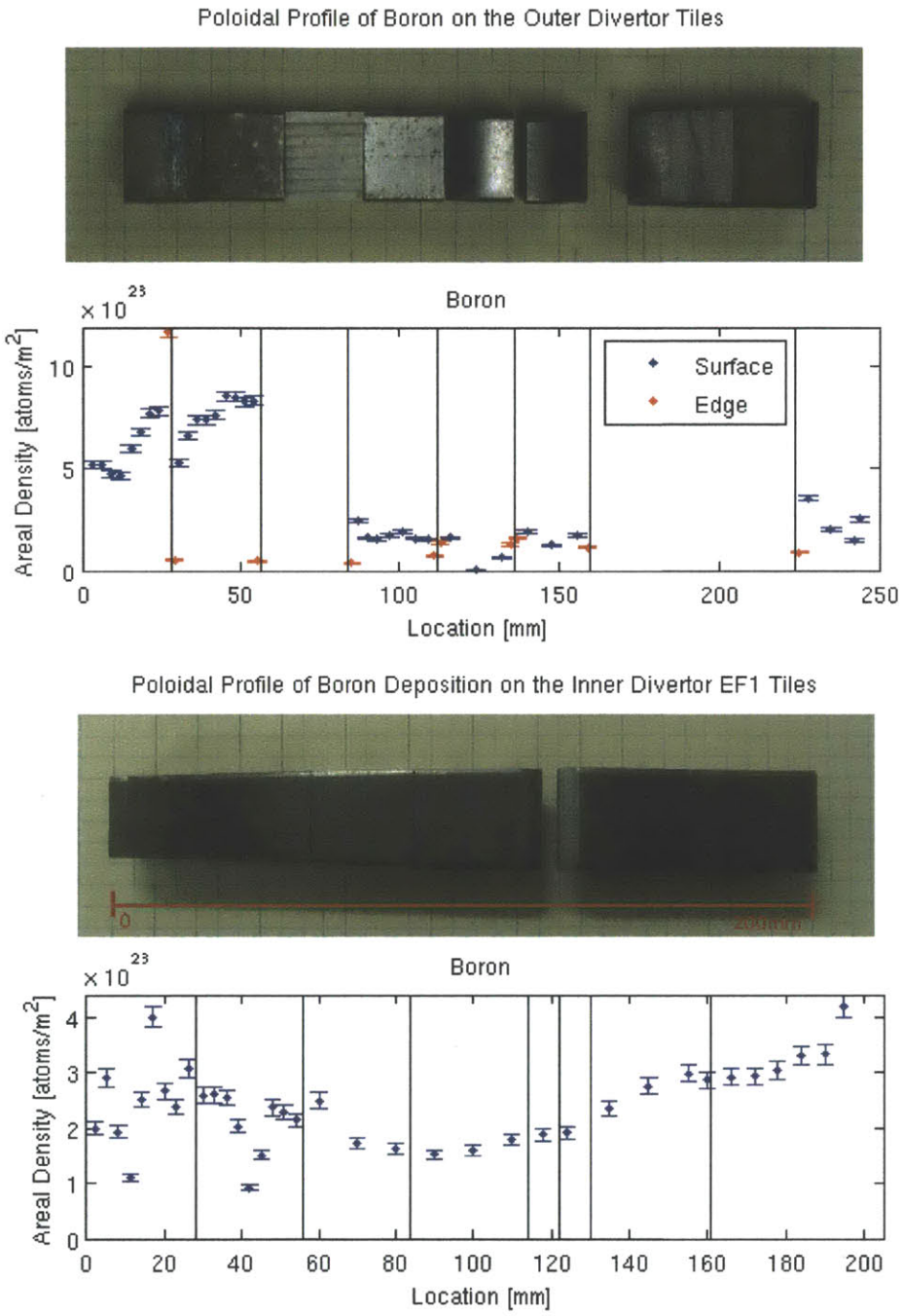

Figure 3-19: Top: spatially resolved boron measurements on a poloidal set of tiles spanning the outer divertor. Bottom: spatially resolved boron measurements on a set of tiles spanning the divertor dome which covers the EF1 poloidal field coil in the lower divertor.

Chapter 4

Integration of a Compact Ion Accelerator with a Tokamak

The AIMS diagnostic technique fundamentally requires the integration of a compact accelerator with a tokamak to study plasma material interactions. The accelerator must provide the necessary ion beam parameters and access to the tokamak plasma-facing surfaces. To date, this is the first integration of an RFQ accelerator with a tokamak and likely the first use of an RFQ for ion beam analysis of materials. The successful implementation of the RFQ on the Alcator C-Mod tokamak represents a unique and important contribution to fusion PMI research.

4.1 Overview of Accelerator Integration

Installing and operating an accelerator in the vicinity of a tokamak for the AIMS diagnostic poses constraints on the accelerator size and design. The accelerator must be small enough to fit within the tokamak shielding cell while also producing a beam in the MeV range with high enough beam current to induce sufficient nuclear reactions to make spectroscopic measurements. In addition, the accelerator cannot have large magnetic components that might interact with the tokamak's fields.

Radio-frequency quadrupole (RFQ) accelerators are well suited to satisfy these criteria. RFQs can accelerate high current beams by $\sim$1 MeV per meter of accelerating structures – significantly more compact than other conventional accelerator technologies such as the electrostatic accelerator used for ex-situ IBA (chapter 3). In addition, RFQ structures are typically made from copper or Cu-plated aluminum which are non-magnetic and do not cause issues with the tokamak's magnetic fields.

RFQ accelerators are resonant RF cavities with four vane structures that a specially machined produce spatially varying fields near the beam axis. The specially designed field structure bunches and accelerates the beam while simultaneously providing strong transverse focusing. The combination of beam bunching, beam focusing, and ion acceleration with RF rather than $\sim$MV DC voltages allows RFQ cavities to be extremely compact high current ion accelerators, typically achieving ion acceleration gradients of 1 MeV/m [48]. RFQ accelerators also produce high quality (low

emittance) beams compared to other similarly sized accelerators. The compact size enables the use of RFQs for the AIMS technique buts comes at the expense of flexibility. Each RFQ is designed and machined for a single mass to charge ratio and final output energy. Therefore, only IBA techniques using a single ion energy can be employed without the use of energy degrading techniques.

The accelerator used for the AIMS diagnostic is a 1990s era prototype RFQ accelerator, called the DL-1, designed by ACCSYS Technologies [1] for use as a neutron source. It was designed to produce neutrons by bombarding a beryllium target with deuterons, inducing the ${}^{9}_{4}\mathrm{Be}(d,n){}^{10}_{5}\mathrm{B}$ reaction. This accelerator was re-purposed for the AIMS diagnostic with comprehensive refurbishment and upgrades to its controls and power systems. In addition, accelerator support structure, RF transmission lines and beamline were redesigned to accommodate operation the tokamak cell.

To achieve C-Mod wall tile size spatial resolution (2-3 cm) on the target PFC surfaces, beam optics are necessary to maintain a focused beam over the beam's ~ 2 m trajectory through the beamline and tokamak vessel. The low emittance of the RFQ beam is important for the beam optics because it allows for a better collimated beam. However, the optical components combined with the non-uniform tokamak fields form a complex beam transport system that requires computational modeling of the fields, trajectories, and evolution of the beam's spatial and velocity distribution for proper implementation (Chapter 5).

For MeV beams, electromagnetic quadrupoles are the most commonly used beam optics because of their strong focusing and versatility. However, standard quadrupoles are not suitable in tokamak ports because their large magnetizable iron components can interact with the tokamak's fields, potentially perturbing the plasma or causing destructive forces on the beamline during plasma shots. Instead, permanent magnet quadrupoles (PMQ) were used because of their compact size, zero net B-field, and ease of implementation. The beamline also requires compact beam diagnostics which were developed to provide reliable current measurement, beam alignment and beam characterization (section 4.7).

4.2 Accelerator: Principles of Operation

The RFQ design process allows for significant flexibility to fit various ion source types and accelerator applications. RFQ cavities can be designed for any ion species, charge state, beam current range up to >10 mA, and beam energy up to several MeV. However, after the cavity design is complete, all of the beam parameters are fully specified by the design. So, after the cavity is fabricated the only free parameter is the RF power which must be set in order produce E-fields with sufficient amplitude to accelerate the particles and compensate for the reduction in E-fields due to the power coupled to the beam. Also, many designs can only operate in pulsed mode because continuous wave (CW) operation may not be possible due to limitations in the RF power system, or would lead to excessive RF heating of the cavity.

RFQ accelerators, despite their lack of operational flexibility, provide several distinct advantages that allow them to be compact. The combination of strong transverse

focusing fields with longitudinal accelerating fields allow RFQs to achieve accelerating gradients as high as 1 MeV/m at high currents in mA range. In both accelerating gradient and beam current, RFQs outperform any other type of similar sized accelerator ion accelerator up to $\sim$ 2 MeV/nucleon. Also, since the RFQs can be designed to efficiently bunch DC beams before acceleration, a compact ion source can be integrated into the accelerator unit without having a separate injector like most other linac designs.

The DL-1 RFQ accelerator from manufactured by ACCSYS, designed to accelerate high current D^+ beams to 900 keV, was used for the AIMS diagnostic. The following sections 4.2.1 and 4.2.2 describe the principles of operation of the RFQ accelerators with emphasis on the design used in the DL-1.

4.2.1 Duoplasmatron source

RFQ accelerators are composed of an ion source coupled to a specially designed resonant RF cavity. The ion source used in the DL-1 is a pulsed duoplasmatron source shown schematically in figure 4-1. The pulse of ions produced by the source is synchronized with the RF power system so that the ions enter the cavity after the cavity has been energized. The DL-1 source ionizes D_2 gas and extracts D^{+1} ions at 25 keV. The source operates in the following sequence:

1. The source's cathode is a filament, made from tantalum mesh coated with barium oxide, that is heated to >1000 K to produce a continuous supply of thermal electrons. The barium oxide has a low work-function and aids the thermal emission process.

2. The filament is pulsed with a negative 200-300 V pulse V_f to initiate a plasma inside of the intermediate electrode (IE). This voltage repels electrons from the filament, ionizing some of the $\sim$200 mTorr of D_2 gas contained in the source to create a plasma arc inside of the IE.

3. As the IE accumulates negative charge, electron current begins to flow though the opening of the intermediate electrode across a gap to the aperture in the anode, creating a secondary plasma in the gap. The low resistance of both of these plasma causes the intermediate electrode to reach a voltage that is roughly $V_f/2$.

4. The IE is made from magnetic steel alloy and concentrates the magnetic field from the solenoid. The field confines and compresses electron flow as it passes through the gap. These confined electron orbits enhance the ionization process of deuterium gas to create a low temperature but high ionization fraction plasma (allows for low emittance, high current extraction).

5. Plasma escapes through the aperture and expands in the insulated plasma expansion cup.

6. The surface of the plasma is shaped by the Pierce anode (biased at 0-300 V) and the D^+ ions extracted from the plasma surface by the 25 kV extraction voltage.

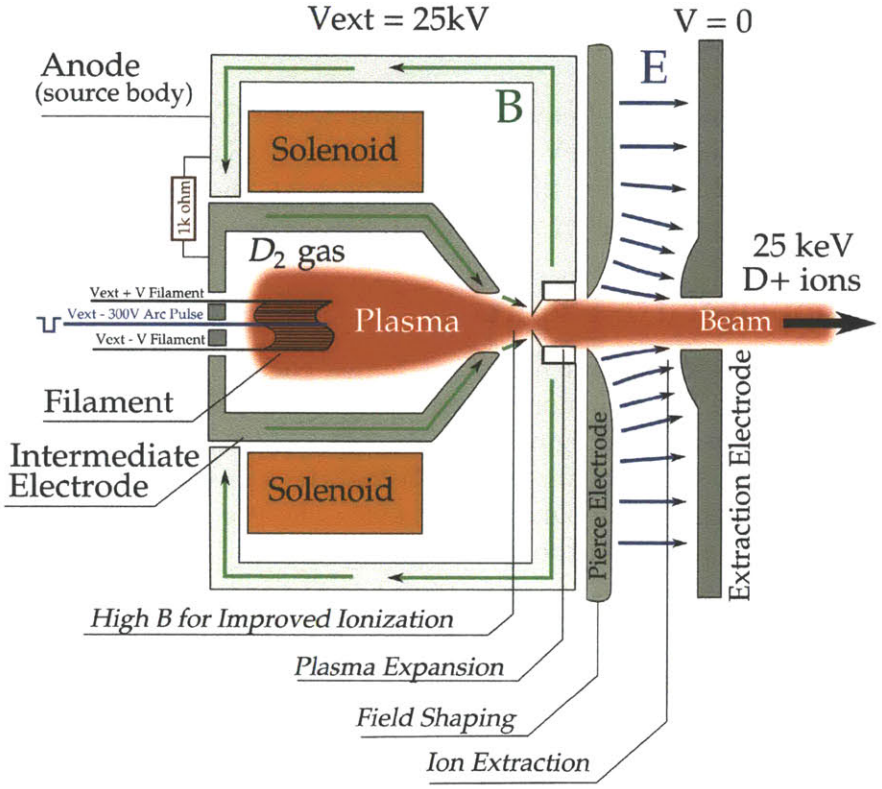

Figure 4-1: Schematic of Duoplalsmatron Ion Source used in the DL-1. Refer to section 4.2.1 for principles of operation and component descriptions. The blue arrows represent electric field lines set by the geometry and the extraction potential. The green arrows represent the magnetic field lines and their paths through the magnetic iron body of the source and in the ionization gap.

This process in the duoplasmatron source produces a low emittance, high current pulse of ions (for the DL-1, emittance = 0.02 πcm·mrad [1], Current$\sim$20 mA). The ions then pass through an electrostatic einzel lens to focus the 25 keV beam and match the ion distribution to the acceptance for the RFQ cavity. Acceptance is defined as the phase volume of particles at the accelerator entrance that will result in stable orbits and acceleration over the length of the cavity.

4.2.2 Radio Frequency Quadrupole

Radio frequency quadrupole accelerators, as the name suggests, use a resonant RF cavity that supports standing wave modes with quadrupole symmetry. More specifically, RFQs are cylindrical cavities designed for a TE_{210}-mode. Four copper vane

structures separate the four lobes of the cavity mode and concentrate the electric field near the beam axis.

As particles travel along the axis of the cavity, the quadrupole component of the transverse field provides alternating gradient focusing, much like a electrostatic quadrupole focusing system except with the fields varying in time rather than space. This effect appears different in the lab frame, but is identical in the frame of the particles.

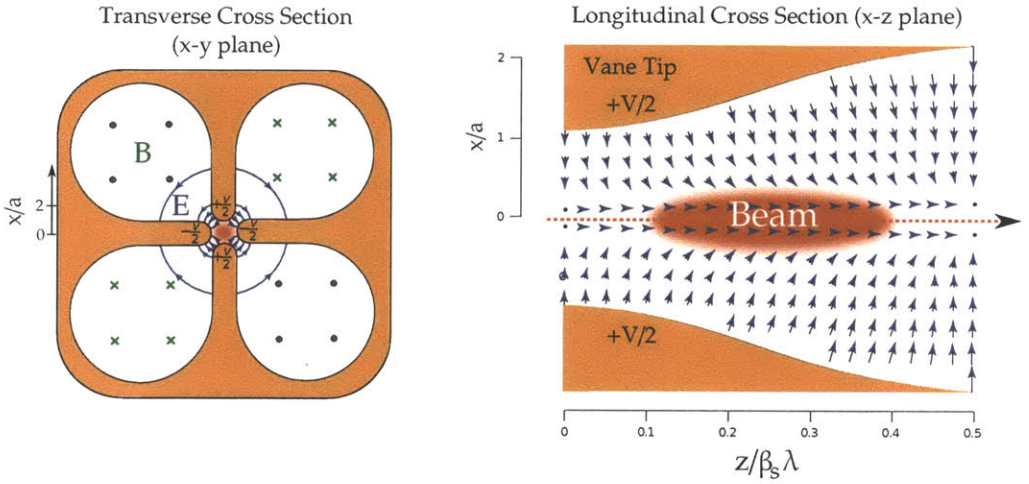

Figure 4-2: Schematic of RFQ field geometry. The transverse cross section (left) shows E and B fields of the TE_{210}-mode creating quadrupole electric fields near the z axis of the cavity for transverse focusing. The longitudinal cross section (right) shows how the transverse modulations of the vane spacing create a net longitudinal E field for acceleration during 1/2 of each RF period. The spatial wavelenth λ of the modulations increase with z to keep each particle bunch with velocity $\beta_s\, c$ in synchronous phase with the time varying RF fields [55].

The spacing of the tips of the vanes $r(z)$ are modulated longitudinally as a function of z, as shown in figure 4-3. This perturbs the E-field of the otherwise purely transverse TE_{210}-mode near the longitudinal axis of the cavity to produce a longitudinal component for accelerating the ions. The modulations are designed such that, as the ion bunch passes from a narrow region to a wider region, the longitudinal component of the E-field accelerates the ions. Then, as the ion bunch passes the middle of the modulation, the RF fields reverse polarity, causing acceleration in the second half of the modulation. In order for the ion bunches to be accelerated over multiple modulations, the width of the modulations must increase continuously in spatial period to allow the particle bunches to remain in synchronous phase with the RF (which is at a fixed frequency) as the velocity increases. This increasing longitudinal spacing occurs primarily in the last 60% of the cavity where most of the acceleration occurs. Before the primary acceleration region, both the transverse spacing between the vanes and the vane profile are optimized for shaping and adiabatic bunching of the beam rather than acceleration.

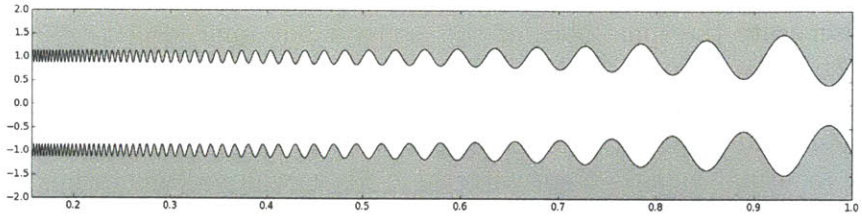

Figure 4-3: Schematic of RFQ vane profile. The modulations increase in spatial period to allow the particle bunches to remain in synchronous phase with the RF as the velocity increases.

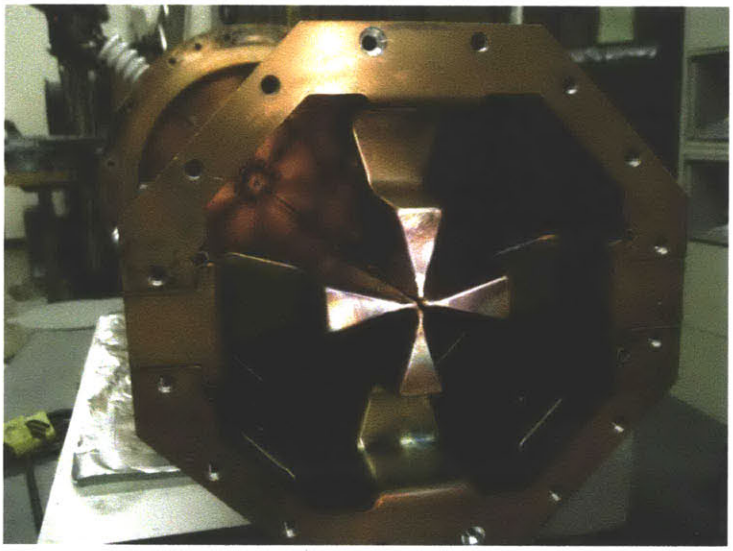

Figure 4-4: Photo of RFQ cavity with the case and end-plate removed, showing the quadrupole symmetry of the cavity and the modulations of the vane tips.

4.3 RFQ Accelerator Refurbishment and Upgrades

The accelerator used for the prototype of AIMS is a refurbished 0.9 MeV deuterium-ion RFQ from ACCSYS called the DL-1 which was originally designed as a prototype for a neutron source. The specifications for the DL-1 and the achieved parameters following refurbishment are shown in table 4.1. The DL-1 was designed for manual operation, using mostly potentiometers, switches, and panel meters on the power supply racks for controls and monitoring. The accelerator, however, needed to operate remotely in the Alcator cell. The C-Mod environment poses significant operational challenges for the accelerator, associated with high radiation, other high-power RF sources, electrical noise, and compliance C-Mods operational requirements. In addition, many of the accelerator's power systems were damaged or unreliable, needing significant repairs. This necessitated a complete overhaul of the accelerator's controls, electronics, and power supplies. These upgrades constituted a major component of the research efforts for this thesis.

Comprehensive upgrades to the accelerator's controls, instrumentation, mechani-

Parameter	Design	Achieved	Unit
Operating Frequency	425	425	MHz
Input Energy	25	25	keV
Final Ion Energy	900	*see section 4.8*	keV
Output Energy Spread	±15	*see section 4.8*	keV
Design Input Current	5-15	10-20	mA
RFQ Cavity Beam Transmission	>90	<10	%
Maximum Final Beam Current	21	1.5	mA
Beam Pulse Length	5-100*	10-50	μs
Maximum Repetition Rate	640*	60	Hz
Maximum RF Duty Factor	2.25	0.3	%
Required RF Power	>39.5*	55	kW
Maximum RF Power	60	60	kW

Table 4.1: Design parameters for a the DL-1 Radio Frequency Quadrupole Accelerator Manufactured by ACCYS [1]. Design parameters are accompanied by achieved parameters after DL-1 refurbishment. * There is some uncertainty in these parameters based on conflicting information from the manual and the manufacturer.

cal support structure and vacuum system were required for integration into the tokamak environment. All of the accelerator's controls and instruments were upgraded from manual control to operate Group 3 fiberoptic loop controllers for remote operation in the Alcator cell. In addition, the mechanical support structure and vacuum system were redesigned to fit in the confined space surrounding the tokamak port while allowing for precision alignment of the RFQ cavity to the port flange.

4.3.1 RFQ Timing

To understand the AIMS diagnostic system and how its components interrelate, it is informative to understand the sequence of events that occurs to produce a beam pulse while measuring signals from the detectors in order to understand the function of the various components in the accelerator system. A timing diagram of the controls, monitor, power systems, and data acquisition is shown in figure 4-5. These pulses typically have pulse widths of ~50 μs with repetition rates of 60 Hz.

To create a beam pulse, first RF gate pulse activates the RF amplifier to produce a 425MHz, 60 kW RF pulse to excite the RFQ cavity. Immediately the forward RF amplitude begins to increase (measured with a directional coupler). A transient reflected RF amplitude signal is measured as fields build up in the amplifier and cavity, but drop to near zero if the amplifier and cavity are properly impedance matched. At this time the fields begin to build up in the cavity and are measured as the cavity RF amplitude by a small pick-up loop in the cavity. The cavity has a finite RF fill time, usually ~5 μs, related to the Q of the cavity. Slightly before the cavity has reached its maximum field the arc gate pulse initiates the arc pulser circuit that generates a plasma in the duoplasmatron source. As the plasma forms in the source,

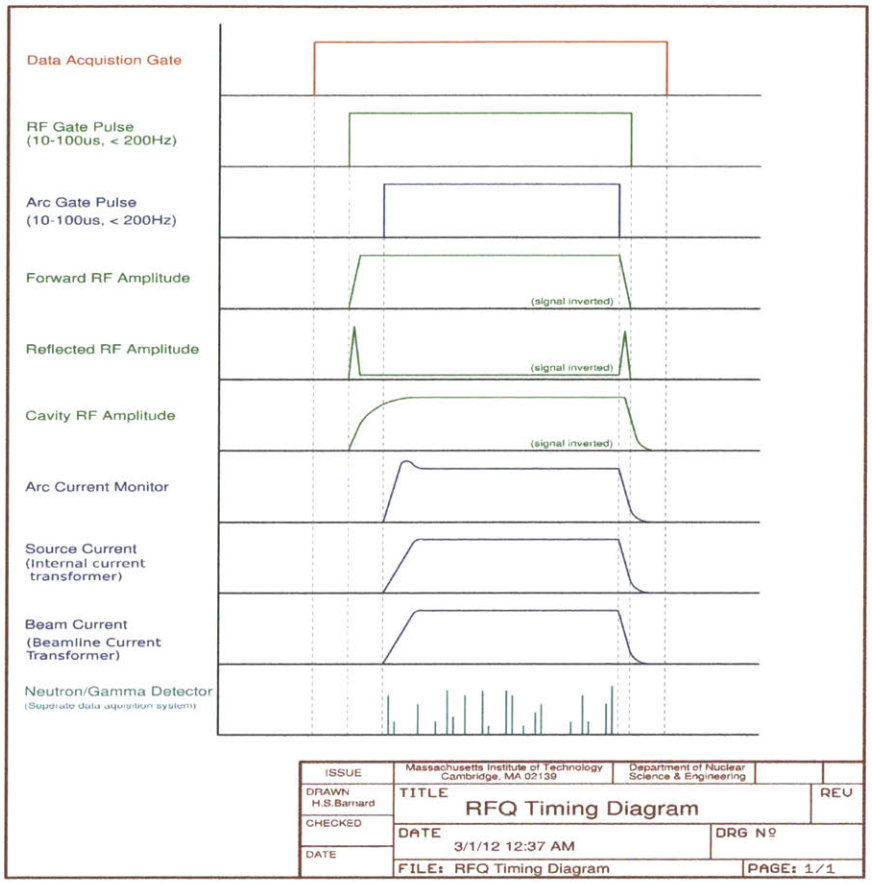

Figure 4-5: RFQ accelerator timing diagram. This diagram schematically shows the voltage waveforms of the accelerators control signals, feedback from instrumentation, and signals from detectors.

the arc current monitor provides a measurement of the current flowing through the plasma and the internal source current transformer provides a measurement of the beam current entering the RFQ cavity.

While the beam pulse is being generated and its ions are inducing reactions on at the PFC target, the digitizer system that collects signals from the neutron/gamma detectors and beam current transformer (installed on the beamline before upstream of where the beam is injected into C-Mod) is enabled by the data acquisition gate pulse, which spans the beginning and end of the beam pulse. After the measurement is complete, the digitized neutron and gamma pulses are then analyzed to produce spectra that are used to quantify isotopes on the target surface. The details of the neutron and gamma post processing techniques are given in reference [21]. This sequence thus describes the complete process of how the AIMS diagnostic operates.

4.4 RFQ Systems and Installation Overview

The hardware upgrades to RFQ systems involve too much engineering complexity and excruciating detail to be described thoroughly in this thesis. Instead the hardware upgrades are briefly summarized with a series of figures and descriptions. Detailed engineering drawings can be found archived by the MIT Nuclear Engineering Department's technical staff.

The RFQ accelerator system has three major groups of components shown in a photograph in figure 4-6: (1) The injector rack contains the power supplies, controls, and monitor for duoplasmatron ion source. (2) The RF power amplifier is a 4 stage system that produces RF pulses up to 100 μs in length and is designed to operate with 100 μs pulses of up to 60 kW. (3) The accelerator contains the ion source and the RFQ cavity to produce the accelerated beam. A complete system level schematic is shown in figure 4-8 which describes how the various components interact to produce the proper timing, beam, and measurements (as described in timing diagram 4-5). A simplified version of this block diagram is also shown in figure 4-9.

All of the accelerator controls and instrumentation redesigned and custom built for the upgraded accelerator. The analog and digital I/O were implemented using Group III [37] programmable logic controllers that interface with PC through fiber optics. These controllers were used in the custom built control modules that replaced the manual controls and are consolidated into the following units: The ion source rack controls (figure 4-10), The RF rack controls (not shown), and the high voltage deck controls (figure 4-11).

All of these control units were operated through a custom interface designed in LabView^{TM} [35]. An image of the user interface is shown in figure 4-12. Through this interface the accelerator operator can control every aspect of the accelerators operation and monitor the accelerators instrumentation. In addition, for signals requiring greater bandwidth than the Group III modules could provide, a digital 100MHz USB oscilloscope was integrated into the injector with an 8-channel signal multiplexer for monitoring timing pulses and high frequency measurements from systems such as the RF power diagnostics.

Following the completion of the refurbishment and upgrade efforts, the RFQ accelerator was installed on the B-port of the Alcator C-Mod tokamak. The installation process began in August of 2012 and was completed in September of 2012. Photographs of the installation are shown in figure 4-14. The general layout of the RFQ hardware in the alcator C-Mod Cell are shown in figure 4-7.

The refurbishment of the DL-1 was a challenging engineering endeavor spanning over 3 years. The successful completion of the accelerator upgrades as part of this thesis followed by its installation enabled the implementation of the AIMS diagnostic, contributing a major and critical component to successful demonstration the AIMS technique.

Figure 4-6: RFQ accelerator (black) with 60 kW amplifier (upper left) and ion source power supply and control rack (upper right).

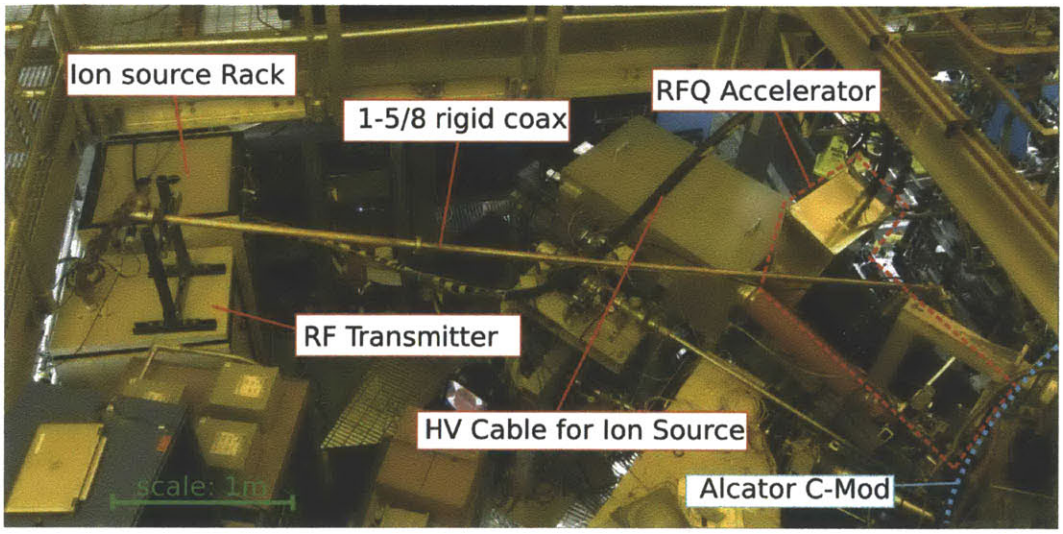

Figure 4-7: Top view showing the layout of the RFQ accelerator's power systems in the C-Mod Cell.

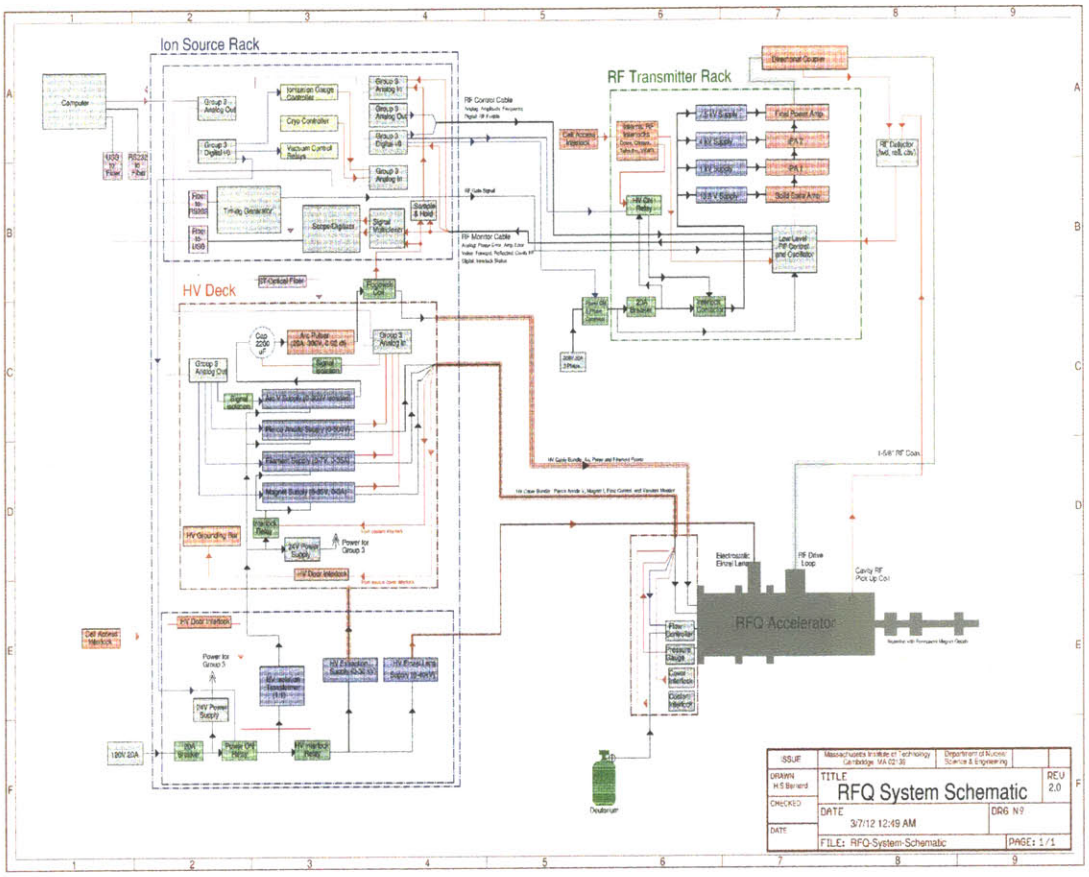

Figure 4-8: Complete schematic of the RFQ accelerator's upgraded controls and power systems. This system wide block diagram shows the interconnections and propagation of signals throughout the RFQ accelerator system. In order to see the details of this diagram use the pdf version of the thesis.

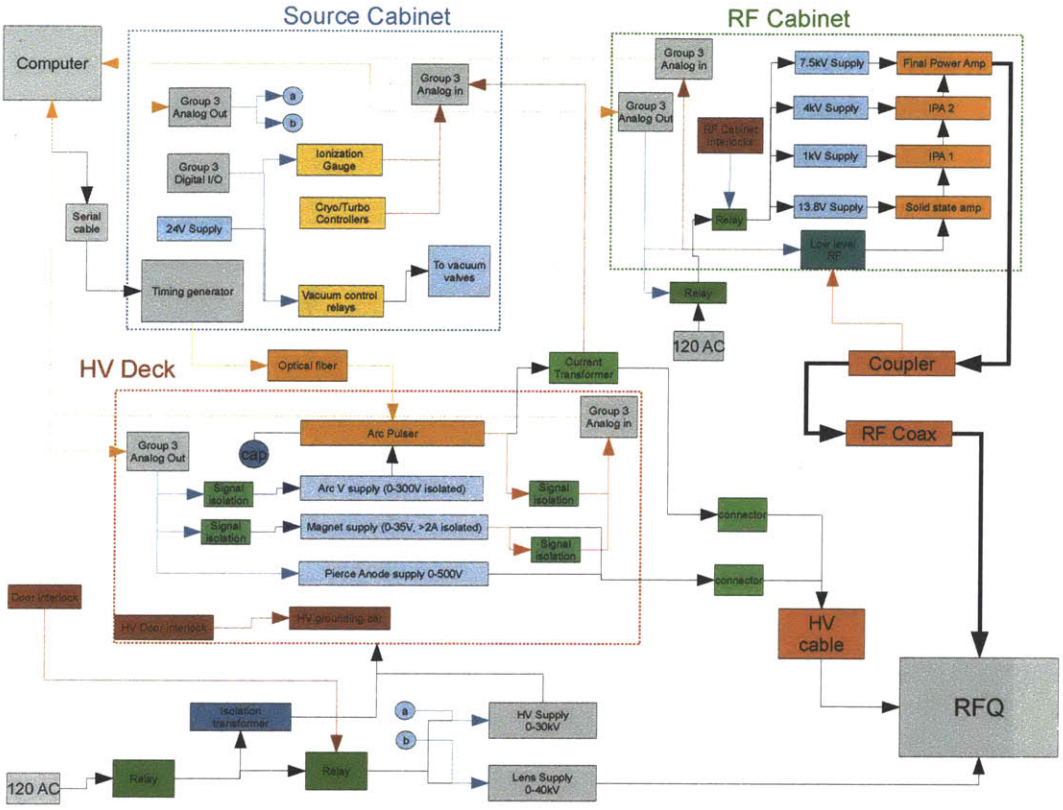

Figure 4-9: Simplified block diagram of the RFQ accelerator's upgraded controls and power systems. This diagram provides a system wide overview of the RFQ accelerator.

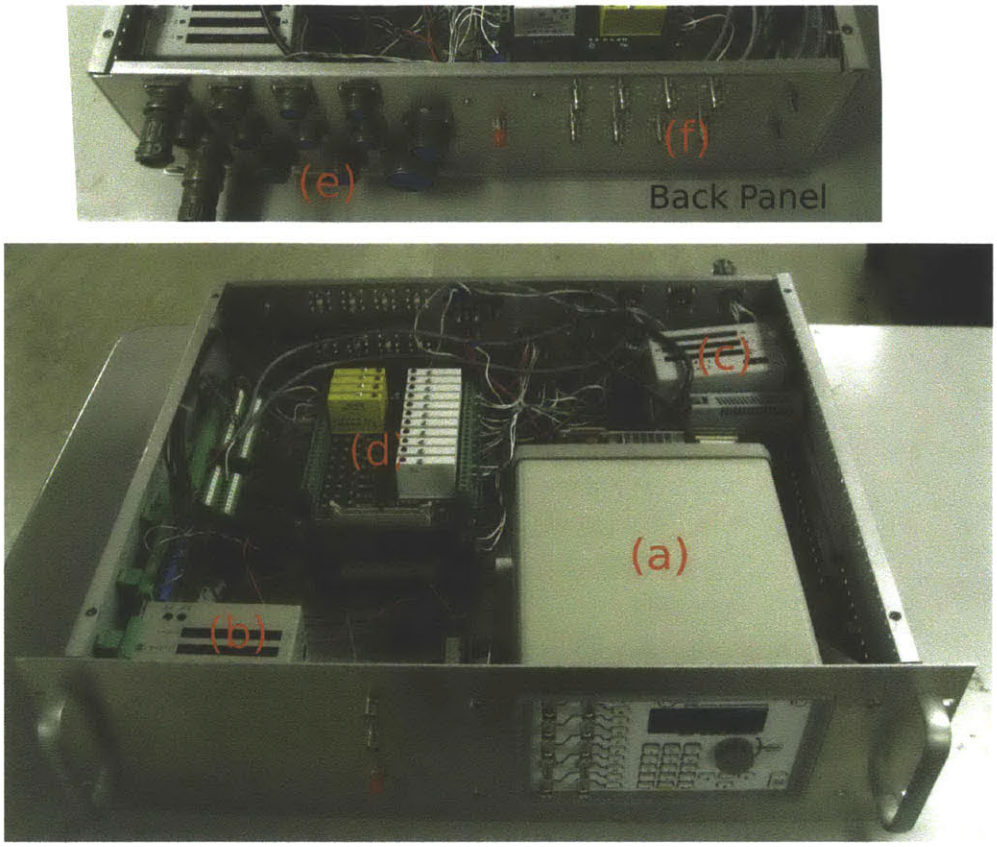

Figure 4-10: Injector control module: (a) Programmable pulse signal generator for synchronizing timing of the accelerators RF, beam, and data operations. (b,c) Group III controllers with digital and analog I/O. (d) modular array for relays used for control and routing of multiple signals and power controls. (e) Control and monitor signals for the high vacuum system. (f) 8 multiplexed signal inputs for the integrated 100 MHz oscilloscope used for measuring high frequency signals from accelerator instrumentation.

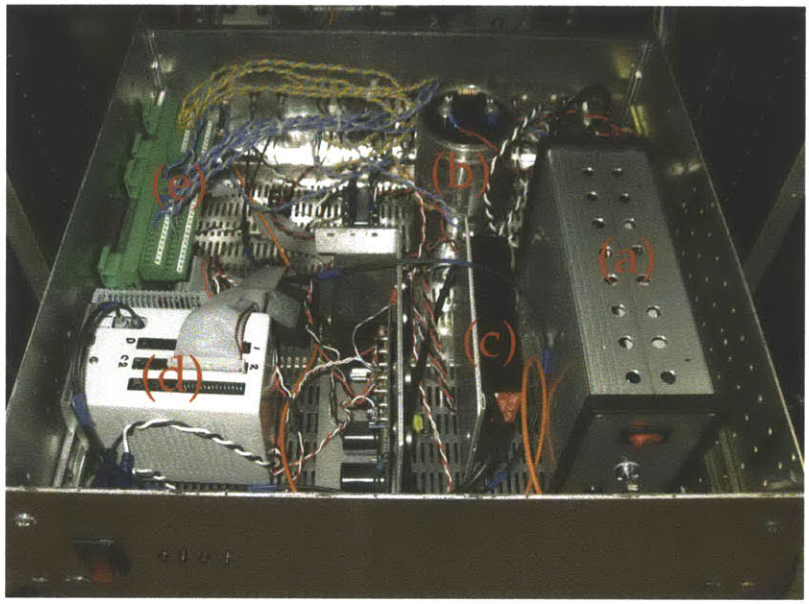

Figure 4-11: High voltage controls: Since the ion source operates at 25 kV, the source controls and power supplies are electrically isolated in a high voltage rack that operates at 25 kV. (a) The arc pulser is used to make -300 V, 20 A pulses to initiate and sustain the plasma in the ion source. This device was redesigned and built with modern components. A schematic is shown in figure 4-13. (b) An electrolytic capacitor is used to store energy between beam puses to provide the wired charge to deliver the arc pulse. The Pierce electrode supply provides the is used store energy between beam pulses to proved the required to deliver the arc pulse to the ion source. (c) The Piece electrode supply provides allows plasma shaping in the extraction region to improve efficiency. (d) Group 3 module provides digital and analog I/O. (e) All of the components are wired into terminal modules that communicate with the group 3 modules.

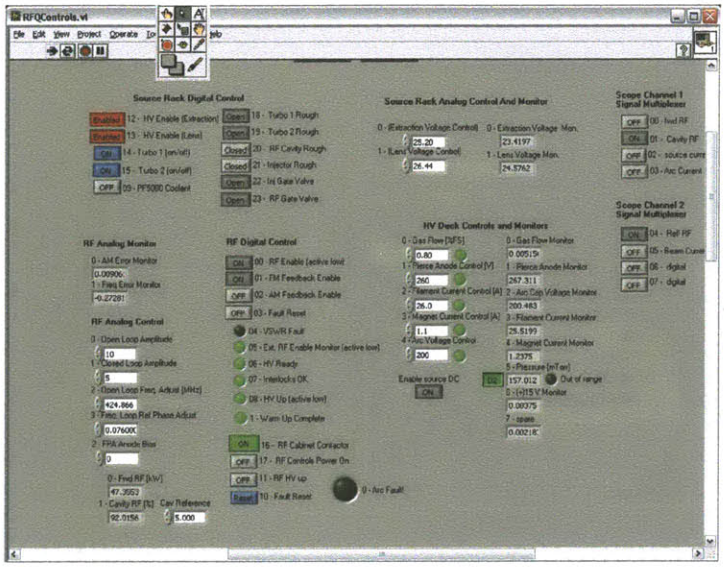

Figure 4-12: A custom computer interface was designed for the accelerator in LabView™ [35]. This interface allows the accelerator operator control every aspect of the accelerator's operation and monitor the accelerator's instrumentation.

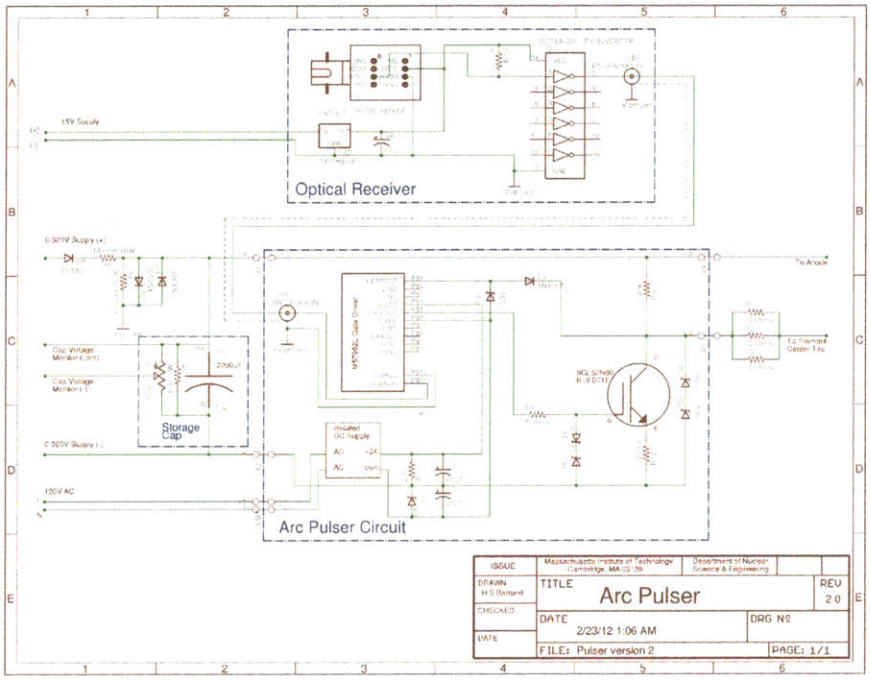

Figure 4-13: Schematic of upgraded arc pulser design. This device is used to produce -300 V, 20 A pulses to initiate and sustain the plasma in the ion source. The arc pulser was redesigned using modern IGBT components and drivers for better reliability and power handling.

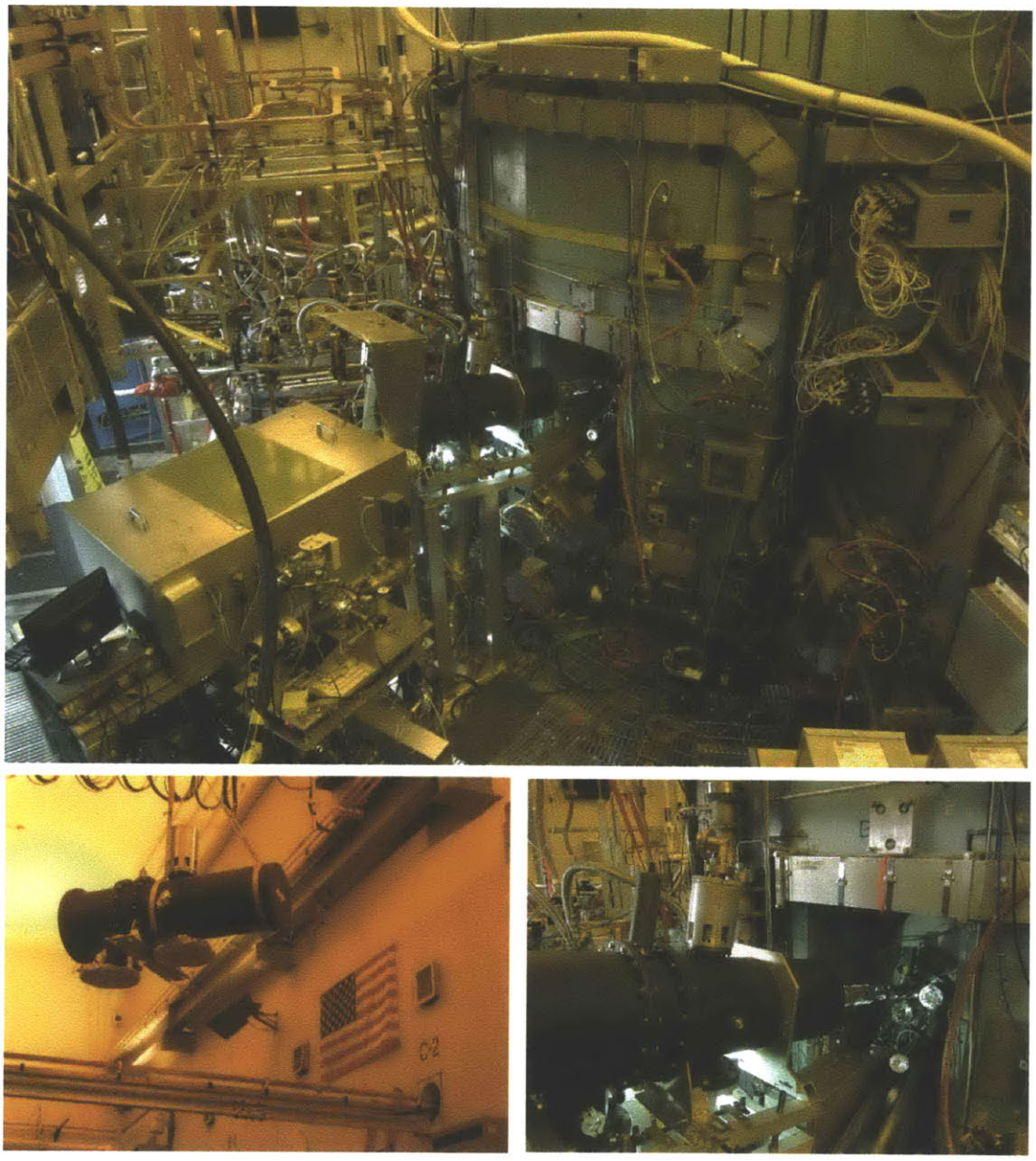

Figure 4-14: View of the RFQ accelerator installed on C-Mod (top). The RFQ accelerator being lifted into place using the gantry crane in the C-Mod cell (lower left). View of the RFQ beamline with permanent magnet quadrupole optics with the beamline connected to the beam injection flange on B-port (lower right).

4.5 Accelerator Integration

The integration of the RFQ accelerator with Alcator C-Mod posed unique hardware and instrumentation challenges. In particular, beam alignment techniques, compact beam diagnostics, and optics were extensively studied and developed and process of integrating the accelerator. The following section describe the beam alignment considerations and the necessary engineering and diagnostic solutions.

4.5.1 RFQ Alignment Geometry

The injection angle and position is important for determining which plasma facing surfaces in the vessel are accessible with AIMS. The assessment and optimization of the initial positioning of the accelerator was performed by Z.S.Hartwig using 3-D Euler integration based trajectory code with boundary detection [21].

Alignment of the accelerator during installation was critical because even relatively small angular misalignments or deviations from collinearity between the axis of the accelerator, beamline, and injection flange can cause the beam be miss the desired target, create severe aberrations in the optics, or cause the beam to be occluded.

For trajectories with small deflections, the beam travels roughly 1 m through the vessel after entering through the port flange and intercepts the inner wall with incident angles of $> 40^{o}$. Every trajectory must be calculated numerically and responds differently to errors in the angular alignment of the accelerator $\Delta\theta_{\text{acc}}$, however, the error in target position Δx can be approximated for small angles using equation 4.1 where s is the path length of the beam.

$$\Delta x \simeq \frac{s}{\cos(\theta_{\text{inc}})}\,\Delta\theta_{\text{acc}} \tag{4.1}$$

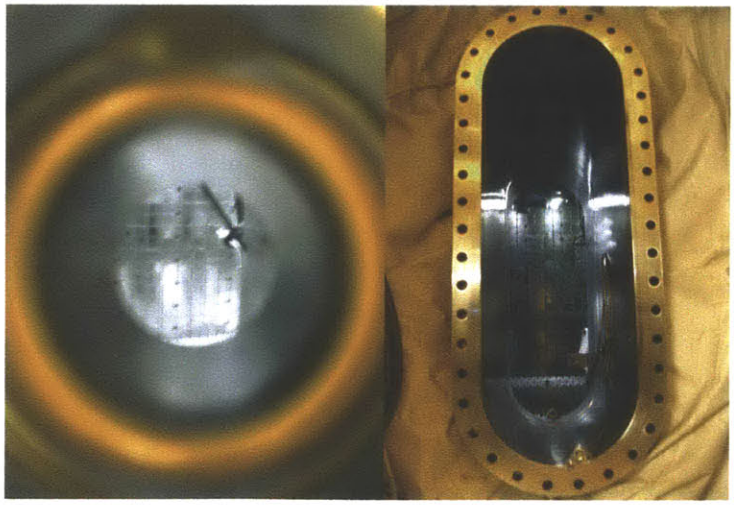

Figure 4-15: Photos of B-Port during Alcator C-Mod vacuum break: View through beam injection port (left). View of open port flange on B-port (right).

Based on this simple estimate it is clear that the target location varies strongly with beam injection angle. For example, an angular misalignment of 1 degree can cause the beam to miss the target by as much as 2.5 cm, roughly the width of a C-Mod molybdenum tile. It is therefore necessary to make the accelerator's alignment as precise as engineering resources will allow and to quantify alignment errors to minimize systematic error in the spatial resolution of the measurements.

When installing the accelerator, collinearity of the beam axis with the center of the injection port flange was measured by mounting a diode laser concentric with the ion source that was carefully adjusted to be aligned with the RFQ vanes. This ensured that the laser would trace the exact path of the beam centroid after exiting the accelerator. This was necessary because it was not possible to use proper surveying equipment severe space limitations and obstacles in the C-Mod cell.

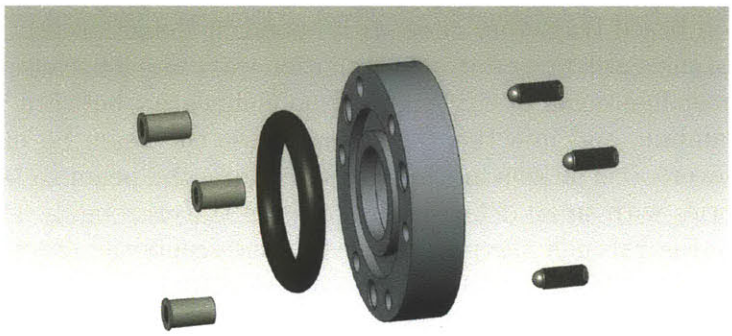

Figure 4-16: Precision alignment flange to adjust beamline angle with respect to the accelerator case.

Alignment of the beamline with the accelerator is also very important because, if the beam does not travel through the center of the beamline quadrupoles, severe beam aberrations can result. It was necessary to attach the beamline rigidly to the accelerator and compliantly to the port with vacuum bellows, adding an extra degree of freedom to the alignment. This was required because if the beam line were rigidly attached to the RFQ and the port, it would be extremely difficult to position all the components precisely enough to make vacuum seal on the conflat flanges. In addition, subtle movements or adjustments of the accelerator's position would bend the beamline – the weakest connecting component.

Since the faceplate on the DL-1's case was not originally fabricated with enough precision to orient the beamline to the accelerator axis, an adjustable alignment flange was needed. The faceplate was also not fabricated with a standard vacuum flange or bolt pattern. In addition, the optics did not allow more than several centimeters of distance between the RFQ and the first quadrupole so a custom, compact, precision alignment flange had to be designed and welded directly to the beamline. The design is shown if figure 4-16. An oversized O-ring is used in place of vacuum bellows, and precision (100 threads/inch) jack-screws are used for adjusting the angle allowing for

Component	Length L [mm]	Gradient $\frac{dB}{dr}$ [T/m]	Inner Radius r_i [mm]	Outer Radius r_o [mm]
Drift	133.47	–	–	–
PMQ 1	70.0	52.4	15.5	26.7
Drift	47.18	–	–	–
PMQ 2	70.0	-36.7	17.7	26.7
Drift	71.25	–	–	–
PMQ 3	35.0	48.1	16.0	26.7
Drift	1000	–	–	–

Table 4.2: Permanent magnet quadrupole parameters (PMQ) [28] with drift spacing optimized with TRACE3D [29] for a 1 cm diameter beamspot at 1 m from the last PMQ. Blue and red are fonts are used for PMQs that focus in vertical and horizontal transverse directions, respectively.

adjustments as small as several milliradians. This flange was used in combination with the beam imaging techniques described in section 4.7.5 to align the beam with axis of the focusing system.

4.6 Beam Optics

The DL-1 is designed to produce a low emittance beam, however, as the beam exits the accelerator, it is small in spatial dimensions so the angular envelope of the beam is large and it diverges rapidly in the transverse dimension. Optical imaging of the beam of the beam indicates that the beam diverges with an angle of $\sim 7^o$ after exiting the accelerator, meaning that the beam will diverge to 24 cm in diameter after traveling only 1 m. Optics are therefore necessary to focus the beam on the target PFCs which are typically $\geq$2 m from the end of the accelerator cavity.

The optics must be compact and must not interact with the tokamaks fields. Permanent magnet quadrupoles (PMQ) are small compared to standard quadrupole magnets. Also, they do not have any magnetizable iron and, being quadrupoles, they have no net magnetic moment so their interactions with Alcator's fields are minimal, making them well suited for the tokamak environment.

A PMQ triplet was used to focus RFQ beam for AIMS. These PMQs were custom made and characterized for an earlier application of the DL-1 for the thesis work or E.B. Iverson [28]. The only reliable source of the PMQ gradients and effective lengths that were available were from [28] are shown in table 4.2.

Preliminary analysis with the TRACE3D [29] beam modeling code was used to show that the PMQs could provide adequate focusing for AIMS. A TRACE3D simulation shown in figure 4-17 shows that a beam from the RFQ with typical parameters (2 mA) and trajectory length (1 m) can be focused to a 1 cm diameter beam spot. Table 4.2 list the optimal amount of 'drift' space between the PMQs that was determined in this simulation.

This simple simulation with no steering fields is a good indication of the effective-

ness of the PMQ system for the trajectories that were accessible with the toroidal field using the available DC supplies for B coils on C-Mod. For a preliminary analysis, this was sufficient because the trajectory lengths did not substantially exceed 1 m and the effect of beam the steering the tends to have net focusing effect on the beam. These assertions are shown more rigorously through advanced simulations in chapter 5 that determine the beam spot size on target.

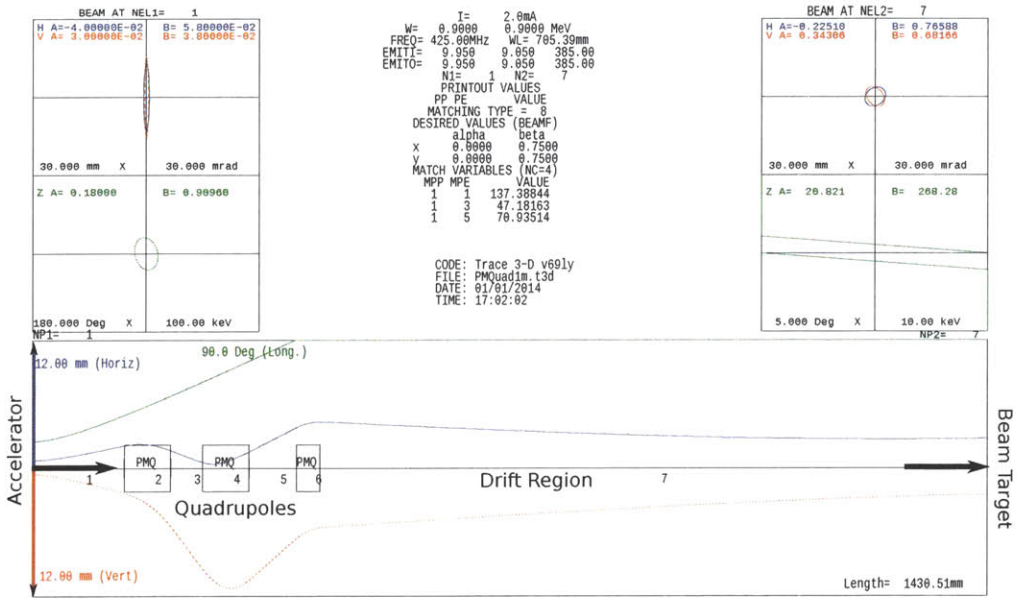

Figure 4-17: TRACE3D [29] simulation of the permanent magnet quadrupole optics demonstrates that the RFQ beam can be focused to a 1 cm diameter beam spot. Upper left: initial beam envelope, upper right: final beam envelope, bottom: plot of transverse vertical (red) and horizontal (blue) beam radius along the trajectory.

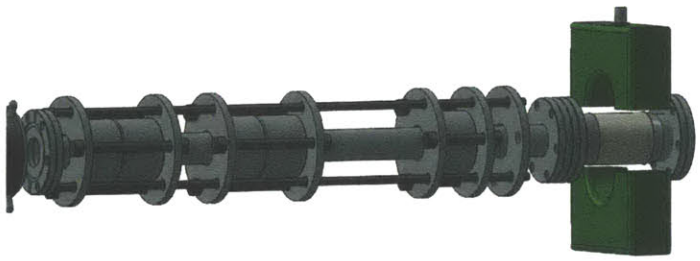

Figure 4-18: AIMS Beamline with three permanent magnet quadrupoles (gray components) for focusing and the toroidal current transformer (green).

4.6.1 Optical Sensitivity and Beam Characterization

The adjustment of the PMQ optics and the measurement of the beam's ellipse parameters require an understanding of the beam's sensitivity to the placement of the

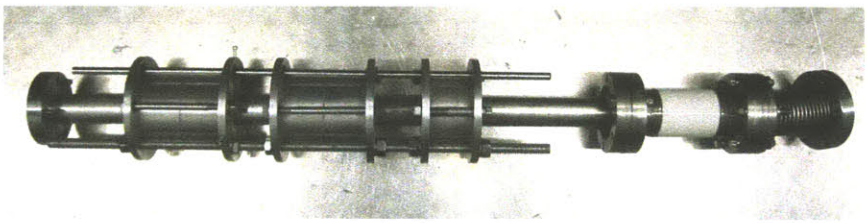

Figure 4-19: Photograph of the AIMS Beamline with permanent magnet quadrupoles for focusing. The white ceramic section to the right is the insulating break required for proper beam current measurement with a toroidal current transformer.

PMQs. Unlike standard electromagnetic quadrupoles, PMQ rely on proper positioning of the PMQ along the beamline to provide the desired focusing effect. The sensitivity of the PMQ positioning can be used for two purposes: 1) To quantify the amount the that the quads must be moved to observe a sufficiently large change in the beam dimensions to determine the ellipse parameters (discussed further in chapter 5. 2) To determine the uncertainty in the spot size of the beam due to error in the positioning of the PMQs.

The sensitivity study was performed using TRACE3D. First, using TRACE3D optimization routines, the positions for the PMQ triplet were determined for a 1 m straight trajectory that reaches its minimum diameter 1 m beyond the PMQ system (optimal spacing shown in table 4.2). Then, the positions of the PMQs were varied independently in increments of 5 mm. The resulting RMS beam width in the transverse directions x, y are plotted in figure 4-20. The ellipse parameter β and its sensitivity to PMQ position are plotted in figures 4-21 and 4-22 for both transverse dimensions.

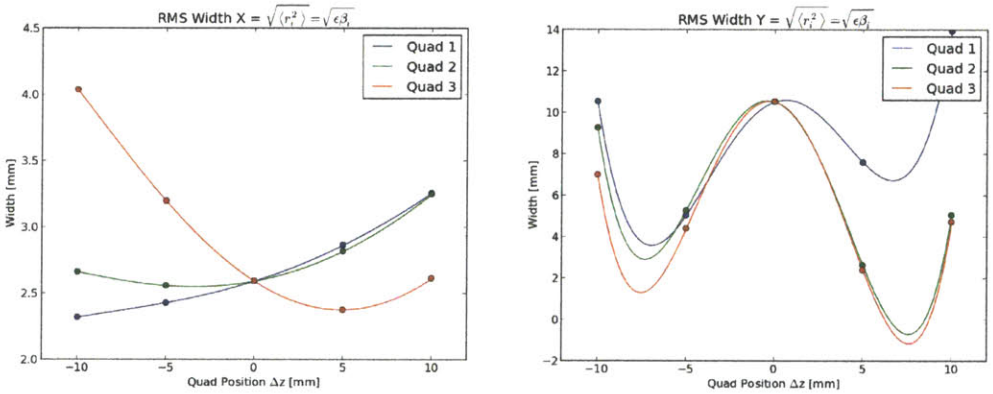

Figure 4-20: Right: RMS Beam width in x (horizontal) direction versus changes in quad position Δz. Left: RMS Beam width in y (vertical) direction versus changes in PMQ position Δz. $\Delta z = z - z_{\text{optimal}}$ is the relative position of the quad positions relative to optimal spacing given in table 4.2.

From these simulation results, since PMQ positioning uncertainties are likely to be < 1 mm, it appears that errors in PMQ positions are inconsequential to beam

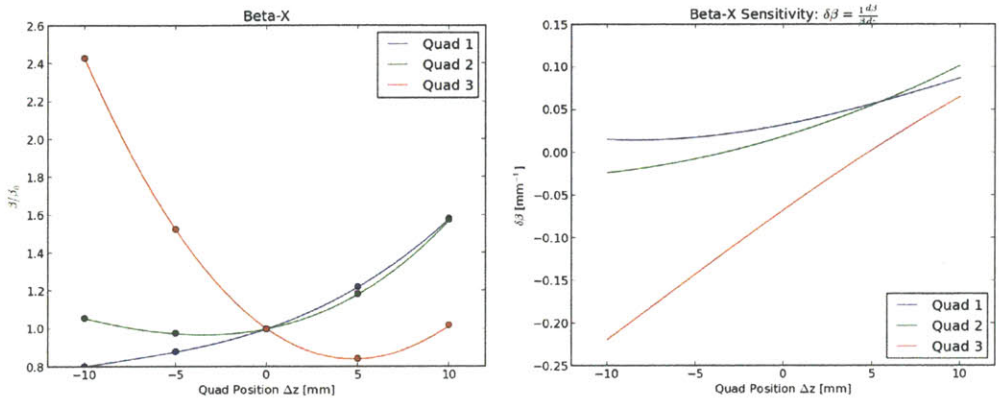

Figure 4-21: In the $x - x'$ phase plane: Relative changes in β and β-sensitivity due to changes in quad position z, where Δz is the perturbation from the optimal spacing given in table4.2.

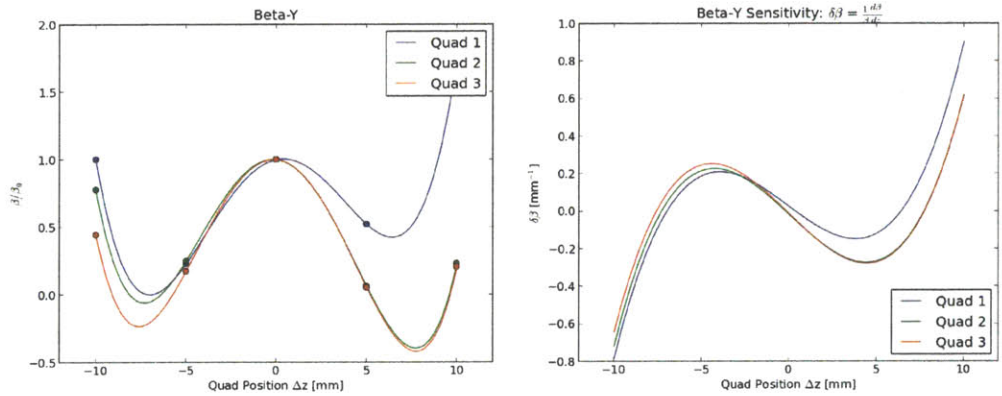

Figure 4-22: In the $y - y'$ phase plane: Relative changes in β and β-sensitivity due to changes in quad position z, where Δz is the perturbation from the optimal spacing given in table4.2.

focusing in this application of AIMS on C-Mod where spatial resolution of 20-30 mm is required. Also, these results indicate that pertubations of ± 1 cm in the PMQ positioning or greater would be required for adequate resolution in determining the ellipse parameters (discussed in section 5.5).

4.7 Beam Diagnostics

Modeling of beam dynamics is strongly dependent on accurate knowledge of beam energy and phase space distribution. All accelerator facilities use beam diagnostics characterize their beams. There is a set of well established techniques that can be applied a variety of applications, beam energy, beam current, and geometric constraints. However, compared to most IBA applications, AIMS is atypical in that the RFQ beam energy is relatively low while the instantaneous current is unusually high, but with low duty factor. For diagnostics that are used during the AIMS analysis, space is also extremely limited in the Alcator cell, so the development of innovative, compact, in-situ diagnostics was necessary.

4.7.1 Current Measurement

For any ion beam induced reaction, the reaction rate is directly proportional to the beam current. Likewise, the total number of reactions that are detected must be normalized to the number of particle that are incident on the target. It is therefore necessary to accurately measure beam current to 1) use as a figure of merit while testing an accelerator to describe beam quality and 2) throughout IBA measurements to integrate the total particles on the target. For initial testing of the accelerator (pre IBA experiments) a Faraday cup is the most accurate and straightforward way to measure beam current and serves as a benchmark for all other beam current measurements. For real time beam current monitoring during the AIMS experiments, current transformers are the best suited diagnostic because they non-perturbatively couple to the beam's magnetic fields without blocking the beam.

Faraday Cup

A Faraday cup is essentially a metal cup that is connected to an ammeter and is used as a beam target. For low energy accelerators with low average beam power ($\sim$ 1 Watt), Faraday cups are the simplest and most accurate way to measure beam current. This is extremely useful when testing the accelerator before installing it as a diagnostic or as a retractable device to be used between experiments.

The difficulty with Faraday cups is the suppression of secondary electrons that are emitted from the target surface as the beam perturbs the electronic structure of the target. 'Suppression' of secondary electrons simply means that the emitted are electrons are re-collected by the Faraday cup conductor so that the secondary electrons do not produce a net current that would interfere with the measurement. This is a significant issue because the secondary electron yield can be as high as several electrons per ion. Since the ammeter cannot distinguish between an absorbed ion and an emitted election, it is very important to suppress these secondary electrons.

Faraday cups are shaped like a cup to reduce the solid angle of emitted electrons so fewer escape the volume of the cup. This is insufficient for suppressing all of the secondary electrons so electric fields are typically used in addition. For DC accelerators this E-field is provided by a biased metallic structure or cage surrounding

the Faraday cup that is connected to a negative voltage source with ~100 V. This produces an E-field that repels the electrons (most having energies 0-50 eV) and directs them back into the cup in order to obtain an accurate beam current reading.

In the case of the DL-1, the beam is pulsed and has a low duty factor so a simple ammeter will not work for the measurement. However, since the instantaneous beam current from the RFQ is relatively high (~1 mA), the current in the Faraday cup can be measured from the voltage drop across a shunt resistor. This voltage drop can easily be measured with a 1 kΩ resistor using an oscilloscope or digitizer (from V=I·R, I = 1 mA/V).

When using the shunt resistor, the election suppression issue must still be addressed. Since the beam current is so high, however, electron suppression can be accomplished with a 100 kΩ resistor in series with with the Faraday cup and shunt resistor as shown in figure 4-23. For a 1 mA beam, the 100 KΩ resistor produces a 100 V potential on the cup which is sufficient for electron suppression.

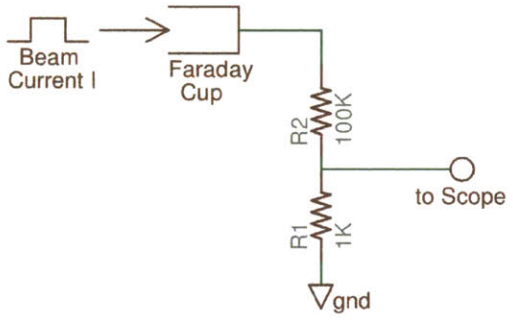

Figure 4-23: Circuit diagram for beam current measurement resistor (R1) and secondary election suppression resistor (R2).

4.7.2 Current Transformer

Current transformers are commonly used for in-situ beam current measurement. Typically, these transformers are toroidally wound coils with air or ferrite cores that encircle the beam. The beam acts as the primary "winding", inducing a signal in the toroidal secondary. For the beam produced by the DL-1, ferrite core transformers are the appropriate choice because of their compatibility with the beam's bunch size, their wide bandwidth and the simplicity of the required electronics. For further reference a tutorial on beam current measurement can be found in [56].

Bandwidth

The macro bunches can range from $10 - 100$ μs in length, separated by ~10 ms, with each macro bunch composed of micro bunches < 1 ns in length with a period 2.35 ns (1/425 MHz). A more detailed explanation of the beam's timestructure is given in section 5.1.1. For the purpose of current measurement for AIMS, it is sufficient to

say that the ~1 ns timescale is very challenging to measure and does not need to be resolved because: 1) the beam's micro structure is shorter than time scale of the beam the particle detection hardware and electronics, and 2) due to conservation of flux, the integral of the measured current trace should be the same regardless of the high frequency ns scale fluctuations in current.

In general, when measuring transient signals, the frequency bandwidth of the transformer is important in resolving the signal. By analyzing the Fourier transform of the signal, a current transformer can be chosen with the appropriate frequency domain parameters (low frequency 3dB cutoff, high frequency 3dB cutoff) to observe the harmonic content of the pulse.

For measuring macro bunches that are essentially square pulses, it is often simpler to choose a suitable transformer based on the time domain parameters of the beam pulse. Manufacturers of fast current pulse transformers often specify the time domain response of the transformers in two easily measurable quantities, the 'rise-time' and the 'droop'. As the name suggest, the rise time is the characteristic timescale that the voltage output from the transformer requires to respond to a step function in the current, typically measured in ns or μs. Likewise, the droop is the rate that the voltage signal droops when responding to step function in the current, typically measured $\%/\mu$s.

Observing that the rise time of the current trace from the Faraday cup is typically $3-5$ μs and the typical flat-top of the current waveform is 50 μs an transformer can be acquired the appropriate pulse specs. For the AIMS measurements, a "Pearson Electronics Wide Band Pulse Current Monitor, Model 4688, Ouput: 1.0 Volts per Amp" transformer was used because of its availability. The Model 4688 has a rise time of 12 ns and a droop of $0.4\%/\mu$s. This rise time spec is sufficient, but the droop spec is too high because it suggests that a 50 μs pulse would decay by 18% over its duration. However when testing this transformer with a pulser and oscilloscope, this spec from Pearson proved to be an extremely conservative estimate, with the measured droop being almost undetectable at ~0.01%.

Isolation and current path

The simplest location to put a current monitor is on the outside of the beamline so it does not have to be high -vacuum compatible. However, beamlines are typically made of conducting metals, most commonly stainless steel. Stainless is not a good conductor compared to copper but its conductivity σ is high enough to interfere with inductive current measurements due to current return paths in the beamline and attenuation of the beam's magnetic. Some form of electrical isolation is therefore necessary to prevent the beam measurements from being attenuated. The diffusion of the magnetic fields from the beam are limited by the beamline's conductivity which can be quantified by an exponential attenuation scalelength called the skin depth δ. For thin, conducting materials, equation 4.2 gives the value for δ where $\rho = 1/\sigma$ is the resistivity and ω is the angular frequency of the AC magnetic field B from the beam [20].

$$\delta = \sqrt{\frac{2\rho}{\mu\omega}}, \quad \frac{B}{B_o} = \exp\left(-\frac{t}{\delta}\right) = -8.69\frac{t}{\delta}\,[\mathrm{dB}] \tag{4.2}$$

With a stainless steel 1/16 inch diameter beam tube it is clear that some of the lower harmonics of the beam's magnetic fields will diffuse through the tube however, the higher harmonics will be severely attenuated and therefore cause significant distortion. Furthermore, if some or all of the beam current returns from the target back to the accelerator through the beamline, it will cancel the flux in the transformer from the beam causing the measured current to be substantially lower than the real current.

These problems are resolved by inserting an insulating section into the beamline with the current transformer on the outside. A grounding strap is also added on the outside of the transformer to provide the return path for the beam current. A schematic of the implementation of the beam current monitor is shown in figure 4-24.

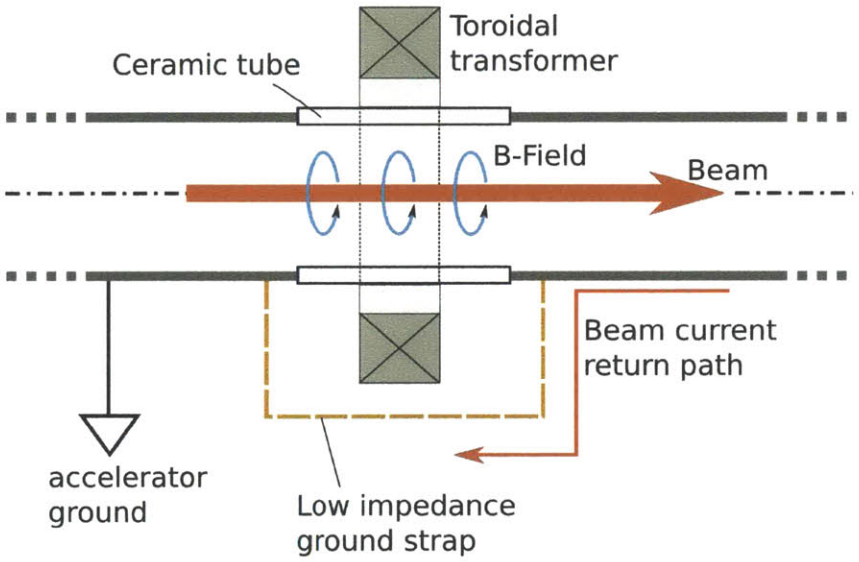

Figure 4-24: Schematic of beamline with current transformer for measuring beam current.

Implementation

Two methods were implemented to solve these issues. The first method – and the one used for the AIMS measurements – was to use a clamp-on transformer from Pearson Electronics (figure 4-25). This transformer was clamped on the beamline over the insulating break as shown in figure 4-18.

However, the clamp on transformer from Pearson tended to pick of noise from the Alcator cell and was not mechanically supported so it had to be removed before any plasma discharges. As a more permanent solution, an effort was made to develop

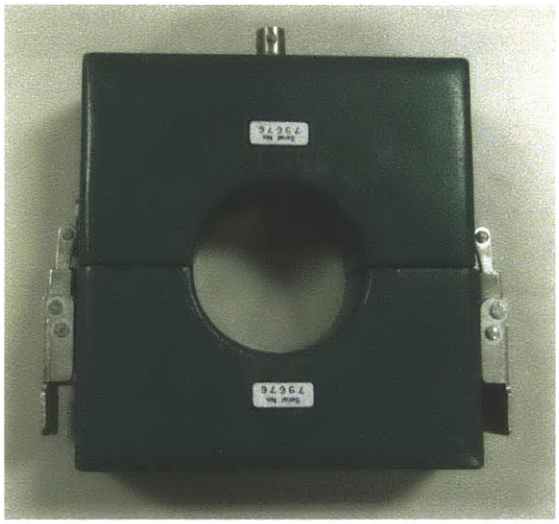

Figure 4-25: Clamp on transformer for beam current measurement. (Pearson Electronics, INC, Wide Band Pulse Current Monitor, Model 4688, Ouput: 1.0 Volts per Amp)

a transformer that could operate in vacuum and be integrated into the beamline so that the beamline would fully shield the transformer. A current transformer to fulfill this purpose was designed, built, vacuum baked, and tested, but was not installed due to time constraints.

High vacuum compatibility was required for the internal components of this transformer. An Amidon FT240J toroidal ferrite was used in this CT and was chosen because it contains no coatings and is designed for pulse signal applications. Alpha Wire 2841/1, 30AWG solid copper wire with Teflon insulation was used as it had been previously qualified for use in C-Mod vacuum and 431 turns (calculated) were wound around the ferrite. A CAD model and photograph of the in-vacuum CT are shown in figure 4-26. A oscilloscope trace of testing and calibration of the in-vacuum CT is shown in figure 4-27.

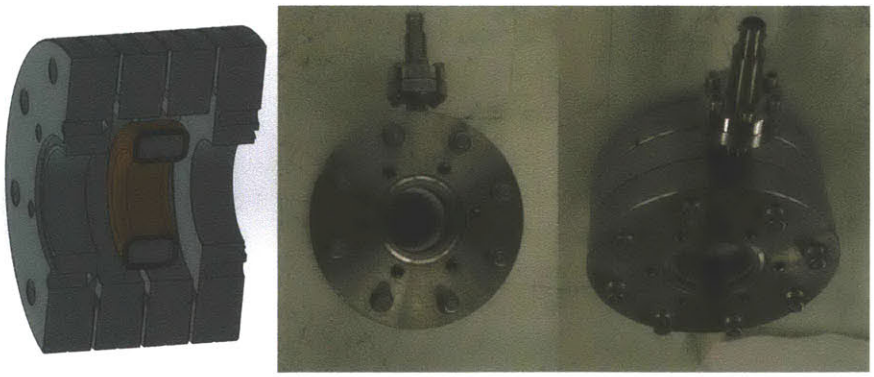

Figure 4-26: In-vacuum integrated current transformer for beam current measurement.

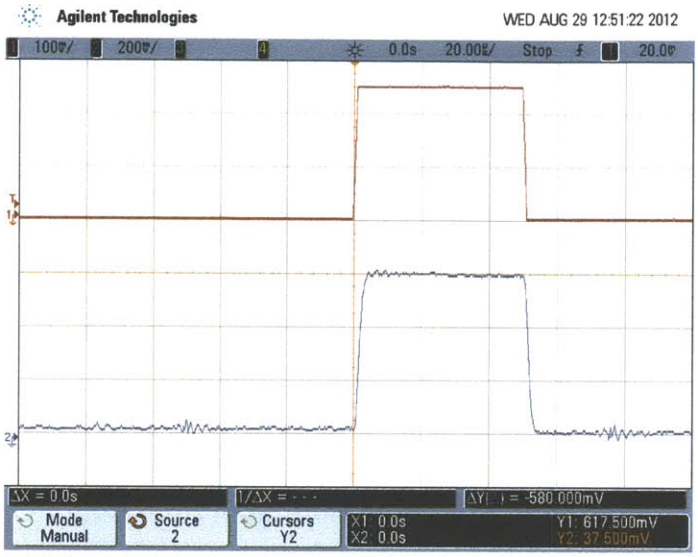

Figure 4-27: Calibration test of the in-vacuum CT for beam current measurement. The top red trace is 250 mV, 5 mA test pulse and lower blue trace is the 600 mV output from the in-vacuum CT and amplifier. The calibration factor is therefore 120 mV/mA

Amplification

Since the Pearson current transformer is calibrated to produce an output voltage of 1 V per amp of measured current, the output is typically less than 2 mV which is comparable or smaller than the electrical noise that is picked up in the cable between the transformer and the digitizer. To improve the signal to noise ratio, an amplifier with 100× gain was built and installed as close to the transformer as possible (< 1 m). In addition the amplifier circuit contained a 4 MHz low pass filter to remove high frequency noise pickup in the transformer and a 50Ω line driver ensure a high quality, impedance matched signal between the amplifier and the digitizer. A schematic of the amplifier circuit is shown in figure 4-28.

4.7.3 Uncertainty in Current Integration

Since the reaction yield is proportional to the total number of incident ions ($N_{ion} = Q/e$), it is important to quantify the error due to random fluctuations in the beam current integration and DC subtraction due to noise pickup. To determine N_{ion}, the total charge Q is determined by integrating digitized current waveforms from all of the beam pulses N_{pulse}. Therefore, the uncertainties in the integrated charge Δ_{pulse} from each pulse should be added in quadrature. However, since all of the beam pulses have approximately the same amplitude, duration, and associated error, the total uncertainty in charge integration ΔQ can be determined for large N_{pulse} using equation 4.3 by first calculating the uncertainty in a single typical current waveform Δ_{pulse}.

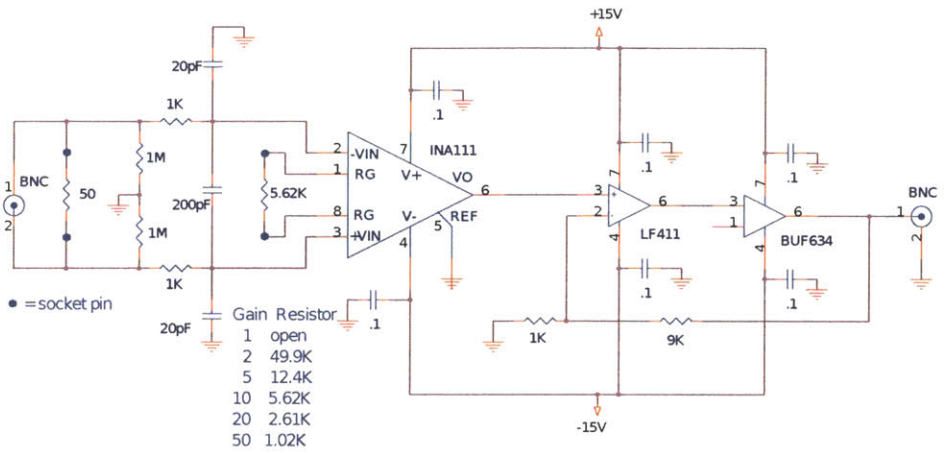

Figure 4-28: Fixed gain 100× amplifier with 4 MHz low pass filtering for current transformer signal.

$$\frac{\Delta Q}{Q} = \frac{1}{\sqrt{N_{\text{pulse}}}} \frac{\Delta Q_{\text{pulse}}}{Q_{\text{pulse}}} \tag{4.3}$$

Uncertainty in DC Subtraction

The DC subtraction routine uses the average $\bar{V}_{\text{DC}}$ of first N_{DC} bins of the digitized current signal to estimate the DC offset, then it subtracts this value from each bin in the waveform. Since $\bar{V}_{\text{DC}}$ is calculated from a series of voltage measurements V_o, each having random noise associated with them, the uncertainty in the mean $\bar{V}_{\text{DC}}$ is proportional to the standard deviation in voltage σ_{Vo} and $1/\sqrt{N_{\text{DC}}}$, given in equation 4.4. This means that the integral of each voltage waveform from the digitized current pulse has an uncertainty of σ_{DC} due to the uncertainty in DC subtraction.

$$\sigma_{\text{DC}} = \frac{\sigma_{V_o}}{\sqrt{N_{\text{DC}}}} \tag{4.4}$$

Uncertainty in Current Integration

The uncertainty in the integration of the current pulse also involves the sum of N_Q digitized voltage measurements V_q. However, it is difficult to distinguish the 'real' signal induced from the beam current from the electrical noise. Since the beam pulse is measured to be a smooth relatively low noise pulse in the laboratory, it is assumed that beam behaves similarly in the noisy C-Mod cell environment. Therefore, to calculate the uncertainty in the current measurement the assumption is made that the real voltage output from current transformer is a smoothly varying function of time for the duration of the pulse. The pulse is then fit to a polynomial function V_{fit} and the standard deviation with respect to the fit is quantified as the uncertainty σ_{Vq} in each digitized voltage V_q. A typical current waveform with voltage uncertainties is shown in figure 4-29.

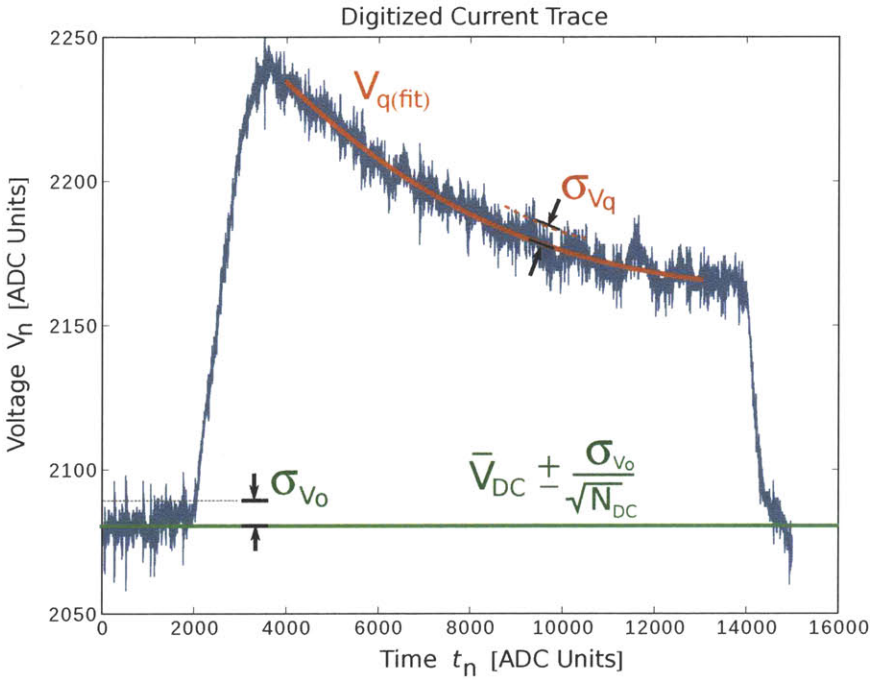

Figure 4-29: Typical digitized output from current transformer plotted with the mean DC offset $\bar{V}_{\mathrm{DC}}$, and uncertainties in digitized voltages σ_{Vq}.

$$\sigma_{V_q} = \sqrt{\frac{1}{N_{\mathrm{DC}}} \sum_{N_{\mathrm{DC}}} \left[V_o(t_n) - V_{\mathrm{fit}}(t_n)\right]^2} \tag{4.5}$$

Since there are N_q measurements, the uncertainty in the integrated charge in a single pulse $\Delta Q_{\mathrm{pulse}}$ with DC subtraction included is given by equation 4.6, where $\bar{V}_q = \langle V_q \rangle - \bar{V}_{\mathrm{DC}}$ is the average voltage during the pulse with DC subtracted.

$$\frac{\Delta Q_{\mathrm{pulse}}}{Q_{\mathrm{pulse}}} = \sqrt{\frac{1}{N_q}\left(\frac{\sigma_{V_q}}{\bar{V}_q}\right)^2 + \left(\frac{\bar{V}_{\mathrm{DC}}}{\bar{V}_q}\,\frac{\sigma_{\mathrm{DC}}}{V_{\mathrm{DC}}}\right)^2} = \frac{1}{\bar{V}_q}\sqrt{\frac{1}{N_q}\,\sigma_q^2 + \sigma_{\mathrm{DC}}^2} \tag{4.6}$$

Since 200 voltage samples determine the DC subtraction and there are >9000 samples in each pulse, the results from this analysis shows that the uncertainty from each pulse is quite small $\Delta Q/Q \simeq 0.0025$. This means that for a typical AIMS run containing $> 10^5$ waveforms, the quantifiable, random error in the current measurement should be vanishingly small as compared to typical Poisson uncertainty in the particle counts.

4.7.4 Energy Measurement of the RFQ Beam

The most common type of high resolution energy spectrometers for ~MeV ions are made with a large iron-core dipole electromagnets that produce an approximately uniform, well characterized magnetic field to measure the beam's energy from its

deflection. However for AIMS, this is not practical in the C-Mod cell because these magnets are large and can weigh as much several tons. Compact energy diagnostics are therefore necessary because of space limitations in the cell and in the vicinity of the beamline.

Calorimeter

Calorimeters provide the simplest method for measuring the average energy of the beam. Though calorimeters do not provide information about the energy distribution, they are a useful check to make sure that the beam is being accelerated and is close to the correct energy.

A beam calorimeter is essentially a thermally isolated beam target with a well characterized mass m and a known heat capacity C_p. From conservation of energy, the average beam energy is given simply by equations 4.7 and 4.8.

$$Q = mC_p\Delta T \longrightarrow \frac{dT}{dt} = \frac{\dot{Q}}{mC_p} \quad \text{where} : \dot{Q}[W] = I[A]\ E[eV] \tag{4.7}$$

$$\langle E[eV] \rangle = m\,C_p \int_0^t \frac{1}{I(t)} \frac{dT}{dt} dt \simeq \frac{m\,C_p}{\langle I \rangle} \frac{\Delta T}{\Delta t} \tag{4.8}$$

These equations assume perfect thermal isolation of the target. In reality, the target must be physically supported and must be designed to minimize losses due to conduction and radiation which tend to make the calorimeter measurement of beam power appear artificially low. Since the beam calorimeter must be used in vacuum, there is no convective heat transfer so the heat losses can be calculated straightforwardly. In the absence of convection, the heat losses Q_{loss} are calculated with equation 4.9.

$$\dot{Q}_{loss} = \frac{k\,A_c}{L}\left(T - T_o\right) + \sigma\epsilon A_s\left(T^4 - T_o^4\right) \tag{4.9}$$

For testing the RFQ beam, a calorimeter was designed and built using a cylindrical 3/4 inch diameter copper beam target suspended in vacuum by a 1/8 inch diameter stainless steel tube containing a thermocouple. Copper was chosen for the target because of its high thermal conductivity k that allows the target to maintain an approximately uniform quasi-static equilibrium temperature profile as it is heating. This ensures that measured temperature rise at the thermocouple contact point is representative of the increased thermal energy of the whole target. A CAD model and the completed calorimeter are shown in figure 4-30.

The dimensions and thermal properties used in this design were inputed into equation 4.9 to give the heat loss from the calorimeter as a function of absolute temperature T normalized to ambient temperature T_o in equation 4.10.

$$\dot{Q}_{loss}[W] = [0.3501]\left(\frac{T}{T_o} - 1\right) + [0.03965]\left(\left[\frac{T}{T_o}\right]^4 - 1\right) \tag{4.10}$$

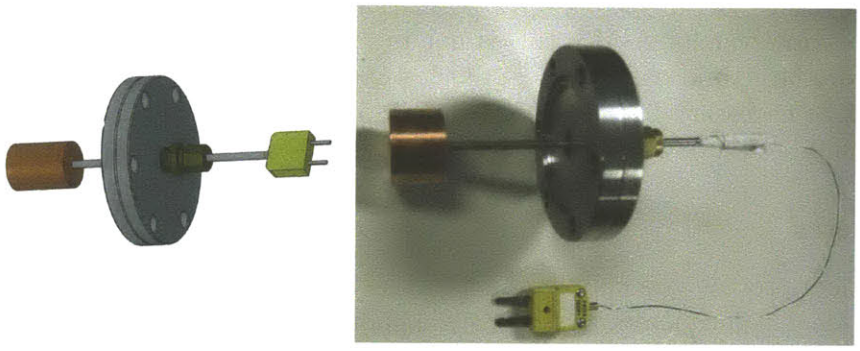

Figure 4-30: Vacuum insulated copper calorimeter design for measuring average beam energy. CAD model (left). Photograph of calorimeter before installation (right)

Both terms are similar in magnitude and are nearly linear near ambient temperature, as shown in figure in figure 4-31. Since the typical operating regime is between 0-20K above, ambient the heat loss is likely to produce ~3% error and can be can be accounted for in the measurement.

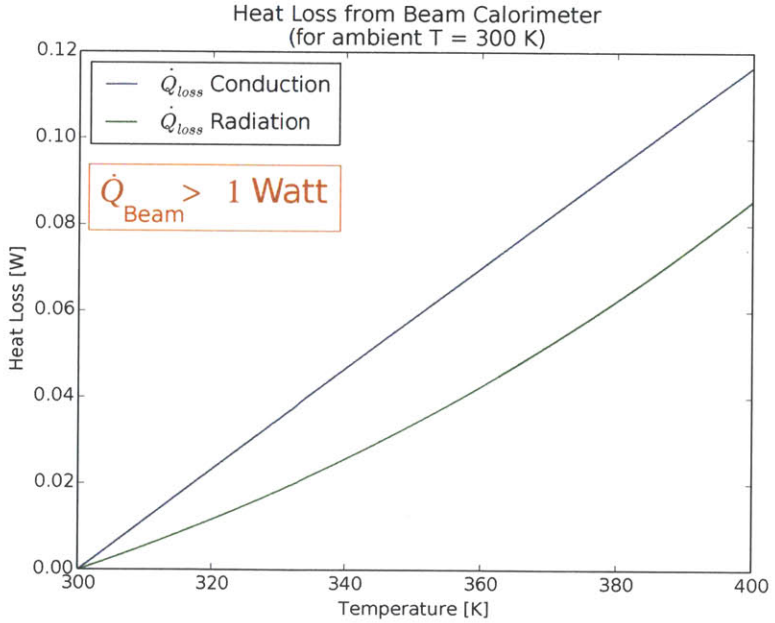

Figure 4-31: Heat loss mechanisms for the beam calorimeter are compared. Since most measurements are taken within 0-20 K above, ambient temperature the heat loss is small, and can be easily accounted for.

The calorimeter was installed on the RFQ on several occasions while the RF system was being tested. The results from three separate calorimetry measurements are shown in figure 4-32 with differing forward RF power, measured from the directional coupler on the RF amplifier's output. From these measurements it is clear that the

average beam Energy is substantially lower than the 900 keV beam energy specified in the DL-1 design. These results also demonstrate the strong dependence of the beam energy on RF power.

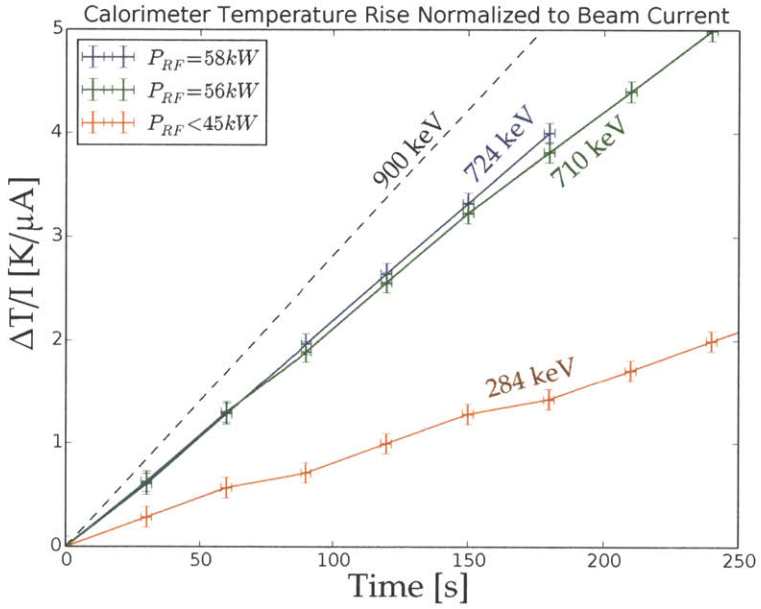

Figure 4-32: Calorimeter time traces are shown for three beam measurements with differing forward RF power measured at the amplifier output. The temperature $\Delta T = T(t) - T_{\text{ambient}}$ is normalized to beam current to show an equivalent comparison. The average beam energy inferred from average $\Delta T/\Delta t$ is displayed adjacent to each data set.

Thin-Film Rutherford Backscattering Spectrometer

A novel compact energy spectroscopy system was designed and built for AIMS based on Rutherford backscattering from a thin-film target inserted into the beam. Standard silicon charged particle detectors including the ORTEC 50-116V10 detector used in this device are compact and have good energy resolution (typically ~10 keV) and are therefore suitable to provide an energy spectrum for the RFQ deuterons. However, like most particle detectors, they are limited to instantaneous count rates of $10^4 - 10^5$ counts per second whereas, a 1 mA singly charged ion beam has a particle current of 6.24×10^{15} ions/sec. Attenuating the particle flux by more than 10 orders of magnitude is infeasible with apertures alone. Rutherford backscattering (RBS), however, can reduce the particle flux by as much as 6 orders of magnitude making the combination of RBS and apertures sufficient for lowering the count rate.

Using backscattered ions from a thick target is not necessarily straightforward because particles of a given energy backscatter with a continuum of energies because some particles slow down in the target more than others before scattering. This is

problematic because the detector resolution is not necessarily fine enough to properly deconvolve the beam's energy spectrum from the RBS spectrum. Instead a thin-film target can be used, as shown in figure 4-33.

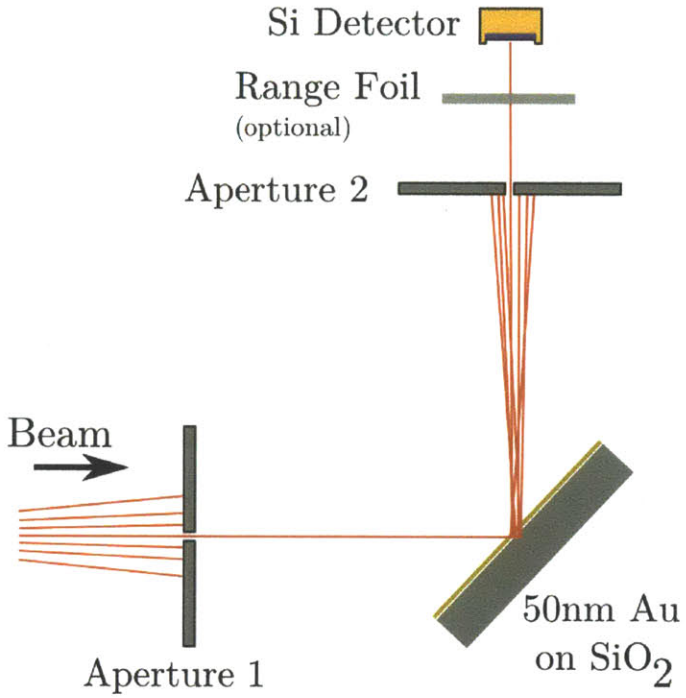

Figure 4-33: thin-film Backscattering Geometry

This is advantageous because when a particle of backscatters off of a thin-film it does not travel enough distance in the target to lose an appreciable amount of energy. Therefore, the backscattered energy is directly related to the incident energy by the kinematic factor κ which is an energy independent function of mass and scattering angle. This means that the thin-film RBS spectrum from a D^+ beam will directly give the beam's energy spectrum, scaled by a factor of κ. For deuterium ions scattering 90^o off of gold, $\kappa_{Au} = 0.9799$ so the scattering energy is nearly the same as the incident energy.

A thin-film backscattering spectrum is shown schematically in figure 4-34. Since it is difficult to produce a sufficiently thin, self-supporting scattering target, a thin-film supported by a substrate is a better choice because of its mechanical robustness. The target must be a high-Z/high-mass element, supported by a low-Z/low-mass substrate. The Z^2 dependence of the Rutherford cross section makes scattering from the film much more probable that the substrate and the mass difference creates a separation in energy between the thin-film peak and the continuum from the substrate due to the mass dependence of the kinematic factor. Using a range foil was considered to prevent the scattered ion from the substrate from reaching the detector to reduce the total count rate. This is problematic, however, because energy straggling in the foil is detrimental to the energy resolution of the technique. The effect of straggling is

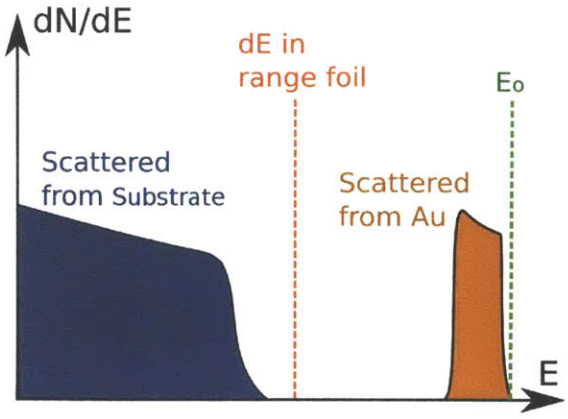

Figure 4-34: Schematic picture of the RBS from a thin-film of gold on a target substrate.

apparent in the straggling width for 900 keV D^+ passing through a range foil, shown in figure 4-35. Furthermore, using a range foil to remove a significant portion of the spectrum is not desirable because it reduces the dynamic range of the technique. After

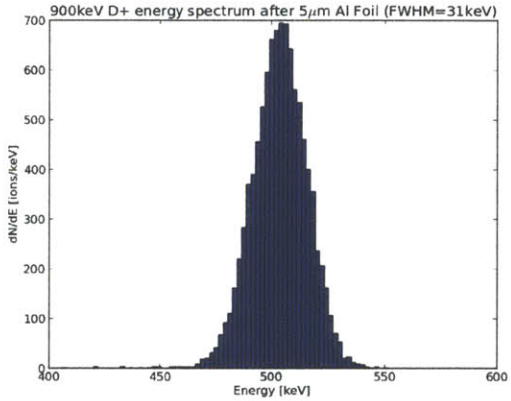

Figure 4-35: If range foils are used to remove backscattered particles from the substrate, straggling of D^+ Ions in the foil degrades the energy resolution. Straggling is shown for a 5 μm aluminum foil, calculated with SRIM [68]

analyzing the recoil spectra of deuterons off of various thin-film targets and substrates with SIMNRA [38], a predictive modeling code for RBS and nuclear reaction analysis, it was determined that the range foils could be avoided by using gold target films on low Z-substrates such as glass, carbon, or beryllium. A series of calculated RBS spectra for a variety of gold thicknesses on silicon dioxide (SiO_2) are shown in figure 4-36. Since gold on SiO_2 targets are readily available and 50 nm provide the sharpest peak with minimal scattering from the substrate, 50 nm gold targets were chosen for the spectrometer.

This novel design for a compact beam energy diagnostic was demonstrated using

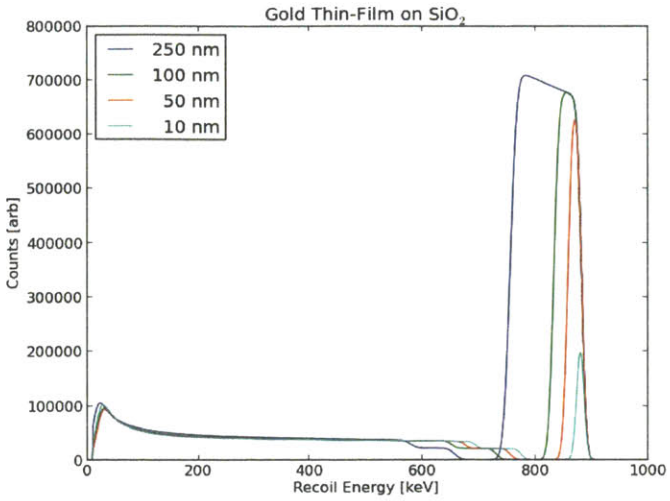

Figure 4-36: RBS Simulations using SIMNRA [38] show that that 50nm gold films on SiO_2 provide good energy resolution with relatively low counts from backscattering from the substrate.

SIMNRA [38], a reliable predictive modeling tool for IBA. It was then fabricated and is shown in figure 4-37. Time constraints and the failure of the DL-1's RF amplifier prevented the final implementation of the diagnostic. However, this is a critical diagnostic for AIMS and will be used in future AIMS implementations.

4.7.5 Beam Imaging

Methods for optically imaging the beam provide a useful tool aligning beamline components and setting up beam optics. The simplest way to image the beam is with a digital camera observing light from a scintillating target that intercepts the beam. Since the light output from scintillators is approximately proportional to the deposited energy, the light emission from the target (corresponding to brightness seen by the camera) provides an image that is representative of the transverse profile of the beam's current density.

A scintillation method was used for aligning the beamline and adjusting the PMQs for the AIMS diagnostic. For this implantation a quartz (SiO_2) vacuum window was used with a 45° mirror so the camera could be mounted perpendicular to beam. This was done due to space constraints and to avoid bombarding the camera with a high fluence neutrons forward directed neutrons from (d, n) reactions with SiO_2. An image of a typical beam spot exiting the accelerator is shown in figure 4-38 along with a CAD model and photograph of the diagnostic. This diagnostic was successfully used to align the RFQ beamline and verify the focusing quadrupole optics.

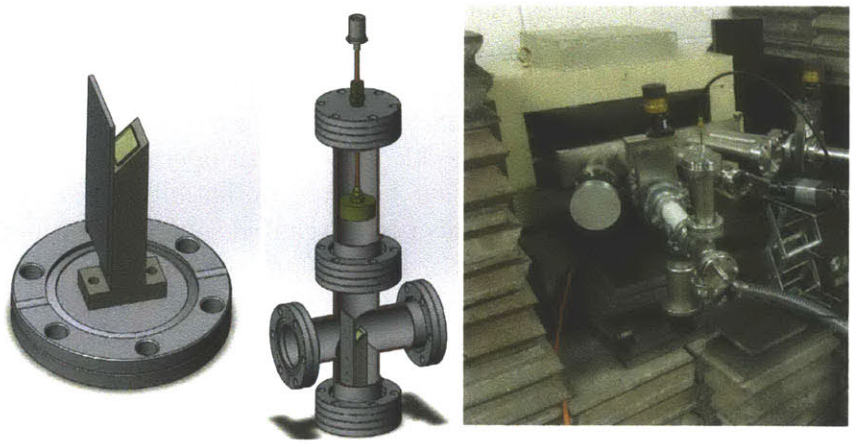

Figure 4-37: Implementation of a fixed target design for a thin-film backscattering spectrometer.

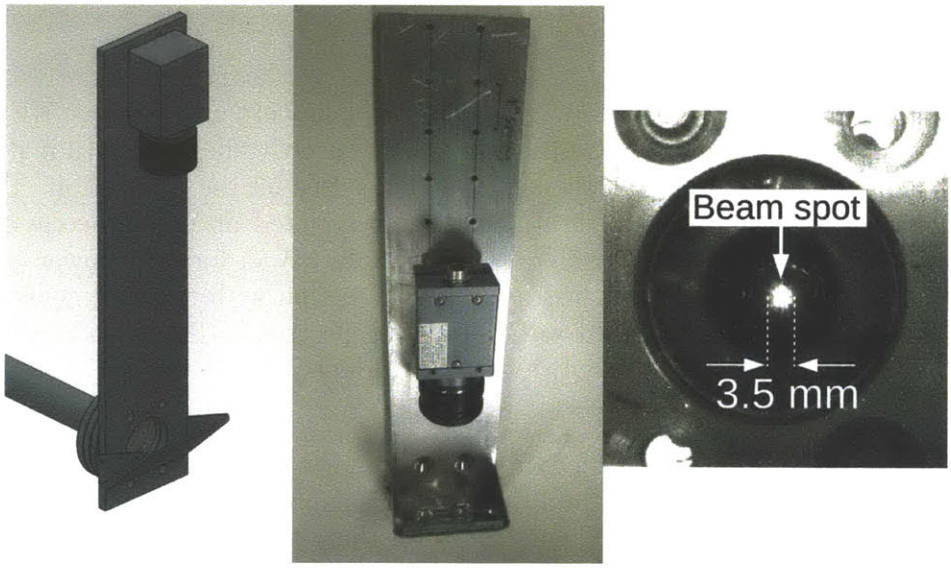

Figure 4-38: Compact beam imaging tool to align the beam with the beamline. A CAD model and photo of the beam imaging diagnostic are shown left and center. A photo (right) of the RFQ beam scintillating on quartz is shown on the right.

4.8 Beam Energy Correlation to RF Power

The RFQ physics and design principles dictate that RFQ acceleators should the produce nearly monoenergic beams of a specific energy (900 keV for the DL-1) if supplied with sufficient RF power and an ion beam that is matched to acceptance envelope of the cavity. However, neutron and gamma count rates, and the calorimeter measurements described in section 4.7.4 suggest that there is a strong correlation between the RF power coupled to the cavity and the average energy of the accelerated beam.

With RFQs at other facilities, detailed measurements of the energy distribution have demonstrated that if the RF cavity fields are substantially below its design requirements, the resulting beam distribution tends to be peaked at the design energy with broad low energy tail that can cause the average beam energy to be substantially lower than the peak [12]. The DL-1's RF system was operating with appropriate power levels for the cavity's specifications, however, potentially similar behavior was being observed. Since ion source alignment issues caused some difficulties in the DL-1 refurbishment, it is possible that poor matching between the ion source beam and the cavity acceptance contribute to improperly accelerated orbits or other anomalous RF dependent behavior, though this could not be confirmed.

Since the gamma count rates and the RF amplitude could be measured reliably but the beam energy could not be sufficiently characterized at the time of the AIMS measurements, a calibration curve f_{RF} was developed experimentally to relate the RF in the cavity A_{RF} to the gamma counts measured in the experiments $N_{\gamma,\mathrm{exp}}$, in the form of equation 4.11.

$$\frac{N_{\gamma,\mathrm{exp}}}{N_{\gamma}} = f_{\mathrm{RF}}\left(\frac{A_{\mathrm{RF}}}{A_{60\mathrm{kW}}}\right) \tag{4.11}$$

The RF field amplitude in the cavity as well as the forward and reflected RF power were measured during each AIMS measurement. The cavity field amplitude directly determines the energy coupled to the beam so it was used for the calibration. The RF amplitude A_{RF} was measured with a pickup loop mounted inside of the cavity and is normalized to the RF amplitude $A_{60\mathrm{kW}}$ at with 60 kW of forward power coupled to the cavity. This measurement was used in conjunction with measurements of the total gamma count rate summed over the entire spectrum. The data required to create this calibration curve was only available at lower RF amplitude so it had to be constructed from two types of measurements:

1. Direct Measurement: Data for direct measurements of gamma yield (summed over all energies) vs RF amplitude was available for cavity RF of 80-91% $[A_{\mathrm{RF}}/A_{60\mathrm{kW}}]$. Since the PFC conditions for these measurements were identical and the cross sections for the known (d,g) and (d,n) reactions increase roughly linearly with energy near 900 keV, the total gamma yield is approximately proportional to the beam energy.

2. Derivative Measurement: Above RF = 91% $[A_{\mathrm{RF}}/A_{60\mathrm{kW}}]$, data for direct comparison of an identical target was not available. However, since three RF readings were recorded for most AIMS runs, it was possible to calculate the derivative $d\dot{N}_{\gamma}/dA_{\mathrm{RF}}$ of the instantaneous gamma count rate $d\dot{N}_{\gamma}$ with respect to the RF amplitude within a each AIMS run. The derivative data was then fit with a polynomial, then integrated to give an approximate functional form for the roll-over and flat top of the curve which was not captured by the measurements from (1).

The data for measurements (1) and (2) are shown in figure 4-39. The direct measurements (1) were straightforward. The RF amplitude was increased from in steps

of 2% [$A_{\mathrm{RF}}/A_{60\mathrm{kW}}$] and the gamma spectra were integrated and normalized to the beam current, then the data were fit to a polynomial. The derivative measurements (2) were more complicated and are shown schematically in figure 4-40.

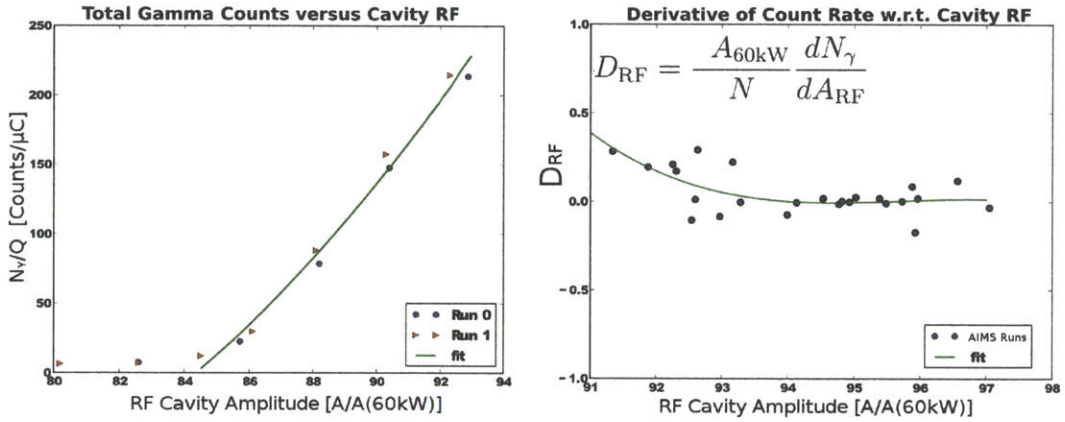

Figure 4-39: Data points and fit for direct measurement of RF amplitude versus gamma counts (left). Derivative of gamma counts N_γ with respect to RF amplitude measured within individual AIMS runs.

Since each AIMS run had up to 3 measurements of cavity amplitude, and the gamma measurements are in the form of pulses digitized as a function of time, the AIMS run could be divided in to smaller sections in time where the average count rate, average charge (for normalization), and average RF amplitude can be determined for each section. Even though the absolute boron counts cannot be compared between different AIMS runs since the targets were not necessarily the same, the derivate can be calculated from the averaged quantities with equation 4.12.

$$\frac{1}{Q}\frac{dN_\gamma}{dA_{\mathrm{RF}}} = \frac{\left(\frac{N_{\gamma 2}}{Q_2}\right) - \left(\frac{N_{\gamma 1}}{Q_1}\right)}{A_{\mathrm{RF2}} - A_{\mathrm{RF1}}} \tag{4.12}$$

After the derivatives were calculated, the were fit to a polynomial which was then integrated to give the functional form of the region of the calibration calibration curve where A_{RF} is high. These two curves from the direct fit and derivative fit were then joined by matching their amplitudes and derivatives. Then the curve was scaled such that it asymptotes to 1 as $A_{\mathrm{RF}}/A_{60\mathrm{kW}} \to 1$ and goes to zero with the experimental data at low $A_{\mathrm{RF}}/A_{60\mathrm{kW}}$. This calibration curve shown in figure 4-41 was critically important for removing the beam energy fluctuation in the results through calibration. It was therefore incorporated into the analysis described in chapter 2 and results in chapter 6.

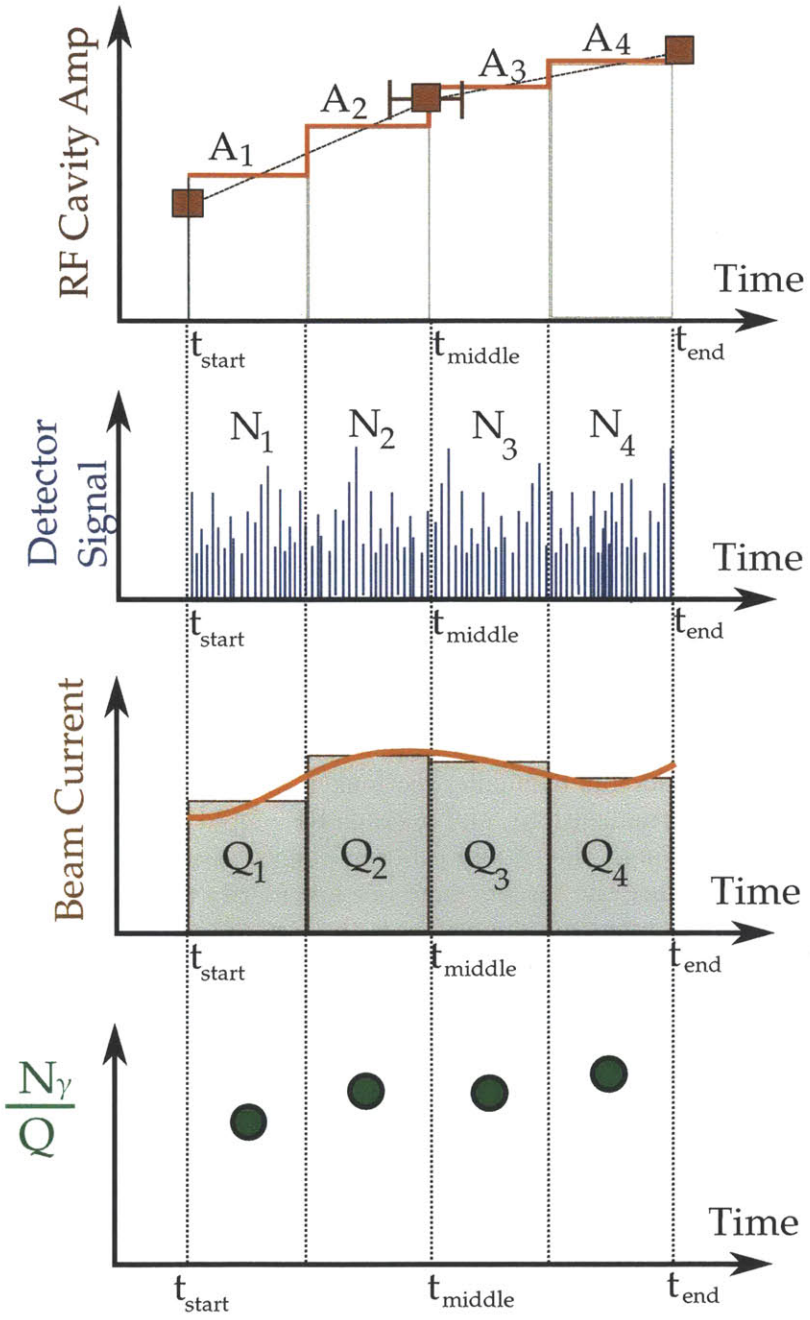

Figure 4-40: Illustration of the derivative measurements used for RF calibration. Each AIMS run is divided into regions where the average RF cavity amplitude A, average gamma count rate N, the integrated beam charge Q. The derivative can then be calculated from neighboring N_γ/Q points with respect to A

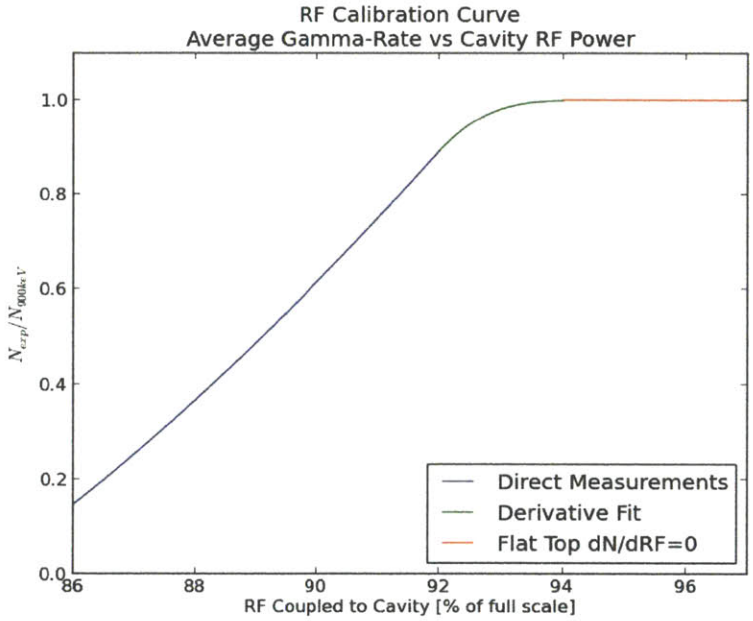

Figure 4-41: Calibration curve to correct for beam energy fluctuations due to changes in RF power. This curve gives the downgraded (expected) number of counts normalized to the ideal number of counts from a 900keV beam.

Chapter 5

Beam Dynamics and Control

One of the fundamental design goals of the AIMS diagnostic technique is to enable spatially resolved measurements of surface properties inside of fusion devices by localizing an injected ion beam onto the desired locations. To achieve this goal, the AIMS technique requires detailed modeling of the beam's trajectory and spot size on target to ensure reliable and quantitative measurements. Since the dynamics of beams in complex fields are not analytically solvable, computational beam dynamics modeling tools were developed and implemented as part of this thesis to provide beam control and to determine the spatial resolution and detection geometry of AIMS measurements.

The D^+ beam used for AIMS, like any charged particle beam, has a finite energy spread, transverse velocity components and finite spatial dimensions which must all be accounted for in the modeling. As the beam passes through the complex magnetic fields of the tokamak, the trajectory of the beam centroid must be calculated numerically in order to determine the location where it intercepts the PFCs. In addition, the evolution of all of the position and velocity components of the beam's distribution must be calculated to determine the spot size at the target PFC and, therefore, the spatial resolution of the measurement. The following sections describe the theory and implementation of the code used to analyze dynamics of the beam used for AIMS.

5.1 Beam parameters

A beam is generally characterized by a 6-dimensional particle distribution function $f(x, y, z, p_x, p_y, p_z)$. It is conventional to use the z direction as the propagation direction for the beam while x,y are the transverse directions. It is also typical to assume that has as small spread in position and momentum about the center of mass with a mean momentum p_{zo} that is much larger than the momentum spread in any of the transverse dimensions.

Beams produced by electrostatic accelerators are spatially continuous in the z direction whereas beams produced by RF accelerators are typically composed of particle bunches that are spatially localized in all dimensions, traveling at velocity v as shown schematically in figure 5-1. There are several parameters that are used to quantify the

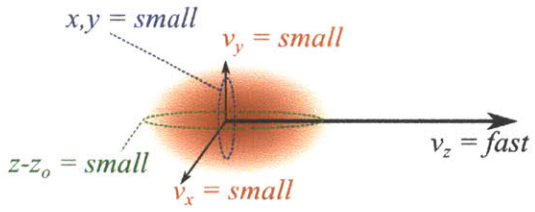

Figure 5-1: Simple illustration of a beam bunch traveling at velocity v_z

beam including the beam energy and momentum, current, time structure, emittance, and phase space distribution. It is important to fully define and understand these parameters to properly model the beam.

5.1.1 Beam Current and Time Structure

With beams from DC accelerators, the current is straightforwardly describes the average number of particles propagating in the beam. RF accelerators are distinctly different in that, the beam current is periodic on the timescale of the RF period and can be pulsed on longer timescales. It is common to discuss the structure of the beam current in the time domain because the 'time structure' of the beam provides an intuitive description of the instantaneous rate that particles arrive at a particular location. Typical values for the timescales of the beam from the DL-1 accelerator, used for AIMS, are given in table 5.1. From the time structure picture, the beam current can also be easily converted to the spatial distribution of the beam where a timescale t relates to length scale of a beam pulse $\ell = \beta ct$ as it moves through the lab frame at velocity βc which is useful for some applications.

Timescale	Symbol	Value [sec]
Micro-bunch width	τ_μ	$\sim 10^{-10}$
Micro-bunch period	T_μ	2.35×10^{-9}
RF period	T_{RF}	2.35×10^{-9}
Macro-bunch width	τ_{pulse}	5.00×10^{-5}
Macro-bunch period	T_{Beam}	1.66×10^{-2}

Table 5.1: Characteristic timescales for the DL-1 accelerator used for AIMS. Graphical definitions are given for the quantities in figure 5-2.

RF accelerators operate by accelerating micro-bunches of particles, each with charge Q and a width τ_μ, which is a fraction of an RF period T_{RF}. RF systems are often pulsed, creating macro-bunches that consist of a train of accelerated micro-bunches that are spaced in time by the micro-bunch period T_μ (equivalent to T_{RF}). These beam macro-bunches have a width τ_{pulse} and period of T_{beam}, or equivalently, a repetition rate of $1/T_{beam}$. The time structure of a typical beam in figure 5-2.

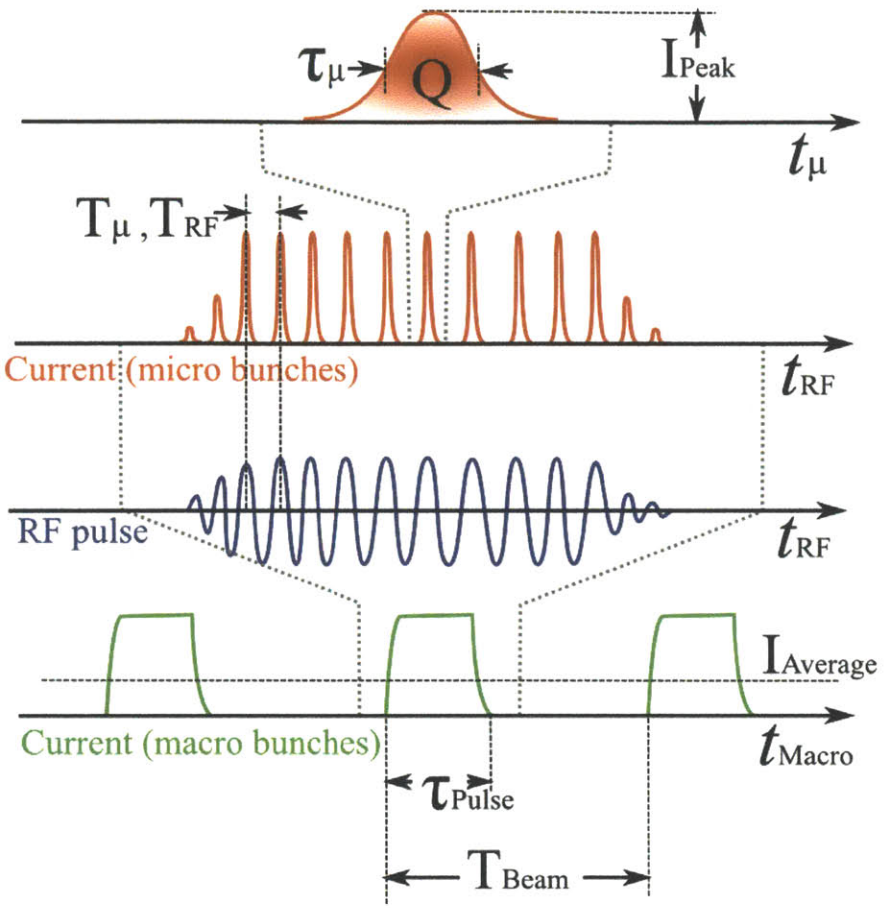

Figure 5-2: A schematic picture of the time structure of a pulsed beam from an RF accelerator. Timescales for the DL-1 RFQ are given in table 5.1.

The time structures of beams have obvious implications for synchrotrons, storage rings, and particle colliders because of the critical role timing plays in the acceleration, transport, and collisions of particles, but also has implications for IBA techniques like AIMS. The DL-1 RFQ used for AIMS has a high instantaneous current a low duty factor compared to any common IBA technique. The average current is related to the average current within a beam pulse by the duty factor D, defined in equation 5.1. The average current $\langle I \rangle_{\text{beam}}$ is related to the current during a beam pulse $\langle I \rangle_{\text{pulse}}$ and the charge Q in each micro-bunch.

$$D = \frac{t_{\text{on}}}{t_{\text{on}} + t_{\text{off}}} = \frac{\tau_{\text{pulse}}}{T_{\text{pulse}}} \tag{5.1}$$

$$\langle I \rangle_{\text{beam}} = D \langle I \rangle_{\text{pulse}} = D \frac{Q}{T_{\text{RF}}} \tag{5.2}$$

$$I_{\text{peak}} \simeq \frac{\Delta\psi}{2\pi} \langle I \rangle_{\text{pulse}} \tag{5.3}$$

These timescales are important to consider because the average current directly determines the time the detector will require to collect sufficient counts while the instantaneous current can lead to count rates that approach the limits of the detector. In addition, high peak beam current can complicate beam optics because space charge effects tend to cause unwanted expansion of the beam.

It is difficult to observe the micro-bunch structure because it requires current measurement with nanosecond resolution. In the case of AIMS, the micro-bunch structure can be ignored because the micro-bunches within a pulse arrive faster than the timescale of the gamma and neutron detection so, for practical purposes, the beam behaves like a DC beam during the pulse. For AIMS, the only consequence of the micro bunches is that the peak current I_{peak} is higher than the pulse current, affecting the space charge expansion of the beam. The peak current I_{peak} can be estimated in equation 5.3 from the range of RF phase $\Delta\psi$ that can support stable orbits in the accelerator and the measured current I_{pulse}. The quantity $\Delta\psi$ depends on the design of the accelerator and is necessarily less than on π/T_{RF}.

5.1.2 Energy and Momentum

It is necessary to measure the beam energy and/or momentum of beam particles to calculate the beams trajectory in E and B fields and to interpret the spectroscopic measurements from beam–target interactions. In addition, the momentum in the traverse direction becomes important when focusing and transporting the beam.

For low energy beams, the average kinetic energy per particle is used to describe the beam energy in units of electron volts [eV]. The beam's energy distribution is also important. Since most charged particle sources rely on thermal processes, the momentum distribution is typically assumed to be Gaussian which continues to be Gaussian as it is propagated through the accelerator system. An illustration of the beam distribution is shown for each position and velocity components is shown in 5-3. The general distribution function for a Gaussian beam with an average momentum vector $\mathbf{P_0}$, traveling in the Z direction with momentum p_{zo} are given equivalently by equations 5.4 and 5.5.

$$f(\mathbf{p})d^3\mathbf{p} = \frac{1}{\sqrt{2\pi\sigma^2}} \exp\left(\frac{(\mathbf{p}-\mathbf{p}_0)^2}{2\sigma^2}\right) \tag{5.4}$$

$$f(\mathbf{p})d^3\mathbf{p} = \frac{1}{(2\pi)^{3/2}\sigma_{px}\sigma_{py}\sigma_{pz}} \exp\left[-\frac{p_x^2}{2\sigma_{px}^2} - \frac{p_y^2}{2\sigma_{py}^2} - \frac{(p_z-p_{z0})^2}{2\sigma_{pz}^2}\right] \tag{5.5}$$

For any good quality beam, the momentum spread σ_p in the longitudinal direction (the direction of propagation) is much smaller the average momentum of the beam p_{z0}, so an expansion about p_{zo} (equation 5.6) shows that the longitudinal distribution can also be approximated as Gaussian in energy E. The important consequence of this expansion is that simple beams can be assumed to be Gaussian in both longitudinal momentum and energy.

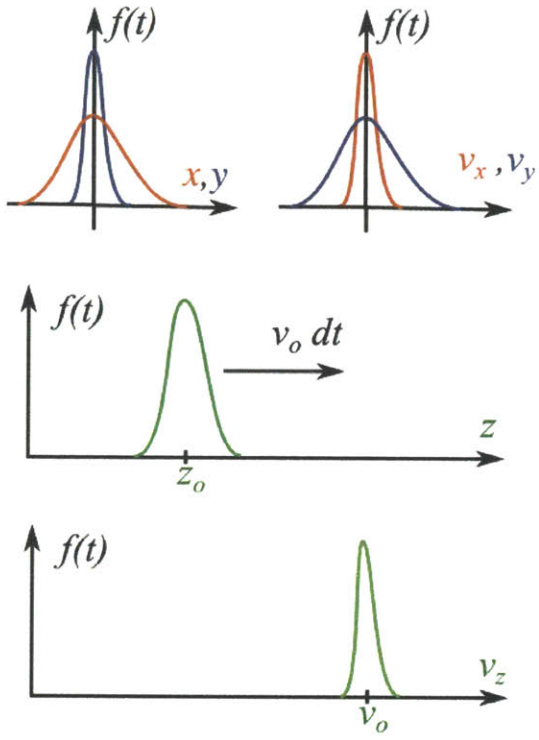

Figure 5-3: Simple illustration of a particle bunch's Gaussian distribution in all spatial and velocity dimensions. The distribution in each dimension has a characteristic width that evolves in time as the beam propagates in the z direction.

$$p_z - p_{zo} = \sqrt{2m(E_0 + \Delta E)} - \sqrt{2mE_0} \simeq \sqrt{2mE_0}\,\Delta E, \quad \text{for}: \frac{\Delta E}{E_0} \ll 1 \tag{5.6}$$

$$f(p_x, p_y, E) = f(p_x, p_y)\frac{1}{\sqrt{2\pi\sigma_{pz}^2}} \exp\left[-\frac{m}{2E_0}\frac{(E - E_0)^2}{2\sigma_{pz}^2}\right] \tag{5.7}$$

This means that the longitudinal momentum $\Delta p/p$ is proportional to the energy coordinate $\Delta E/E$ so they can be used interchangeably, differing only by a numerical factor of $1/2$ for non-relativistic beams. This fact is useful because magnetic beam optics such as quadrupoles, sector magnets, and B-fields in general are analyzed most naturally in momentum coordinates while accelerating structures are typically analyzed with potentials and energy coordinates. This is also true for a relativistic beams where the beam's total energy E from the relativistic Hamiltonian is more commonly used (equation 5.8) where the relationship between energy and momentum coordinates is given by 5.9.

$$\mathcal{H} = eV + \sqrt{(c\mathbf{p} - e\mathbf{A})^2 + m^2c^4} \longrightarrow E = \sqrt{c^2p^2 + m^2c^4} \tag{5.8}$$

$$\frac{\Delta p}{p} = \frac{\gamma}{1+\gamma}\frac{\Delta E}{E} \tag{5.9}$$

5.1.3 Beam Distribution in Phase Space

As described in the previous section, most simple beams produced by RF accelerators have approximately distributions Gaussian in momentum. Since the spread in momentum tends to cause the particles to spread in spatial extent, it is typical that beams can be assumed spatially Gaussian as well. When using linear models to calculate the evolution of these beams, the distribution also remains Gaussian as the beam is transported or accelerated.

In many cases it is sufficient to model the beam more simply as an envelope surrounding the beam distribution. For distributions of particles, where particles and momentum are conserved, Liouville's theorem asserts that the phase volume in position-momentum phase space occupied by the distribution remains constant. As a direct consequence, a distribution can be represented by surfaces enclosing conserved phase volumes regardless of the shape of the distribution. For simple distributions (e.g. Gaussian in spatial dimensions and in momentum), ellipsoidal envelopes can be used to model the beam in each phase plane, described in more detail in section 5.1.5. In addition, the entire distribution can be modeled as a 6-dimensional ellipsoid that is centered about a coordinate system (section 5.1.4) that moves with the beam centroid along an ideal trajectory.

To model the evolution of the distribution, semi-analytic methods are used. The equations of motion of single particles in the fields of the transport system are linearized and then used to derive matrix transformations that can be applied to the entire distribution. The transformations can either represent the net effect of single components or a series of transformations that are applied iteratively to model complex field geometries.

These linear transformations are referred to 'transfer matrices'. These transfer can also be self consistently applied to an envelope function enclosing the entire distribution in 6-dimensions, particularly if the envelope is assumed to be ellipsoidal. An illustration of how the beam envelope relates to the evolution of the beam in z is shown in figure 5-4. A more in depth description these transformations and beam envelopes are described in sections 5.2 and 5.3.

5.1.4 Phase Space Coordinate System

To model beam dynamics in a complicated geometry it is important to establish an appropriate coordinate system. The most convenient choice is a curvilinear orthogonal coordinate system that follows the ideal trajectory of the beam's centroid (referred as Frenet-Serret coordinates, shown in figure 5-5). This system maintains a direction z that is parallel to the trajectory and a transverse plane that is perpendicular to the trajectory, spanned by orthogonal directions x, y. The unit vectors representing these directions are listed below in 5.10 [58].

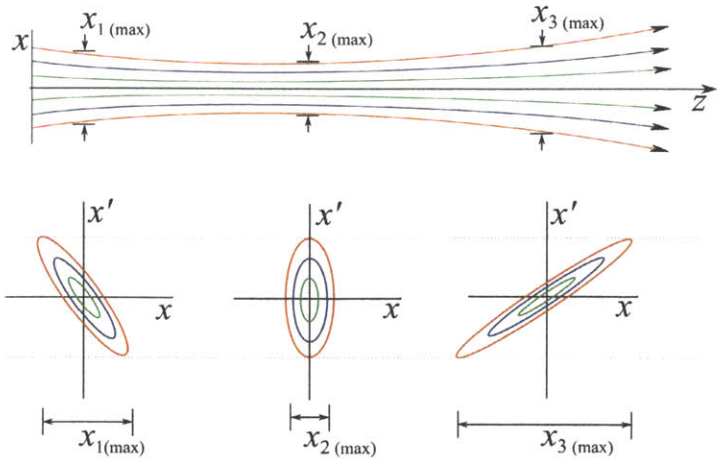

Figure 5-4: Illustration of the beam envelope in the transverse position-momentum x-x' phase plane. An initially converging beam is shown drifting in z. The minimum transverse dimension at x_2 is due to space charge forces and non-laminar effects of the beam. The x coordinate represents the spatial width of the beam and x' coordinate is the canonical momentum x' in the x direction, equivalent to the beam's angular width and analagous to the beam's transverse velocity.

$\hat{\mathbf{u}}_z(z)$	position unit vector $\parallel$ to trajectory
$\hat{\mathbf{u}}_x(z)$, $\hat{\mathbf{u}}_y(z)$	orthogonal position unit vectors $\perp$ to trajectory
$\hat{\mathbf{p}}_z(z)$	momentum unit vector $\parallel$ to trajectory
$\hat{\mathbf{p}}_x(z)$, $\hat{\mathbf{p}}_y(z)$	orthogonal momentum unit vectors $\perp$ to trajectory

(5.10)

Since the beam (relativistic or not) interacts with fields and components that are stationary in the lab frame and are typically time invariant on the timescale of a particle transit, canonical momenta $u_i'(z) = du_i/dz$ are a more convenient coordinate choice than velocity. They provide a more natural choice of coordinates because they relate directly to the spatial variation of the beam transport system in z, are appropriately time invariant, and normalize out the relativistic effects which can be incorporated into the parameters of the transfer matrices.

Another useful interpretation is the following: It is more convenient to solve for motion of particles in terms of a "trace equation" in the form $d^2x/dz^2 = f(z)$ which gives particle's trajectory rather than an "equation of motion" in the form $d^2x/dt^2 = f(z,t)$ which gives the particle's position as a function of time. As such, the forces and momentum coordinates are transformed to be canonical time invariant and are used in the solutions the trace equation.

The magnitudes of the transverse canonical momenta are defined as $x'(z) = dx/dz$ and $y'(z) = dy/dz$. The transverse momenta effectively cause a deflection angle with respect to the ideal trajectory. Since p_x and p_y are generally orders of magnitude smaller than the total momentum p_0 the simple approximations shown in (5.11,5.12)

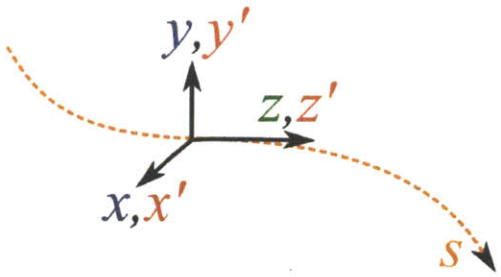

Figure 5-5: Frenet-Serret coordinates: curvilinear coordinate system maintaining two transverse coordinates x and y and the longitudinal coordinate z with respect to the ideal trajectory s.

give the relationship between momentum and canonical momentum shown in (5.13) to a high degree of accuracy despite the approximation. From 5.11 and 5.12, it also follows that x' and y' have units of radians. This is analogous to the paraxial approximation commonly used with charged particle beam optics.

$$x' = \tan(d\theta_x) \approx d\theta_x \tag{5.11}$$

$$\frac{p_x}{p_0} = \sin(d\theta_x) \approx d\theta_x \tag{5.12}$$

$$p_x \simeq p_0 x' \ , \ p_y \simeq p_0 y' \quad \text{for } p_{x,y} \ll p_0 \tag{5.13}$$

The longitudinal coordinates are important to consider because of the momentum dependent dispersive effects caused by a non-uniform beam distribution. For transport systems that use magnetic steering and focusing, it is most useful to define longitudinal momentum as $\delta = \Delta p/p_0$ and longitudinal position as a length $\ell = z - z_0$ relative a to beam centroid. For RF accelerators, where the average RF potential during a particle's transit directly relates to the change in kinetic energy, it is more useful to convert from the momentum or energy coordinate to a phase angle ψ relative to the synchronous RF phase of the accelerating structure. For reference, a vector representing a location in phase space is defined in general by equation 5.14 and in matrix form in equation 5.15.

$$\vec{\mathbf{u}}(z) = x\,\hat{\mathbf{u}}_x + y\,\hat{\mathbf{u}}_y + \ell\,\hat{\mathbf{u}}_z + x'\,\hat{\mathbf{p}}_x + y'\,\hat{\mathbf{p}}_y + \delta\,\hat{\mathbf{p}}_z \tag{5.14}$$

$$\vec{u} = \begin{bmatrix} x\ (m) \\ x'\ (rad) \\ y\ (m) \\ y'\ (rad) \\ \ell\ (m) \\ \delta\ (rad) \end{bmatrix} \tag{5.15}$$

5.1.5 Ellipse Parameters

Simple distributions such as Gaussians can be described by a characteristic width such as σ_{RMS}, FWHM, etc. When the distribution is projected onto any phase plane, the width parameter will trace out an ellipse in the plane. In addition, a non-collisional, dense distribution of any shape that can be enclosed by an ellipsoid can be represented by that ellipsoid because of Liouville's theorem. As such, ellipses and ellipse transformations are well suited to model beam distributions.

Twiss Parameters for Ellipses

Any 2-D ellipse centered about the origin can be uniquely specified by three parameters. A fourth parameter ϵ is typically factored out of three parameters to reflect the area of the ellipse. This set of four parameters α , β , γ , ϵ are called "Twiss parameters" and are defined on the x-x' phase plane by equation 5.16.

$$\gamma x^2 + 2\,\alpha x x' + \beta x'^2 = \epsilon \tag{5.16}$$

$$\beta\gamma - \alpha^2 = 1 \tag{5.17}$$

In this form β and γ determine the eccentricity, α determines the inclination angles of the axes of the ellipse, and ϵ is equal to $1/\pi$ times the area of the ellipse. Since only three parameters are required, equation 5.17 relates α, β , and γ. Some useful relationships between the Twiss parameters and ellipse geometry are shown in figure 5-6.

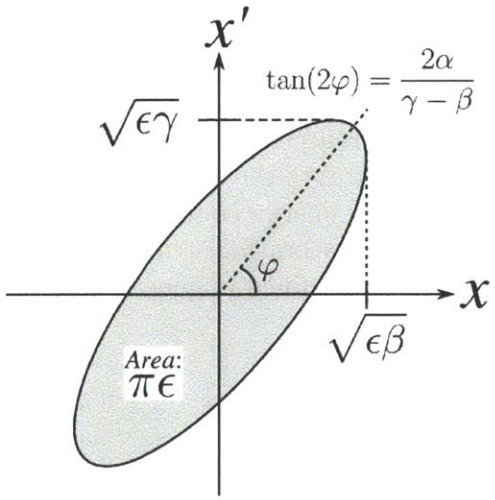

Figure 5-6: Ellipse geometry relationships for Twiss parameters of envelope functions.

Phase Incompressibility and Emittance Conservation

The ellipse parameter ϵ is called the emittance and is important because it represents the phase space volume (or area in 2-D) enclosed by an envelope surrounding the distribution. The physical consequence of ϵ is that it quantifies the simultaneous spread in position and momentum, thus quantifying the 'disorder' contained within a distribution. For example, the minimum focal spot size of a beam is limited by the emittance. This fundamental limit on beam focusing makes large ϵ beams much more difficult to accelerate and transport and low ϵ beams desirable.

An important characteristic of ϵ is that, in the absence of acceleration, it is a conserved quantity under a wide range of beam optics components and electromagnetic fields if the applied forces can be linearized. The 2-D definition of ϵ is given in equation 5.18 and can be generalized by integrating over all N dimensions.

$$\epsilon_x \equiv \iint \frac{1}{\pi} dx' dx \quad [\pi\ m\ rad] \tag{5.18}$$

Though emittance ϵ is not conserved with acceleration, there is another quantity called normalized emittance $\epsilon_N = \beta\gamma\epsilon$ that is conserved (where β and γ are the relativistic factors, not ellipse parameters). This is important because the conservation of β_N, starting from the ion source and propagating through the accelerator components, indicates that the emittance of the final beam is a fundamental parameter set by the accelerator hardware that cannot be improved and can only be worsened by non-linearities in accelerator components [23].

Now that the useful properties of the emittance have been stated, the use of ellipsoidal envelope functions must be justified. This justification is provided by Liouville's theorem which states that the phase volume that a distribution occupies is conserved under the following conditions which are typically satisfied by particle beams [24]:

1. The particle distribution must be dense, having a large number of particles $N \ggg 1$ contained within a relevant phase volume.

2. The beam must be non-collisional with forces varying smoothly in space and time.

3. Velocity dependent frictional forces within the beam must be negligible.

The validity of Liouville's theorem is derived rigorously in [24] and [58]. This conservation principle, often called 'phase incompressibility', implies that if a boundary is defined for a phase volume containing the distribution, and boundary transformed by the same physics as the particles that it contains, the particles will necessarily remain within that boundary. This result provides the justification for using an envelope function to model the whole distribution.

For most beams, including the beam used for AIMS, all of the Liouville criteria are satisfied so an envelope function is appropriate. Using ellipsoidal envelope functions, the emittance ϵ is therefore equivalent to the phase volume and is conserved when the

forces are linear with position. Though Liouville's theorem does not require linear forces, the forces must be linear for the envelope to remain in the shape of an ellipsoid. In the case of non-linear forces the ellipse becomes distorted requiring a larger ellipse to contain the same volume of the distribution. This expansion of the envelope to fit the skewed distribution is referred to as emittance growth and is typically avoided because it is non-reversible and effectively reduces the quality of the beam [23].

As a practical consequence, if linear transformations can be used to apply fields and forces to single particles, the same transformations can also be applied self consistently to the envelope of the distribution (described in section 5.3.1). If the forces in each direction are uncoupled, each phase plane can be transformed independently, conserving emittance $\epsilon_x, \epsilon_y, \epsilon_z$ in each plane. Furthermore, even if forces are coupled, the 6-D envelope defining a characteristic width of the distribution in all of its dimensions can be transformed, conserving the phase volume of the distribution.

5.1.6 Beam Generated Force and Emittance Force

Beam generated forces such as space charge repulsion and the effects of emittance lead to fundamental limits on the beam transport system. It is therefore instructive to study these limits intuitively and analytically to guide the computational efforts described in the following sections.

Electromagnetic forces that are generated within the beam can have a significant impact on the beam's dynamics, especially for low energy, high current ion beams. The charged particles that make up the beam repel due to the Coulomb force causing the beam to expand. The beam's current also produces a magnetic field that counteracts the E-field reducing the expansion. The resulting changes to beam evolution are generally referred to as space charge effects. As the beam energy increases, the ratio of B_θ/E_r scales like $(v/c)^2$ causing space charge effects to be most significant at low energies and negligible as the beam becomes highly relativistic [25].

A realistic beam with a finite emittance is non-laminar. This limits the minimum focal spot size of the beam and generally affects beam transport. Though the non-laminar mechanism is much different than space charge expansion, the effects on the beam envelope are similar as illustrated in figure 5-7. Both the non-laminar effects and the space charge will cause a collimated beam to expand and will limit the minimum diameter of a focused beam. As a result, the expansion due to emittance can be quantified by introducing an emittance force $F_{\text{emittance}}$.

For beam transport systems, the effects of space charge require numerical solutions. However, it is useful to quantify the relative importance of space charge with a dimensionless parameter K called the perveance that appears in the equation of motion for simple beams.

In deriving the radial equation of motion for particles in a non-laminar cylindrical beam with beam generated electromagnetic forces (specifically, Coulomb repulsion and magnetic compression), two force terms appear as shown in equation 5.19 [25]. With a beam at constant energy, this equation of motion can then be converted to canonical coordinates recognizing that $\frac{d}{dt} = \beta c \frac{d}{dz}$ from the chain rule, where R is the

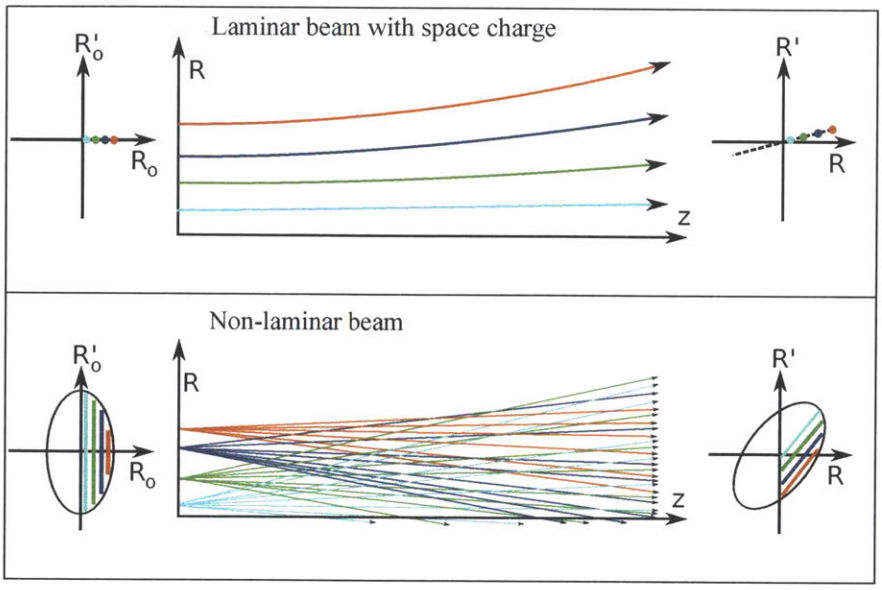

Figure 5-7: Top: particle trajectories within a high-current, laminar beam where space charge dominates. Bottom: particle trajectories within an non-laminar beam with finite emittance. Where R and R' are the transverse position and momentum coordinates of a beam with circular cross section. Initial and final transverse phase-space beam envelopes are shown on the left and right, respectively.

radius of a circular beam and β,γ are relativistic factors.

$$\frac{d}{dt}\left(\gamma m_o \frac{dR}{dt}\right) = \frac{eI}{2\pi\epsilon_o \beta c \gamma^2}\frac{1}{R} + \frac{(\gamma m_o v_z^2)\epsilon^2}{R^3} \quad \longrightarrow \quad \frac{d^2R}{dz^2} = K\frac{1}{R} + \epsilon^2\frac{1}{R^3} \tag{5.19}$$

The term containing K (defined in equation 5.20) corresponds to the effects of space charge while the term containing ϵ corresponds to the non-laminar effects related to the emittance ϵ.

$$K = \frac{qI_{peak}}{2\pi\epsilon_o m_o(\beta\gamma c)^3} \tag{5.20}$$

If the beam is laminar, meaning that ϵ is negligible, the remaining term containing perveance K, which is proportional to the charge density of the beam, will determine the minimum focal size of the beam. Likewise, if the K is negligible, the emittance effects will dominate and will be the primary limitation on focusing. Equation 5.19 also lends itself to analytic solutions in these regimes for certain special cases described in [25].

Since real beams have non-zero emittance and always contain charge, it is informative to compare K to the emittance ϵ (from section 5.1.5). Comparing the two quantities can therefore determine which is the dominant effect limiting the minimum beam spot size and, consequently, can determine where which of the effects are important to model for a specific application.

Since the emittance term has a $1/R^3$ dependence and ϵ is constant, while the

space charge term has a K/R dependence, and both terms behave like forces, the relative importance of K and ϵ can been compared with the dimensionless ratio given in equation 5.21, where $F_{\text{emittance}}$ is the effective 'emittance force' caused by the non-laminar effects and F_{charge} is the beam generated space charge force.

$$\frac{F_{\text{emittance}}}{F_{\text{charge}}} = \frac{\epsilon^2}{KR^2} \approx \frac{\Delta R'^2}{K} \tag{5.21}$$

This comparison is plotted in figure 5-8 for a range of beam currents and beam radii assuming a constant emittance $\epsilon = 9.950$ πmm mRad (the transverse emittance of the beam from the DL-1).

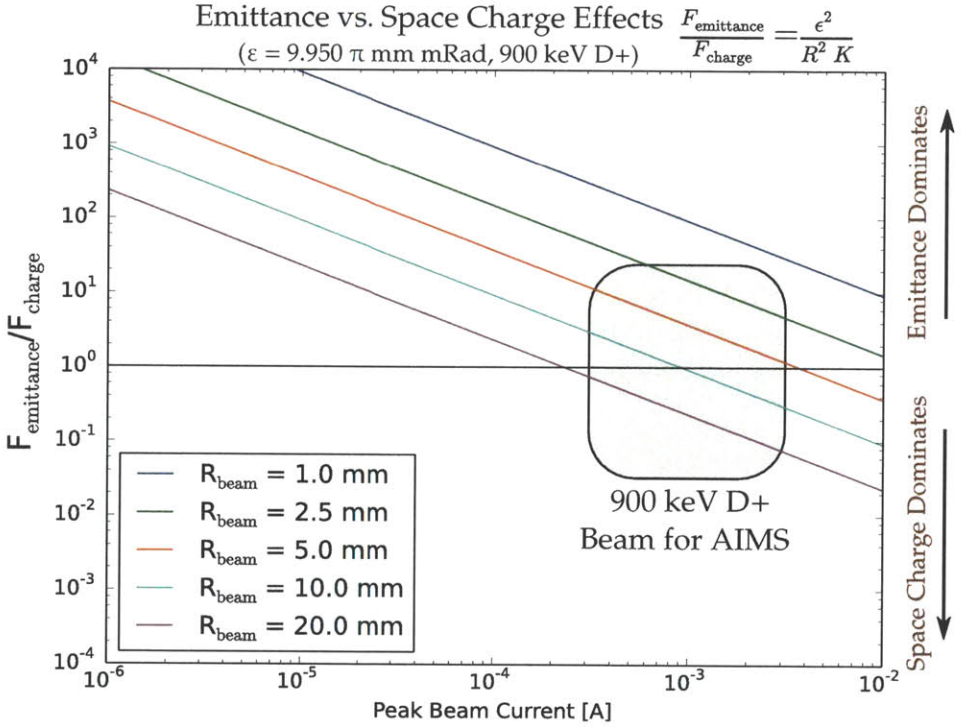

Figure 5-8: Comparison of space charge force to emittance force for 900 keV D^+ ion beams over a range of beam currents and radii. A constant emittance $\epsilon = 9.950$ πmm·mRad is assumed which corresponds to transverse emittance of the beam from the DL-1 accelerator. The outlined shaded region highlights the operating space of the DL-1 beam used for AIMS. Since $F_{\text{emittance}}/F_{\text{Charge}}$ ratio is of order 1, both space charge and emittance are important for AIMS beam dynamics calculations.

Since the DL-1 accelerator, which was used for AIMS, operates in the ~1 mA range with typical collimated beam sizes with 0.5-1.0 cm radii, it is clear that $F_{\text{emittance}}/F_{\text{Charge}}$ is within an order of magnitude of 1. This means that beam is neither space charge dominated nor emittance dominated. As a result, it is necessary to include both effects in the dynamics calculation to accurately model the beam for AIMS.

5.2 Single particles and transfer matrices

The most straightforward method to model the evolution of the beam in a transport system is to use a beam with much smaller spatial dimensions than the gradient scale length of all of the forces, then discretize the system into small enough sections that there is very little variation of each component in z. These conditions allow the forces to be approximated as linear and, therefore, allows linear transformations to be derived for single particles which can later be applied to envelope function. The concepts used to describe these equations and matrix transformations will be developed in this section for the x-x' phase plane assuming that there is no coupling with other phase planes leaving the coupled effects to be described later in section 5.4.

The transformations, in matrix form, operate on vectors representing individual particles in phase space or matrices representing the beam's phase volume. A general example of the equations of motion in one phase plane is shown in equation 5.22 where each m_{ij} is a function of the centroid position z along the trajectory. Each m_{ij} term describes how the x_n and x'_n coordinates evolve and couple as the centroid moves from z_n to z_{n+1}.

$$\begin{aligned} x_{n+1} &= f_n(x_n, x'_n) = m_{11}\, x_n + m_{12}\, x'_n \\ x'_{n+1} &= f'_n(x_n, x'_n) = m_{21}\, x_n + m_{22}\, x'_n \end{aligned} \tag{5.22}$$

Likewise, these linear equations are used to define a matrix $\mathbf{M}_{ij}$ for the x-x' plane is give by equation 5.23 where $\mathbf{M}_{ij}$ describes the interaction of the particle with the fields at z. These matrices are referred to as 'transfer matrices' because they transfer a particle vector from one position or time to the next.

$$\begin{bmatrix} x \\ x' \end{bmatrix}_{n+1} = \begin{bmatrix} m_{11} & m_{12} \\ m_{21} & m_{22} \end{bmatrix}_n \begin{bmatrix} x \\ x' \end{bmatrix}_n \quad \Rightarrow \quad \vec{u}_{n+1} = \mathbf{M}_n\, \vec{u}_n \tag{5.23}$$

It important to note, a more common notation of the elements of the transfer matrix are shown in equation 5.24 [59]. This is due to the fact that nearly all realistic focusing elements, including quadrupoles, contain cos or cosh like terms abbreviated with C and sin or sinh like terms abbreviated with S along with C' and S', their derivatives with respect to z.

$$\mathbf{M} \equiv \begin{bmatrix} C & S \\ C' & S' \end{bmatrix}, \quad \mathbf{M}^{-1} \equiv \begin{bmatrix} S' & S \\ -C' & C \end{bmatrix} \tag{5.24}$$

A simple example of a transfer matrix for the transverse motion of a particle in the x-x' plane when moving from position n to $n+1$ separated by a distance Δs is given in equation 5.25.

$$\begin{aligned} x_{n+1} &= x_n + \Delta s\, x'_n \\ x'_{n+1} &= x'_n \end{aligned} \quad \Rightarrow \quad \begin{bmatrix} x \\ x' \end{bmatrix}_{n+1} = \begin{bmatrix} 1 & \Delta s \\ 0 & 1 \end{bmatrix} \begin{bmatrix} x \\ x' \end{bmatrix}_n \tag{5.25}$$

For certain components that are relatively uniform in along the beam axis, the entire component can be represented by a single transfer matrix. For example the impulse from an ideal lens with focal length f on a particle in the $x - x'$ plane is

given by equation 5.26.

$$\begin{array}{rcrcl} x_{n+1} & = & x_n & & \\ x'_{n+1} & = & -\frac{1}{f}\, x_n & + & x'_n \end{array} \quad \Rightarrow \quad \begin{bmatrix} x \\ x' \end{bmatrix}_{n+1} = \begin{bmatrix} 1 & 0 \\ -\frac{1}{f} & 1 \end{bmatrix} \begin{bmatrix} x \\ x' \end{bmatrix}_n \tag{5.26}$$

Another more realistic example is the magnetic quadrupole. Transfer matrices for the focusing plane (x, x') and defocusing plane (y, y') are given by equation 5.27 and 5.28. Where B' is the magnetic field gradient and constant k and the magnetic rigidity B_ρ are given by equation 5.29.

$$\mathbf{M}_{xx'} = \begin{bmatrix} \cos(k\Delta s) & \frac{1}{k}\sin(k\Delta s) \\ -k\sin(k\Delta s) & \cos(k\Delta s) \end{bmatrix} \tag{5.27}$$

$$\mathbf{M}_{yy'} = \begin{bmatrix} \cosh(k\Delta s) & \frac{1}{k}\sinh(k\Delta s) \\ k\sinh(k\Delta s) & \cosh(k\Delta s) \end{bmatrix} \tag{5.28}$$

$$k = \left| \frac{B'}{B_\rho} \right|^{1/2} \qquad B_\rho = \frac{m_o c \beta}{q} \tag{5.29}$$

In some cases, including the beam steering with magnetic fields, coupling occurs between the orthogonal phase planes. For example, in the case of magnetic fields, the longitudinal momentum component δ couples to the transverse phase planes. Since this technique is formulated based on a linear theory, transfer matrices $\mathbf{M}$ can be combined and applied to higher dimensional phase space vectors representing all of the beam's relevant spatial and angular components, as shown in equation 5.30. Transformations like these allow for the evolution of the phase space coordinates of particles to be calculated iteratively. Furthermore, these transformations can be applied to phase space volumes to capture collective effects of beams consisting of many charged particles.

$$\begin{bmatrix} \vdots \\ \vec{u} \\ \vdots \end{bmatrix}_{n+1} = \begin{bmatrix} [\mathbf{M}_{xx'}] & [\mathbf{M}_{xy'}] & [\mathbf{M}_{x\delta}] \\ [\mathbf{M}_{yx'}] & [\mathbf{M}_{yy'}] & [\mathbf{M}_{y\delta}] \\ [\mathbf{M}_{\ell x'}] & [\mathbf{M}_{\ell y'}] & [\mathbf{M}_{\ell\delta}] \end{bmatrix} \begin{bmatrix} \vdots \\ \vec{u} \\ \vdots \end{bmatrix}_n \tag{5.30}$$

5.3 Linear Transformations of Beam Parameters

Particle tracking codes that use Monte Carlo methods are also possible, in principle. These methods involve stochastically sampling many test particles from the initial distribution then tracking their trajectories through applied fields. With enough tracked particles, the final distribution will eventually converge to a realistic distribution. This technique is rarely the first resort because computation provides very little intuition for the beam dynamics and it is difficult to include collective effects like beam generated forces.

The linear transformation methods have several distinct advantages: 1) The transformations are reversible and this allows for the initial beam parameters to be calculated from a desired result. 2) Matrix transformations are not computationally

expensive compared to particle tracking. 3) For periodic focusing or accelerating systems, the matrices can be solved as an eigenvalue problem to determine stable orbits and other important properties of the system. This is of particular importance with periodic systems like RF accelerators and storage rings.

For unitary transformations ($\det|\mathbf{M}| = 1$) in x and x' given by equation 5.24, the Twiss parameters transform according to the matrix equations 5.24 and 5.31.

$$\begin{bmatrix}\beta\\ \alpha\\ \gamma\end{bmatrix}_{n+1} = \begin{bmatrix} C^2 & -2CS & S^2 \\ -CC' & CS'+C'S & -SS' \\ C'^2 & -2C'S' & S'^2 \end{bmatrix}_n \begin{bmatrix}\beta\\ \alpha\\ \gamma\end{bmatrix}_n \tag{5.31}$$

This matrix formulation works well if each phase plane is independent, but it cannot be used when momentum couples between phase planes. Instead, the sigma matrix formulation is developed for more convenient computation with the incorporation of the coupling terms.

5.3.1 Sigma matrix formulation

The sigma matrix formulation is an alternative method for representing phase space ellipses is in terms of a symmetric matrix $\boldsymbol{\sigma}$ defined by equation 5.32. This formulation is frequently used because it can be easily scaled to N-dimensional phase spaces.

$$\vec{u}^T\,\boldsymbol{\sigma}^{-1}\,\vec{u} = 1 \quad \longrightarrow \quad \begin{bmatrix} x & x' \end{bmatrix} \begin{bmatrix}\sigma_{11} & \sigma_{12}\\ \sigma_{21} & \sigma_{22}\end{bmatrix}^{-1} \begin{bmatrix} x \\ x' \end{bmatrix} = 1 \tag{5.32}$$

Carrying out the matrix multiplication in equation 5.32, the result is the equation for an ellipse, as shown in equation 5.33.

$$\sigma_{11}^{(-1)} x_1^2 + 2\sigma_{12}^{(-1)} x_1 x_2 + \sigma_{22}^{(-1)} x_2^2 = 1 \tag{5.33}$$

Similarly, since the general equation for an N-dimensional hyper-ellipsoid is given by equation 5.34, the $\boldsymbol{\sigma}^{-1}$ matrix for an ellipsoidal boundary in N-dimension phase space can be defined using the constants a_{ij} as the $\sigma_{ij}^{(-1)}$ entries in an $N \times N$ matrix.

$$\sum_i^N \sum_j^N a_{ij} u_i u_j = 1 \tag{5.34}$$

Starting from the general definitions of $\boldsymbol{\sigma}^{-1}$ and the transfer matrix $\mathbf{M}_n$ that models the evolution of a vector $\vec{u}_n$ from position n to $n+1$ (equation 5.35), with some matrix manipulation, it can be shown the ellipse parameters contained in $\boldsymbol{\sigma}_n^{-1}$ can also be evolved by pre and post multiplying by $\mathbf{M}_n$ and its transpose (equation 5.36).

$$\vec{u}^T \boldsymbol{\sigma}^{-1} \vec{u} = 1\ , \quad \vec{u}_{n+1} = \mathbf{M}_n\,\vec{u}_n \tag{5.35}$$

$$\boldsymbol{\sigma}_{n+1} = \mathbf{M}\,\boldsymbol{\sigma}_n\,\mathbf{M}^{\mathrm{T}} \tag{5.36}$$

The important conclusion from this result is that this allows the evolution of

the beam envelope to be calculated iteratively if the transfer matrices $\mathbf{M}$ of the beam transport system that are known and derived purely from the single particle behavior.

$$\boldsymbol{\sigma}_{6D} = \begin{bmatrix} [\boldsymbol{\sigma}_{xx'}] & [\boldsymbol{\sigma}_{xy'}] & [\boldsymbol{\sigma}_{x\delta}] \\ [\boldsymbol{\sigma}_{yx'}] & [\boldsymbol{\sigma}_{yy'}] & [\boldsymbol{\sigma}_{y\delta}] \\ [\boldsymbol{\sigma}_{\ell x'}] & [\boldsymbol{\sigma}_{\ell y'}] & [\boldsymbol{\sigma}_{\ell\delta}] \end{bmatrix} \tag{5.37}$$

$$\boldsymbol{\sigma}^{-1} = \frac{1}{\epsilon^2}\begin{bmatrix} \beta & \alpha \\ \alpha & \gamma \end{bmatrix} \longrightarrow \boldsymbol{\sigma} = \begin{bmatrix} \gamma\epsilon & -\alpha\epsilon \\ -\alpha\epsilon & \beta\epsilon \end{bmatrix} \tag{5.38}$$

Furthermore, from the 6-D sigma matrix that represents the envelope of the entire distribution (equation 5.37) and the 2-D definition of sigma (equation 5.33), the Twiss parameters for the boundary ellipse in any phase plane can easily be extracted with the relationship given in 5.38. This formalism provides the foundation for linear dynamics codes to calculate the evolution of beam distributions.

5.4 Beam Dynamics in a Magnetic Field

The Lorentz force acting on a beam passing through a magnetic field causes the beam's trajectory to bend. The dimensions of the beam about the trajectory of the beam centroid effect the shape of the beam envelope. The finite transverse dimensions of the beam produce a slight focusing effect while field gradients can have a focusing or defocusing effect depending on the direction of the gradient with respect to the beam's curvature. These effects are illusrated in figure 5-10. Definitions for Frenet-Serret coordinates in the bending plane are illustrated in figure 5-9 along with an illustration of the many trajectories that are possible for different values of x and x'. Definitions for curvilinear coordinates and field parameters are also given in table 5.2.

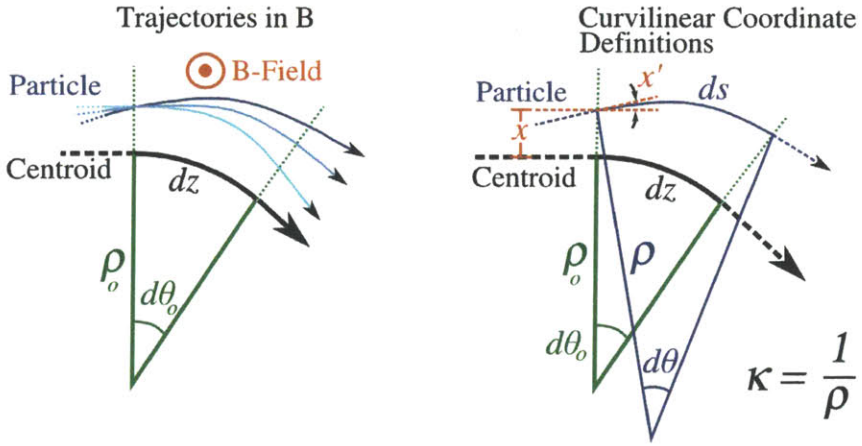

Figure 5-9: Left: Multiple trajectories can be observed for particles in a B-field for the same differential angle $d\theta_o$ depending on x and x'. Right: definitions for the Frenet-Serret coordinates in the bending plane are illustrated.

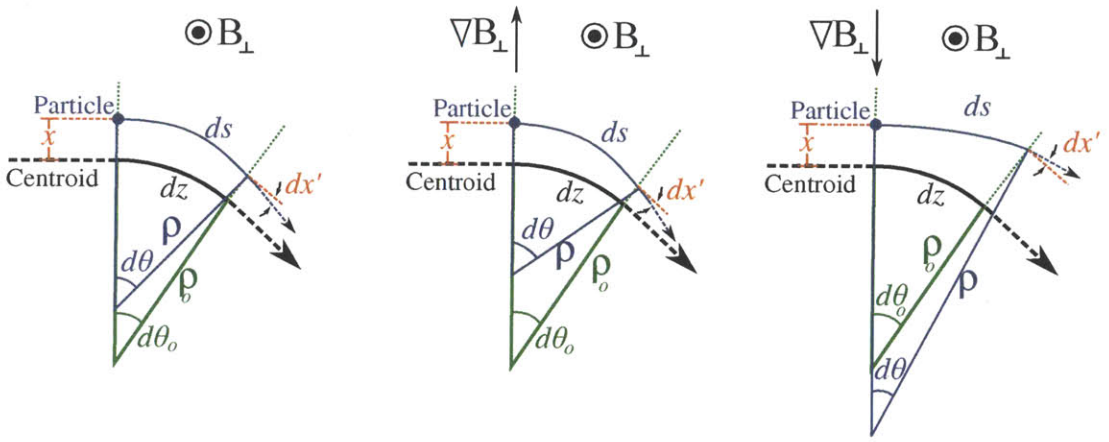

Figure 5-10: Left: A uniform B-field produces a weak focusing effect. Middle: A B-field with gradient ∇B that is parallel to the radius of curvature increases focusing. Right: A B-field with ∇B that is anti-parallel to the radius of curvature decreases focusing and if ∇B is large enough, can cause defocusing.

Description	Symbol	Definition
Momentum	p	$p = \gamma m \beta c$
Momentum Coordinate	δ	$\delta = \frac{\Delta p}{p}$
Transverse Coordinate	u	$u = u_o + \Delta u,\ u \parallel \rho$
Magnetic Field Magnitude	B	$B = \lvert B_\perp(x,z) \rvert$
Radius of Curvature	ρ	$\rho = \frac{p}{qB}$
Curvature	κ	$\kappa = \frac{1}{\rho} = \frac{qB}{p}$
Focusing Strength	k	$k = \frac{q}{p}\frac{dB}{du}$
Differential Angle	$d\theta_o,\ d\theta$	$d\theta_o = \kappa_o\, dz,\ d\theta = \kappa\, ds$
Arc Length of Centroid	dz	$dz = \rho_o d\theta_o = \frac{1}{\kappa_o} d\theta_o$
Arc Length of Particle	ds	$ds = (1 + \kappa_0 u) dz + \ldots$

Table 5.2: Definitions of curvilinear coordinates and field parameters for beams in a magnetic fields. Coordinates with subscript o are associated with the ideal centroid trajectory, coordinates without a subscript are associated with a particle

5.4.1 Equations of Motion

The motion of individual particles can be calculated straightforwardly by simply applying the Lorentz force $F = qv \times B$ without using specialized coordinate system. However, since curved trajectories are significantly affected by variations and path length and field intensity due to finite transverse dimensions in the curved geometry, the curvilinear system must be defined properly to capture the geometry effects on the beam envelope. A detailed description of the following derivation is given in Chapter

2 and 3 of reference [59, 60], first in terms of Taylor expansions and second based on Hamiltonian mechanics.

For the simplest derivation, the equation of motion for a single particle is first transformed to a Frenet-Serret coordinate system following a beam centroid as the reference trajectory, shown in equation 5.39 where the effects of the transformed Lorentz force are incorporated into a magnetic curvature function $K(u, u', \delta)$ and a dispersion function $D(u, u', \delta)$. Note: K is not the same as perveance discussed in section 5.1.6.

$$\frac{d}{dt}\left(\gamma m_o \frac{du}{dt}\right) = qc\vec{\beta} \times \vec{B} \quad \longrightarrow \quad \frac{d^2u}{dz^2} = -K(u, u', \delta)u + D(u, u', \delta)u \tag{5.39}$$

Using the definitions given in table 5.2, keeping only the first order terms in ds, the trace equation can be rewritten as equation 5.40.

$$u'' = -\left(\frac{d\theta}{dz} - \frac{d\theta_o}{dz}\right) \quad \longrightarrow \quad u'' = -(1 + \kappa_o u)\kappa + \kappa_o \tag{5.40}$$

To linearize and solve this equation, κ must be expanded. The expansion of $B_\perp$ (equation 5.41) is now required, where the focusing strength k is introduced, in addition to the expansion of $1/p$ (equation 5.42).

$$B_\perp = B_o + \left(\frac{p_o\, k}{q}\right) u \; + \; \mathcal{O}(u^2)\,, \quad k = \frac{1}{f\Delta z} = \frac{q}{p_o}\left[\frac{dB}{du}\right]_{u=0} \tag{5.41}$$

$$\frac{1}{p} = \frac{1}{p_o(1+\delta)} \approx \frac{1}{p_o}\big(1 - \delta + \mathcal{O}(\delta^2)\big) \tag{5.42}$$

Combining the expansions with the definition of κ retaining only the first order terms gives equation 5.43 which is inserted back into equation 5.40. The result is the trace equation describing the particles trajectory in the curvilinear system, providing the proper geometric effects on the trajectory's curvature (equation 5.44).

$$\kappa = \kappa_o(1 - \delta) + ku \tag{5.43}$$

$$u'' + Ku = D\delta \quad \longrightarrow \quad u'' + (k + \kappa_o^2)u = \kappa_o^2\delta \tag{5.44}$$

This differential equation provides the basis for deriving transfer matrices for particles and envelope functions in magnetic fields. This equation is solved in more detail in section 5.6.7 for the beam's 6-D phase space to develop the transfer matrices for the beams dynamics in B.

5.5 Measurement of Beam Parameters

For modeling beam the results of the calculations rely on accurate initial beam parameters. This requires verifying or measuring the Twiss parameters of the beam

envelope. Since it is not necessarily possible to measure each Twiss parameters independently methods have been established to infer these parameter from those that can be measured. The spatial width of a beam, related to the parameter β, can be measured most directly by beam imaging or with a wire scanner, or other beam profile monitors.

Simply measuring the beam width down stream of the accelerator is insufficient to determine the Twiss parameters. Some well characterized beam optics must be used between the accelerator and the measurement location. Since an ellipse is fully specified by 3 parameters, width measurements must be made under at least three distinctly different optical conditions. A common way this can be done is by varying the fields in a set of quadrupole while operating some type of beam profile monitor installed downstream.

$$\beta_1 = \begin{bmatrix} C^2 & -2CS & S^2 \end{bmatrix} \begin{bmatrix} \beta_0 \\ \alpha_0 \\ \gamma_0 \end{bmatrix} \tag{5.45}$$

From the transfer matrix modified for Twiss parameters shown in equation 5.31, the first row of the matrix gives the relationship between the parameter β after a focusing element and the initial Twiss parameters $\beta_o, \alpha_o, \gamma_o$, as shown in equation 5.45. Using this relationship for multiple optics, assuming that the C and S parameters of the optics are well known, a matrix equation (5.46) can be constructed that relates measured β values to the initial Twiss parameters.

$$\begin{bmatrix} \beta_1 \\ \beta_2 \\ \vdots \\ \beta_n \end{bmatrix} = \begin{bmatrix} C_1^2 & -2C_1S_1 & S_1^2 \\ C_2^2 & -2C_2S_2 & S_2^2 \\ \vdots & \vdots & \vdots \\ C_n^2 & -2C_nS_n & S_n^2 \end{bmatrix} \begin{bmatrix} \beta_0 \\ \alpha_0 \\ \gamma_0 \end{bmatrix} = \mathbf{M} \begin{bmatrix} \beta_0 \\ \alpha_0 \\ \gamma_0 \end{bmatrix} \tag{5.46}$$

Since it is unlikely that exactly 3 measurements and the inverse of $\mathbf{M}$ will provide an exact solution due to uncertainties in the experiment, the Twiss parameters are most effectively determined by applying a least-squares fitting method to $\gg 3$ measurements. Using the definition of M from equation 5.46, the least squares solution for the intial Twiss parameters are from a set of β measurements is given in equation 5.47.

$$\begin{bmatrix} \beta_0 \\ \alpha_0 \\ \gamma_0 \end{bmatrix} = (\mathbf{M}^T\mathbf{M})^{-1}\mathbf{M}^T \begin{bmatrix} \beta_1 \\ \beta_2 \\ \vdots \\ \beta_n \end{bmatrix} \tag{5.47}$$

It is important to note that β cannot be measured directly either, however, it can be determined from its relationship to the measured RMS width $\sqrt{\langle x^2 \rangle}$. The relationship between the sigma matrix, physical RMS parameters, and the Twiss parameters are listed in equation 5.48 [61].

$$\begin{aligned} \sigma_{11} &= \langle x^2 \rangle &&= \epsilon\beta \\ \sigma_{22} &= \langle x'^2 \rangle &&= \epsilon\gamma \\ \sigma_{12} &= \langle x\, x' \rangle^2 &&= -\epsilon\alpha \\ \sigma_{12} &= \sigma_{21} \end{aligned} \tag{5.48}$$

With these relationships, the least squares method in equation 5.47 can be rewritten in terms of the physically measurable RMS width $\sqrt{\langle x^2 \rangle}$ as shown in equation 5.49.

$$\begin{bmatrix} \epsilon\beta_0 \\ \epsilon\alpha_0 \\ \epsilon\gamma_0 \end{bmatrix} = \begin{bmatrix} \langle x_0^2 \rangle \\ \langle x_0'^2 \rangle \\ \langle x_0\, x_0' \rangle^2 \end{bmatrix} = (\mathbf{M}^T\mathbf{M})^{-1}\mathbf{M}^T \begin{bmatrix} \langle x_1^2 \rangle \\ \langle x_2^2 \rangle \\ \vdots \\ \langle x_n^2 \rangle \end{bmatrix} \tag{5.49}$$

$$(\epsilon\beta)(\epsilon\gamma) - (\epsilon\alpha)^2 = \epsilon^2 \tag{5.50}$$

From this equation, the initial Twiss parameters multiplied by the emittance can be determined. Provided that emittance growth is minimal in the optics, this result can be with the relationship given in equation 5.50 to determine all of the initial Twiss parameters $\alpha_o, \beta_o, \gamma_o, \epsilon_o$.

5.6 Beam dynamics code

The beam code for AIMS was developed and operates in two parts: 1) the AIMS trajectory code calculates the beam trajectory in the C-Mod with user specified toroidal and vertical fields and 2) the AIMS dynamics code calculates the evolution of the beam's 6-D phase space envelope along the trajectory. Both codes were implemented in Python [16] to provide the modeling capability needed to provide the AIMS to determine the beam trajectories, target locations, particle detection geometry, and beam spotsize on target.

5.6.1 Trajectory Calculation

Calculating the trajectory of the beam is the first step in modeling the beam. To properly apply the transfer matrices to the beam distribution with the linear theory described in section 5.4, the trajectory and fields along that trajectory must first be calculated.

The trajectory can be calculated by integrating Newton's law with the application of the Lorentz force shown in equation 5.51.

$$m\ddot{\mathbf{R}} = q\dot{\mathbf{R}} \times \mathbf{B} \tag{5.51}$$

The simplest method to calculate the position $\mathbf{r}$ and velocity $\mathbf{v}$ components along the trajectory is Euler integration where the acceleration $\mathbf{a}$, velocity $\mathbf{v}$, and position

vectors $\mathbf{r}$ are calculated recursively over time steps Δt. The recursive form of the Euler method is given in equations 5.52, 5.53, 5.54.

$$\mathbf{a}_n = \frac{q}{m}[\mathbf{v}_n \times \mathbf{B}(\mathbf{r}_n)]\Delta t \tag{5.52}$$

$$\mathbf{v}_{n+1} = \mathbf{v}_n + \mathbf{a}_n \Delta t \tag{5.53}$$

$$\mathbf{r}_{n+1} = \mathbf{r}_n + \mathbf{v}_n \Delta t \tag{5.54}$$

Since the deflection of the beam in a magnetic field occurs in approximately the same radial direction over many time steps, the error in the trajectory accumulates proportionally to the step size Δt. To reduce this error, a variant of the Euler method, called the leapfrog method can be used.

5.6.2 Leapfrog Method

The leapfrog method staggers the calculation of $\mathbf{r}$ and $\mathbf{v}$ by $\Delta t/2$ to alternately advance $\mathbf{r}$ by the average acceleration as shown in equations 5.55, 5.56, 5.57.

$$\mathbf{r}_n = \mathbf{r}_{n-1} + \mathbf{v}_{n-\frac{1}{2}} \Delta t \tag{5.55}$$

$$\mathbf{a}_n = \frac{q}{m}[\mathbf{v}_n \times \mathbf{B}(\mathbf{r}_n)]\Delta t \tag{5.56}$$

$$\mathbf{v}_{n+\frac{1}{2}} = \mathbf{v}_{n-\frac{1}{2}} + \mathbf{a}_n \Delta t \tag{5.57}$$

In effect this calculates the force on the particle at the center of its step rather than at the edge. This is particularly important for AIMS trajectories where the beam bends primarily in one direction because the staggered steps cancel out first order error that occurs in Euler integration. Also, the leapfrog method conserves energy (unlike 4th order Runge Kutte) [24]. These features allow the leapfrog method to provide accurate, energy conserving trajectory calculations. This method was therefore implemented in the AIMS trajectory code because of its simplicity and accuracy. A block diagram of how this code functions is shown figure 5-11.

5.6.3 Adaptive Circular Arc Method

The adaptive circular arc method was derived for this thesis though it has similarities to other methods used for particle simulation in plasmas [52]. The equations are given in 5.58, 5.59, 5.60. Where $\hat{\boldsymbol{\kappa}}$ is the curvature vector, $\hat{\mathbf{b}}$ is the unit vector in the magnetic field direction, ω_c is the cyclotron frequency, and $\Delta\theta$ is the constant angular step size.

$$\hat{\mathbf{v}} = \frac{\mathbf{v}}{|\mathbf{v}|}, \quad \hat{\mathbf{b}} = \frac{\mathbf{B}_\perp}{|\mathbf{B}_\perp|} = \frac{\hat{\mathbf{v}} \times \mathbf{B}}{|\hat{\mathbf{v}} \times \mathbf{B}|}, \quad \hat{\boldsymbol{\kappa}} = \frac{q}{|q|}\, \hat{\mathbf{v}} \times \hat{\mathbf{b}} \tag{5.58}$$

$$\kappa = \frac{q}{p}\,|\mathbf{B}_\perp|, \quad \Delta s = \kappa \omega_c \Delta t = \kappa \Delta\theta \tag{5.59}$$

$$\Delta \mathbf{r} = \frac{1}{\kappa} \sin(\Delta\theta)\ \hat{\mathbf{v}} - \frac{1}{\kappa}[1 - \cos(\Delta\theta)]\ \hat{\boldsymbol{\kappa}} \tag{5.60}$$

This method is basically an adaptive method that uses constant angular step size and makes semi-circular arc steps which have an arc-length that is proportional to the radius of curvature. This is useful because this method more accurately calculates trajectories in large field gradients because the step size is also proportional the local magnetic field strength rather than maintaining a constant linear step size like many other methods. The adaptive circular arc method was successfully developed and programmed, however it was not used because the spatially varying step made the subsequent 6-D dynamics more complicated.

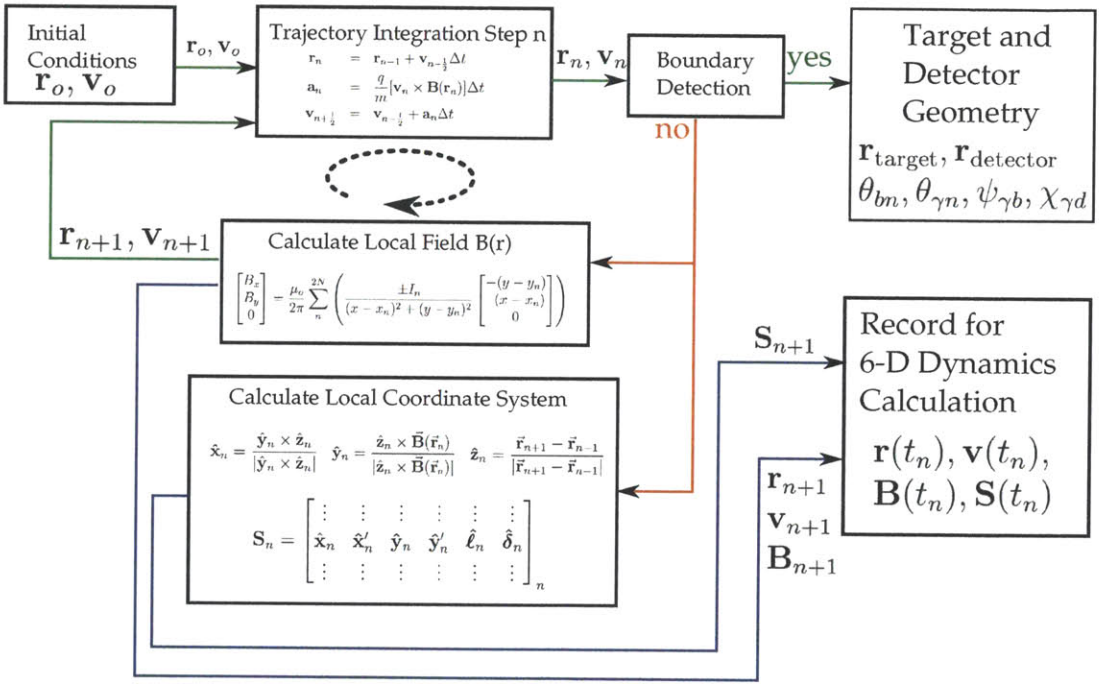

Figure 5-11: Block diagram of iterative procedure used to calculate trajectories using the leapfrog method. This code also defines a local F-S coordinate system during every time step and calculates the local B-fields that are later used for the beam dynamics calculations.

5.6.4 Basis Transformations to Maintain F-S Coordinates

As the beam moves through the magnetic field, the direction of the beam changes. If the longitudinal and transverse components of the beam are desired, as with Frenet-Serret coordinates, the coordinate system of the beam must rotate as the beam evolves. Defining $\hat{\mathbf{z}}$ as the direction of the motion of the beam centroid, a local coordinate system can be defined for the beam in the magnetic field by equations 5.61, 5.62, and 5.63. The x coordinate was chosen to remain parallel to the transverse component

of B-field with the other transverse direction y orthogonal to x and z.

$$\hat{\mathbf{z}}_n = \frac{\vec{\mathbf{r}}_{n+1} - \vec{\mathbf{r}}_{n-1}}{|\vec{\mathbf{r}}_{n+1} - \vec{\mathbf{r}}_{n-1}|} \tag{5.61}$$

$$\hat{\mathbf{y}}_n = \frac{\hat{\mathbf{z}}_n \times \vec{\mathbf{B}}(\vec{\mathbf{r}}_n)}{|\hat{\mathbf{z}}_n \times \vec{\mathbf{B}}(\vec{\mathbf{r}}_n)|} \tag{5.62}$$

$$\hat{\mathbf{x}}_n = \frac{\hat{\mathbf{y}}_n \times \hat{\mathbf{z}}_n}{|\hat{\mathbf{y}}_n \times \hat{\mathbf{z}}_n|} \tag{5.63}$$

The basis vectors for this coordinate system are calculated after the centroid trajectory is complete. Since all of the position vectors $\vec{\mathbf{r}}$ are already known, a forward step $(n+1)$ and a backward step $(n-1)$ are used calculate the vectors at n to reduce the 1st order error in the calculation, much like the leapfrog method.

$$\mathbf{S}_n = \begin{bmatrix} \vdots & \vdots & \vdots & \vdots & \vdots & \vdots \\ \hat{\mathbf{x}}_n & \hat{\mathbf{x}}'_n & \hat{\mathbf{y}}_n & \hat{\mathbf{y}}'_n & \hat{\boldsymbol{\ell}}_n & \hat{\boldsymbol{\delta}}_n \\ \vdots & \vdots & \vdots & \vdots & \vdots & \vdots \end{bmatrix}_n = \begin{bmatrix} x_1 & 0 & y_1 & 0 & z_1 & 0 \\ 0 & x_1 & 0 & y_1 & 0 & z_1 \\ x_2 & 0 & y_2 & 0 & z_2 & 0 \\ 0 & x_2 & 0 & y_2 & 0 & z_2 \\ x_3 & 0 & y_3 & 0 & z_3 & 0 \\ 0 & x_3 & 0 & y_3 & 0 & z_3 \end{bmatrix}_n \tag{5.64}$$

Using this basis, transfer matrices can be projected onto the rotated basis by applying the basis matrix $\mathbf{S}_n$ given in equation 5.64. Since $\mathbf{S}_n$ is composed of an orthonormal set of vectors, the inverse transformation can generated simply from its transpose: $\mathbf{S}_n^{-1} = \mathbf{S}_n^T$. Vectors and matrices can be projected from one basis to the next using equations 5.65 and 5.66.

$$\mathbf{S}_{n+1}\vec{u}_{n+1} = \mathbf{S}_n\,\vec{u}_n \quad \longrightarrow \quad \vec{u}_{n+1} = \mathbf{S}_{n+1}^T\mathbf{S}_n\,\vec{u}_n \tag{5.65}$$

$$\mathbf{S}_{n+1}\,\mathbf{M}_{n+1}\,\mathbf{S}_{n+1}^T = \mathbf{S}_n\,\mathbf{M}_n\,\mathbf{S}_n^T \quad \longrightarrow \quad \mathbf{M}_{n+1} = \mathbf{S}_{n+1}^T\,\mathbf{S}_n\,\mathbf{M}_n\,\mathbf{S}_n^T\,\mathbf{S}_{n+1} \tag{5.66}$$

$$\mathbf{S}_{\text{lab}}\vec{F}_{\text{lab}} = \mathbf{S}_n\,\vec{F}_n \quad \longrightarrow \quad \vec{F}_n = \mathbf{S}_n^T\vec{F}_{\text{lab}} \tag{5.67}$$

$$\mathbf{S}_{\text{lab}}\,\mathbf{M}_{\text{field}}\,\mathbf{S}_{\text{lab}}^T = \mathbf{S}_n\,\mathbf{M}_n\,\mathbf{S}_n^T \quad \longrightarrow \quad \mathbf{M}_n = \mathbf{S}_n^T\,\mathbf{M}_{\text{field}}\,\mathbf{S}_n \tag{5.68}$$

In addition, the fields that act on the beam are generated in the lab frame. Since it is convenient to calculate the forces in a Cartesian coordinate system with a basis matrix $\mathbf{S}_{\text{lab}} = \mathbf{1}$ equal to the identity matrix, the transformation given in equations 5.67 and 5.68 can, in general, be used to rotate force vectors $\vec{F}_{\text{lab}}$ and transfer matrices $\mathbf{M}_{\text{field}}$ calculated in the lab frame to the frame of the beam.

5.6.5 Representation of Beam Envelope for Modeling

The beam envelope is defined to enclose some fraction of the beams phase volume. For symmetric ellipsoidal envelopes, the envelope essentially represents a surface who's radius is proportional to the second moment of the distribution. For the purposes of this code, the beam envelope is take to be the RMS width of the beam in all spatial and momentum directions (e.g. the 1-σ width if the beam is Gaussian).

Since the dynamics theory is linear and the phase volume of the distribution is conserved, the envelope can arbitrarily be scaled by a constant to enclose more or less of the beam. This is true for any beam envelope where the dimensions of the beam are small enough relative to the field gradients for the linear theory to be valid.

However, when space charge effects are included, the spatial dimensions of the beam directly influence the forces generated within the beam. The space charge model used in the AIMS code and TRACE3D assumes the charge distribution in the beam is uniform with an equivalent RMS width. In general, the radius r of a uniform beam has a RMS width of $1/\sqrt{5}\ r$. Therefore, a Gaussian with RMS width σ is equivalent in RMS width to a uniform beam of radius $r_{equiv} = \sqrt{5}\sigma$. As a result, the spatial dimensions of the beam must be scaled by a factor of $\sqrt{5}$ before applying the space charge model, then scaled back after the model has been applied (described further in 5.6.8 and in references [29][46]).

5.6.6 Calculation of Fields

Small deviations in the magnetic field and its traverse gradients can have significant effects on the beam targeting and spot size. Accurate modeling of fields is therefore necessary for the trajectory and the transverse dynamics calculations.

$$B = \frac{\mu_o N I}{2\pi R} = B_0 \frac{R_0}{R} \tag{5.69}$$

The toroidal field (TF) can be accurately modeled inside of the TF coils simply by equation 5.69. However, the transition region where the beam passes from outside of the TF to inside occurs over ~10 cm in radial position and does not have a simple functional dependence. The most accurate way to calculate the fields in this region would be to use numerically calculate the fields from each coil with Biot-Savart Law given in equation 5.70.

$$\mathbf{B}(\mathbf{r}) = \frac{\mu_o}{4\pi} \sum_n \int_{\text{coil}} \frac{I \mathbf{dl}' \times (\mathbf{r} - \mathbf{r}')}{|\mathbf{r} - \mathbf{r}'|^3} \tag{5.70}$$

Since the beam enters the TF close to the midplane, the TF field has minimal variation in the vertical direction and can be reduced to a 2D problem to reduce computation time. In doing so, the Biot-Savart Law integral is reduced to the sum over the field produced by the each vertical leg TF coils that approximated as current elements that is infinite in the vertical direction. With z as the vertical direction and x, y defining the horizontal plane, the simplified solution to equation 5.70 is given by equation 5.71 and in vector form by equation 5.72.

$$\mathbf{B}(x,y) = \frac{\mu_o}{2\pi} \sum_{n}^{2N} \frac{I_n \left[(y-y_n)\hat{\mathbf{x}} + (x-x_n)\hat{\mathbf{y}}\right]}{(x-x_n)^2 + (y-y_n)^2} \tag{5.71}$$

$$\begin{bmatrix} B_x \\ B_y \\ 0 \end{bmatrix} = \frac{\mu_o}{2\pi} \sum_{n}^{2N} \left(\frac{\pm I_n}{(x-x_n)^2 + (y-y_n)^2} \begin{bmatrix} -(y-y_n) \\ (x-x_n) \\ 0 \end{bmatrix} \right) \tag{5.72}$$

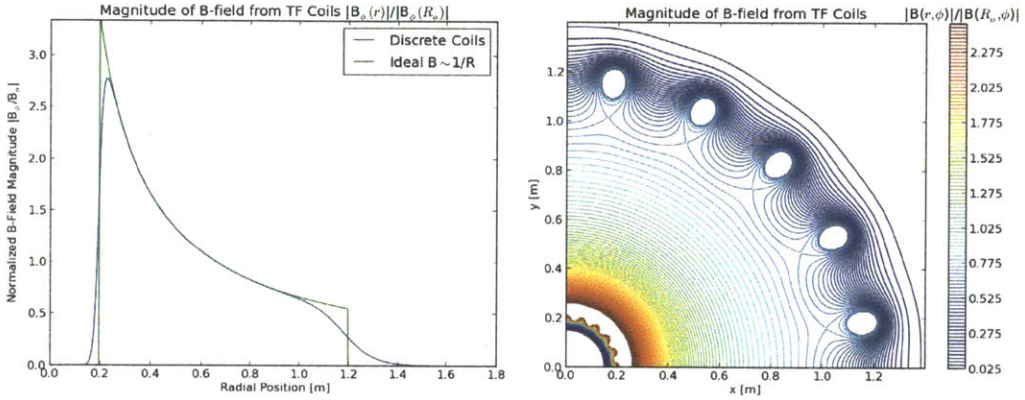

Figure 5-12: Toroidal field magnitude at $\phi = 0$ compared to the ideal $1/R$ fields in a tokamak (left). Two dimensional contour map of the tokamak toroidal field magnitude viewed from the top (right). Tokamak coils are approximated as filament currents for these calculations.

The vertical field (VF) used for steering the beam in the horizontal plane is produced by two coils which are otherwise used for radial plasma positioning during tokamak plasma discharges. The VF is nearly uniform within the plasma region of the vacuum vessel but, like the TF, the beam enters the VF through a non-uniform transition between the coils. More sophisticated modeling is therefore needed to capture these edge effects.

Since the cross-sectional dimensions of the conductors in the VF coils are very small compared to the radius the coils can be approximated as ideal current loops. For an ideal current loop, a classic E&M derivation provides the analytic solution for the vector potential $A_\phi(r,z)$ shown in equations 5.73 and 5.74 in terms of complete elliptic integrals of the first $K(k)$ and second kind $E(k)$. The following solutions are described in reference [45].

$$k^2 = \frac{4\, r\, r_c}{(r+r_c)^2 + (z-z_c)^2} \tag{5.73}$$

$$A_\phi(r,z) = \frac{\mu_o I}{2\pi r} \sqrt{(r+r_c)^2 + (z-z_c)^2} \left[\left(1 - \frac{k^2}{2}\right) K(k) - E(k) \right] \tag{5.74}$$

Where the coil dimensions are defined by their radius r_c and the distance z_c from

z=0 plane. Close to the axis and plane of the coil where $r \ll r_c$ and $k \ll 1$, A_ϕ does not depend on ϕ causing the A_ϕ to simplify to equation 5.75. This yields a simple form of the magnetic field B_z near the axis given in equation 5.76.

$$A_\phi(r,z) = \frac{\mu_o I r_c^2}{4} \frac{r}{[r_c^2 + (z-z_c)^2]^{\frac{3}{2}}} \tag{5.75}$$

$$B_z(z) = \frac{\mu_o I}{2} \frac{r_c^2}{[r_c^2 + (z-z_c)^2]^{\frac{3}{2}}} \quad , \quad B_z(z=z_c) = \frac{\mu_o I}{2r_c} \tag{5.76}$$

The simplified solution in 5.76 is adequate for plasma regions, however, it is necessary to capture the non-uniformity at larger r using the full-field solution without approximations. The magnetic field components B_r and B_z for the complete solution are derived from vector potential in equation 5.74 using the definition $\mathbf{B} = \nabla \times \mathbf{A}$, resulting in equations 5.77 and 5.78.

radial B_r and vertical B_z components of the field has been derived and is given in equations 5.77, 5.78, from reference [45].

$$B_r(r,z) = \frac{\mu_o I}{2\pi r} \frac{z-z_c}{\sqrt{(r+r_c)^2 + (z-z_c)^2}} \left[-K(k) + \frac{r_c^2 + r^2 + (z-z_c)^2}{(r_c-r)^2 + (z-z_c)^2} E(k) \right] \tag{5.77}$$

$$B_z(r,z) = \frac{\mu_o I}{2\pi} \frac{1}{\sqrt{(r+r_c)^2 + (z-z_c)^2}} \left[K(k) + \frac{r_c^2 - r^2 - (z-z_c)^2}{(r_c-r)^2 + (z-z_c)^2} E(k) \right] \tag{5.78}$$

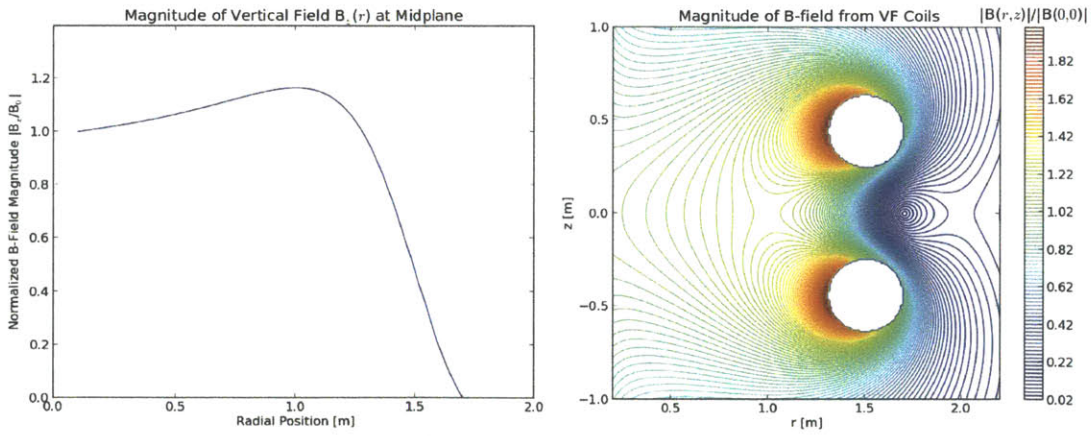

Figure 5-13: Vertical field magnitude at the midplane $z = 0$ (left). Two dimensional contour map of the vertical field magnitude in the R-Z plane (right).

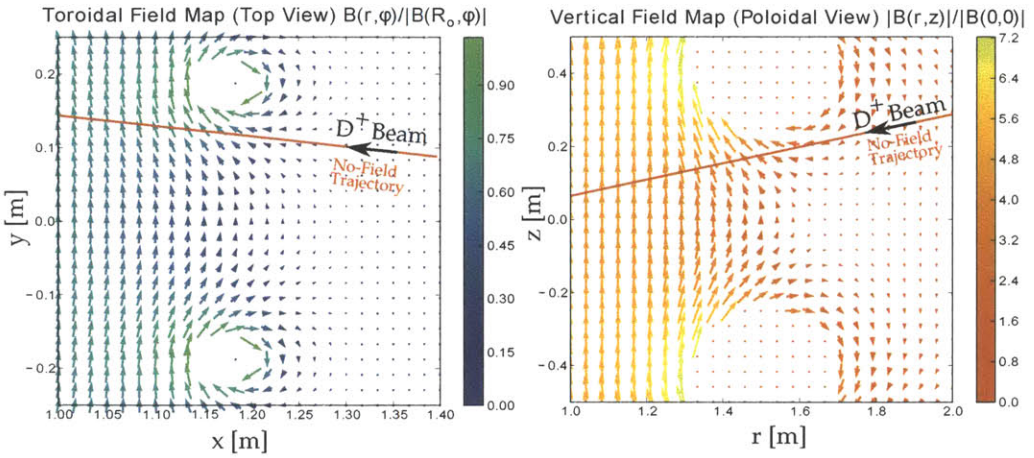

Figure 5-14: A toroidal field map (left) and vertical (right) field map are shown with a nominal beam trajectory for AIMS on C-Mod shown in red. This illustrates the complexity of the fields that occur in the transition regions between coils.

5.6.7 Transfer Matrices for B-Fields and Gradients

For the simplest case where the B-field is uniform, there are no gradients and $k = 0$. Solving for the behavior of the transverse coordinate u between longitudinal position z_n and $z_{n+1} = z_n + \Delta z$, gives the system of coupled linear equations shown in 5.79. This linear system fits well into the general transfer matrix form for transverse dynamics in B with dispersion (equation 5.80) where $\mathbf{M}$ is given in equation 5.81.

$$\begin{array}{lcrcrcr} u_{n+1} &=& \cos(\kappa_o \Delta z)\, u_n &+& \frac{1}{\kappa_o}\sin(\kappa_o \Delta z)\, u'_n &+& \frac{1}{\kappa_o}(1-\cos(\kappa_o \Delta z))\, \delta_n \\ u'_{n+1} &=& \kappa_o \sin(\kappa_o \Delta z)\, u_n &+& \cos(\kappa_o \Delta z)\, u'_n &+& \sin(\kappa_o \Delta z)\, \delta_n \\ \delta_{n+1} &=& \delta_n & & & & \end{array} \tag{5.79}$$

$$\vec{u}_{n+1} = \mathbf{M} \cdot \vec{u}_n \quad \longrightarrow \quad \begin{bmatrix} u \\ u' \\ \delta \end{bmatrix}_{n+1} = \begin{bmatrix} C(z) & S(z) & D(z) \\ C'(z) & S'(z) & D'(z) \\ 0 & 0 & 1 \end{bmatrix}_n \cdot \begin{bmatrix} u \\ u' \\ \delta \end{bmatrix}_n \tag{5.80}$$

$$\mathbf{M} = \begin{bmatrix} \cos(\kappa_o \Delta z) & \frac{1}{\kappa_o}\sin(\kappa_o \Delta z) & \frac{1}{\kappa_o}(1-\cos(\kappa_o \Delta z)) \\ \kappa_o \sin(\kappa_o \Delta z) & \cos(\kappa_o \Delta z) & \sin(\kappa_o \Delta z) \\ 0 & 0 & 1 \end{bmatrix} \tag{5.81}$$

For modeling complex 3-dimensional fields, however, this model is too simple; field gradients in both transverse directions x,y must be included while accounting for curvature that does not necessarily align with the local coordinate system. To include the gradient effects, it is important to first note that $K = k + \kappa_o^2$ can be positive or negative because the sign of k depends on the direction of the gradient. This means that the trace equation (5.44) will have trigonometric solutions for positive

K (focusing) and hyperbolic solutions for negative K (defocusing) [62]. In addition, to globally conserve phase volume, dispersion terms $D_{x,y}$, $D'_{x,y}$ that act on the transverse planes must also operate inversely on the longitudinal phase plane (e.g. compression in the transverse direction must cause expansion in the longitudinal direction, etc). When the gradient effects are included, the matrix form of the solutions for the 6-D space containing all the spatial and momentum components is given in equation 5.82, with its entries $C(z), S(z), D(z)$, etc. given in equation 5.83.

$$\mathbf{M}_B = \begin{bmatrix} C_x(z) & S_x(z) & 0 & 0 & 0 & D_x(z) \\ C'_x(z) & S'_x(z) & 0 & 0 & 0 & D'_x(z) \\ 0 & 0 & C_y(z) & S_y(z) & 0 & D_y(z) \\ 0 & 0 & C'_y(z) & S'_y(z) & 0 & D'_y(z) \\ -D'_x(z) & -D_x(z) & -D'_y(z) & -D_y(z) & 1 & dz/\gamma^2 \\ 0 & 0 & 0 & 0 & 0 & 1 \end{bmatrix} \quad \text{for : } \vec{u} = \begin{bmatrix} x \\ x' \\ y \\ y' \\ \ell \\ \delta \end{bmatrix} \tag{5.82}$$

$$K = k_{x,y} + \kappa^2_{xo,yo} > 0 \quad \begin{cases} C &= \cos(\sqrt{K}\Delta z) \\ C' &= -\sqrt{K}\sin(\sqrt{K}\Delta z) \\ S &= \frac{1}{\sqrt{K}}\sin(\sqrt{K}\Delta z) \\ S' &= \cos(\sqrt{K}\Delta z) \\ D &= \frac{1}{\sqrt{K}}\left(1 - \cos(\sqrt{K}\Delta z)\right) \\ D' &= \sin(\sqrt{K}\Delta z) \end{cases}$$

$$K = k_{x,y} + \kappa^2_{xo,yo} < 0 \quad \begin{cases} C &= \cosh(\sqrt{|K|}\Delta z) \\ C' &= \sqrt{|K|}\sinh(\sqrt{|K|}\Delta z) \\ S &= \frac{1}{\sqrt{|K|}}\sinh(\sqrt{|K|}\Delta z) \\ S' &= \cosh(\sqrt{|K|}\Delta z) \\ D &= \frac{1}{\sqrt{|K|}}\left(1 - \cosh(\sqrt{|K|}\Delta z)\right) \\ D' &= \sinh(\sqrt{|K|}\Delta z) \end{cases} \tag{5.83}$$

Now that the gradients and extra dimensions are included, the final step is to account of the bending plane which in general is not aligned with the transverse directions. The most straightforward way to accomplish this is to rotate the transverse coordinates to align with the magnetic bending plane. Using this method, the rotation is performed by calculating transverse field $\vec{B}_\perp$ and the rotation angle α with respect to the yz plane using equation 5.86.

$$\vec{B}_\perp = \begin{bmatrix} \vec{B}\cdot\hat{x} \\ \vec{B}\cdot\hat{y} \\ 0 \end{bmatrix}, \quad \alpha = \tan^{-1}\left(\frac{\vec{B}_\perp\cdot\hat{y}}{\vec{B}_\perp\cdot\hat{x}}\right) \tag{5.84}$$

$$\kappa_{Ry} = \frac{q}{p_o}|B_\perp|, \quad k_{Rx} = \frac{q}{p_o}\left(\hat{x}\cdot\nabla B\right), \quad k_{Rx} = \frac{q}{p_o}\left(\hat{y}\cdot\nabla B\right) \tag{5.85}$$

$$\mathbf{R}_\alpha = \begin{bmatrix} \cos\alpha & 0 & \sin\alpha & 0 & 0 & 0 \\ 0 & \cos\alpha & 0 & \sin\alpha & 0 & 0 \\ -\sin\alpha & 0 & \cos\alpha & 0 & 0 & 0 \\ 0 & -\sin\alpha & 0 & \cos\alpha & 0 & 0 \\ 0 & 0 & 0 & 0 & 1 & 0 \\ 0 & 0 & 0 & 0 & 0 & 1 \end{bmatrix} \tag{5.86}$$

The rotation angle α is then used to generate the rotation matrix $\mathbf{R}_\alpha$ in equation 5.86. In addition, the values for κ and k are calculated in the new rotated system with equations 5.85. With the rotation matrix $\mathbf{R}_\alpha$ and the B-field transfer matrix $\mathbf{M}_{B\perp}$ calculated in the rotated system the beam's sigma matrix can be stepped forward using the matrix multiplication shown in equation 5.87

$$\vec{u}_{n+1} = \mathbf{R}_\alpha^T\, \mathbf{M}_{B\perp}\, \mathbf{R}_\alpha\, \vec{u}_n \quad \longrightarrow \quad \boldsymbol{\sigma}_{n+1} = \mathbf{R}_\alpha^T\, \mathbf{M}_{B\perp}\, \mathbf{R}_\alpha\, \boldsymbol{\sigma}_n\, (\mathbf{R}_\alpha^T\, \mathbf{M}_{B\perp}\, \mathbf{R}_\alpha)^T \tag{5.87}$$

5.6.8 E Field Impulses for Space Charge Effects

The implementation of the space charge model uses the same model used in TRACE3D [29]. The model applies the effects of beam generated forces in the form of E-field impulses that couple to velocity components of the distribution with each simulation step. The model is based on the following two assumptions:

1. The evolution of the rms envelope of the beam depends only on the linear parts of the space-charge forces.

2. The beam generated forces depend primarily on the second moments of the charge distribution (e.g. width σ for Gaussians).

These assumptions are valid because the behavior of space charge expanding beams is very insensitive to the distribution for most beams that have 'equivalent dimensions', where equivalent means that the distributions with equal second moments. It has been shown that beams with Gaussian, parabolic, annular, and uniform circular beams of equivalent charge density and RMS width behave almost identically when expanding due to space charge [46]. This allows the space charge force model to be derived more straightforwardly assuming a uniform beam. The uniform beam solution can then applied to any beam where the second moment of the distribution is known. The model used in the TRACE3D and the AIMS dynamics code was derived was derived in [36] (in French) and explained in [29] (in English). This model provides the E field impulses as a function of the beams linear dimensions showing in equations 5.88, 5.89, 5.90.

$$E_x = \frac{1}{4\pi\epsilon_0}\frac{3I\lambda}{c\gamma^2}\frac{(1-f)}{r_x(r_x+r_y)r_z)}\,x \tag{5.88}$$

$$E_y = \frac{1}{4\pi\epsilon_0}\frac{3I\lambda}{c\gamma^2}\frac{(1-f)}{r_y(r_x+r_y)r_z)}\,y \tag{5.89}$$

$$E_z = \frac{1}{4\pi\epsilon_0}\frac{3I\lambda}{c}\frac{f}{r_x r_y r_z}\,z \tag{5.90}$$

From the E-fields, the impulses on the momentum components u' are then applied with using equation 5.91.

$$\Delta(\beta\gamma)_u = \frac{qE_u\Delta s}{m_0 c^2 \beta} \tag{5.91}$$

A numerical form factor f is used in these equations is given in tables in the literature. A more convenient polynomial fit was calculated for the AIMS code and is given equation 5.93. Furthermore, it is important to note that this model only works for an 'upright' system, meaning that its major and minor axes align with the x, y, z coordinates.

$$\begin{aligned}
p &= \frac{\gamma r_z}{\sqrt{r_x\, r_y}} \\
f &= a_0 + a_1\, p + a_2\, p^2 + a_3\, p^3 + a_4\, p^4 \quad (\text{for} : 0 < p < 1) \\
a_n &= [0.32685993, -1.10422029, 1.64157723, -1.52987752, 0.99919503] \\
f &= b_0 + b_1\,\frac{1}{p} + b_2\,\frac{1}{p^2} + b_3\,\frac{1}{p^3} + b_4\,\frac{1}{p^4} \quad \left(\text{for} : 0 < \frac{1}{p} < 1\right) \\
b_n &= [0.39122685, -0.97242357, 0.74316934, 0.1744343, -0.0020169]
\end{aligned} \tag{5.92}$$

Since the AIMS dynamics code primarily computes the effects of magnetic fields that tend to spatially rotate the distribution, rotation matrices must be applied to the distribution to rotate it upright before applying the space charge model, then the inverse must be applied after space charge impulses are applied. The rotation angles in and their associated planes denoted by their subscripts are given in equation 5.94.

$$\begin{aligned}
\Theta_{xy} &= \frac{1}{2}\,\tan^{-1}\left(\frac{2\,\sigma_{13}}{\sigma_{33} - \sigma_{11}}\right) \\
\Theta_{yz} &= \frac{1}{2}\,\tan^{-1}\left(\frac{2\,\sigma_{34}}{\sigma_{55} - \sigma_{33}}\right) \\
\Theta_{zx} &= \frac{1}{2}\,\tan^{-1}\left(\frac{2\,\sigma_{51}}{\sigma_{11} - \sigma_{55}}\right)
\end{aligned} \tag{5.93}$$

5.6.9 Beam Projection

When the beam intercepts the wall at a non-zero incidence angle, the transverse beam dimensions must be projected onto the PFC surface. For large incident angles, the beam projection is often the largest contributor to the broadening of the spatial size of the beam. This projection is done simply by applying the inverse coordinate

transformation matrix as shown in equation 5.94. Where $\hat{x}_b$, $\hat{y}_b$ are transverse basis vectors in the beam coordinate system and $\hat{x}_t$, $\hat{y}_t$ are the transverse basis vectors in the target system (i.e. orthogonal vectors that are tangent to the PFC surface).

$$\begin{bmatrix} x_b \\ y_b \end{bmatrix} = \left(\begin{bmatrix} \cdots & \hat{x}_b & \cdots \\ \cdots & \hat{y}_b & \cdots \end{bmatrix} \begin{bmatrix} \vdots & \vdots \\ \hat{x}_t & \hat{y}_t \\ \vdots & \vdots \end{bmatrix} \right)^{-1} \begin{bmatrix} x_t \\ y_t \end{bmatrix} \tag{5.94}$$

5.7 Beam Dynamics Code: Results for AIMS

The AIMS trajectory code was successfully implemented in Python [16] as a computational tool to use for AIMS and as a major contribution to this thesis. It provides the modeling capability determine ion beam trajectories in C-Mod and the particle detection geometry with user specified toroidal and vertical fields. In addition, the AIMS beam dynamics code provides comprehensive tools for calculating, plotting, and analyzing the evolution of the beam distribution's 6-D RMS envelope and project it onto the target PFCs to predict beam spotsize, and thus spatial resolution for the PFC measurements.

5.7.1 Trajectory and Beam Dynamics Calculation

For each AIMS measurement the AIMS trajectory code was used to calculate the trajectories and target locations and all of the parameters describing the detection geometry. The detection parameters for the four most studied AIMS locations are shown in table 5.3, with a 3-D projection of the trajectories and geometry shown in figure 5-15.

Toroidal Field	$\mathbf{B_o}$	**0.000**	**0.0582**	**0.1135**	**0.1618**	**T**
Magnet Current	I_{TF}	0.000	1600	3120	4450	A
Target Radial Position	R	0.440	0.440	0.460	0.468	m
Target Vertical Position	Z	-0.0818	-0.1693	-0.2547	-0.4039	m
Target Toroidal Angle	ϕ	35.31	37.99	39.06	47.37	deg
Beam Incident Angle	θ_{bn}	44.67	53.05	55.98	81.78	deg
Gamma-Target Angle	$\theta_{\gamma n}$	63.02	66.28	67.22	78.59	deg
Gamma-Beam Angle	$\psi_{\gamma b}$	157.32	154.76	151.54	149.40	deg
Detector-Gamma Angle	$\chi_{\gamma d}$	27.82	28.79	31.00	34.61	deg
Gamma Path Length	L_γ	1.0724	1.0965	1.1080	1.2034	m
Detector Efficiency	η/η_o	2.4356	2.4179	2.3674	2.2638	-

Table 5.3: Calculated target and detection geometry parameters for the 4 most common trajectories used for AIMS measurements of the Alcator C-Mod inner wall, organized by toroidal field strength. Refer to section 2.6.7 in chapter 2 for definitions of geometric quantities.

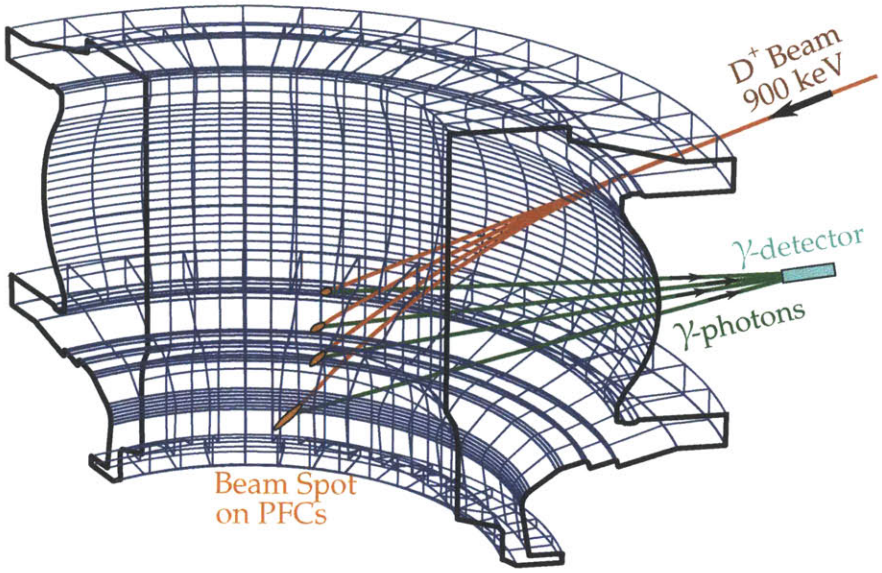

Figure 5-15: 3-D projection of calculated 900 keV D^+ trajectories and γ-detection geometry, for 4 toroidal field settings (B_ϕ = 0,0.0582, 0.1135, 0.1618 T). The blue grid denotes the plasma facing surfaces inside Alcator C-Mod.

In the process of calculating the trajectory, the code also calculates and records the local magnetic fields and field gradients that are used in the dynamics code. The AIMS dynamics code is able to use this information to calculate the evolution of the beam's distribution in 6-D spatial and canonical momentum phase space. The AIMS dynamics code was applied to all of the beam trajectories used for AIMS measurements to calculate the evolution of the distribution resulting in a beam spot on the target PFCs. The results are shown in figure 5-16.

5.7.2 Validation of Trajectory Calculation

Since the AIMS technique relies on accurate calculation of the beam trajectory, it is important to validate the numerical methods that were implemented in the AIMS trajectory code. The most straightforward way to do this is to compare a numerically calculated trajectory to a trajectory that is analytically solvable such as a circular orbit in a uniform magnetic field. Also since the trajectory is calculated in 3-D, a velocity component can be added parallel to the field to make the orbit helical. Since each step of the numerical calculation represents a differential section of a circular orbit in 3-dimensions, the deviation from a perfect helical orbit is a good indication of the quality of the calculation. The parametrized equations for a helical trajectory used for comparison are given in equation 5.95 and 5.96.

$$\begin{aligned} x(s) &= R_c \cos(c_\perp s) \\ y(s) &= R_c \sin(c_\perp s) \\ z(s) &= c_\parallel s \end{aligned} \tag{5.95}$$

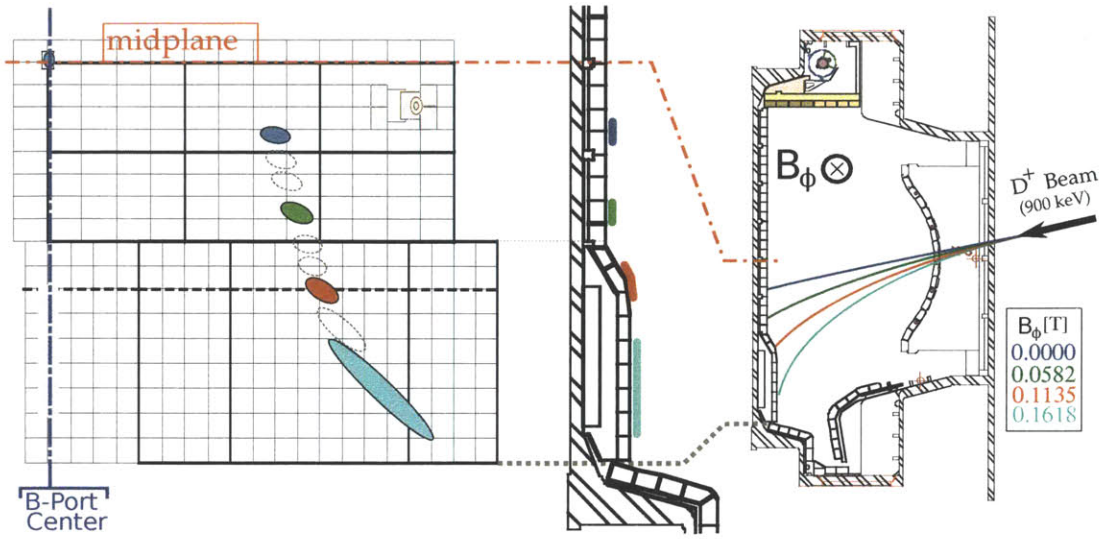

Figure 5-16: Calculated beam spot geometry on target PFCS. The ellipses represent the 1-σ envelope of the beam distribution projected on the target geometry at to location where the beam centroid intercepts the PFCs. The filled in ellipses correspond to the most studied PFC locations and the dotted-grey ellipses correspond to the additional locations studied while performing a higher resolution poloidal sweep.

$$R_c = \frac{mv_\perp}{qB}\,, \quad c_\perp = \frac{v_\perp}{v_o\, s_o}\,, \quad c_\parallel = \frac{v_\parallel}{v_o\, s_o} s\,, \quad s = \frac{n\Delta s}{N} \tag{5.96}$$

Where s is the distance along the trajectory, R_c is the Larmor radius, v_o is the velocity of the particle, and $v_\perp$ and $v_\parallel$ are the velocity components $\perp$ and $\parallel$ to the magnetic field B. An ideal helix with a pitch angle of 10^o (roughly the beam injection angle in the horizontal plane) was compared to a trajectory with equivalent input parameters that was integrated using the leapfrog method with 1 mm steps, described in section 5.6.2. The result of this calculation is shown in figure 5-17 where Δr is the deviation in transverse position from the ideal trajectory.

This error calculation shows that the error in radius of curvature grows steadily but is insignificant on the scale of the 1 m trajectories that are expected in the C-Mod. In the calculation of these trajectories an error of less than 0.4 mm is expected due to the trajectory integration which likely to be negligible compared to the other geometric uncertainties associated with the code inputs.

5.7.3 Validation of 6-D Dynamics Calculation

The 6-dimensional beam dynamics calculation implemented in the AIMS beam dynamics code was successfully validated against equivalent calculations using TRACE3D which has been validated as part of its development at Los Alamos.

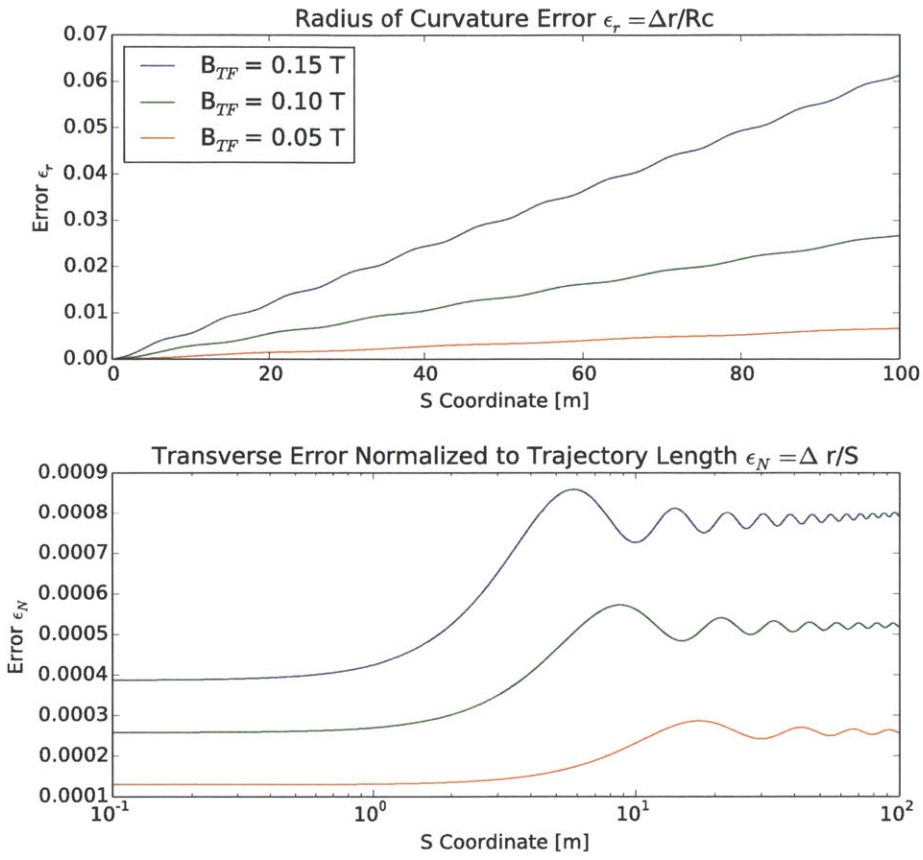

Figure 5-17: Error analysis of the beam trajectory calculation using the leapfrog method with 1 mm steps. Δr is the deviation in transverse position from an ideal helical trajectory with a pitch angle of 10°.

Mismatch Factor

To test agreement between the AIMS code results and the TRACE3D results, the beam envelopes were compared in each phase plane. A dimensionless parameter M called the 'mismatch factor' was used to quantify the overlap in the Twiss parameters of the ellipsoidal envelopes from each code. This quantity M is essentially a measure of the relative difference in major radius, minor radius, and ellipse angle between two ellipses. In geometric terms, M is the factor by which one ellipse must be scaled to fully encircle the other.

A simple example is an ellipse with major R_E and a circle with radius R_o. The Mismatch factor is given by equation 5.97.

$$M = \frac{R_E}{R_o} - 1 \tag{5.97}$$

The mismatch factor is further generalized so that it can be applied to any two mismatched ellipses (1,2) defined by their Twiss parameters $\alpha_1, \beta_1, \gamma_1$ and $\alpha_2, \beta_2, \gamma_2$ as in equation 5.98.

$$\beta_{1,2}x^2 + 2\alpha_{1,2}x\,x' + \gamma_{1,2}x'^2 \tag{5.98}$$

For the general case, the mismatch factor is given by equation 5.99 where R is given by equation 5.101 and has units [m·radians]. An alternative form of the mismatch factor M_A is given in equation 5.100 which quantifies the overlap in area of the two ellipses.

$$M = \left[\frac{1}{2}\left(R + \sqrt{R^2 - 4}\right)\right]^{1/2} - 1 \tag{5.99}$$

$$M_A = \frac{1}{2}\left(R + \sqrt{R^2 - 4}\right) - 1 \tag{5.100}$$

$$R = \beta_1\gamma_2 + \beta_2\gamma_1 - 2\alpha_1\alpha_2 \tag{5.101}$$

Both mismatch factors are useful for relating the envelopes of two distributions because M indicates the mismatch in the linear spatial dimensions of the beam while M_A indicates the overlap in area which is related to the number of particles that are shared between the two distributions. M is used for this analysis because it directly relates linear dimensions of the beam which related to the spatial resolution of the AIMS technique.

Direct Comparison of Dynamics Codes

The comparisons between the AIMS beam code and TRACE3D are given in the form of ellipse projections of the sigma matrices from each code and their associated mismatch factors. The projections on the x-x', y-y' planes represent the envelopes of the distribution in transverse direction. The ℓ-δ plane shows the envelope in the longitudinal direction. In addition the projection on the x-y plane is shown because it directly gives the transverse shape of the beam spot where the radius is equivalent to 1-σ width for Gaussian beams. The first scenario that was analyzed for comparison is the straight through trajectory with no beam steering fields. The results of this comparison are shown in figure 5-18.

This calculation is in nearly perfect agreement between both codes. Even though drift space with no B-fields appears simple, for 1 mA beams, beam generated forces are still important so this result serves mostly as a validation of the space charge model. Another important comparison of a 1 mA beam and a 1 μA beam, shown in figure 5-19. This result shows that the dimensions of the beam can vary by as much as 15% as indicated by the mismatch factor, even for the simplest trajectories. This demonstrates that the space charge effects are relevant for simulating beams in the mA range.

The second scenario that was analyzed was a 90^o steering magnet with uniform fields with a radius of curvature $R_c = 1$ m. The results from this comparison are shown

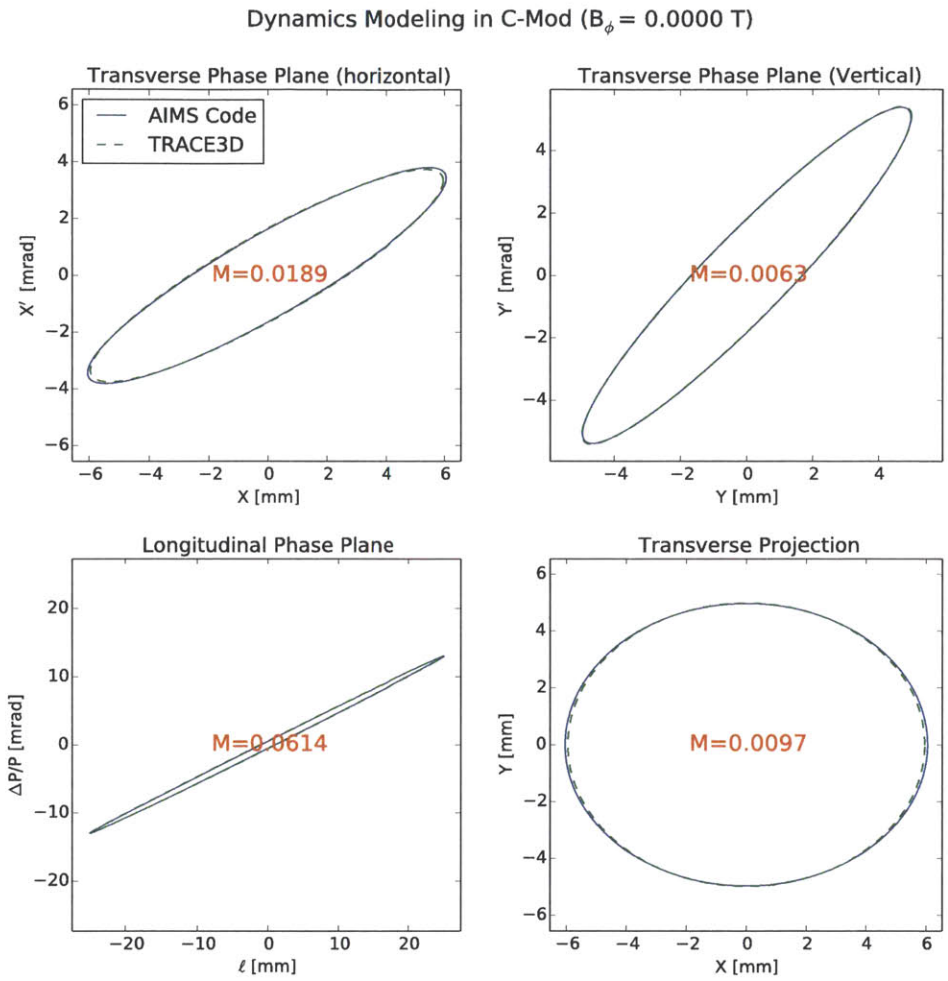

Figure 5-18: Comparison of AIMS beam dynamics code with TRACE3D for the $B_\phi = 0$ T trajectory in C-Mod. Transverse and longitudinal phase planes projections are shown in addition to an transverse spatial projection with respect to the beam coordinate system.

in figure 5-20. This comparison shows very good agreement between the two codes demonstrating that magnetic fields cause the proper beam evolution, thus validating the two primary components of the AIMS dynamics code.

Discretized Tokamak Fields for TRACE3D

Since TRACE3D is designed to calculate beam dynamics with standard beam optics, insertion devices, and other beamline components, the complex fields of a tokamak cannot simply be inputted into TRACE3D's fortran based input files. In addition TRACE3D only does calculations in the coordinate system of the beam centroid and cannot model trajectories.

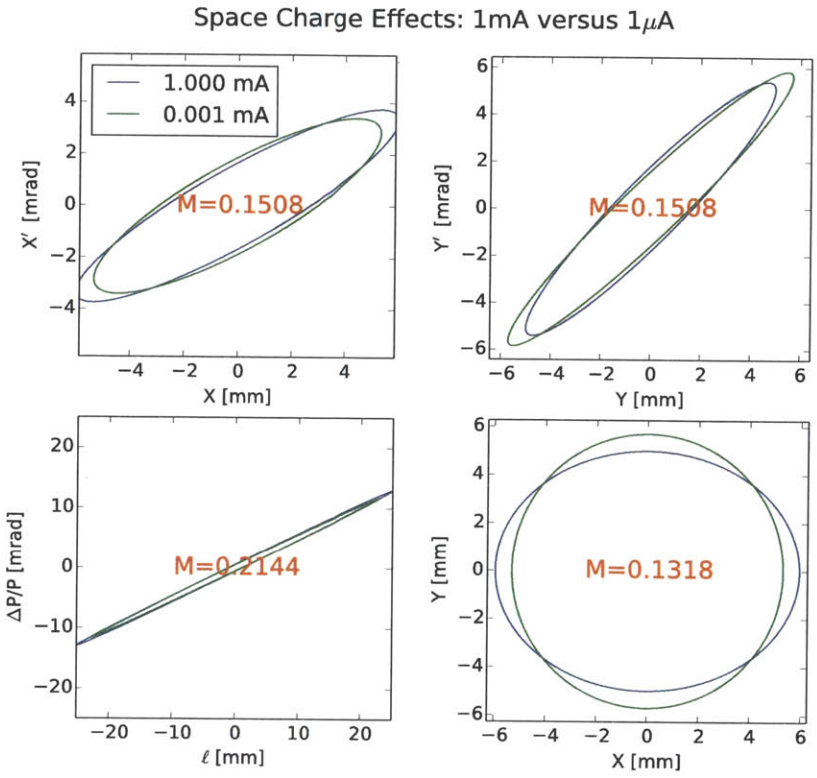

Figure 5-19: AIMS beam dynamics code results comparing a 1 mA beam where space charge effects are significant to a 1 μA beam. Both trajectories are 1.5 m in length with no externally applied fields

To make a comparison between the AIMS code and TRACE3D in a C-Mod like evironment, the tokamak fields along the beams trajectory had to be calculated and converted to TRACE3D inputs. This was done by calculating magnetic fields and field gradients using the already validated (section 5.7.2) trajectory module of the BDC then converting the field profile to as set of 10-15 equivalent sector-magnets – standard beamline components that combine steering fields with gradients.

Since the AIMS code can calculate the trajectory with arbitrarily small step size (typically set to 1 mm to calculate an accurate trajectory), the calculated B fields and gradients appear to vary smoothly along the trajectory. If each step were converted into a sector magnet input for TRACE3D, it would require 1500 magnet elements for a 1.5 m trajectory which is far more beamline components than TRACE3D is designed to handle. The calculated magnetic field and ∇B along the trajectory, shown in figure 5-21, was averaged over 10 cm lengths to provide a discretized field profile that was used to generate the input parameters for the sector magnet elements in TRACE3D.

Strictly speaking, the sector magnets are not equivalent because they only compute the effects of ∇B in plane of curvature and the discretization of a non-linear

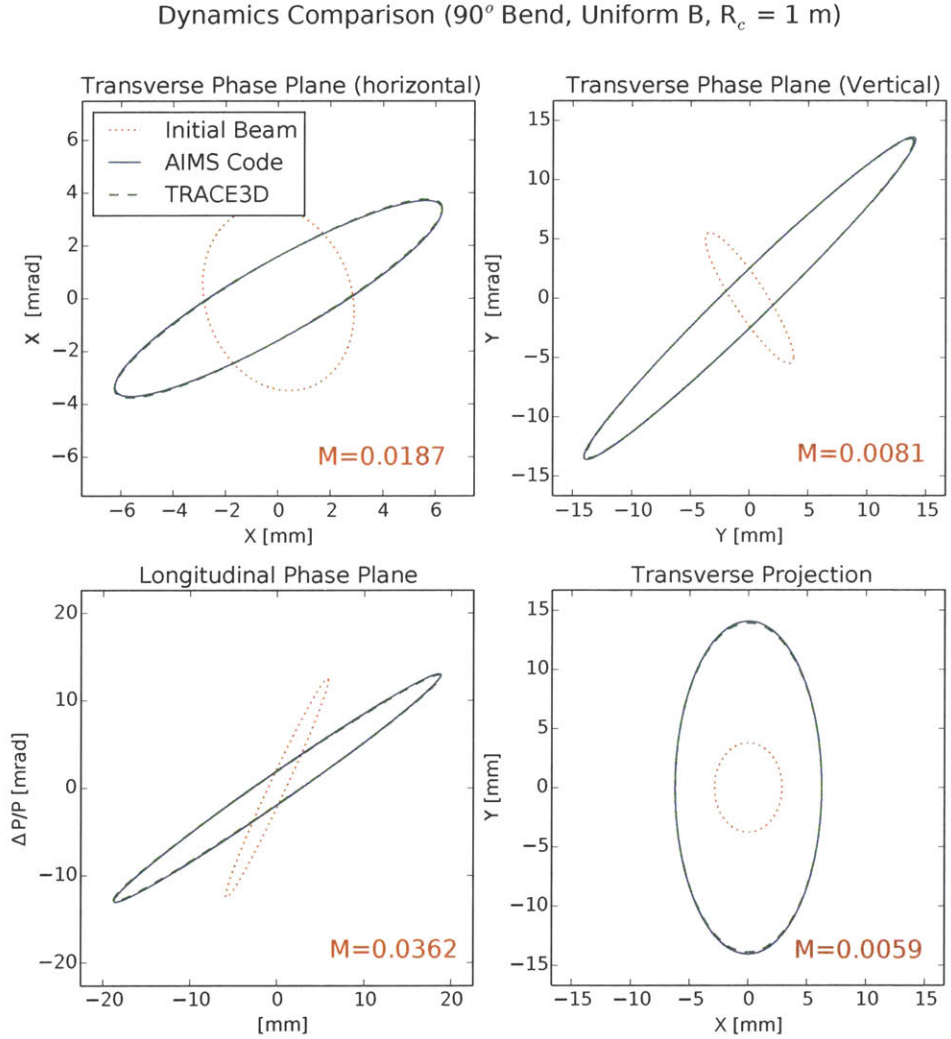

Figure 5-20: Comparison of AIMS beam dynamics code with TRACE3D for a 90° sector magnet with uniform field and a bending radius of curvature $R_c = 1$ m. Transverse and longitudinal phase planes projections are shown in addition to an transverse spatial projection.

profile in 10 cm steps is inherently different than 1 mm steps. However, since B profile is fairly smooth over 10 cm lengths and the ∇B is primarily in the direction of the radius of curvature for most of the trajectory (except near the coils), this discretized model provides a scenario that is as equivalent to tokamak fields as for a TRACE3D comparison. The TRACE3D output is shown in figure 5-22 for one of the trajectories with $B_\phi = 0.0582$ T steering fields on axis.

The comparisons of phase plots between the discretized TRACE3D model and the AIMS model with the full fields are shown in figure 5-23.

Though this result does not show perfect agreement with the AIMS dynamic model, it does result in a transverse x-y projection that matches within 3.8%, which is the quantity of interest for AIMS. Also, it is interesting to note that size and shape

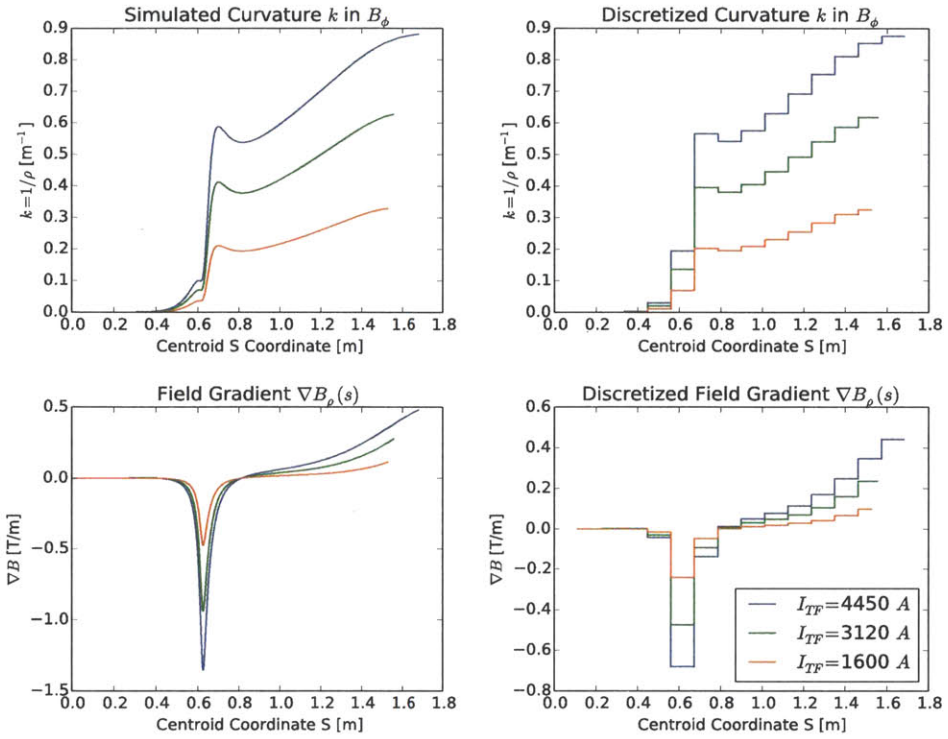

Figure 5-21: Discretized B-field Curvature for TRACE3D input.

of the beam envelope matches reasonably well between within each phase plane but differ primarily in rotation.

Magnetic fields tend to focus the distribution in the direction perpendicular to B and couple transverse momentum with transverse momentum while gradients tend to focus (or defocus if they are anti-parallel to R_c). Considering these effects, since steering is primarily in the y-z plane, this scenario suggests that the mismatch in the y-y' plane is due to discrepancies in ∇B_x (which is not included in TRACE3D) and the mismatch in the in x-x' plane is due to discrepancies in the combination of B_y and ∇B_y. Likewise the mismatch in the ℓ-$\Delta p/p$ plane is most likely due to the discrepancies in B_y.

Since the B field and the space charge modules of the beam dynamics code have been validated the AIMS dynamics solution is most likely the more correct prediction. This and the previous comparisons demonstrate the need for full field simulation of beam dynmamics in order to accurately predict the proper distribution on target. Further, it is clear that space charge effects, continuous fields and gradient profiles along the trajectories must be included for accurate result.

5.7.4 Reverse Dynamics for Active Focusing Applications

Solving the beam dynamics problem in reverse by first specifying the beam envelope at the target then calculating its reverse evolution back to the accelerator optics is

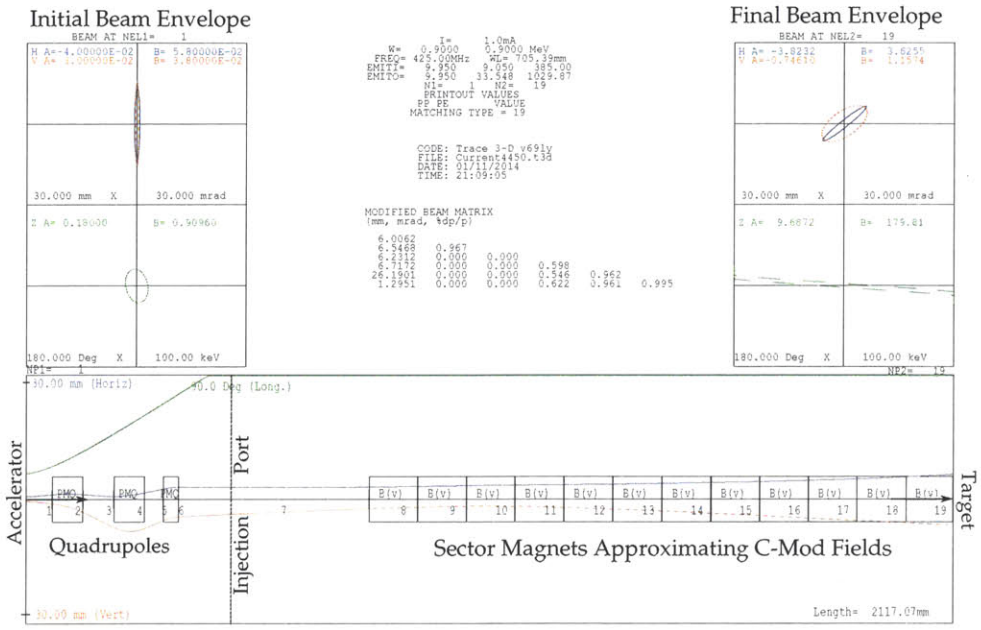

Figure 5-22: Example of TRACE3D output from discretized fields. Sector magnets are used to apply magnetic fields and magnetic gradients to the beam. This plot corresponds to the fields for in C-Mod a toroidal field on axis of $B_\phi = 0.0582$ T ($I_{TF} = 1600$ A) shown in figure 5-21. The 'modified beam matrix' parameters are used to construct a sigma matrix for comparison to the AIMS beam dynamics code.

a powerful tool for designing beam optics for a wider range of trajectories. This technique is useful because it allows an acceptable beam envelope or 'acceptance' envelope to be determined for the beam optics that will result in a desired spot size. Since the beam dynamics code is entirely built on linear transformations that preserve phase volume (implying determinant = 1), all of the transformations are necessarily invertible, guaranteeing that the dynamics calculation can be performed in reverse.

The reverse calculation, which has been successfully verified, is done by first calculating the trajectory of the beam and the fields along the trajectory in the forward direction. Then, from the fields along the trajectory, all of the transfer matrices from the applied fields can be calculated explicitly. With all of the transfer matrices determined and the beam envelope at the target specified, the space charge impulse matrices can be calculated implicitly from the local beam dimensions as the evolution of the beam envelope is calculated in the reverse direction.

Knowledge of the acceptance envelope allows beam optics codes like TRACE3D [29] or TRANSPORT [7] to be applied to the design of the optics in the beamline that prepare the beam for injection into the tokamak fields. These codes have optimization routines that can calculate the necessary gradients and fields in standard optical components to match the beam to the acceptance envelope determined by the reverse dynamics calculation. As practical result, this information can be used to determine the specs of the required quadrupole elements and can also be used to determine the optimal quadrupole settings for any trajectory.

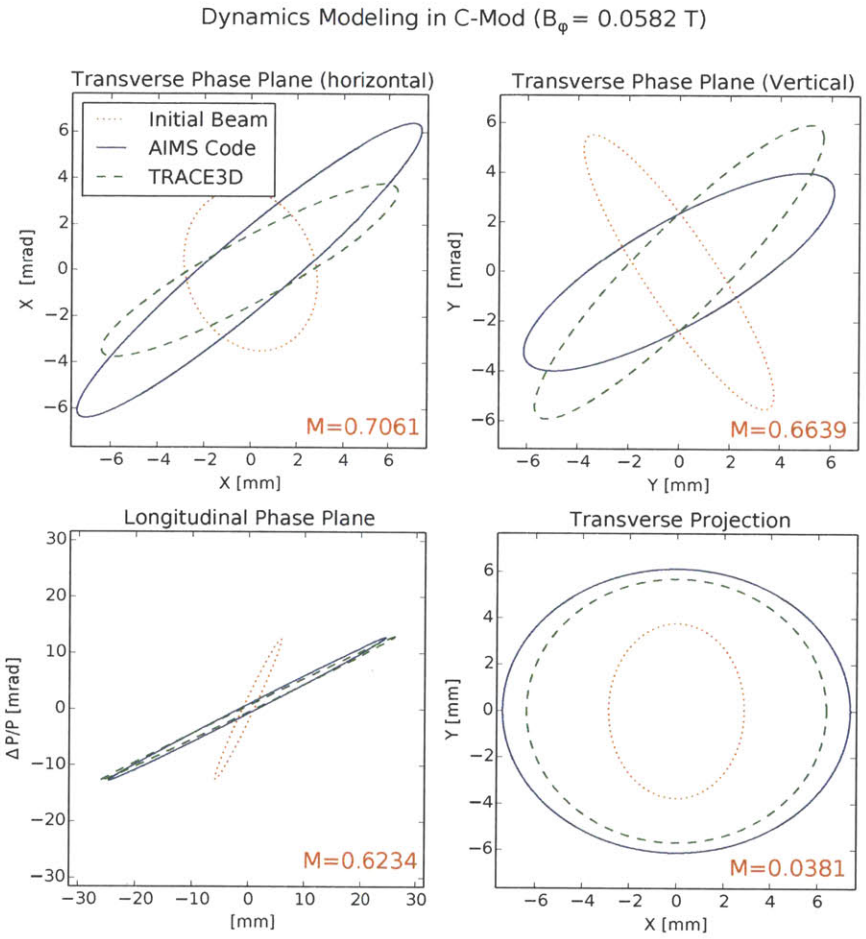

Figure 5-23: Discretized B-field Curvature for TRACE3D input.

Chapter 6

Results and Discussion

AIMS was successfully implemented and applied to study boron erosion and deposition on the surface of plasma facing components (PFC) in Alcator C-Mod. The retention of deuterium was also studied in [21]. Since AIMS is a first of a kind, prototype of an in-situ PFC diagnostic, a major goal of the AIMS measurements and this thesis, is to demonstrate the viability of the AIMS technique and identify areas to improve in future implementations of AIMS diagnostics. The second goal is to understand or quantify any interesting physics results that were observed in the measurements. Both of these goals were achieved. The successful implementation of the AIMS diagnostic, despite significant time constraints due to the uncertainty of funding for the C-Mod facility, have also allowed us to identify experimental difficulties that will allow AIMS to be greatly improved in the future.

Measurements were made on the inner wall of Alcator C-Mod using the AIMS technique before, during, and after the last run day of the 2012 C-Mod campaign to observe the effects of plasma discharges. Subsequent measurements were taken during the months following the campaign to observe changes due to plasma conditioning operations that include boronization, electron cyclotron discharge cleaning (ECDC), and glow discharge cleaning (GDC). The AIMS geometry and timeline are presented and discussed in sections 6.1 and 6.2. Results from these measurements are presented in 6.3 through 6.7.

The AIMS photopeak analysis was able to successfully identify the 953 keV photopeak from the $^{11}\mathrm{B}(d,p\gamma)^{12}\mathrm{B}$ reaction and use it to quantify boron content on the C-Mod plasma-facing surfaces. However, temperature stability issues in the gamma detector and low time averaged count rates caused some difficulty with the measurement of Boron photopeak for certain AIMS runs.

Following AIMS analysis, 4 tile-modules containing a total of 64 Molybdenum tiles were removed from the vessel and were analyzed using the external beam PIGE technique (chapter 3) to provide reliable quantitative measurements of the boron content on the PFC surfaces to compare with the overlapping AIMS measurements in order to validate the AIMS technique. The PIGE results and comparison to AIMS are presented in section 6.5 and 6.6.

In addition to the PIGE method, which provides quantitative assessment of the boron areal density, the intensity of down-scattered neutrons from deuteron-boron

reactions was found to correlate with the AIMS gamma measurements for boron. While AIMS photopeak analysis provides unambiguous, quantitative boron measurements, the neutron detection provided significantly better counting statistics. The two measurement techniques were therefore combined in order best quantify the time-evolution of boron in C-Mod. Furthermore, the external PIGE measurements were combined with relative boron measurements from neutron scattering to provide a statistically significant validation of the quantitative capability of AIMS photopeak analysis.

6.1 AIMS and PIGE Geometry

Measurements were taken at 4 poloidal locations for the majority of the AIMS runs spanning the maximum range of beam deflection allowed by toroidal field coils' DC power supplies. The calculated trajectories are shown projected on the midplane and poloidal plane in figure 6-1. The steering, target geometry, and detection parameters for these target locations were calculated with the methods described in chapter 5 are given in table 5.3. A poloidal sweep with finer spatial resolution was also performed over 9 locations spanning the same poloidal extent. The locations that were studied with AIMS and with PIGE are overlaid with the inner wall tile-map are shown in figure 6-2.

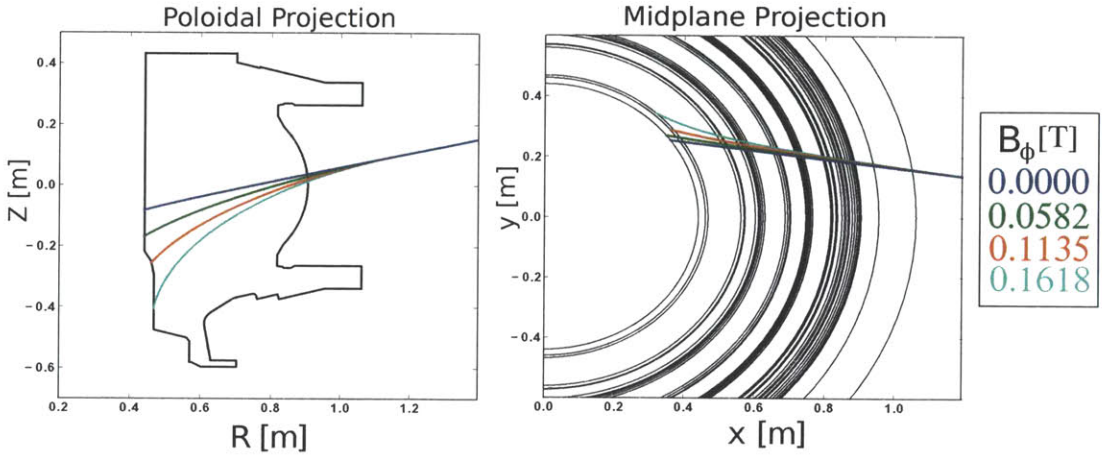

Figure 6-1: Calculated Beam trajectories for the four most common trajectories used for AIMS measurements on Alcator C-Mod.

6.2 AIMS and PIGE Timeline

AIMS measurements were taken before, during, and after the last run day of the 2012 C-Mod campaign to measure changes in PFC surfaces on the 1 run day timescale and demonstrate the feasibility of inter-shot AIMS measurements. A timeline for these measurements and plasma operations is given in table 6.1. In the months follow-

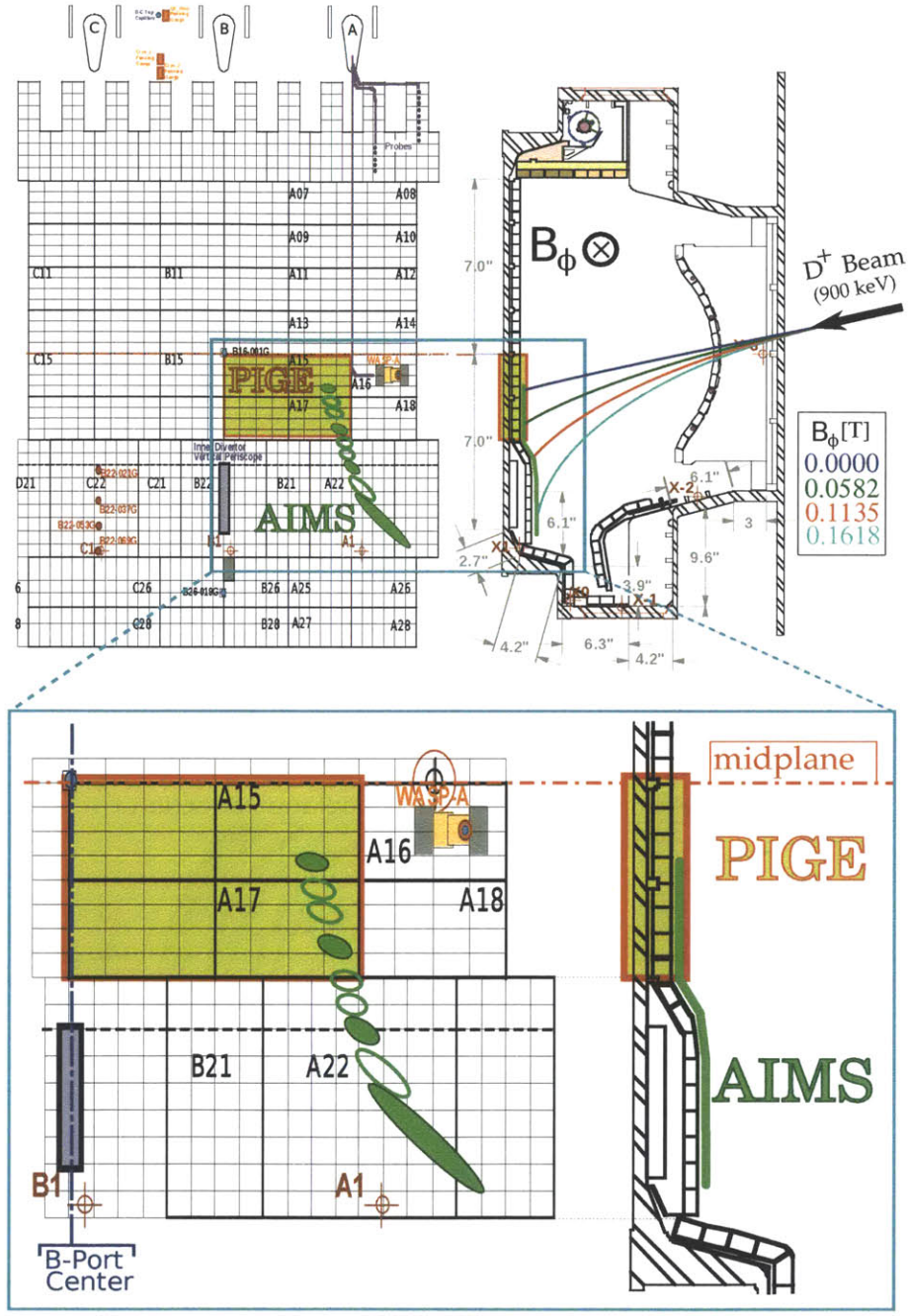

Figure 6-2: Top: Tile map of the C-Mod inner wall, upper divertor, and lower divertor EF-1 shelf, toroidally spanning the A,B, and C port regions. Bottom: Zoomed-in tile map showing the locations of the PIGE and AIMS measurements. Top Right: Deuteron beam trajectories are shown for four trajectories spanning the range of the AIMS measurements. The tiles highlighted in yellow/red were removed and PIGE analyzed following AIMS measurements. The green ellipses indicate the calculated location and beamspots for AIMS measurements based on modeling (chapter 5). The filled ellipses represent the four locations used for the majority of the AIMS measurements corresponding to toroidal beam steering fields $B_\phi = \{0.000, 0.0582, 0.1135, 0.1618\}$ Tesla (in order from top to bottom).

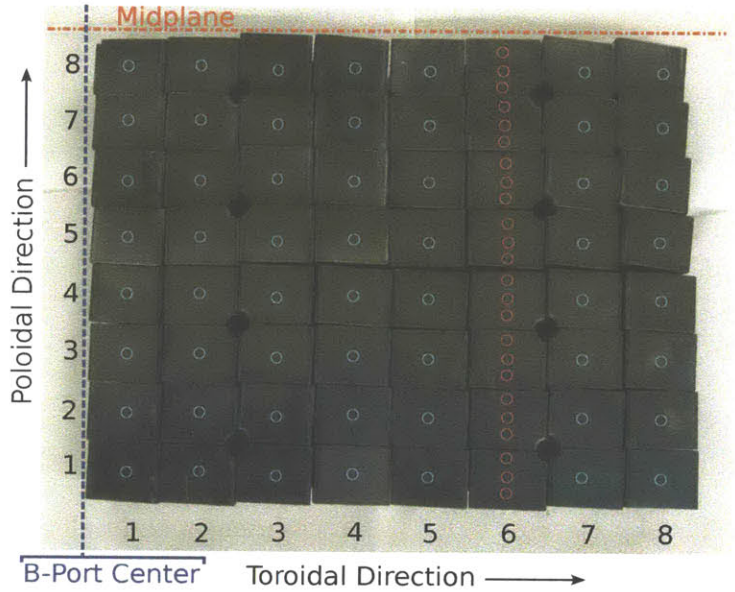

Figure 6-3: Photograph of PIGE analyzed tiles: Circles represent beam spot sizes and locations for each measurement. Refer to figure 6-2 for tile locations in C-Mod.

ing the campaign two boronizations were performed in an attempt to measure the amount of deposited boron during the boronization process. This was followed by two electron cyclotron discharge cleanings (ECDC) and a glow discharge cleaning (GDC) to observe boron erosion and/or the effects of these standard wall conditioning techniques. A timeline for these measurements and plasma wall conditioning operations is given in table 6.2.

Date	Event	Expected Effect
10/01	**AIMS measurements at 4 locations**	–
10/02	18 lower single null shots	Unknown
10/02	**AIMS measurements at 1 location**	–
10/02	2 Inner wall limited (IWL) shots	Erosion
10/02	Attempted IWL shot resulting in disruption	Erosion
10/02	**AIMS measurements at 1 location**	–
10/02	2 Inner wall limited shots	Erosion
10/03	**AIMS measurements at 4 locations**	–

Table 6.1: Timeline of AIMS measurement during the 2012 C-Mod campaign. Red represents processes that are expected to cause net erosion. The effect of the lower single null discharges on the inner wall is unknown and is shown in green.

Date	Event	Expected Effect
10/11	**AIMS Poloidal Sweep: 9 locations**	–
11/12	**AIMS measurements at 4 location**	–
11/12	Standard Overnight Boronization	Deposition
11/13	Inner Wall Overnight Boronization	Deposition
11/14	**AIMS measurements at 4 location**	–
11/14	Electron Cyclotron Discharge Cleaning (ECDC)	Erosion
11/15	**AIMS measurements at 4 location**	–
11/15	Electron Cyclotron Discharge Cleaning (ECDC)	Erosion
11/15	**AIMS measurements at 4 location**	–
11/15	Glow Discharge Cleaning (GDC)	Erosion
11/16	**AIMS measurements at 4 location**	–
12/12	**64 inner wall tiles removed followed by PIGE analysis**	–

Table 6.2: Timeline of post-campaign AIMS measurement and wall conditioning. Red and blue represent processes that are expected to cause net erosion and deposition of boron, respectively.

6.3 AIMS Photopeak Analysis: Boronization and Wall Conditioning

Gamma spectra taken with the lanthanum bromide ($LaBr_3$) detector were analyzed to observe the 953 keV gamma peak from the $^{11}B(d,p\gamma)^{12}B$ reaction. Using the methods described in chapter 2 section 2.6, the integrated counts in these peaks and the geometric parameters given is table 5.3 were used to calculate the areal density of the boron on the tiles. A typical spectrum used for quantifying boron is shown in figure 6-4. The following features are observed in the spectrum and are denoted by their gamma energies:

- 953 keV: Photopeak from the $^{11}B(d,p\gamma)^{12}B$ reaction used for quantifying boron with AIMS.
- 511 keV: annihilation gammas produced from β^+ decay of short-lived reaction products from deuteron induced reactions or nearby pair-production.
- 847 keV: Inelastic neutron scattering $^{56}Fe(d,n'\gamma)^{56}Fe$ from steel structural materials in C-Mod.
- 661 keV: Gamma emission from ^{137}Cs calibration source. This source is intentionally placed beside the detector during the AIMS measurements for energy calibration
- 1173 keV and 1332 keV: Gamma emission from ^{60}Co calibration source for energy calibration (only distinguishable in spectra when beam is off).

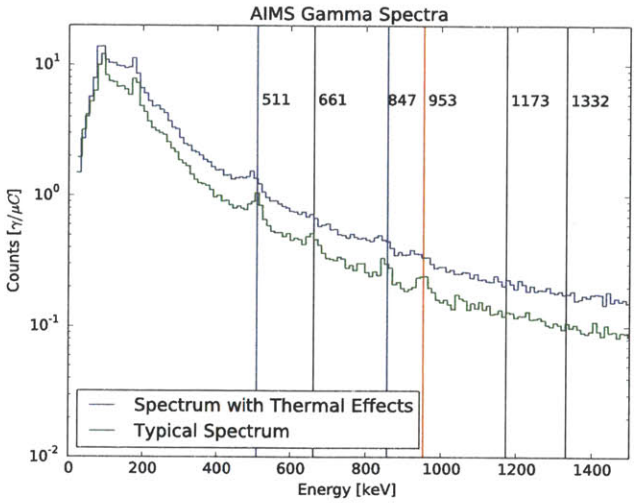

Figure 6-4: Plot of gamma spectra from two different AIMS measurements. In the typical spectrum a 953 keV photopeak from the $^{11}\mathrm{B}(d,p\gamma)^{12}\mathrm{B}$ reaction is observed. From the spectrum that is blurred by thermal drift in the gain, the 953 keV peak and other features cannot be easily distinguished from background.

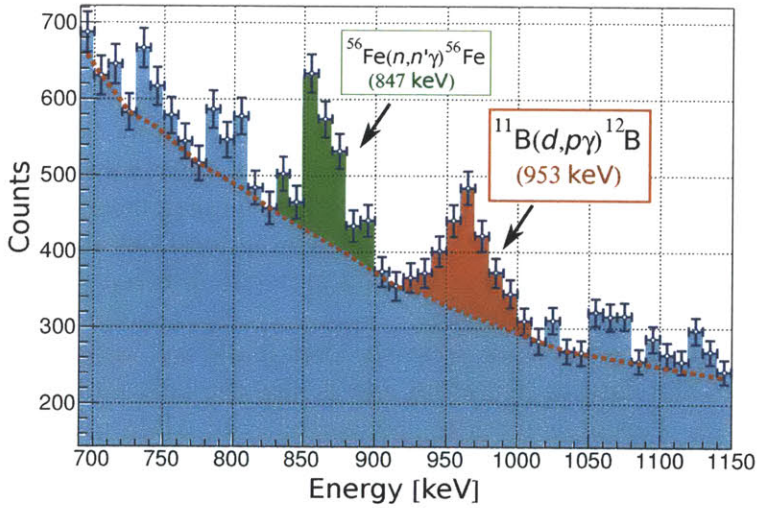

Figure 6-5: Close up view of a 953 keV photopeak in an AIMS gamma spectrum from the $^{11}\mathrm{B}(d,p\gamma)^{12}\mathrm{B}$. Poisson error bars are shown for each bin and demonstrate that the peak is statistically significant and distinguishable from background. The 847 keV gammas from inelastic neutron-scattering off iron is also visible and clearly distinguishable from the 953 keV photopeak.

The observed 953 keV gamma peak has relatively few counts compared to the large continuum from scattered gammas which is a consequence of the high reaction

yield and small detector solid angle. The peak, however, is statistically significant as can be seen in close up of the gamma spectrum in the neighborhood of 953 keV, shown in figure 6-5. Despite the low number of counts (typically 800-1000 counts), leading to Poisson uncertainty of up to ±3.5%, the peak uniquely identifies and quantifies the boron content.

The Boron areal density from the post campaign measurements, taken between boronization, ECDC, and GDC conditioning operations are shown in units of boron thickness in figure 6-6. These constitute the first-ever in-situ quantitative measurement of solid surface properties in a fusion device using ion beam analysis. Some of these data are missing because of issues that arose due to the temperature fluctuations in the silicon photodiode of the $LaBr_3$ detector. A spectrum that was blurred from thermal drift of the detector gain is shown plotted next to a spectrum measured with stable gain for comparison in figure 6-4.

The detector temperature instability was likely due to radiative heat transfer between the vessel and the re-entrant tube with temperature fluctuations caused by liquid nitrogen cooling used for C-Mod's coils and heaters used to prevent icing around the ports. Despite using compressed air to cool the detector and provide a stable temperature, the temperature fluctuations caused the detector's gain to shift over the course of some of the measurements causing the peaks to be blurred into the background signal. This identifies a design issue that can be addressed in future implementations of AIMS with thermal engineering solutions.

6.3.1 Discussion of Photopeak Results

The photopeak results in figure 6-6 show that the measured boron at the first two locations ($B_\phi = 0$ T and $B_\phi = 0.582$ T) are approximately $300 - 400$ nm. This observation appears promising because the range of their values shows reasonable agreement with the well established external PIGE measurements of boron described later in section 6.5. Also, comparing between spatial locations and within each location, there are statistically significant spatial patterns observed as well as changes at each location due to wall conditioning.

The boron 953 keV photopeak is clearly identifiable and integrable in the spectra corresponding to the data in figure 6-6 and is also the only major (d, g) photopeak that is observable. This demonstrates the capability of AIMS to detect boron, while validating the assumption that boron is the dominant low-Z, non-fuel isotope in C-Mod while oxygen, nitrogen, and carbon are negligible in comparison.

The measurements also directly demonstrate a dynamic range of AIMS measurements from 50 nm ($B_\phi = 0.16$ T, lower divertor) to 500 nm ($B_\phi = 0$ T, near the midplane). Furthermore, based on the correlation derived in section 2.6.3, the range should not be limited to 500 nm and should extend to around 8000 nm. Since boron on C-Mod tiles typically forms layers that are less than several μm thick, this dynamic range meets and exceeds the requirements for quantitative boron measurement in C-Mod.

The successful analysis of these photopeaks demonstrates the quantitative boron detection capability of AIMS. The level of uncertainty in the data and missing data

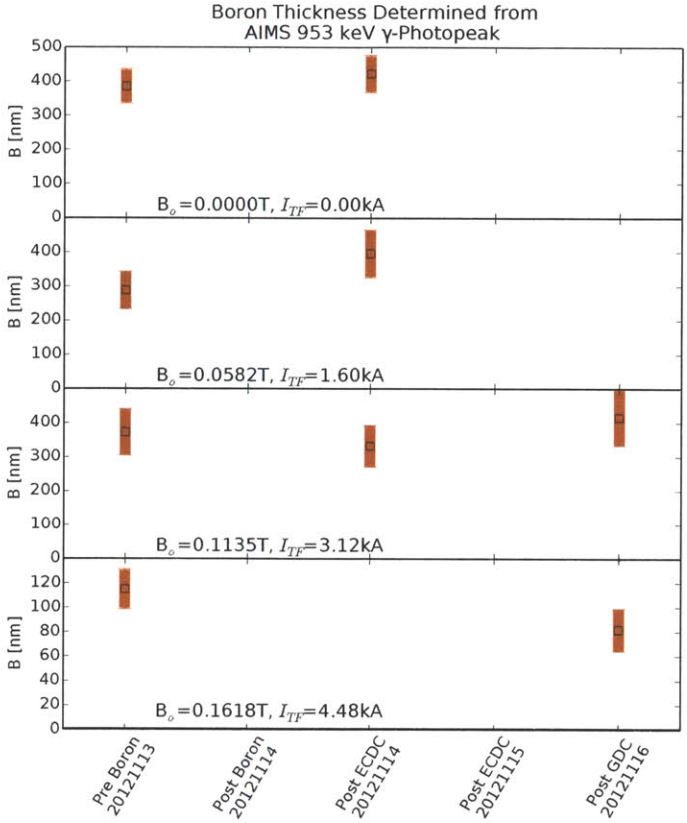

Figure 6-6: Boron thickness determined with AIMS at four poloidal locations from measurements of the 953 keV $^{11}\mathrm{B}(d, p\gamma)^{12}\mathrm{B}$ photopeak.

in the boron time history highlight the need for resolving the thermal drift issues and improving the counting statistics of the measurement.

6.3.2 AIMS Neutron Detection of Boron

With the success of the photopeak analysis in detecting boron as well as the experimental issues preventing the photopeaks from producing a complete boron time history, AIMS neutron analysis was studied as a method to corroborate and improve upon the photopeak results.

Energy resolved measurement of the neutrons were taken concurrently with the gamma measurements using an EJ301 liquid organic scintillator coupled to a photomultiplier tube residing outside of the C-Mod field coils. The details of the neutron detection equipment and theory are given in [21]. Though these neutron spectra do not contain distinct features that identify boron, the integral of the high energy neutrons in the spectra are suspected to be indicative of the boron content. This technique was demonstrated then used to make relative measurements of boron to extrapolate trends between the sparse gamma data.

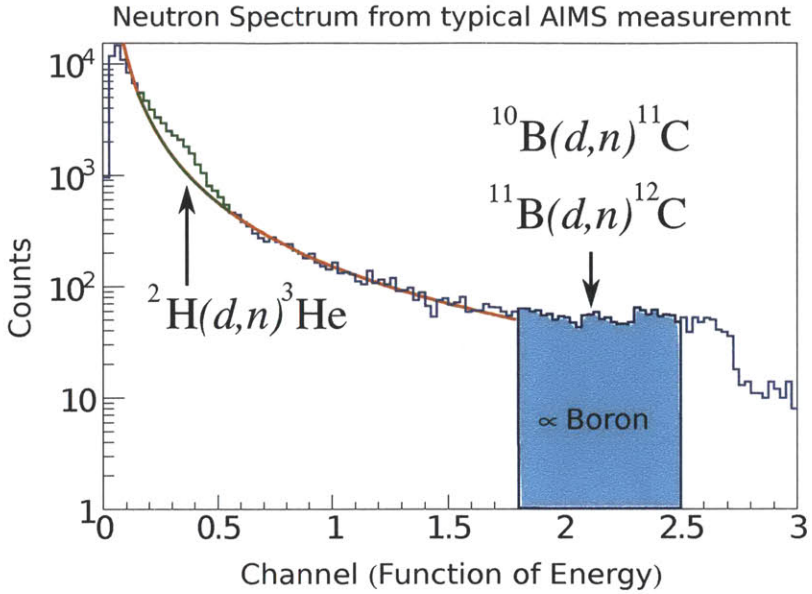

Figure 6-7: Relative measurements of boron are made from the AIMS neutron spectra by integrating the high high energy portion of the spectrum shown in blue, corresponding to neutron from the $^{10}B(d,n)^{11}C$ and $^{11}B(d,n)^{12}C$ reactions. The 'channels' on the spectrum correspond to the binning of charge output from the detector which is related to scintillator light output and is a non-linear function of energy. The region of integration shown from 1.8 - 2.5 corresponds a region of in which only neutrons from boron are energetically allowed [21].

Making neutron-based measurements of boron by simply integrating a certain segment of the neutron spectrum is not possible in general. However, it is possible in C-Mod because 0.9 MeV deuterons can only react with a few low-Z isotopes that are present on PFCs due to C-Mod's strict high-vacuum and impurity requirements. Only boron and deuterium should be present with trace amounts of oxygen which can emit neutrons through the reactions shown in table 6.3. The lack of other low-Z isotopes was also verified with the photopeak measurements.

Boron Reactions	Q [keV]	Other Reactions	Q [keV]
$^{10}B(d,n)^{11}C$	6464.804	$^{2}H(d,n)^{3}He$	3268.914
$^{11}B(d,n)^{12}C$	13732.283	$^{16}O(d,n)^{17}F$	-1624.296
$^{11}B(d,n\,2\alpha)^{4}He$	6457.542		
$^{11}B(d,n\,\alpha)^{8}Be$	6365.701		

Table 6.3: Deuteron induced neutron-producing reactions and their Q-values for low-Z isotopes on C-Mod PFCs.

The oxygen reaction is not energetically allowed and the maximum energy for neutrons from d-d fusion is lower than Q-value for the boron reactions. Assuming that these are the only reactions present, it follows that any detected neutron with

energy greater than the Q value of the $^2\mathrm{H}(d,n)^3\mathrm{He}$ reaction plus the beam energy is guaranteed to have been produced in a boron reaction due to kinematics and conservation of energy. Integrating the continuum of scattered neutron counts in the high energy region of the spectrum (figure 6-7), therefore, should give a result that is proportional to the amount boron that is present. In addition, the large neutron to gamma yield ratio for boron provides measurements with better Poisson statistics than the gamma photopeaks.

Proportionality of Neutron and Gamma Measurements

The correlation between neutron and gamma measurements must be demonstrated before neutron spectra can be used together to quantify boron. For each AIMS measurement location and AIMS run where valid gamma and neutron data were available (i.e. identifiable photo peak and sufficient RF power in the accelerator), the relationship between gamma counts N_γ and neutron counts N_n were compared. This comparison is shown in figure 6-8 where each point represents an AIMS measurement where N_n and N_g were measured simultaneously with the same target, beam current, and acquisition time.

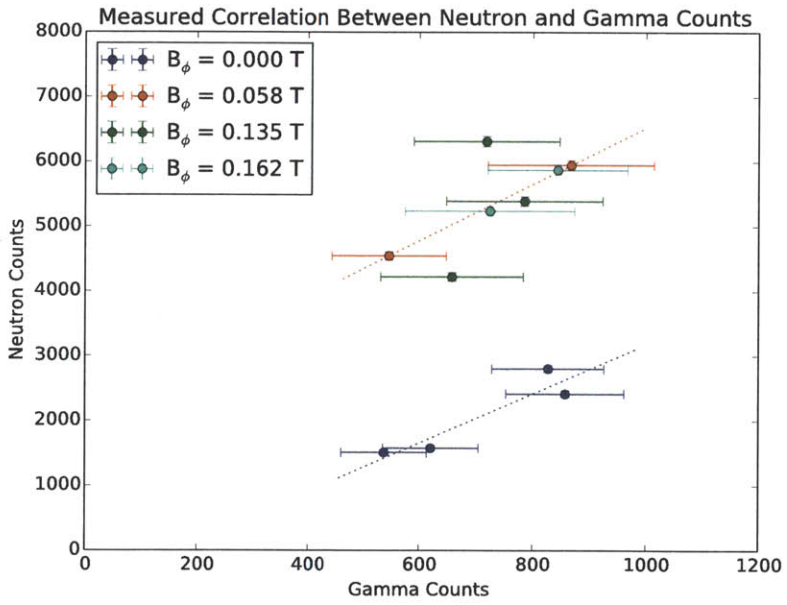

Figure 6-8: Measured correlation between neutron N_n and gamma N_γ counts from AIMS measurement at four locations. Each point represents an AIMS measurement where N_n and N_γ were measured simultaneously with the same target, beam current, and acquisition time. A linear fit is drawn for data sets that show a statically significant correlation.

Observing the relationship between the neutrons counts N_n and gamma counts N_γ shows that, for the zero field case and the 0.058 T case, there is a clear, sta-

tistically significant correlation between between the two detection techniques which appears to be linear, tracking a 50% change in boron induced counts. This confirms the proportionality relationship $N_n \propto N_\gamma$. For the other two target locations with steering fields, fewer gamma points were available, and the counting uncertainty in the photopeaks is relatively large. This made it more difficult to conclusively establish the proportionality between the N_n and N_γ measurements, although within the statistical uncertainty, the results do not disagree with the proportionality.

The physics is essentially identical between each location, only differing in beam and detection geometry. There is also no physical reason to expect that another element to be present at only specific locations which could contribute to the neutron continuum. It is therefore likely that likely that a proportionality relationship exist for each of the four locations.

From studying the results from these four locations in figure 6-8, it is also clear that the proportionality of the measurements between N_n and N_γ does not remain the same between locations. This is not unexpected and is likely due to a variety of factors including the angular dependence of the cross sections, detection geometry, complex neutron scattering geometry, and differing mean free paths of neutrons and gammas in the presence of obstructions in the detection geometry.

As a result of establishing the relationship between N_n and N_γ, this simple integration of the high energy neutron counts can thus be used to provide a relative measurement of boron content that can be absolutely calibrated from the gamma photopeaks to allow trends in the boron evolution to be studied in the absence of a contiguous set of gamma measurements.

Boron Time History with Neutron and Gamma Data

The integrated high energy neutron counts, measured after each plasma wall conditioning operation are shown in figure 6-9 at 4 beam locations. The data shown are neutron yields. The data shown are neutron yields, i.e. the neutron counts have each been individually normalized to the integrated beam current at each measurement. Then, at each spatial location, the data are scaled so that the final measurement occurring after wall conditioning (GDC) is set to unity. Thus these data provide a relative measurement for the time history of the boron at each location. These data provide a relative measurement of time history of boron. Normalizing to the final AIMS measurement is arbitrary but it is convenient for the first two traces because they can be calibrated to the PIGE measurements taken at the same locations to compare to the AIMS photopeak measurements, as described in section 6.6.

As can be seen in figure 6-9 the AIMS technique can readily observe relative changes in the boron content of a few percent due the more favorable counting statistics provided by the neutron spectra. In some locations the changes are modest, while at the lowest measurement point the boron changes by over a factor of two. This is critical because it shows that the surface conditions are evolving in a complex manner even from straightforward wall conditioning techniques, thus indicating the necessity of making in-situ measurements.

Since a contiguous set of there AIMS gamma data was not available to observe

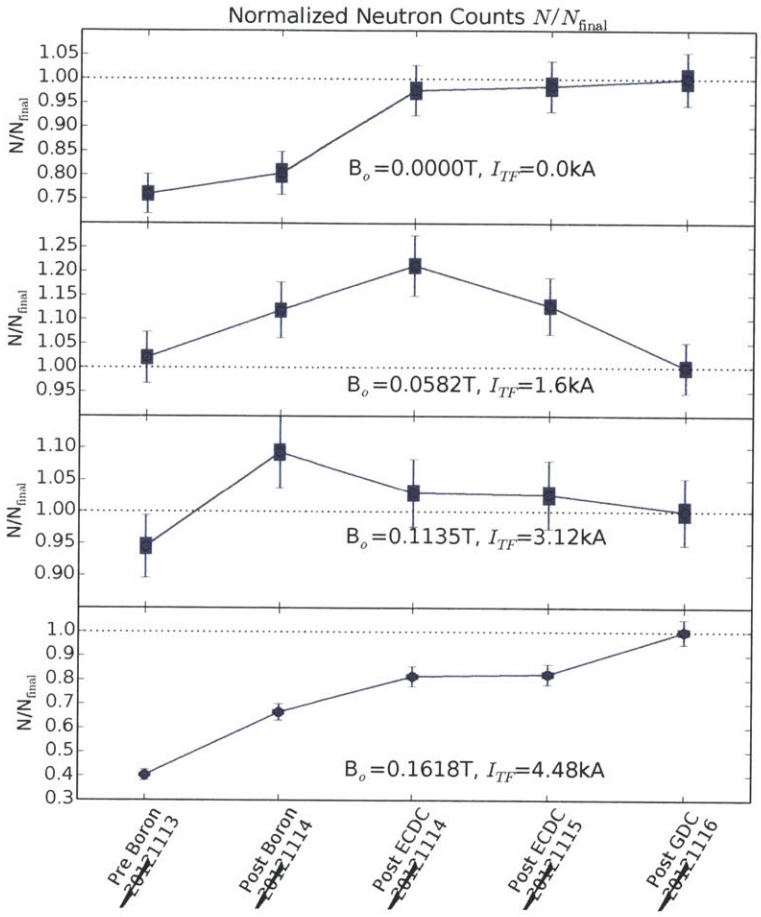

Figure 6-9: Time history of high energy neutron counts corresponding to scattered neutrons from boron reactions. The height of each marker indicates the Poisson uncertainty in uncertainty of neutron counts. The error bars represent experimental uncertainties in charge integration and beam energy calibration.

the changes in boron between every experiment, the trends in neutron data were essentially used to bridge the gaps. This was done by scaling the neutron data to best-fit the gamma data where concurrent N_g and N_n measurements were made. This is effectively equivalent to calibrating the neutron data based on the proportionally relationships shown in figure 6-8. The calibrated neutron data is given in figure 6-10 showing the boron time history spanning the post-campaign plasma wall conditioning experiments.

The error bars shown in figure 6-10 indicate the uncertainty in the absolute boron content from the neutron and gamma detection methods. These uncertainties are much larger than the relative uncertainties based on counting statistics of the neutron measurement (indicated by the height of the data markers). These large uncertainties are due to the propagated errors in normalizing the neutron count rate to absolute

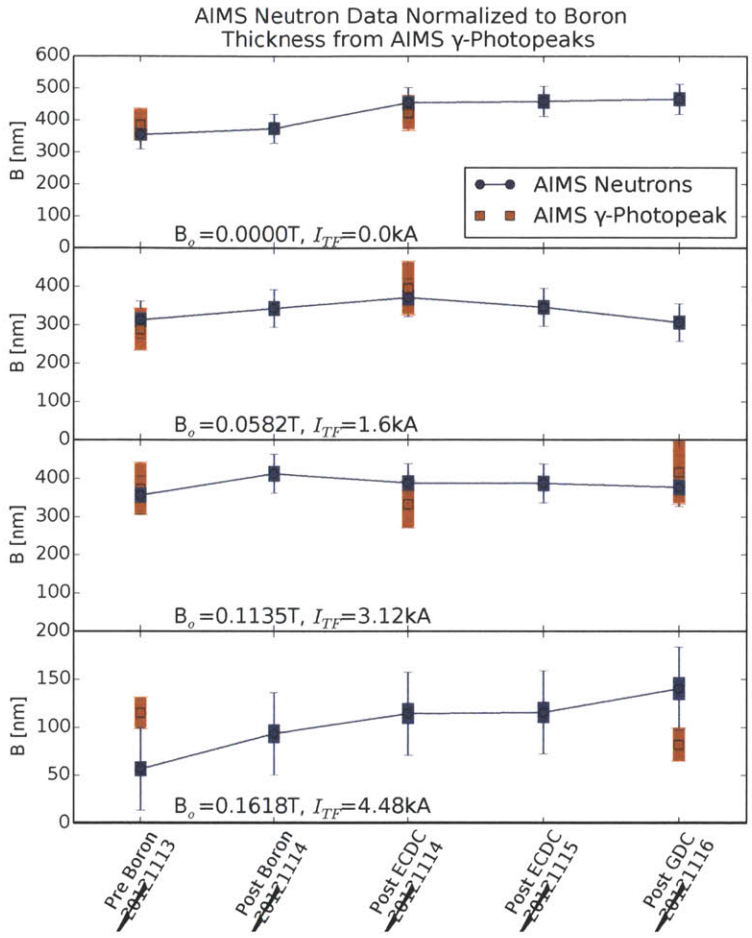

Figure 6-10: Time history of boron inferred from high energy neutron counts and calibrated to best fit the AIMS gamma results. The height of the data markers indicate Poisson error and the error bars indicate the absolute error from measurement and calibration.

boron content through the gamma detection. The uncertainty is calculated using equation 6.1 by combining the Poisson error associated with the neutron counts and current integration (1st and 2nd term), the standard error of the mean associated with the gamma measurements (3rd term) and the standard deviation of between the neutron and gamma data (4th term).

$$\frac{\Delta B_n}{B_n} = \left[\frac{1}{N_n} + \left(\frac{\Delta Q}{Q} \right)^2 + \frac{1}{M_\gamma} \sum \left(\frac{\Delta B_\gamma}{B_\gamma} \right)^2 + \frac{1}{M_\gamma} \sum (B_\gamma - B_n)^2 \right]^{1/2} \tag{6.1}$$

From these measurements, qualitatively it appears that some amount of boron may be deposited during boronization and a small amount could be removed ECDC

and GDC. Though it is difficult to make this result precise due to the large uncertainty in the measurement, it is clear that changes boron thickness can be observed on the time scale of plasma conditioning operations, especially if the uncertainty is reduced simply by improving detection statistics and solving detector issues.

The AIMS measurements show that boron deposition is limited to 50-100 nm at the innerwall. Previous studies have examined the in-situ boron deposition rate with a Quartz Micro Balance [41] and found the deposition rate to be strongly reduced just slightly radially inboard of the EC resonance layer and the peak deposition to be located at the uppper hybrid resonance, typically 5-10 cm outboard of the EC resonance. This phenomenon is illustrated in figure 6-11. While not known precisely the range of deposition rates of ~0.3 nm/minute at the EC resonance, which would extrapolate to ~ 36 nm based on the 120 minutes of the boronization which is consistent with the range of boron deposition measured with AIMS. This demonstrates the need for AIMS which can directly measures boron content on material surfaces (unlike the QMB). It also captures the complexities of the alignment of surface to the B field and the complexities of particle transport which are both difficult or potentially impossible to extrapolate from plasma knowledge alone.

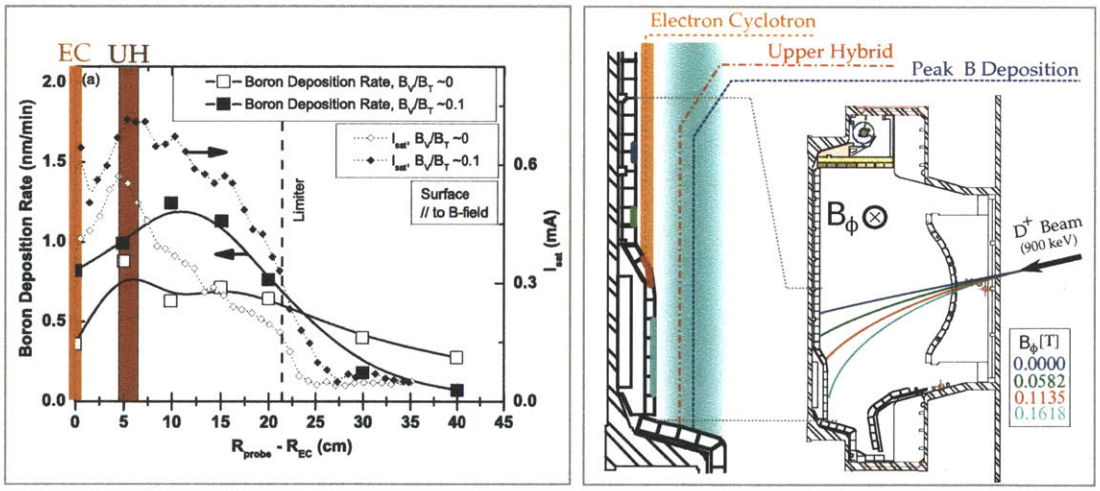

Figure 6-11: Left: Deposition profile of boronizaion measured with a quarts microbalance (QMB). Peak deposition is observed at or outboard of the upper hybrid resonance (UH) while deposition decreases sharply approaching the electron cyclotron (EC) resonance layer. The left plot was reproduced from [41] and adapted for this figure. Right: The relative position of the EC, UH, and peak boron deposition regions are shown illustrate their proximity to the AIMS measurement locations.

From these results seen in figure 6-10, it can be seen that boron wall conditioning techniques in C-Mod have relatively little effect on the boron trends at the inner wall. It is also observed that the largest boron deposition occurred at the lower two AIMS measurements which are located on the section of the inner wall that protrudes several cm radially in the direction of the expected deposition peak. Qualitatively, this result is consistent with deposition profile measured in [41]. These results, though

qualitative due to the large uncertainty, should further motivate the continued use of AIMS to better understand the complexities of even simple wall conditioning operations and should motivate the need expand and improve upon the capabilities of AIMS.

6.4 AIMS Poloidal Sweep with Single Tile Resolution

A poloidal sweep was performed with fine spatial resolution was attempted after the end of the C-Mod campaign to generate a poloidal boron profile with single tile resolution to demonstrate its feasibility. This was a sweep of all of the 9 AIMS locations shown in figure 6-2 where most of these measurements have beam spots sizes that are comparable to the size of a tile.

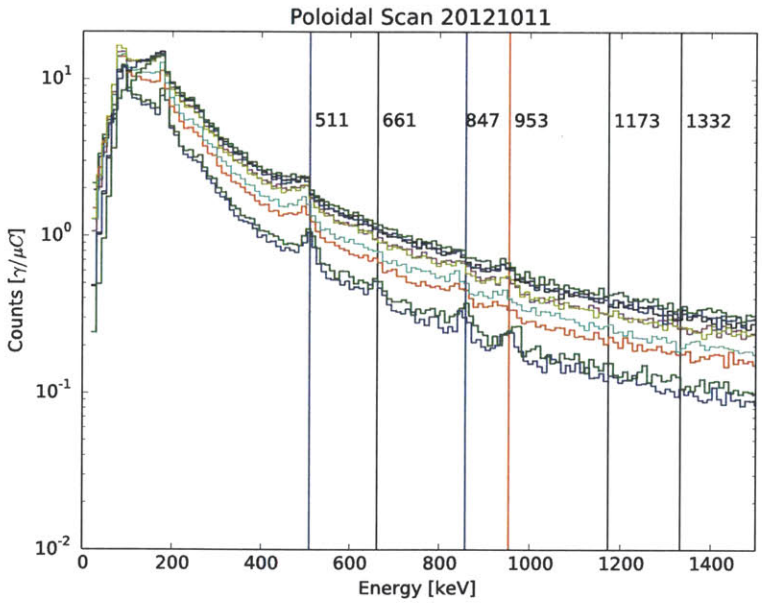

Figure 6-12: Gamma spectra from AIMS poloidal sweep with single tile resolution. It appears that, only two of these spectra have photopeaks that are suitable for quantifying boron.

Unfortunately, due to thermal effects in the detector, only two of the spectra contained photopeaks that were suitable for quantifying the boron. Since the neutron to gamma ratio clearly does not remain constant with position, as shown in figure 6-8, the neutron data could not be used to make these spatially resolved measurements.

Though generating a poloidal boron profile that include every tile along a poloidal sweep was not successful, it is important to note that, with the thermal issues in the detector resolved, a poloidal sweep with single-tile resolution should be achievable in

a straightforward manner if gamma detection is improved. This is motivated by the observation that the overall gamma count yield clearly is modified between the different locations in figure 6-12, indicating that there is indeed a complex spatial pattern of boron films evolving at the surfaces and that AIMS is capable of distinguishing the pattern.

6.5 External PIGE Results

After the 2012 C-Mod campaign, there was a brief vacuum break during which four inner wall tile modules (each with a 4×4 arrangement of tiles) were removed from the inner wall and analyzed. PIGE analysis was performed on all 64 of the available tiles. For each tile, at least one measurement was taken at the center of the plasma facing surface with a 3 mm diameter proton beam using the setup shown in figure 3-15. A photograph of the analyzed tiles is shown in figure 6-3 with outlines drawn to represent location and size of the proton beam used for each measurement.

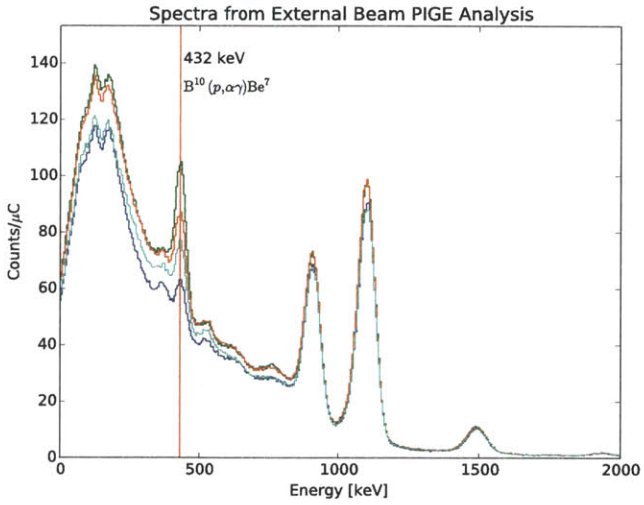

Figure 6-13: Several overlaid gamma spectra used from external PIGE measurements of boron using the ${}^{10}_{5}\mathrm{B}(p,\alpha\gamma){}^{7}_{4}\mathrm{Be}$ reaction. The three higher energy peaks are reactions induced in the aluminum structure supporting the beam window.

Typical spectra from these PIGE measurements are shown figure 6-13. From these spectra the 432 keV gamma peaks from the ${}^{10}_{5}\mathrm{B}(p,\alpha\gamma){}^{7}_{4}\mathrm{Be}$ reaction can clearly be observed. These peaks were background subtracted and integrated using peak integration routines in the Maestro spectroscopy software package from ORTEC [42].

These peaks typically contain $\sim 5 \times 10^4$ counts so Poisson error in the peak and current integration typically contributes $< 1\%$ error. Other experimental uncertainties also contribute but are relatively small, giving typical uncertainties of $\pm 3\%$.

The correlation derived in section 2.5.5 was used to convert the gamma yields from these measurement to areal density of boron. The areal density is represented

as 'boron thickness' assuming that the boron is found in a uniformly distributed surface layer of pure boron of where 1 nm = 1.30×10^{20} atoms/m^2. Due to low experimental uncertainty of these measurements, PIGE analysis provides reliable boron measurements that can be used to understand spatial pattern on PFC and can be compared to AIMS for validation.

6.5.1 PIGE Poloidal Scan

The first result shown is from a poloidal sweep that was performed with finer spatial resolution in column six to observe spatial variation in boron thickness within tiles. The results of these measurements are shown in figure 6-14. The top plot shows the gamma ray yield from the tiles, normalized to the thick target yield from a solid boron nitride (BN) target with error bars indicating only the Poisson error and the lower plot shows the boron thickness with experimental uncertainties included.

These measurements show that, in this region of the inner wall, the boron thickness is $\leq 1\mu$m for most tiles but in some cases thick as ~ 3 μm. For many tiles the boron is fairly uniform however boron thickness varies by as much as a factor of two within a single tile. From this result, it is clear that for adequate diagnosis of PMI issues, tile-sized resolution or better is required. This reinforces the importance of the efforts and contributions of this thesis to provide adequate spatial resolution through advanced beam dynamics calculations.

Since each PIGE measurement only corresponds to a 3 mm diameter beam spot while AIMS measurements typically have a tile sized beam spot, it is important quantify how much the boron varies, on average, within a tile. This provides the uncertainty in the AIMS validation process due differing spot sizes between AIMS and PIGE.

The tiles with greater than $1 - 2$ μm of boron tend to have the largest boron variation and appear to be amorphous crystalline layers of boron. Whereas, tiles with < 1 μm to be more uniform, possibly due to a different boron erosion or deposition mechanism.

Since all of AIMS gamma measurements and all PIGE measurements in the vicinity of the AIMS beam spots showed less than < 1 μm of boron, the tiles measured in the poloidal sweep with < 1 μm of boron were used to infer the boron variation within each tile. For each of these tiles, the standard deviation in boron thickness measured with PIGE between the three location on each tile is between 5% and 28% with an average of 17%. Even though the uncertainty in boron measurements from PIGE is very small, the uncertainty in the comparison of absolute boron measurements between AIMS and PIGE is expected to be on the order of 17%.

6.5.2 2-D Tile Map of Post Campaign Boron Areal Density

After performing a poloidal scan of the tile modules a PIGE measurement was made in the center of each of the 64 available inner wall tiles. The resulting map of measured boron thickness (areal density) is shown in figure 6-15. These measurements were

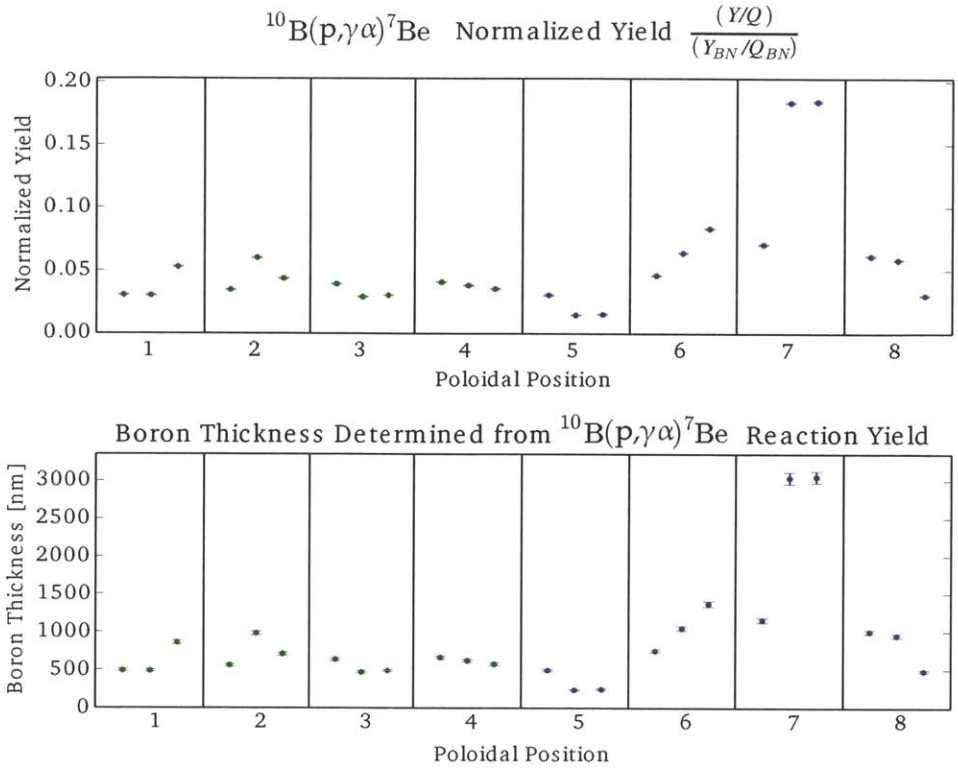

Figure 6-14: Top trace: poloidal profile of normalized gamma yield from the sixth column of tiles. Bottom: poloidal profile of boron areal density represented in boron thickness (assuming a solid boron surface layer).

also used to provide a direct comparison to validate the AIMS technique against the proven PIGE analysis techique as described in section 6.6.

The tile map (figure 6-15) shows a significant variation in boron between tiles. Some tiles have been polished by the plasma to extent where they have no detectable boron and other tiles have several microns of boron present. This means that over the course of a campaign, inner wall tiles can experience anything from net deposition rates on the order of several nanometers per second ($\sim$1 cm/year) to net erosion that is sufficient to leave tiles devoid of boron. This result further motivates the necessity of diagnosing and understanding the changes is PFC surfaces on timescales that are shorter than a run campaign with tile sized spatial resolution.

From observing the tiles visually, it appears that the misalignment of the tiles is quite small and could be be due to disruption induced eddy current forces. However the PMI involve magnetic fields that intercept the surfaces with such shallow angles in this region (and in general for divertor surfaces) that even these small misalignments can greatly change the local balance of erosion and deposition as well as plasma heat flux. This demonstrates how critical the effects of PMI are and further motives diagnostics like AIMS which provide 2-D mapping of the surfaces.

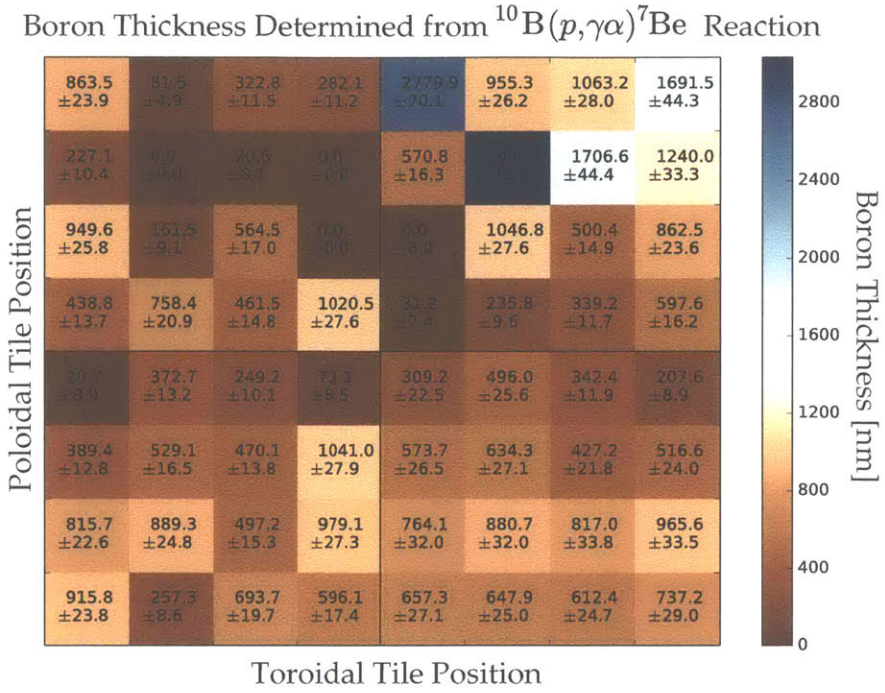

Figure 6-15: Boron thickness measured with external proton beam PIGE analysis

6.6 Quantitative Boron Measurements with Combined AIMS and PIGE Results

The locations of AIMS measurements corresponding to no steering field and 0.0582 Tesla overlap with the boron map that was made from PIGE measurements. Since boron was measured with neutrons and gammas from AIMS followed by measurement with the established PIGE technique at these locations, these overlapping measurements serve as validation of the AIMS technique.

Since the AIMS gamma results provide a quantitative boron measurement from the photo peak, they should be compared directly to the PIGE boron measurement. At these two overlapping PIGE/AIMS locations, however, the spectra from the final AIMS measurements could not provide an adequate photopeak due to the temperature drift issue discussed earlier. Instead, a slightly different strategy was employed. Using data from ex-situ PIGE results to be the absolute B thickness after the campaign, neutron data was used to extrapolate backward in time. This extrapolation provided and quantitative time history of the boron thickness while also providing a means to compare AIMS gamma photopeak results to another quantitative technique for validation.

6.6.1 Uncertainty in Beam Target Location

To make a valid comparison between PIGE and AIMS measurements, the same locations must beam locations must be compared.

The accelerator, beamline, and optics were aligned as precisely as possible with respect to the beam injection flange on B-port using engineering resources that were available. However, it was not possible to align the accelerator directly with a point of reference on the C-Mod inner wall. This meant that the accelerator could only be aligned with respect to the beam injection flange.

Measurements of the beamline showed that the last flange on the beamline before the vacuum bellows was parallel to the injection flange to within better than $\pm 0.7^o$, indicating good alignment (considering the accelerator is a 400 pound device mounted on slightly compliant floor). However, the welding of either flange, uneven compression of copper gaskets attaching the flanges, and other such uncertainties could compound to cause a misalignments of $> 1^o$. In terms of wall position this could mean that the location on the PFC targets could be off by $\sim$1 C-Mod tile width from the design location.

A photograph of the view through the injection flange (figure 6-16) was used to make an estimate of the actual alignment of the beam. The photograph was taken approximately concentric with the injection flange after the accelerator was removed and was analyzed to predict the location of the beamspot with no steering fields. This image indicates that the beam was likely misaligned such that the no-field trajectory intercepted the wall roughly one tile above the location expected from the engineering design of the injection flange even though it is within design tolerances. This location, indicated by figure 6-16, was taken to be the true location of the beamspot with no steering fields. This observation also motivates the need for an optical method of in-situ beam alignment and calibration.

6.6.2 Validation of Neutron and Gamma Results

The AIMS neutron data with a relatively high number of counts was shown to be correlated with the photopeak in section 6.3.2. As demonstrated in section 6.3.2, neutron data can therefore be used to make quantitative measurements of boron if the are scaled to known absolute measurements.

Gamma measurements were not available after the final GDC that occurred before PIGE analysis for a direct comparison. However, post GDC neutron measurement were successful. Therefore, in order make a quantitative comparison between AIMS and PIGE, the neutron data was scaled so that the final neutron measurement matches the boron thickness measured with PIGE.

This neutron time history was calibrated to the trusted PIGE measurement and could therefore be used to extrapolate the boron thickness from the time of the final vacuum break, past the wall conditioning operations to where the AIMS photopeaks were observed. Though the PIGE measurements have very small error bars, the uncertainty in the comparison between AIMS beamspots and PIGE is dominated by the estimated $\sim$17% inherent uncertainty in the comparison due to the vastly different beam spot sizes (described in 6.5.1).

For the PIGE locations that were determined from photographic analysis of the beamline, this comparison is shown in figure 6-17. The same comparison is shown in figure 6-18 for the PIGE locations that are predicted from the engineering design

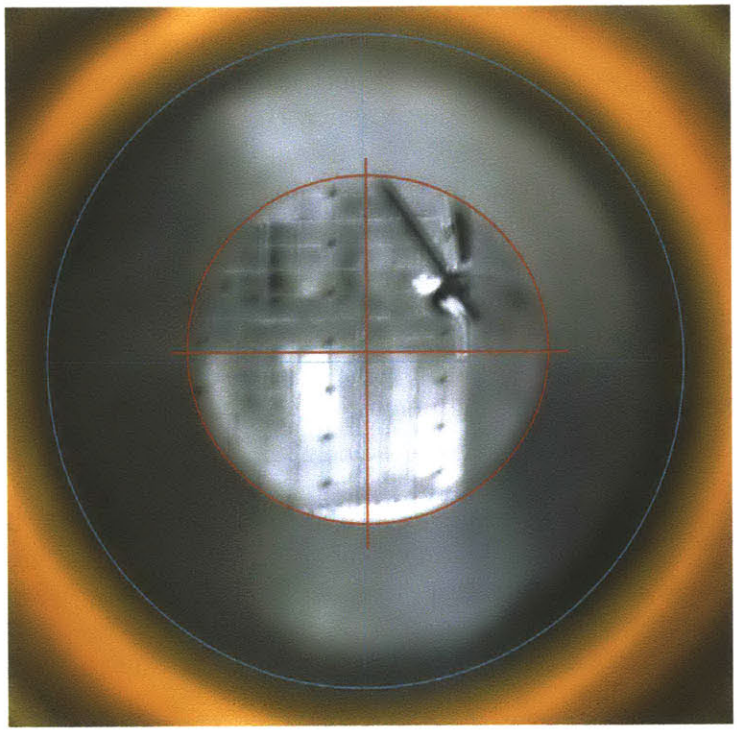

Figure 6-16: Photograph taken concentric to the beam port indicates that the no-field beam trajectory intercepts the wall one tile above the original engineering design. This offset is within the expected tolerances.

assuming perfect alignment.

Figure 6-17 shows that three of the four boron measurements made from the photopeaks agree with the combined neutron-PIGE results within the uncertainty of the measurements. Whereas, figure 6-18 shows a correlation that is physically inconsistent.

Despite the uncertainty in the beam alignment with the locations of the PIGE measurements and the differing spot sizes, this result is a strong indication that the AIMS analysis yields a real and quantitative in-situ measurement of boron; a milestone achievement for AIMS and a significant advancement for the field of PMI research.

6.7 AIMS Intershot Measurements

A major goal of developing the AIMS technique was to observe changes on PFC surfaces between plasma shots. Inter-shot measurements were attempted on the last day of the C-Mod 2012 campaign at one PFC location with no beam steering fields. The time line of these measurements is shown in table 6.1. A measurement was made before the run day, then after the 18 lower single null I-Mode discharges, then after two inner wall limited plasmas including a disruption, then following the run day after

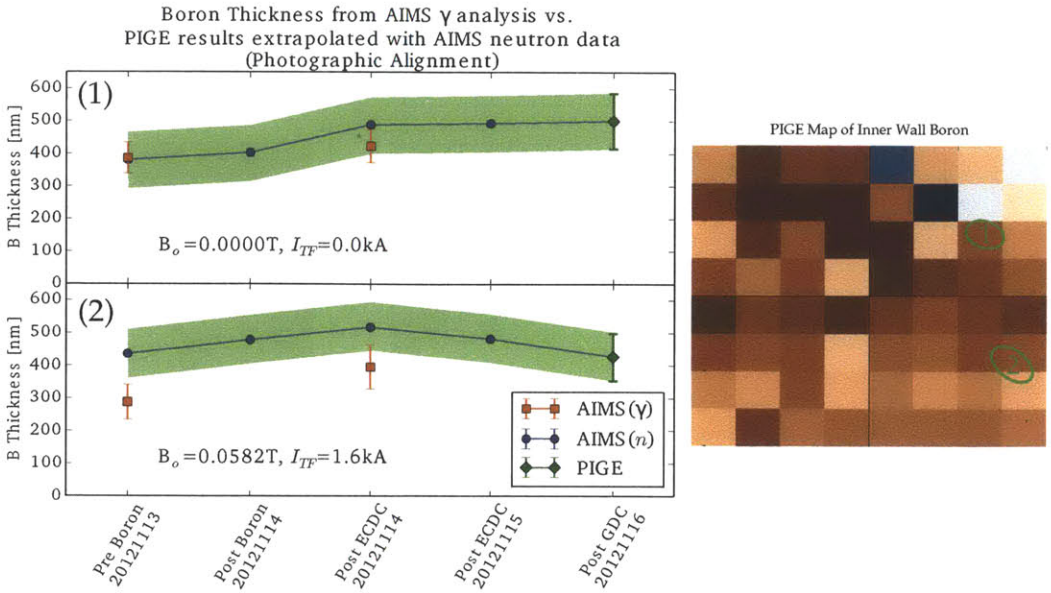

Figure 6-17: Left: Boron time history comparing AIMS(γ) photopeak results to PIGE measurements by scaling AIMS(n) neutron data for extrapolation. AIMS neutron data were scaled to match the final PIGE measurements. The shaded green area represents the inherent uncertainty in the comparison due to the differing beam spot sizes between PIGE and AIMS. Right: Map of boron measured with PIGE analysis with overlaid AIMS beamspots. The AIMS beamspots were assumed to be at the location that is indicated by a photograph taken concentric to the beam injection port (one tile above the design location).

two more inner wall limited discharges. The inner wall limited discharges were done specifically to attempt to remove boron, and the disruption, whil unplanned might be expected to remove boron as well.

The AIMS photopeak measurement before and after the run day were successful, however, the inter-shot photopeak measurements were not. Neutron spectra however were measured successfully for all AIMS measurements during the run day. With the relationship between high energy neutrons and photopeak gammas established in section 6.3.2, the methods in section 6.3.2 were used to calibrate the relative boron measurement from the neutrons to the absolute boron measurements from the photopeaks to give quantitative inter-shot measurements of boron. The result is shown in figure 6-19.

This result shows that the boron on the the inner wall increased by 200 nm during the first 18 I-Mode shots indicating that these shots cause net deposition. The first AIMS measurements were made on the October 2nd, the last run day of the Alcator C-Mod 2012 campaign. The plasma discharges correspond to shot numbers 1121002XXX. This run day began with a series of lower single null discharges to study I-Mode (shot numbers 1121002001-1121002024). These experiments constituted 18 full length lower single null discharges. Over these 18 discharges, the boron thickness

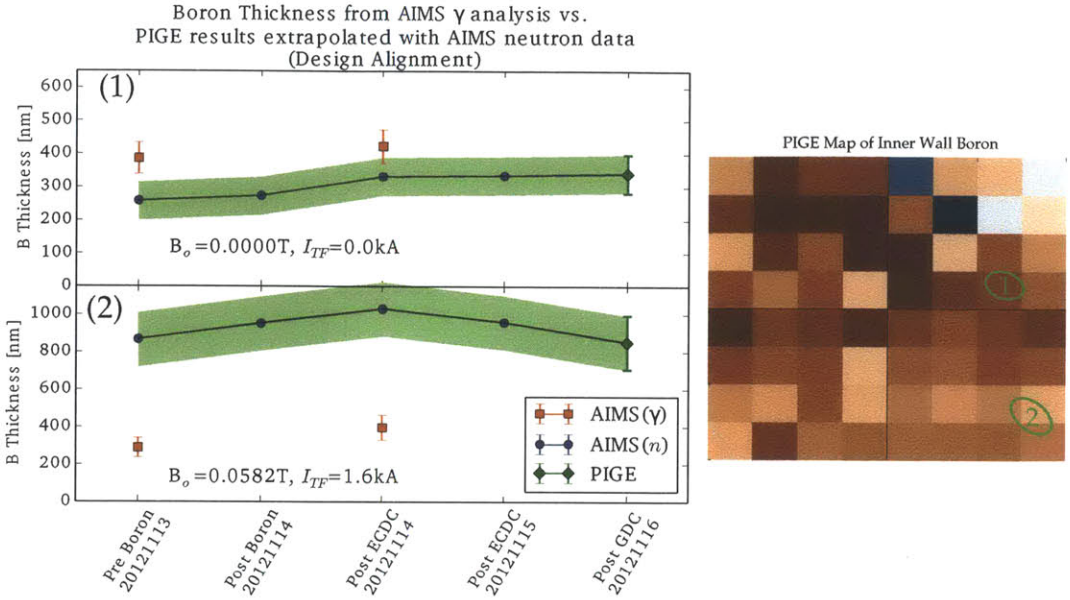

Figure 6-18: Left: Boron time history comparing AIMS(γ) photopeak results to PIGE measurements by scaling AIMS(n) neutron data for extrapolation. AIMS neutron data were scaled to match the final PIGE measurements. The shaded green area represents the inherent uncertainty in the comparison due to the differing beam spot sizes between PIGE and AIMS.The AIMS beamspots were assumed to be at the location that is expected from the design of the diagnostic

increased by 210 ± 50 nm, corresponding to an average of 12 ± 3 nm/discharge.

From the external PIGE measurements showed campaign averaged boron deposition rates on the order of 0.5 nm/discharge resulting in 500.4 nm of boron at location of the AIMS measurement. This was the integrated result over a campaign containing a variety of plasma discharges including I-mode, H-mode, and various ICRF and LHCD experiments. From an earlier study IBA study of C-Mod PFCs before the discovery of I-Mode, it was shown that tiles removed from C-Mod after a 1090 shot run campaign showed a boron areal density of 18 ± 2 [10^{22}atoms/m^2] in the region near the AIMS measurement location. This corresponds to a thickness of 770 ± 85 nm of boron with an average boron deposition rate of 0.7 nm/discharge. The simple observation that deposition rates of boron during I-mode shots were measured with AIMS to be more than an order of magnitude higher than the campaign averaged values for a campaign with and without I-Mode demonstrates that the PMI effects of any particular plasma configuration cannot be resolved with campaign integrated measurements.

Following the I-mode experiments, a series of inner wall limited (IWL) discharges were dedicated to making AIMS measurements of boron and deuterium on the centerpost on a shot-to-shot timescale. Since the AIMS analysis was limited to the centerpost due to the B field power supply limitations. Inner-wall limited magnetic configuration was chosen in order to place the location of maximum plasma-material

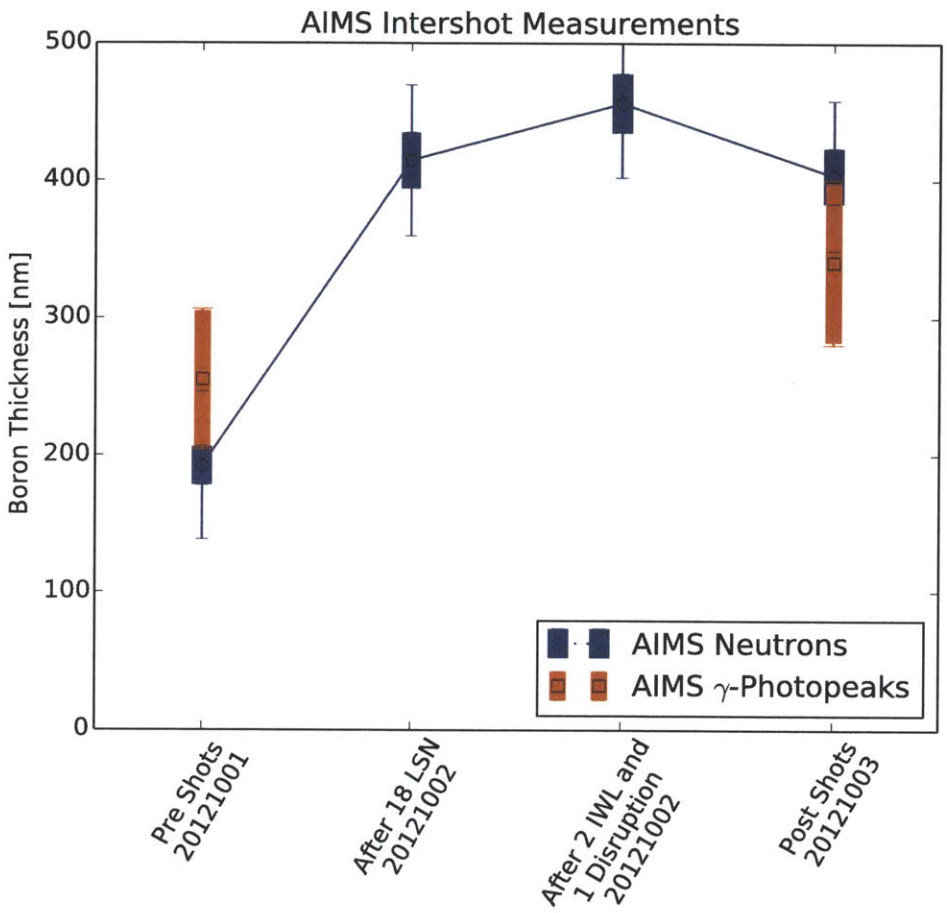

Figure 6-19: Boron measurements through out a C-Mod run day using combined neutron and gamma data to demonstrate inter-shot AIMS measurements.

interaction (recycling, erosion) near the AIMS measurement location.

However one of the discharges, 1121002030, underwent a full-current disruption at ~0.45 seconds, before the RF power was applied. The disruption was apparently caused by a high-Z injection of material into the plasma, leading the abrupt (ms timescale) termination of the plasma, depositing the plasmas energy at a rate of $>$ GW at or near the location of the AIMS measurement.

The plasma interaction with the centerpost is qualitatively interpreted by using the visible light camera (WIDE1) which views the toroidal location near B-port where AIMS also measures. The visible light, which is dominated by H-alpha emission is a relative measure of the particle flux density that is incident on the PFCs. Images from WIDE1 are shown in figure 6-20 with a the superimposed outline of the beam spot. These images show the emission from a stable inner wall limited discharges, the intense emission during the disruption and the following glow due transient heating

of the tiles.

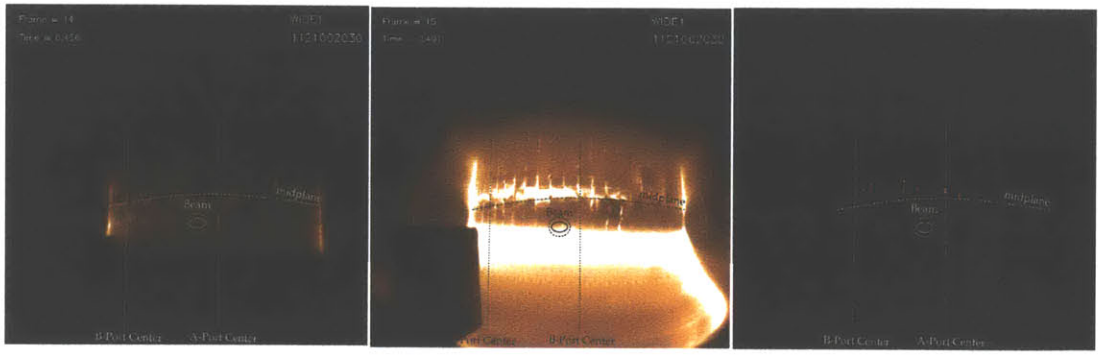

Figure 6-20: Views from the WIDE1 visble camera. Left: Stable ohmic inner wall limited plasma. Middle: View of plasma during disruption. Right: Black body radiation is observed as a red-orange glow tiles heated by the disruption. Solid ellipse denotes predicted beam spot, dotted ellipse denotes predicted uncertainty in position.

The IWL configuration shows a "band" of light at the center-post as expected, since the inner wall is the primary material target for recycling and power exhaust in such a configuration (the last-closed flux surface is resting on the inner wall). The disruption also seems to have concentrated its particles at the inner-wall, however with such strong intensity that it saturates the camera (this verifies intense PMI but no quantitative assessment of local plasma conditions can be made).

The intense PMI caused by the disruption indicated by the camera frame immediately following the disruption. Thermal emission is can be seen tiles near the midplane indicating substantial transient heating due to the disruption (the thermal emissions are absent in the following frame). Interestingly this region just below the midplane of intense interactions/heating with the disruption is the same as measured by AIMS.

Disruptions rapidly cool the plasma so significantly increased sputtering (which would require prolonged higher edge temperatures) is unlikely. However, disruptions can deposit enough thermal energy, causing melting of the molybdenum surfaces. If such melting were to occur it would likely disturb boron surface layer leading to a change in boron that would be observable with AIMS. Since no significant change was observed during the disruption, AIMS suggests that no surface melting is likely to have occurred.

This is confirmed by a simple estimate by considering the expected heating of the PFC surface cause by the disruption in the vicinity of the AIMS measurement. If all of the estimated plasma stored energy $U = 45$ kJ is lost directly the the centerpost region shown in the last camera frame, the resulting estimated energy density $\epsilon = 160$ kJ/m^2 deposited on the tiles in the region of plasma contact (assuming the height of the plasma wetted area $z_w = 0.1$ m and circumference $= 2\pi \times 45$ cm). With the relevant plasma parameters and thermal properties, an estimate of the surface temperature rise is given assuming energy density ϵ is delivered over the transient timescale τ in equation 6.2.

$$\left.\begin{array}{rcll} B_\phi & = & 5.4 & [\mathrm{T}] \\ I_p & = & 0.8 & [\mathrm{MA}] \\ n_e & = & 1.25 \times 10^{20} & [\mathrm{m}^{-3}] \\ \langle T \rangle & \approx & 800 & [\mathrm{eV}] \\ U & \approx & 45 & [\mathrm{kJ}] \\ R_{\mathrm{wall}} & \approx & 0.45 & [\mathrm{m}] \\ z_{\mathrm{wetted}} & \approx & 0.1 & [\mathrm{m}] \\ \epsilon & \approx & 160 & [\mathrm{kJ/m^2}] \\ \tau & \approx & 1 & [\mathrm{ms}] \\ \rho\, c_v & \approx & 3 \times 10^6 & [\mathrm{J/m^3K}] \\ \kappa_{Mo}, \kappa_B & = & 138,\ 27.4 & [\mathrm{W/mK}] \\ \kappa_{B,Mo} & \approx & 100 & [\mathrm{W/mK}] \end{array}\right\} \quad \Rightarrow \quad \Delta T = \frac{2}{\sqrt{\pi\, \rho\, c_v\, \kappa}} \frac{\epsilon}{\sqrt{\tau}} \approx 330 \text{ K} \tag{6.2}$$

With the estimated 330 K estimated temperature rise, melting of the Mo could not have occured. This estimate is far from exact due the imprecise methods for determining the plasma wetted area or the thermal properties of the surface of the mixed Mo-B surface. However, AIMS clearly indicates a negligible change in the surface properties through the measurement of boron that agrees the conclusion of this estimate. Furthermore, such measurements of boron surface conditions were previously not available for any plasma shots under any conditions. This therefore demonstrates why a diagnostic like AIMS is required since the response of the surface to PMI cannot be quantified or understood without direct measurement of surface properties before and after the PMI event occurs.

6.7.1 Complete Time Boron History

With the demonstrated AIMS measurement of boron during the C-Mod run day, it was then possible to combine all of the AIMS measurements of the $B_\phi = 0$ T location spanning the entire duration of the AIMS Campaign. The compilation is shown in figure 6-21. This plot was generated from the high energy neutron scattering data, scaled to minimize the deviation from photopeak measurements. As described in table 6.2 and 6.1, these measurements span several months containing 22 C-Mod plasma discharges, 1 disruption and 5 plasma wall conditioning operations. The success of the intershot measurements and the success of the measurements of wall conditioning combined with the continuity of the measurements within uncertainty over a 1 month gap in operations provides a thorough demonstration of the capabilities of the AIMS technique and provides successful demonstration of AIMS as a first of a kind PMI diagnostic.

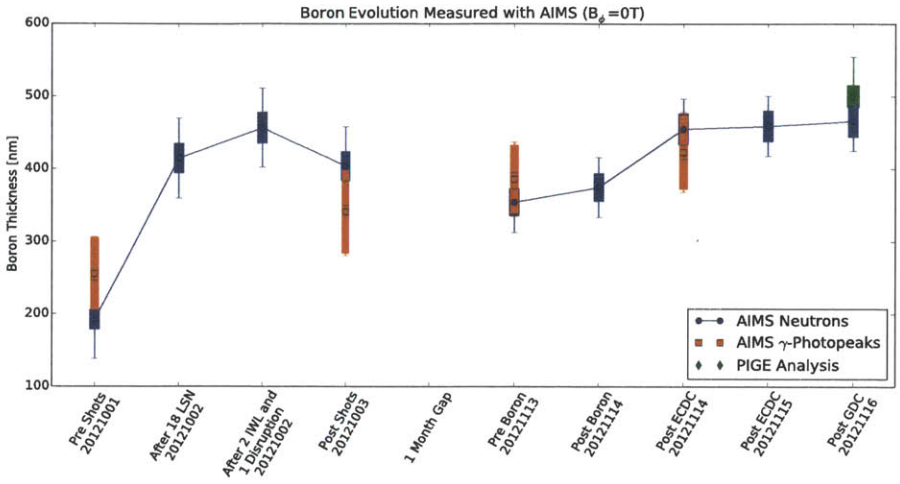

Figure 6-21: Boron time history spanning the entire AIMS run campaign 1 day of C-Mod operations followed by wall conditioning operations at the $B_\phi = 0$ T location. The PIGE measurement at the end of the campaign is also shown for comparison.

6.8 Conclusions

The AIMS diagnostic was successfully implemented on Alcator C-Mod yielding the first spatial resolved and quantitative in-situ measurements of boron in a tokamak. By combining AIMS neutron and gamma measurements, time resolved and spatially resolved measurements of boron were made, spanning the entire AIMS run campaign which included lower single null plasma shots, inboard limited plasma shots, a disruption, and C-Mod wall conditioning procedures. These measurements demonstrated the capability if AIMS to perform inter-shot measurements at a single location and spatially resolved measurements on over longer timescales (with great potential for improved timescales and resolution). This demonstration showed the first in-situ measurements of surfaces in a magnetic fusion device with spatial and temporal resolution which constitutes a major step forward in fusion PMI science.

An external ion beam system was also implemented to perform ex-situ ion beam analysis (IBA) on large components removed from Alcator C-Mod. This system was used to perform particle induced gamma emission (PIGE), a well established IBA technique, on tile modules to validate the AIMS technique. From these external PIGE measurements, a spatially resolved map of boron areal density was constructed for a section of C-Mod inner wall tiles that overlapped with the AIMS measurement locations. These measurements showed the complexity of the poloidal and toroidal variation of boron areal density between PFC tiles on the inner wall ranging from 0 to 3μm of boron. Using these well characterized ex-situ measurements to corroborate the in-situ measurements, AIMS showed reasonable agreement with PIGE, thus validating the quantitative boron detection capability of the AIMS technique.

6.9 Future Directions for AIMS

With the successful demonstration of AIMS, there is now the opportunity to expand on the AIMS prototype create a more versatile diagnostic with improved spectroscopy techniques in addition to improvements in accelerator technology, beam instrumentation, and detector optimization. Ideas and methods for improving on the AIMS technique are discussed below and are outlined in appendix A.

Accelerator Technology

The RFQ accelerator used for AIMS produces a 900 keV beam. This beam energy is adequate but was chosen primarily because of the availability of the accelerator and was not necessarily the optimal choice for IBA. Energies >1.5 MeV would be advantageous for AIMS because of the increased cross sections for boron and other low-Z reactions [49]. However, if a different accelerator with increased beam energy E_{new} is considered, increased steering fields ($B_{\text{new}}/B_o = \sqrt{E_{\text{new}}/E_o}$) will be required to access the same range of target locations.

The refurbished DL-1 RFQ used for AIMS contributed significant unexpected technical difficulties to the implementation of the diagnostic. The first major issue was the low beam duty factor which was typically 0.3%. This is a factor of 15 lower than the design duty factor so the measurements required significantly longer acquisition times for the detectors. The second major issue was the uncertainty in the beam energy (described in section 4.8) which increased the uncertainty in the spectroscopic measurements. Both of these issues can be dramatically improved with more refined accelerator technology and better beam characterization.

Beam Instrumentation and Control

Advanced simulation tools were developed for AIMS, however, these modeling efforts rely on accurate beam parameters for their inputs. The beam's phase space parameters should be well characterized for the beam dynamics simulation which can be done using theoretical methods described in section 5.5. Accelerator alignment proved to be a major issue in the AIMS measurements. Provisions must made in the future to determine alignment of the beam with respect to the inside of the tokamak rather than just the injection flange. An in-vessel boron nitride scintillating beam target would be a very helpful installation to validate determine the alignment and validated AIMS beam trajectory modeling. A preliminary design for such a target can be found in [21].

Some of the necessary beam diagnostics were already developed and used for AIMS (described in section 4.7). These can be improved upon and made retractable for permanent installations in beamline. Some preliminary designs for a retractable RBS spectrometer for measuring beam energy and a retractable scintillating beam imaging tool for in-situ characterization of the beam's transverse dimensions are described in appendix B.

Upgrades to the C-Mod DC supplies would also improve the capabilities of AIMS

by enabling additional beam trajectories with a large range of deflection, thus improving the poloidal and/or toroid extent of AIMS measurements. Significantly expanding the accessible trajectories would undoubtedly require AIMS to use active control of remotely adjustable beam optics and to keep the beam sufficiently focused on target PFCs. The theory and modeling that this would require are described in chapter 5 and the necessary hardware is discussed in appendix B.

In addition energy, control could be advantageous for AIMS if higher energy beam were available. The ability to make measurements at multiple energies make depth profiling theoretically possible, however, the experimental feasibility is yet to be demonstrated. For a fixed energy beam like an RFQ, this capability would require the implementation of energy degrading techniques such as interchangeable degrader foils or using an inert gas filling the vessel to the slow the beam. Both of these techniques are described in appendix B.

Detectors and Spectroscopy

The most pressing issue for boron detection is the temperature related gain stability of the $LaBr_3$ detector. This issue was unexpected but was a major obstacle to the AIMS measurements but can likely be solved in a straightforward way by engineering an active cooling system for the detectors.

The low count rates from boron photopeaks were also made boron detection challenging and lead to long acquisition times ($\sim$10 minutes) making spatially resolved measurements from induced gammas challenging while also causing undesirable levels of uncertainty in the measurements. This is partly because the detector was placed further away from the target PFCs as not to occlude other diagnostics. Consequently, the spectra were dominated by scattered gammas rather than distinct photo peaks. Moving the detectors closer with a longer re-entrant tube would be advantageous in improving gamma counts. However, observing typical digitized waveforms from AIMS measurements (figure 2-7), it is not possible to increase the solid angle of the detector more than a factor of several with out exceeding the count rate limits of the detector.

Therefore, to improve quality of the spectroscopic measurements and decrease the acquisition time of the detector more detectors should be added in parallel. In addition, efforts should be made to find a technically feasible, optimal solution that would allow the detectors to be as close to the PFC targets as possible without exceeding their count rate limits while maintaining a high time averaged beam current but simultaneously increasing beam duty factor and decreasing the instantaneous current.

The technology exists to increase beam current by at least a factor of 10, detector solid angle increased by 50% by moving the detectors less than 20% closer, and 3 additional detectors can probably fit in the re-entrant tube. With these conservative estimates for possible improvements, for the same acquisition time, the Poisson error in the measurement could be reduced by a factor of $\sqrt{60}$, a factor of nearly 8. This also means that a technically feasible improvement involving more detectors, better accelerator equipment, and more optimal detection geometry, the beam acquisition

time could be reduced by at least a factor of 60. This would effectively improve AIMS measurement timescale from 10s of minutes to 10s of seconds. Now that AIMS has been proven as a successful first of a kind in-situ PMI diagnostic, with some future improvements AIMS could become a truly revolutionary diagnostic for PMI science.

Appendix A

Road Map for the Future of AIMS

A.1 Next Generation AIMS

AIMS can be significantly improved in next generation implementations with refinements to various aspects of its conceptual and engineering design. An outline of how the capabilities of AIMS can be expanded is presented:

A.1.1 Accelerator

The capabilities of the AIMS could be improved with optimized accelerator technology. An improved RFQ accelerator mounted near a horizontal port is a likely choice for the next generation implementation of AIMS. A larger accelerator with more flexible beam parameters such as a tandem accelerator mounted farther from the tokamak with a more elaborate beam transport system is also a possibility and would be immensely beneficial for the versatility of AIMS because of ion species and beam energy that it could provide. However, an RFQ based design will be the focus of this discussion to retain engineering similarity to the current version of AIMS.

Beam Energy

One of the most significant improvements in the capability of AIMS would come from the increasing the beam energy to 1.5 MeV or greater. Higher energy would allow AIMS to access many reactions that cannot be observed with a 900 keV beam. For example cross section for the $^{11}\mathrm{B}(d,p\gamma)^{12}\mathrm{B}$ (E_γ = 953 keV) would be substantially larger as well as the D-D fusion cross section. Other reactions such as $^{11}\mathrm{B}(d,p\gamma)^{12}\mathrm{B}$ (E_γ = 1674 keV) and $^{16}\mathrm{O}(d,p\gamma)^{17}\mathrm{O}$ (E_γ = 656 keV) would also be available in addition to many others [49].

Beam Current

The other major improvement that can be made with accelerator hardware is improvements in the time-structure of the beam. Presently, beam pulses have very high instantaneous current (> 1 mA) and low duty factor (0.15-0.30%). While this has

advantages for background rejection, it makes spectroscopy more difficult due to the low time averaged beam current and count rates.

A.1.2 Beam Accessibility

The next improvement would be the installation DC toroidal and vertical field power supplies that could deliver higher fields for beam steering to increase the spatial extent of the tokamak wall that the AIMS diagnostic can access. Further optimization of the port location and injection geometry would also benefit accessibility. Increasing the range of available trajectories would undoubtedly require increased require improved, actively controlled beam optics that could be tuned for each trajectory.

A.1.3 Detection and Spectroscopy

With the improvements on accelerator performance (energy and/or beam current) discussed earlier, many of the detection difficulties will be reduced significantly. However more detectors would dramatically improve the quality of the AIMS spectroscopic measurements, especially for the gamma measurements which have been shown to produce relatively low count rates in current configuration of AIMS. Higher detection rates would decrease the acquisition time and improve the detection statistics.

A.1.4 Other IBA techniques using AIMS

If AIMS were to use a higher energy accelerator (1.5 - 2 MeV), other ion beam analysis techniques would become available. For example, particle induced X-ray emission (PIXE) would be possible since the kinematics of D^+ collisions with electrons at these energies would allow the beam to induce X-ray transitions. The addition of X-ray detectors with direct line-of-sight to the target location would be required and might cause some engineering challenges. However, the use of PIXE analysis in-situ would allow measurement of high-Z elements and would be a major improvement to the versatility of the AIMS diagnostic.

A.1.5 AIMS on Other Tokamaks

AIMS is a technique that can and should be applied to tokamaks other than Alcator C-Mod. There are several considerations that should addressed when scaling the current implementation of AIMS to other tokamaks.

1. **Beam transport:** As tokamaks get larger the optics and transport of the beam become more difficult because the beam target is must much farther from the last optic which is outside of the tokamak. The beam must therefore travel to several meters of distance or more before reaching its target. Low current beams with low emittance are required because the space and non-laminar effects within the beam are a fundamentally limit to optics ability collimate the beam over long distances.

2. **Steering fields:** Alctor is particularly well suited for AIMS because of its high field design. However, not all tokamks have the necessary DC power-supplies or magnet cooling to provide sufficient magnetic fields to steer the beam to all of the desired locations. In addition, superconducting tokamaks may not be able to rapidly change their fields to provide the spatially resolved measurements are an feature of AIMS measurements. This could limit the use of AIMS to only start up and shutdown phases of the TF coils operation in superconducting tokamaks.

3. **Beam and detection geometry:** As with Alcator C-Mod, port space is major constraint on the injection geometry of the beam into the tokamak. An analysis of accessibility with consideration of the port space limitation is necessary for installation on any tokamak. The detection geometry also becomes more difficult if the tokamak is larger because the solid angle decreases like $1/r^2$. For large tokamaks, retractable detectors should be considered to improve the detector solid angle.

A.2 Improvements on the Current AIMS Diagnostic

The AIMS performed very well as a proof of principle diagnostic, however, with some improvements to its hardware and geometry, the diagnostic could be improved substantially. A discussion of high priority, short term, and long term engineering improvements for AIMS are outlined below.

A.2.1 High Priority

1. **Reliable RF system:** The original RF system is currently unreliable and performs below its design specifications due damaged tubes and possibly some design issues. Since it has been shown that the average beam energy varies with RF power it is necessary to have a stable RF system that can repeatably couple sufficient power (50-60 kW) to the RFQ cavity. Substantial repairs or replacement of the original RF system could improve the reliability measurements and is absolutely necessary for the AIMS diagnostic.

2. **Thermal stabilization of detectors:** Thermal stabilization of $LaBr_3$ detector is necessary for gamma spectroscopy measurement. Many of the spectra taken with AIMS were unusable due to drift in the detector's gain. This was likely due to temperature fluctuations in the avalanche photo-diode in the $LaBr_3$ detector which could have been caused by radiative heat transfer from the vessel walls due to liquid nitrogen cooling of the toroidal field coils and heaters around B-port. The implementation of a liquid cooling or gas cooling system for the detector would likely solve this problem.

3. **Beam characterization:** Currently, the accelerator's design specifications are used as inputs for the beam modeling codes. The beam was shown to deviate significantly from these parameters, especially in its energy distribution. Therefore, the beam requires better characterization so that a reliable set of beam parameters can be used for modeling and spectroscopy calculations.

4. **Beam alignment and calibration:** Uncertainty in beam alignment was problematic in modeling of trajectories and the analysis of AIMS measurements. To resolve this issue, there must be at least one point of reference on the C-Mod wall to verify the no-field alignment. This can be done with a that laser aligned with the RFQ vanes and pointed through the injection flange onto the inner wall. This would provide a high degree of certainty in where the beam target is located and could be used to determine the geometric inputs for the trajectory calculation. A scintillating target such as boron nitride, mounted inside of the vessel would also be advantageous because, scintillation light from the target could provide verification of the beam shape and location on target and would provide a known calibration standard for the detectors.

A.2.2 Short Term Improvements

Beam Accessibility and Spectroscopy

1. **Optimization of beam injection geometry:** The accessibility of certain regions of C-Mod could be improved without modification to the toroidal field supplies through small changes in the beam injection geometry. For example, the inner divertor could be accessed if the beam injection angle was increased by $4^o - 5^o$. This is possible with small modifications to the accelerator stand. An optimization study should be performed using the full-field trajectory modeling code developed in chapter 5 to determine the best beam injection geometry to access locations where physically interesting PMI can be observed such as the inner divertor.

2. **Reverse B-field operation:** The accessibility of the beam trajectories could be improved in the short term by adding a remotely operated switching system that could change the polarity of the toroidal field coils. The capability to switch the direction of current through the coils remotely would effectively double the range of AIMS trajectories without upgrades to the power supply.

3. **More detectors:** With more detectors, the quality of the AIMS spectroscopic measurements could be improved, especially for the gamma measurements. Since the digitizer is already equipped with 8-channels (of which only 3 are used), this would be a simple solution that would decrease the necessary required acquisition time proportionally with the increase in the number of detectors. It would also improve the Poisson uncertainty of the measurements since more counts would be detected.

Hardware and Controls

1. **New software interface:** The current computer interface that controls the RFQ is programmed in LabView. The reliability of the accelerator would benefit from a more stable interface that can be maintained with by C-Mod staff.

2. **Improved source current monitor:** The current transformer that measures the injector current is intermittent and unreliable. Replacing it would provide for reliable source current measurement to determine beam transmission through the RFQ.

3. **New deuterium flow controller:** The mass flow controller that delivers deuterium gas to the ion source is unreliable and needs replacement

A.2.3 Long Term Improvements

1. **Injector alignment:** The RFQ is extremely sensitive to the injection angle of the source beam and its collinearity with the axis of the cavity. Misalignment typically leads to poor beam transmission, however we suspect it also contributes to the uncertainty of the final accelerated beam energy and its sensitivity to RF amplitude. The current design does not allow for any adjustment of source alignment. A completely redesign and remachined injector would be required allow the necessary flexibility to align the source with the RFQ. This upgrade is major engineering commitment but should be done as soon as possible to ensure a reliable beam with minimal energy spread.

2. **Upgrade toroidal field supply:** Increasing the toroidal field would significantly improve accessibility of the RFQ beam. C-Mod's magnet supplies currently produce a maximum 4500 amps of DC current to the toroidal field coils. To access the lower and outer divertor regions, 10000-12000 amps are required. This upgrade is possible because such power supplies are available and preliminary analysis has shown that the coils have adequate cooling. This upgrade should be made but it will require substantial engineering efforts and is not expected occur on a short timescale.

3. **Upgrade toroidal field supply:** The DC power supplies for the vertical field coils are currently inadequate for steering the beam. Upgrades to the vertical field coil supplies would also be beneficial for improved spatial resolution. Further analysis is required to determine the optimal requirements for the vertical field.

Appendix B

Future Beamline Developments

New beam hardware developments could greatly expand the verstaility and extend the capabilities of AIMS in future implementations of the diagnostic. Some of ideas for new beamline innovations were studied and presented.

B.1 Beam Steering and Active Focusing

It would be advantageous for the AIMS diagnostic to have the capability of analyzing a larger range of the C-Mod PFCs. For the current implementation, the range of trajectories is relatively small due to limitations of the magnet power supplies. With this limited set of trajectories, the permanent magnet quadrupoles can be set to fixed positions in a way that provides acceptable focusing for all trajectories. Larger magnet supplies would allow for greater range of trajectories but with increasingly different beam path lengths and trajectory curvature. For larger deflections, it will no longer be possible to adequately focus the beam for all trajectories with non-adjustable focusing.

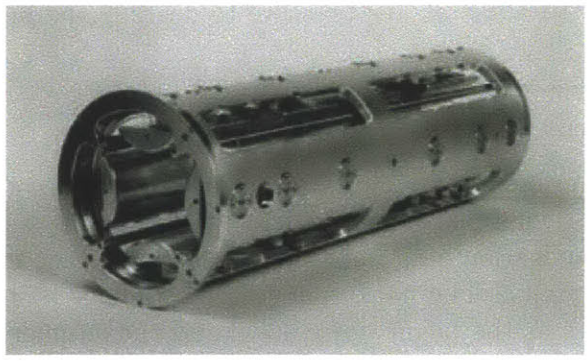

Figure B-1: Electrostatic quadrupole doublet from National Electrostatics Corporations [8].

To accommodate improved beam steering capability, active control the beam optics are required. The main criterion for these optics that they must be adjustable

in a way that is reliable and repeatable. They must also be non-magnetic to avoid interactions with the tokamak fields and the must be small enough to satisfy geometric constraints. Appropriate solution would be the use of non-magnetic quadrupoles such as the electrostatic quadrupole doublets available from NEC [8]. The use of electrostatic quads combined with beam dynamics modeling techniques described in chapter 5 for active focusing could allow for finer and more reliable spatial resolution for a larger set of trajectories.

B.2 Retractable Beam Diagnostics

Beam imaging through scintillation has already been demonstrated using a quartz window for beam imaging and alignment. If adjustable optics are implemented it will be necessary to periodically measure the beam shape to observe the transverse shape of the beam to verify the settings of the optics and the beam quality. A retractable design for a beam imaging system is shown in figure B-2. A beam energy spectrometer like the one described in section 4.7.4 would also be useful to verify the energy spread of the beam. This is necessary to characterize the longitudinal momentum component of the distribution for modeling purposes and to verify that the beam is approximately mono-energetic in order to make reliable spectroscopic measurements. This can be done in-situ using the retractable thin film RBS spectrometer shown in figure B-2.

B.3 Energy Control for Fixed Energy Beams

Beam energy control can greatly increase the versatility of diagnostic system. Some ion beam applications, medical irradiations in particular, combine a fixed energy accelerator with an adjustable energy "degrader" to slow the beam to a desired energy. This is typically done with thin target foils or movable wedge plates for continuously variable energy control. In a tokamak environment however, it is also possible to fill the vacuum vessel with a gas at low pressure to degrade the beams energy over its entire trajectory.

Solid foils for energy control

For ~1 MeV beams only thin ($\sim$ 1 μm) foils can be used because of the low beam energy. This makes wedge plates impractical. Metallic foils such as aluminum are well suited for this application because of their availability, vacuum compatibility, and high thermal conductivity. The performance of these foils is limited by the energy straggling that occurs as the beam slows down and the number of foils that can be applied.

In principle, the optimal method of applying foils is by having a set of n foils of distinct thickness τ_n that can be independently inserted into the beam's path in any combination. Each foil then cause an energy loss $\delta_n = S\,\tau_n$ given by equation B.1. To uniformly span the energy range E_0 to E_{min}, δ_n should be chosen based on a

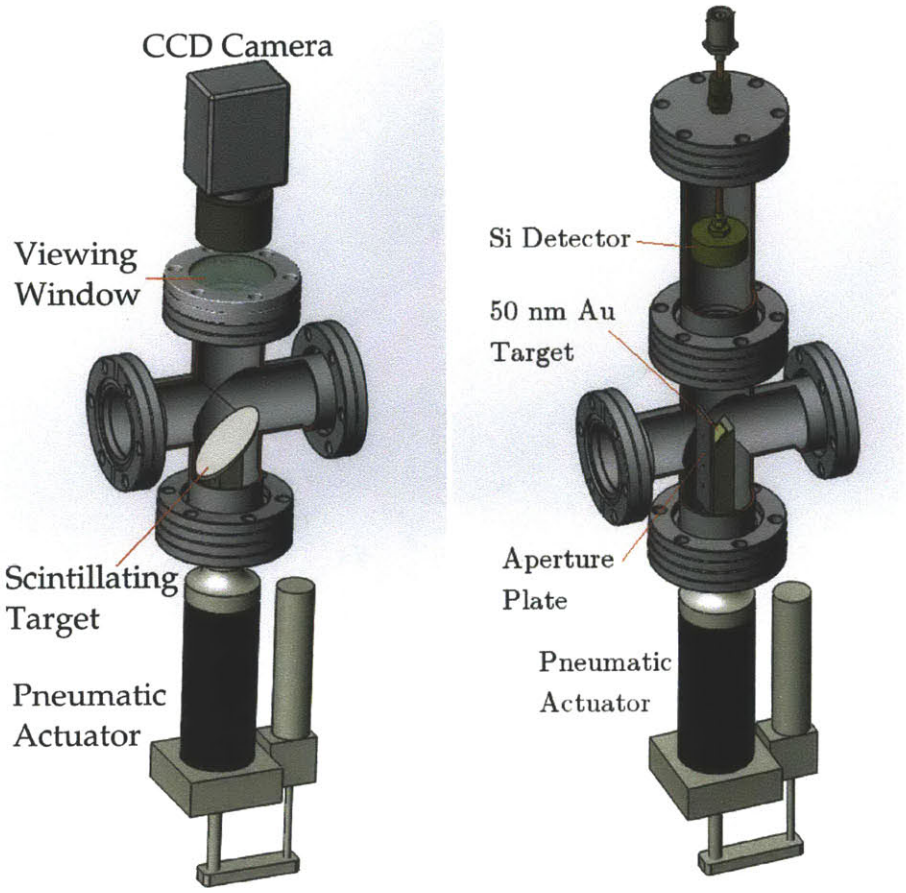

Figure B-2: Left: Design for a compact retractable beam imaging target. Right: Design for a compact retractable thin film backscattering beam energy spectrometer.

geometric series $1/s^n$ given by equation B.2. With all of the 2^n possible combinations, ignoring straggling, this provides energy resolution of $(E_0 - E_{min})/2^n$.

$$E_0 - (\delta_1 + \delta_2 + ... + \delta_n) = E_{min} \tag{B.1}$$

$$\delta_1 + \delta_2 + ... + \delta_n = \frac{E_0 - E_{min}(1 - \frac{1}{2^n})}{2^n} \left(\frac{1}{2} + \frac{1}{4} + \frac{1}{8} + ... + \frac{1}{2^n} \right) \tag{B.2}$$

Realistically, it may be difficult to implement enough vacuum actuators or fabricate enough foils of the appropriate thickness to make such a system with large n. An alternative system to simplify fabrication could use an indexed rotating disks with a selection of n foils to span the desired energy range. The energy resolution this rotating system would have less desirable energy resolution, $(E_0 - E_{min})/n$, but would only require one rotating feedthrough.

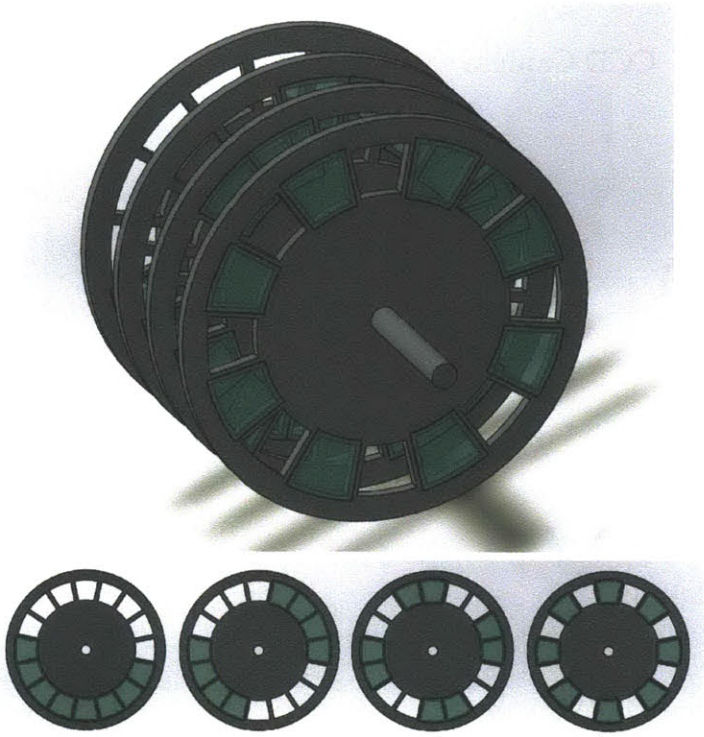

Figure B-3: Energy degrader disks using indexed foils to reduce beam energy in discrete increments. The design shown with 4 disks allows for 16 distinct energy settings.

A thermal analysis should be perform to ensure sufficient heat dissipation in these foils. However, this is not expected to be an serious limitation. Since the RFQ beam is $\sim$1 cm in diameter, even if it approaches 10μA of time averaged current, the heating will be comparable to that of the beam exit foils for external ion beam analysis in chapter 3. If aluminum foils are used, thermal analysis can be performed simply with a 1-D conduction model since the thermal conductivity is relatively high.

Gas fill for energy control

Filling the vessel with a low pressure gas such as helium, or argon could be used as a method to slow the beam for energy control. The gas densities required to slow a 0.9 MeV beam within the range 0.2-0.8 MeV were calculated numerically using stopping data from SRIM [68] and is shown in figure B-4. This shows that with realistic gas pressures of $0.01 - 0.1$ atmospheres, the energy can be sufficiently controlled.

The vacuum-gas interface between the accelerator and the vessel must be considered. The vacuum-gas interface can be made straightforwardly using a beam window like the external beam exit foils developed in chapter 3 or by using differential pumping methods.

The effects of the gas on the beam distribution must also be taken under consider-

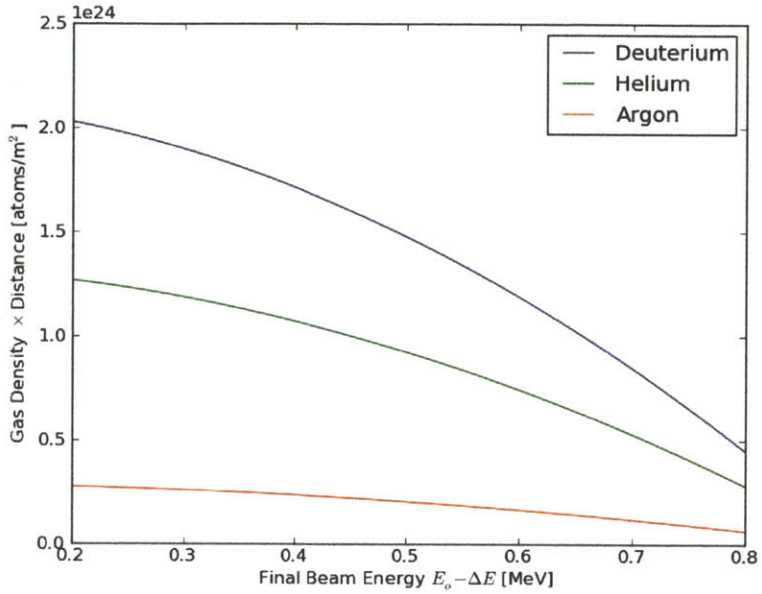

Figure B-4: The gas density required for degrading the beam energy per unit trajectory length was calculated using stopping data from SRIM [68].

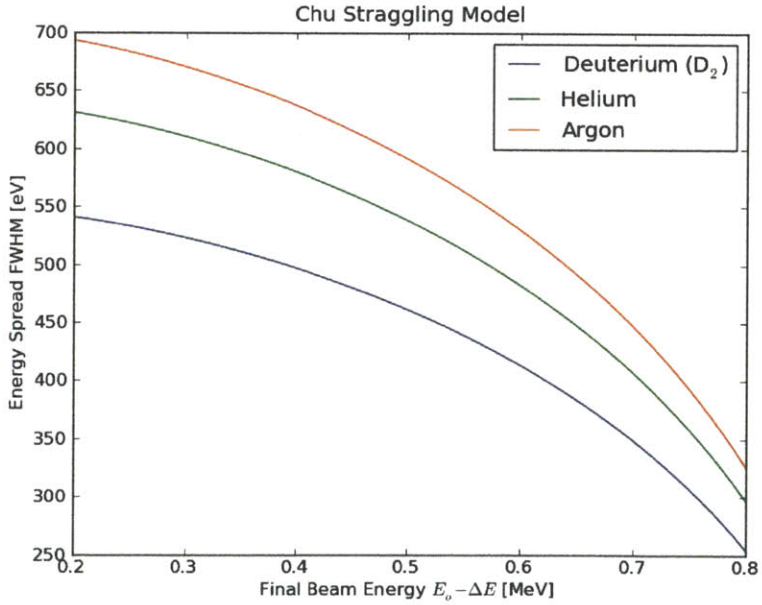

Figure B-5: The Chu model [67] was used to calculate the energy straggling of the beam passing through a gas filled chamber

ation. The energy straggling as a function of final beam energy was calculated using the Chu model [67] and plotted figure B-5. The result indicates that energy straggling is less than 1 keV and is therefore inconsequential. The effects on the particle distribution however may be complicated since the gas exchanges momentum with the beam causes emittance growth. This effect and the continuously varying beam energy will have to be properly modeled in the beam trajectory and dynamics codes.

Bibliography

[1] AccSys Technology, Inc, 1177 A Quarry Lane, Pleasanton, CA 94566. *Operation Manual for Model DL-1 Linac Neutron Generator System - Serial Number 001: for the U.S. Department of Transportation - Transportation Systems Center*, October 1994.

[2] C. Angulo, M. Arnould, M. Rayner, P. Descouvemont, D. Baye, C. Leclercq-Willain, A. Coc, S. Barhoumi, Aguer, C. Rolfs, R.Kunz, J.W. Hammer, A. Mayer, T. Paradellis, S. Kossionides, C. Chronidou, K. Spyrou, P. DeglInnocenti, G. Fiorentini S., B. Ricci, S. Zavataelli, C. Providncia, H. Wolters, J. Soares, C. Grama, J. Rahighi, A. Shotter, and M. Lamehi Rachti. A compilation of charged-paricle induced thermonuclear reaction rates. *Nuclear Physics A*, 656:3–183, 1999.

[3] Harold Salvadore Barnard. External proton beam analysis of plasma facing materials for magnetic confinement fusion applications. Master's thesis, Massachusetts Institute of Technology, 2009.

[4] HS Barnard, B Lipschultz, and DG Whyte. A study of tungsten migration in the alcator c-mod divertor. *Journal of Nuclear Materials*, 415(1):S301–S304, 2011.

[5] B.L.Doyle, D. S. Walsh, and S.R. Lee. External micro-ion-beam analysis (x-miba). *Nuclear Instruments and Methods in Physics. Section VII. Materials applications: B. Other Applications*, B54:244–257, 1991.

[6] PT Bonoli, R Parker, Stephen J Wukitch, Yijun Lin, Miklos Porkolab, John C Wright, E Edlund, T Graves, Liang Lin, J Liptac, et al. Wave-particle studies in the ion cyclotron and lower hybrid ranges of frequencies in alcator c-mod. *Fusion Science and Technology*, 51(3):401–436, 2007.

[7] KL Brown, DC Carey, Ch Iselin, and F Rothacker. Computer program for designing charged particle beam transport systems. *SLAC-91 (1973 Rev.), NAL*, 91:80–04, 1973.

[8] National Electrostatics Corporation. Negative ion beam sources. www.pelletron.com.

[9] Tim Davis. *Beam Profile Monitors*. National Electrostatics Corporation, April 2004. URL: http://www.pelletron.com/bpm.htm.

[10] Robert B. Day and Torben Huus. Gamma radiation from b^{10} bombarded by protons. *Physical Review*, 95(4):1003–1006, 1954.

[11] R.D. Deslattes, E.G. Kessler Jr., P. Indelicato, L. de Billy, E. Lindroth, J. Anton, J.S. Coursey, D.J. Schwab, J. Chang, R. Sukumar, K. Olsen, and R.A. Dragoset. Physical reference data: X-ray transition energies. National Institute of Standards and Technology, September 1996. URL: http://physics.nist.gov/PhysRefData/XrayMassCoef/cover.html.

[12] JP Duke, DJS Findlay, AP Letchford, and J Thomason. Improved results from the gas scattering energy spectrometer on the isis rfq test stand. In *Particle Accelerator Conference, 2003. PAC 2003. Proceedings of the*, volume 4, pages 2542–2544. IEEE, 2003.

[13] Dupont. *General Specifications for Kapton® Polyimide Film.* URL: http://www2.dupont.com/Kapton/en$_U$S/*index.html*.

[14] B. Lipschultz E. Marmar, Y. Lin, D. Whyte, P. Bonoli, C. Fiore, M. Greenwald, I. Hutchinson, J. Irby, M. Reinke, J. Rice, S. Scott, J. Terry1, S. Wolfe1, S., Wukitch, and Alcator Team. Operation of alcator c-mod with high-z plasma facing components with and without boronization. *33rd EPS Conference on Plasma Phys,Rome*, 30I, June 2006.

[15] Gianfranco Federici, Charles H Skinner, Jeffrey N Brooks, Joseph Paul Coad, Christian Grisolia, Anthony A Haasz, Ahmed Hassanein, Volker Philipps, C Spencer Pitcher, Joachim Roth, et al. Plasma-material interactions in current tokamaks and their implications for next step fusion reactors. *Nuclear Fusion*, 41(12):1967, 2001.

[16] Python Software Foundation. Python 3.0 programming language. 1990-2013.

[17] Jeffrey Freidberg. *Plasma Physics and Fusion Energy*, chapter 1. Uniersity Press, 2007.

[18] General Ionex Incorporated. *1.7 MV Tandetron Manual*, 1982.

[19] General Ionex Incorporated. *Cesium Sputtering Source 860*, 1982.

[20] David Jeffrey Griffiths and Reed College. *Introduction to electrodynamics*, volume 3. prentice Hall Upper Saddle River, NJ, 1999.

[21] Zachary S. Hartwig. *An in-situ accelerator-based diagnostic for plasma-material interactions science in magnetic fusion devices.* PhD thesis, Massachusetts Institute of Technology, 2014.

[22] Zachary S Hartwig, Harold S Barnard, Richard C Lanza, Brandon N Sorbom, Peter W Stahle, and Dennis G Whyte. An in situ accelerator-based diagnostic for plasma-material interactions science on magnetic fusion devices. *Review of Scientific Instruments*, 84(12):123503, 2013.

[23] Stanley Humphries and Stanley Humphries Jr. *Charged particle beams*, chapter 3: Introduction to beam emittance. DoverPublications.com, 2013.

[24] Stanley Humphries and Stanley Humphries Jr. *Charged particle beams*, chapter 2: Phase space description of charged-particle beams. DoverPublications.com, 2013.

[25] Stanley Humphries and Stanley Humphries Jr. *Charged particle beams*, chapter 5: Introduction to beam generated forces. DoverPublications.com, 2013.

[26] Ian H Hutchinson, R Boivin, F Bombarda, P Bonoli, S Fairfax, C Fiore, J Goetz, S Golovato, R Granetz, M Greenwald, et al. First results from alcator-c-mod@ f—. *Physics of Plasmas*, 1:1511, 1994.

[27] ITER. *The ITER Project.* URL: http://www.iter.org.

[28] Erik Boyd Iverson. *Windowless gas targets for neutron production.* PhD thesis, Massachusetts Institute of Technology, 1997.

[29] D.Rusthoi K.Crandall. *Trace3D Documentation.* LANL, 1997.

[30] M Keilhacker, A Gibson, C Gormezano, PJ Lomas, PR Thomas, ML Watkins, P Andrew, B Balet, D Borba, CD Challis, et al. High fusion performance from deuterium-tritium plasmas in jet. *Nuclear Fusion*, 39(2):209, 1999.

[31] Glenn F. Knoll. *Radiation Detection and Measurement*, chapter 3: Counting Statistics and Error Propagation. John Wiley and Sons Inc., thrid edition, 2000.

[32] Glenn F. Knoll. *Radiation Detection and Measurement*, chapter 8: Scintillation Detector Principles. John Wiley and Sons Inc., thrid edition, 2000.

[33] Glenn F Knoll. *Radiation detection and measurement.* Wiley. com, 2010.

[34] Brookhaven National Laboratory. Experimental nuclear reaction data (exfor / csisrs). URL:http://www.nndc.bnl.gov/exfor/exfor00.htm, 2008.

[35] LabVIEW. National instruments. *Austin, Texas*, pages 78730–5039, 2009.

[36] P. Lapostolle. *CERN Report AR/Int SG/65-15: Effects de la charge d'espace dans un accelerateu lineaire a protons.* CERN, 1965.

[37] Group3 Technology Ltd. Group3 loop controller. *Auckland, Auckland*, page www.group3technology.com, 2012.

[38] Matej Mayer. Simnra user's guide. 1997.

[39] M.Greenwald. *Priorities, Gaps and Opportunities: Towards A Long-Range Strategic Plan For Magnetic Fusion Energy.* A Report to the Fusion Energy Sciences Advisory Committee, October 2007.

[40] Roy Middleton. A negative ion cookbook. *University of Pennsylvania*, 1989.

[41] Roman Ochoukov, Dennis Whyte, Bruce Lipschultz, Brian LaBombard, Niels Gierse, and Soren Harrison. Study and optimization of boronization in alcator c-mod using the surface science station (s3). *Fusion Engineering and Design*, 87(9):1700 – 1707, 2012.

[42] Ortec. *MAESTRO-32: MCA Emulator for Microsoft Windows 2000 Professional and XP Professional, A65-B32 Software User's Manual.* Software Version 6.0, Revision L.

[43] E. Rauhala and J. Räisänen. Stopping powers of 0.5 – 8.3 mev protons in havar, nickel, kapton, and mylar. *Nuclear Instruments and Methods in Physics Research B35*, pages 130–134, 1988.

[44] M. Rubel, P. Wienhold, and D. Hildebrandt. Ion beam analysis methods in the studies of plasma facing materials in controlled fusion devices. *Vacuum*, 70(23):423 – 428, 2003. ¡ce:title¿The International Symposium on Ion Implantation and Other Applica tions of Ions and Electrons - {ION} 2002¡/ce:title¿.

[45] Stephan Russenschuck. *Field computation for accelerator magnets.* John Wiley & Sons, 2011.

[46] Frank J Sacherer. Rms envelope equations with space charge. *Nuclear Science, IEEE Transactions on*, 18(3):1105–1107, 1971.

[47] Peter C. Stangeby. *The Plasma Boundary of Magnetic Fusion Devices*, chapter 1: Simple Analytic Models of the Scrape-Off Layer. Institue of Physics Publishing, 2000.

[48] Richard H Stokes and Thomas P Wangler. Radiofrequency quadrupole accelerators and their applications. *Annual Review of Nuclear and Particle Science*, 38(1):97–118, 1988.

[49] GÁ Sziki, A Simon, Z Szikszai, Zs Kertész, and E Dobos. Gamma ray production cross-sections of deuteron induced nuclear reactions for light element analysis. *Nuclear Instruments and Methods in Physics Research Section B: Beam Interactions with Materials and Atoms*, 251(2):343–351, 2006.

[50] David R. Tesmer and Michael Nastasi, editors. *Handbook of Modern Ion Beam Materials Analysis*, chapter 7 Nuclear Reaction Analysis, Particle–Gamma Reactions by J.P. Hirvonen. Materials Research Society, 1995.

[51] Joseph R Tesmer, Michael Anthony Nastasi, J Charles Barbour, Carl J Maggiore, and James W Mayer. *Handbook of modern ion beam materials analysis.* Materials Research Society Pittsburgh, PA, 1995.

[52] John P Verboncoeur. Particle simulation of plasmas: review and advances. *Plasma Physics and Controlled Fusion*, 47(5A):A231, 2005.

[53] W. R. Wampler. Ion beam analysis for fusion energy research. *Nuclear Instruments and Methods in Physics Research B*, (219220):836845, 2004.

[54] W.R. Wampler, B. LaBombard, B. Lipschultz, G.M. McCracken, D.A. Pappas, and C.S. Pitcher. Molybdenum erosion measurements in alcator c-mod. *Journal of Nuclear Materials*, 266-269(Section 2):217–221, 1999.

[55] Thomas P Wangler. *RF Linear accelerators.* Wiley. com, 2008.

[56] Robert C Webber. Tutorial on beam current monitoring. In *AIP Conference Proceedings*, volume 546, page 83, 2000.

[57] John Wesson. *Tokamaks*, volume 149. Oxford University Press, 2011.

[58] Helmut Wiedemann. *Particle accelerator physics*, chapter 5: Particle beams and phase space. Springer London, Limited, 2007.

[59] Helmut Wiedemann. *Particle accelerator physics*, chapter 2: Particle dynamics in electromagnetic fields. Springer London, Limited, 2007.

[60] Helmut Wiedemann. *Particle accelerator physics*, chapter 3: Electromagnetic fields. Springer London, Limited, 2007.

[61] Helmut Wiedemann. *Particle accelerator physics*, chapter 8: Particle beam parameters. Springer London, Limited, 2007.

[62] Helmut Wiedemann. *Particle accelerator physics*, pages 919–923 Appendix C: Transfer Matrices in Beam Dynamics. Springer London, Limited, 2007.

[63] BD Wirth, K Nordlund, DG Whyte, and D Xu. Fusion materials modeling: Challenges and opportunities. *MRS Bull*, 36:216–222, 2011.

[64] Brian D Wirth, Rick J Kurtz, and Lance L Snead. Fusion materials science and technology research needs: Now and during the iter era. In *Fusion Engineering (SOFE), 2013 IEEE 25th Symposium on*, pages 1–8. IEEE, 2013.

[65] CPC Wong, DG Whyte, RJ Bastasz, J Brooks, WP West, and WR Wampler. Divertor materials evaluation system (dimes). *Journal of nuclear materials*, 258:433–439, 1998.

[66] Graham Wright. *The Dynamics of Hydrogenic Retention in Irradiated Molybdenum.* PhD thesis, University of Wisconsin-Madison, 2007.

[67] Q Yang, DJ O'Connor, and Zhonglie Wang. Empirical formulae for energy loss straggling of ions in matter. *Nuclear Instruments and Methods in Physics Research Section B: Beam Interactions with Materials and Atoms*, 61(2):149–155, 1991.

[68] James F Ziegler, Jochen P. Biersack, and Matthias D. Ziegler. Stopping and range of ions in matter (srim2008). Software, 2008.